Springer Series in Light Scattering

Alexander Kokhanovsky *Editor*

Springer Series in Light Scattering

Volume 6: Radiative Transfer, Light Scattering, and Remote Sensing

Springer

Springer Series in Light Scattering

Series Editor

Alexander Kokhanovsky, VITROCISET Belgium, A Leonardo Company, Darmstadt, Germany

Editorial Board

Thomas Henning, Max Planck Institute for Astronomy, Heidelberg, Germany

George Kattawar, Texas A&M University, College Station, USA

Oleg Kopelevich, Shirshov Institute of Oceanology, Moscow, Russia

Kuo-Nan Liou, University of California, Los Angeles, USA

Michael Mishchenko, NASA Goddard Institute for Space Studies, New York, USA

Lev Perelman, Harvard University, Cambridge, USA

Knut Stamnes, Stevens Institute of Technology, Hoboken, USA

Graeme Stephens, NASA Jet Propulsion Laboratory, Los Angeles, USA

Bart van Tiggelen, J. Fourier University, Grenoble, France

Claudio Tomasi, Institute of Atmospheric Sciences and Climate, Bologna, Italy

The main purpose of is to present recent advances and progress in light scattering media optics. The topic is very broad and incorporates such diverse areas as atmospheric optics, ocean optics, optics of close-packed media, radiative transfer, light scattering, absorption, and scattering by single scatterers and also by systems of particles, biomedical optics, optical properties of cosmic dust, remote sensing of atmosphere and ocean, etc. The topic is of importance for material science, environmental science, climate change, and also for optical engineering. Although main developments in the solutions of radiative transfer and light scattering problems have been achieved in the 20th century by efforts of many scientists including V. Ambartsumian, S. Chandrasekhar, P. Debye, H. C. van de Hulst, G. Mie, and V. Sobolev, the light scattering media optics still have many puzzles to be solved such as radiative transfer in closely packed media, 3D radiative transfer as applied to the solution of inverse problems, optics of terrestrial and planetary surfaces, etc. Also it has a broad range of applications in many branches of modern science and technology such as biomedical optics, atmospheric and oceanic optics, and astrophysics, to name a few. It is planned that the Series will raise novel scientific questions, integrate data analysis, and offer new insights in optics of light scattering media. ***SPRINGER Series in Light Scattering***.

More information about this series at http://www.springer.com/series/15365

Alexander Kokhanovsky
Editor

Springer Series in Light Scattering

Volume 6: Radiative Transfer, Light Scattering, and Remote Sensing

Springer

Editor
Alexander Kokhanovsky
Vitrociset Belgium
Darmstadt, Hessen, Germany

ISSN 2509-2790 ISSN 2509-2804 (electronic)
Springer Series in Light Scattering
ISBN 978-3-030-71253-2 ISBN 978-3-030-71254-9 (eBook)
https://doi.org/10.1007/978-3-030-71254-9

© The Editor(s) (if applicable) and The Author(s), under exclusive license to Springer Nature Switzerland AG 2021
This work is subject to copyright. All rights are solely and exclusively licensed by the Publisher, whether the whole or part of the material is concerned, specifically the rights of translation, reprinting, reuse of illustrations, recitation, broadcasting, reproduction on microfilms or in any other physical way, and transmission or information storage and retrieval, electronic adaptation, computer software, or by similar or dissimilar methodology now known or hereafter developed.
The use of general descriptive names, registered names, trademarks, service marks, etc. in this publication does not imply, even in the absence of a specific statement, that such names are exempt from the relevant protective laws and regulations and therefore free for general use.
The publisher, the authors and the editors are safe to assume that the advice and information in this book are believed to be true and accurate at the date of publication. Neither the publisher nor the authors or the editors give a warranty, expressed or implied, with respect to the material contained herein or for any errors or omissions that may have been made. The publisher remains neutral with regard to jurisdictional claims in published maps and institutional affiliations.

This Springer imprint is published by the registered company Springer Nature Switzerland AG
The registered company address is: Gewerbestrasse 11, 6330 Cham, Switzerland

Contents

$\sqrt{\epsilon}$ Law: Centennial of the First Exact Result of Classical Radiative Transfer Theory 1
V. V. Ivanov

Solar Heating of the Cryosphere: Snow and Ice Sheets 53
Leonid A. Dombrovsky and Alexander A. Kokhanovsky

Stereological Methods in the Theory of Light Scattering by Nonspherical Particles 111
Aleksey Malinka

Inverse Methods in Studies of Terrestrial Atmosphere 175
Michael Yu. Kataev

Index 195

$\sqrt{\epsilon}$ Law: Centennial of the First Exact Result of Classical Radiative Transfer Theory

V. V. Ivanov

1 Introduction

Nowadays probably nobody knows when and where the term "$\sqrt{\epsilon}$ law" was coined. But as early as in 1975 in the title of one of the papers we find "$\sqrt{\epsilon}$ *revisited*" (Frisch and Frisch 1975). Hence someone has already *visited* it earlier. And then it started: "*An alternative derivation for* $\sqrt{\epsilon}$" (Landi Degl'Innocenti 1979), "*The* $\sqrt{\epsilon}$ *law*" (Hubeny 1987), "*...A generalization of the* $\sqrt{\epsilon}$ *law* " (Landi Degl'Innocenti and Bommier 1994), "*A generalized* $\sqrt{\epsilon}$*-law* " (Štěpán and Bommier 2007), "*...general form of the* $\sqrt{\epsilon}$ *law*" (Grachev 2014) and, finally, the title of this document initially was "$\sqrt{\epsilon}$ *law: retrospective*". Well, and what indeed is this $\sqrt{\epsilon}$, and why does it need so many generalizations?

The $\sqrt{\epsilon}$ law in its usual astrophysical formulation is the assertion that the degree of excitation of two-level atoms at the boundary of semi-infinite isothermal atmosphere is lover than its equilibrium Boltzmann value by a factor of $1/\sqrt{\epsilon}$. Here, ϵ is the probability of destruction of a photon of resonance line per scattering undergone by photons in its specific random walk in the atmosphere. The specific feature of this walk is caused by the possibility of tiny changes of photon frequency upon scattering. This leads to drastic changes in their mean free path length; averaged over the line, it is infinite (the so called Lévy flights). In stellar atmospheres, for strong resonance lines one has $\epsilon \ll 1$. The result is that, due to the escape of radiation, there are large deviations from thermodynamic equilibrium near the boundary of the atmosphere. Elucidating the structure of the non-equilibrium optically thick boundary layer is the key problem of the theory of stellar atmospheres. A mathematically similar problem is the calculation of thermal equilibrium of a model solar atmosphere heated from below by radiation originating in Sun's interior. Polarization of the radiation emerging from

V. V. Ivanov (✉)
St. Petersburg University, Saint Petersburg, Russia
e-mail: viva1934@yahoo.com

© The Author(s), under exclusive license to Springer Nature Switzerland AG 2021

A. Kokhanovsky (ed.), *Springer Series in Light Scattering*, Springer Series in Light Scattering, https://doi.org/10.1007/978-3-030-71254-9_1

a scattering atmosphere also bears valuable information on its physics. In calculating this polarization, the $\sqrt{\epsilon}$ law (in a generalized form) is also helpful.

This paper presents an overview of evolution (spanning a century) of investigations of several radiative transfer problems. It may also be considered as an author's personal account (it seems, somewhat immodest) on one of his research fields.

Assertions that are known in astrophysics as "the $\sqrt{\epsilon}$ law", are *mathematically equivalent* to this one. If we have the Wiener–Hopf integral equation

$$S(\tau) = (1-\epsilon)\int_0^\infty K(\tau-\tau')\,S(\tau')\,d\tau' + \epsilon \tag{1}$$

with symmetric non-negative normalized to unity kernel function $K(\tau)$, so that

$$K(-\tau) = K(\tau), \qquad K(\tau) \geq 0, \qquad \int_{-\infty}^{\infty} K(\tau)\,d\tau = 1, \tag{2}$$

then

$$S(0) = \sqrt{\epsilon}, \qquad S(\infty) = 1. \tag{3}$$

However, the form in which $\sqrt{\epsilon}$ appears in astrophysical literature is usually different, and so its essence remains unclear.

Along with Eq. (1) it is natural to consider its limiting form for $\epsilon = 0$, i.e. homogeneous equation

$$S_h(\tau) = \int_0^\infty K(\tau-\tau')\,S_h(\tau')\,d\tau', \tag{4}$$

the solution of which will be normalized so that

$$S_h(0) = 1. \tag{5}$$

Comparison of (1) and (3) with (4)–(5) shows that

$$S_h(\tau) = \lim_{\epsilon\to 0}\frac{S(\tau)}{\sqrt{\epsilon}}\,. \tag{6}$$

Asymptotic behavior of the solution of homogeneous equation (4) for $\tau \to \infty$ may be looked at as a counterpart of the $\sqrt{\epsilon}$ law for the limiting case $\epsilon = 0$.

Physical significance of Eqs. (1) and (4), kernel function $K(\tau)$, solutions $S(\tau)$ and $S_h(\tau)$, as well as the parameter $\epsilon,\ 0 \leq \epsilon \leq 1$, in various astrophysical problems (and all the more in problems of other branches of physics) differ. In terminology and notation $\big(\tau,\ \epsilon,\ H(\mu)$ etc.$\big)$ we follow astrophysical tradition (mainly Western, rather than Russian).

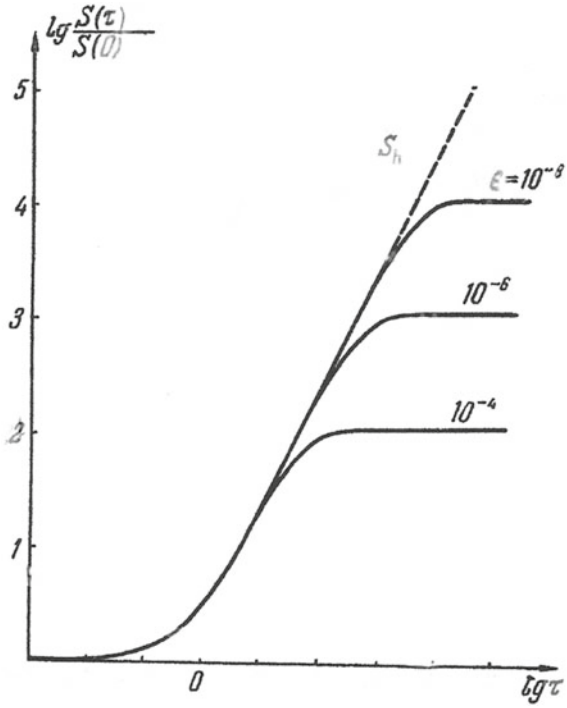

Fig. 1 Behavior of solutions of Eqs. (1) and (4) with a probabilistic kernel $K(\tau)$

Behavior of solutions $S(\tau)$ of the Eq. (1) with a probabilistic kernel $K(\tau)$ as well as that of the corresponding homogeneous equation (4), $S_h(\tau)$, is illustrated in Fig. 1.

The outline of the paper is as follows. Section 2 is an elementary introduction to the solution of the Wiener–Hopf equations with probabilistic kernels. The derivation of the $\sqrt{\epsilon}$ law is provided, one of the simplest among a multitude of all the available. Section 3 presents a brief historical overview of the first appearance of $\sqrt{\epsilon}$ in astrophysics. In Sect. 4 we discuss specific features of multiple scattering of photons of resonance lines in dilute gaseous media. The notion of the boundary layer is introduced and its structure is briefly outlined. In Sect. 5 we consider radiation in a resonance line emerging from semi-infinite scattering atmosphere. Crucial role of continuum absorption in quenching multiple scattering and hence in line formation is discussed. In Sect. 6 the $\sqrt{\epsilon}$ law is used as the basis in studying scaling of radiation fields in atmospheres of finite optical thickness. The large-scale description of transfer of line radiation is introduced. In Sect. 7 we enumerate the methods that has been used to derive the $\sqrt{\epsilon}$ law. Generalizations of the $\sqrt{\epsilon}$ law necessary for treating polarized radiation are the subject of Sect. 8. Problems of both non-magnetic multiple resonance scattering and scattering in atmospheres with weak magnetic fields are briefly discussed. In Sect. 9 the $\sqrt{\epsilon}$ law combined with the asymptotic solution of the homogeneous Eq. (4) are used as the basis for constructing an approximate solution of

the Wiener–Hopf equation (1) that describes the so called Levý flights (kernels with "tails" decreasing so slowly that even the first moment of $K(\tau)$ diverges). Finally, in Sect. 10 we summarize the results.

2 Mathematical Prologue

2.1 The Green Function

Let $G(\tau, \tau_1)$ be the Green function of Eq. (1), i.e. the solution of the equation

$$G(\tau, \tau_1) = (1 - \epsilon) \int_0^\infty K(\tau - \tau')\, G(\tau', \tau_1)\, d\tau' + \delta(\tau - \tau_1), \tag{7}$$

where $\delta(\tau - \tau_1)$ is the delta–function. Let, further, $G_0(\tau)$ be the value of the Green function for $\tau_1 = 0$ (surface Green function; physically—the source at the boundary of the medium):

$$G_0(\tau) \equiv G(\tau, 0) = G(0, \tau). \tag{8}$$

Simple probabilistic considerations show that

$$G(\tau, \tau_1) = \int_0^{\underline{\tau}} G_0(\tau - t)\, G_0(\tau_1 - t)\, dt, \qquad \underline{\tau} = \min(\tau, \tau_1). \tag{9}$$

Somewhat unexpectedly, G_0 appears here non-linearly. As we shall see shortly, it is this non-linearity which is at the root of the $\sqrt{\epsilon}$ law, non-linearity of the H–equation etc. Equation (9) reveals the key role of the surface Green function $G_0(\tau)$ in all half-space problems.

Physically, Eq. (9) is nearly obvious. Transfer of particle (in our case, a photon) occurs along a trajectory. Let t be the depth at which the trajectory approaches the surface most (the highest point of the trajectory, if the boundary is at the top). Evidently $t \le \min(\tau, \tau_1)$. At this point t scattering occurs, since otherwise the photon would continue to approach the boundary. This scattering event divides the trajectory leading from τ_1 to τ in two parts. The probability of transition from τ_1 to t along the first part of the trajectory is evidently $G(0, \tau_1 - t)$, since presence of the layers above t is not felt, and otherwise the trajectory is arbitrary. After scattering at t, random walk continues, again without intersecting this level. Hence we may assume that a new photon is injected at the boundary of a half-space, and it has to arrive at $\tau - t$. The corresponding transition probability is obviously $G(\tau - t, 0)$. Since there is no memory in the random walk, the total transition probability $\tau_1 \to \tau$ along all the trajectories with the highest point at t is the product of the transition probabilities

before scattering at t, i.e., $G(0, \tau_1 - t)$, and after it, $G(\tau - t, 0)$. Taking into account symmetry of $G(\tau, \tau_1)$ and summing the contributions from the trajectories with all $t,\ t \leq (\tau, \tau_1)$, we arrive at (9).

Now we derive a non-linear equation satisfied by the surface Green function G_0. This equation, along with Eq. (9), is the basis of our analysis in this Section of the paper. Essentially, it is a limiting form of Eq. (9).

First we introduce the infinite medium Green function $G_\infty(\tau)$ satisfying

$$G_\infty(\tau) = (1 - \epsilon) \int_{-\infty}^{\infty} K(\tau - \tau')\, G_\infty(\tau')\, d\tau' + \delta(\tau). \tag{10}$$

Evidently,

$$G_\infty(\tau) = \lim_{T \to \infty} G(\tau + T, T), \tag{11}$$

$$G_\infty(-\tau) = G_\infty(\tau). \tag{12}$$

Let us now turn to Eq. (9). We substitute $\tau + T$, T and $-t$ for $\tau,\ \tau_1$ and t, respectively, and then go to the limit $T \to \infty$. The result is

$$G_\infty(\tau) = \int_0^{\infty} G_0(t)\, G_0(\tau + t)\, dt, \qquad \tau \geq 0. \tag{13}$$

This is the desired equation for G_0. Its probabilistic interpretation is similar to that of Eq. (9). (Strangely enough, this non-linear equation can be easily solved, nearly by inspection, provided some natural assumptions on G_0 are met. For model problems of radiative transfer theory these assumptions usually hold. Discussion of these matters is given in Sect. 5 of Ivanov 1994).

2.2 Derivation of the $\sqrt{\epsilon}$ Law

Equation (13) enables one to derive the $\sqrt{\epsilon}$ law literally in one line. Indeed, by integrating Eq. (10) over all τ, we get

$$\int_{-\infty}^{\infty} G_\infty(\tau)\, d\tau = \epsilon^{-1}. \tag{14}$$

This result is trivial: mean number of photon scatterings in an infinite medium is the reciprocal of the probability of its destruction per single scattering.

Now, by integrating Eq. (13) over all $\tau \geq 0$ and using (14), we immediately find that

$$\int_0^\infty G_0(\tau)\, d\tau = \epsilon^{-1/2}. \tag{15}$$

This is one of the forms of the $\sqrt{\epsilon}$ law, and physically it is the most transparent one. In words it may be formulated as follows. **The mean number of scatterings of a particle starting symmetrical random walk at the boundary of half-space equals the square root of the mean number of its scatterings in full space.** The important point is that no restrictions are imposed on distribution function of particle's free flights. The corresponding probability density is $K(\tau)$. The only requirement is that it is symmetric, see Eq. (2). If one considers random walk on semi-axis, the words *photon, half-space, exit through the boundary etc.* may be replaced by, respectively, *particle, semi-axis, reaching the origin etc.*

However, there are two points of crucial importance. The first one is homogeneity of the medium. By removing a layer of an arbitrary thickness we remain with essentially the same semi-infinite atmosphere (or, equivalently, the semi-axis remains the semi-axis even if we cut part of it). The second point is the loss of memory at every scattering, so that the information on the direction of propagation before scattering and on initial frequency within the line are forgotten. Hence the $\sqrt{\epsilon}$ law is not directly applicable to problems of anisotropic scattering and line formation with partial frequency redistribution.

In astrophysics, by the $\sqrt{\epsilon}$ law one usually means a result which is very close to the one just formulated, but not identical to it. It is a simple consequence of Eq. (15). Indeed, let us denote by $\overline{G}(\tau; s_1)$ the Laplace transform in variable τ_1 of the Green function $G(\tau; \tau_1)$; parameter of the transform is s_1. By applying the Laplace transform to Eq. (7) we obtain the equation for $\overline{G}(\tau; s_1)$ of the form

$$\overline{G}(\tau; s_1) = (1-\epsilon) \int_0^\infty K(\tau - \tau')\, \overline{G}(\tau'; s_1)\, d\tau' + \mathrm{e}^{-s_1 \tau}. \tag{16}$$

In astrophysics, $\overline{G}(\tau; s_1)$ is known as the source function in the medium with exponentially distributed primary sources. Comparison of Eqs. (1) and (16) immediately shows that

$$S(\tau) = \epsilon\ \overline{G}(\tau; 0). \tag{17}$$

By applying the Laplace transform in τ_1 to Eq. (9), we get

$$\overline{G}(\tau; s_1) = \overline{G}_0(\tau; s_1) \int_0^\tau G_0(\tau - t) \mathrm{e}^{-s_1 t}\, dt. \tag{18}$$

Finally, we set $s_1 = 0$ in Eq. (18) and then $\tau = 0$ in the last two formulae. Taking into account contribution to the integral in Eq. (18) from the δ-function of G_0, we find that

$$S(0) = \epsilon\ \overline{G}(0;0) = \epsilon\ \overline{G}_0(0;0) = \epsilon \int_0^\infty G_0(\tau)\, d\tau = \epsilon^{1/2}. \tag{19}$$

Such a way of obtaining this so to say "astrophysical version" of the $\sqrt{\epsilon}$ law is definitely not the simplest one in a collection of many of available ways of its derivation (see Sect. 7). Its advantage is that it clearly shows its surprisingly simple and transparent root, i.e. Eq. (15).

In this Section the presentation closely follows the author's paper (Ivanov 1994).

3 Ancient History of $\sqrt{\epsilon}$

3.1 Scattering Atmospheres

It seems that in astrophysics $\sqrt{\epsilon}$ first appeared in the paper of Ambartsumian (1942). He studied radiation fields in scattering atmospheres of planets and the Sun. The result equivalent to the $\sqrt{\epsilon}$ law appeared in Ambartsumian's paper as

$$A(\mu) = 1 - \sqrt{\epsilon}\, H(\mu), \tag{20}$$

where $H(\mu)$ is the solution of non-linear integral equation

$$H(\mu) = 1 + \frac{1-\epsilon}{2}\mu H(\mu) \int_0^1 \frac{H(\mu')}{\mu + \mu'}\, d\mu'. \tag{21}$$

Here $1 - \epsilon$ is single scattering albedo (so that ϵ is photon destruction probability per scattering); $A(\mu)$ is plane albedo of semi-infinite isotropically scattering atmosphere illuminated by parallel rays; μ is the cosine of the angle of incidence of the rays with the normal to the layer. And there is no Wiener–Hopf integral equation on the scene!

We note that simple transformations enable one to recast Eq. (21) in alternative form, with $\sqrt{\epsilon}$ appearing explicitly:

$$H(\mu)\left(\sqrt{\epsilon} + \frac{1-\epsilon}{2}\int_0^1 H(\mu')\,\frac{\mu'\, d\mu'}{\mu + \mu'}\right) = 1. \tag{22}$$

Elucidating the relation between the *non-linear* Eq. (21) and *linear* Wiener–Hopf equation (1) was one of the main results found by Ambartsumian (1942). Late

in the XIX century "founding fathers" of the radiative transfer theory have shown (Chwolson 1889; Lommel 1889) that finding the radiation field in isotropically scattering semi -infinite medium illuminated by parallel rays, with the angle of incidence arccos μ_0 with the inner normal, reduces to solving the Eq.

$$S(\tau, \mu_0) = \frac{1-\epsilon}{2} \int_0^\infty E_1(|\tau - \tau'|) S(\tau', \mu_0)\, d\tau' + \mathrm{e}^{-\tau/\mu_0}\,. \tag{23}$$

This is the Wiener–Hopf equation with exponentially decreasing free term and the kernel function

$$K(\tau) = \frac{1}{2} E_1(|\tau|), \tag{24}$$

where $E_1(\tau)$ is the exponential integral:

$$E_1(\tau) = \int_0^1 \mathrm{e}^{-\tau/\mu'}\, d\mu'/\mu', \qquad \tau > 0. \tag{25}$$

The kernel function (24) is known as *the Milne kernel*. In the classical approach the solution $S(\tau, \mu_0)$ of Eq. (23) is then used to find the intensity of radiation reflected with directional cosine μ with the outer normal:

$$I(0, \mu, \mu_0) = \int_0^\infty S(\tau, \mu_0)\, \mathrm{e}^{-\tau/\mu}\, d\tau/\mu. \tag{26}$$

In the pre-space era $I(0, \mu, \mu_0)$ was the only quantity one could hope to obtain from observation of planets with optically thick atmospheres. Hence finding $I(0, \mu, \mu_0)$ was the most desired result of the theory. Ambartsumian (1942) has shown that there is another, and much more direct, approach to get $I(0, \mu, \mu_0)$. One only needs to solve Eq. (21) or its alternative form (22) (say, by iteration; the convergence is rapid). The reflected intensity is immediately expressed in terms of the H–function:

$$I(0, \mu, \mu_0) = \frac{H(\mu) H(\mu_0)}{\mu + \mu_0}\, \mu_0\,, \tag{27}$$

so that variables μ and μ_0 are essentially separated. It was also shown that

$$H(\mu) = S(0, \mu). \tag{28}$$

This relation appeared in the paper of Ambartsumian (1942) as an intermediate result used in the derivation of the H–Eq. (21) from the Wiener–Hopf equation (23).

Soon $\sqrt{\epsilon}$ appeared, so to say, "in a pure form" (Ambartsumian 1948) as a statement that the number of scatterings of photons emitted isotropically by a source located at the boundary of isortopically scattering semi-infinite atmosphere equals to

$$N(0) = \frac{1}{\sqrt{\epsilon}}\,. \tag{29}$$

This is exactly Eq. (15) (in different notation). It was found by Ambartsumian (1948) by using non-linear Eq. (21).

3.2 Milne–Eddington Model

Somewhat later $\sqrt{\epsilon}$ showed itself also in the early theory of stellar atmospheres. According to the Milne–Eddington model of line formation by monochromatic scattering (Eddington 1926, Chap. XII; Eddington 1929; Milne 1930) in case of an isothermal atmosphere one essentially deals here with the Wiener–Hopf Eq. (1) with the Milne kernel function. However, in discussing the Milne–Eddington model, Eq. (1) is usually not written explicitly. Instead, one explores the equivalent problem of solving the radiative transfer equation

$$\mu\,\frac{dI(\tau,\mu)}{d\tau} = -I(\tau,\mu) + S(\tau), \qquad I(0,\mu) = 0, \quad \mu > 0, \tag{30}$$

with

$$S(\tau) = \frac{1-\epsilon}{2}\int_{-1}^{1} I(\tau,\mu')\,d\mu' + \epsilon. \tag{31}$$

In 1947 S. Chandrasekhar has shown (see Chandrasekhar 1947—this paper is practically completely reproduced in Chandrasekhar 1950, Sect. 84) that the intensity of radiation in a spectral line emerging from isothermal atmosphere at an angle arccos μ with the normal expressed in units of the blackbody intensity in the adjacent continuum is equal

$$r_\nu(\mu) = \sqrt{\epsilon}\,H(\mu), \tag{32}$$

where $H(\mu)$ is the same H–function as in Eq. (20), i.e., the solution of Eq. (21). Parameter ϵ (depending on frequency ν) is here

$$\epsilon = \frac{\beta}{\beta + \phi(x)}\,, \tag{33}$$

where β is the ratio of the absorption coefficient in adjacent continuum to line absorption coefficient, $\phi(x)$ is line absorption profile (normalized to unity) and, finally, x

is dimensionless frequency measured from the center of the line in appropriate units (as a rule, in Doppler widths). The profile of the line is given by the dependence of $r_\nu(\mu)$ on frequency x. We note that the values of $H(\mu)$ depend on parameter ϵ, but this dependence is weak (variation by less than a factor 3, while the values of ϵ change within a strong line by several orders of magnitude, from $\beta \ll 1$ (say, 10^{-4}) to 1).

The elegant result expressed by Eq. (32) was close to being "classified" by Chandrasekhar. Discussion of the Milne–Eddington model, which played an important role in astrophysics of that time, is postponed nearly to the end of his famous book, to its Chapter XII "Further Astrophysical Problems". To find out Eq. (32), one has to put $B^{(1)} = 0$ in Eq. (66) of Sect. 84, i.e., to assume that the atmosphere is isothermal and—the main point!—to understand that the essence of the problem is finding the dependence on frequency within the line, and not on the angular variable μ. "To help the reader", in the derivation of Eq. (32) the subscript ν is omitted, and the dependence of r_ν on frequency, contrary to its dependence on μ, is neither discussed nor even mentioned.

In discussing the Milne–Eddington model the essence of the problem is that, since there is scattering, an absorption line originates even in an isothermal atmosphere. This fact is usually obscured by assuming that temperature, and hence the Planck function, increases with depth. According to Eqs. (32) and (33), the order of magnitude of residual intensity in the center of a strong line ($\beta \ll 1$) is $\sqrt{\beta}$. In the center of stellar disk ($\mu = 1$) it is approximately three times larger than at the limb ($\mu = 1$), because $H(\mu)$ decreases from $H(1) = 2.91$ to $H(0) = 1$.

The reason why the lines are formed in an isothermal Milne–Eddington atmosphere (and in general, provided there is scattering) is simple. Photon emitted within a line at some depth, before its exit from the atmosphere, due to scattering moves (it would be more appropriate to say *propagates*, but we sacrifice accuracy for simplicity) along a zig-zag trajectory. As a result, its path length is larger than the path length of a photon of the adjacent continuum since the latter moves along a straight line. Larger path length causes an increase of probability of photon destruction due to absorption either in flight or in scattering events due to electron collisions and photoionizations from the upper level (to simplify formulae, we ignored the second possibility). As a result, at line frequencies boundary of the atmosphere is reached by a smaller fraction of photons than at frequencies of the adjacent continuum.

We note in passing that in the 1950s V. V. Sobolev studied line formation in the Milne–Eddington model atmosphere using simple probabilistic reasoning, and this enabled him to completely reproduce Chandrasekhar's results (Sobolev 1963, Chap. VI, §§ 3–5).

3.3 Milne Equation

Let us now turn to the problem that was the very first one in which the homogeneous equation (4) with the Milne kernel function appeared:

$$S_h(\tau) = \frac{1}{2}\int_0^\infty E_1(|\tau - \tau'|)\, S_h(\tau')\, d\tau'. \tag{34}$$

This equation is now known as the *Milne equation*. In 1921 E. Milne has shown that the solution of this equation determines temperature distribution in a model solar atmosphere (Milne 1921). More precisely, he found that $S_h(\tau) \propto T^4(\tau)$, where τ is the optical depth (see, e.g., Hubeny and Mihalas 2015, Chap. 17). It was assumed that the atmosphere is in local thermodynamic equilibrium (LTE) and is gray, i.e. its absorption coefficient does not depend on frequency. Hopf (1934) has found that the solution of the Milne equation has the following structure:

$$S_h(\tau) = \sqrt{3}\,\big(\tau + q(\tau)\big), \tag{35}$$

where the function $q(\tau)$ increases monotonically from $q(0) = 1/\sqrt{3} = 0.577...$ (the so-called *Hopf–Bronstein relation*—Bronstein 1929; Hopf 1930) to $q(\infty) = 0.710...$ (Hopf's constant — Hopf 1934, p. 85). As we shall see later, the asymptotic behavior of the solution of the Milne equation $S_h(\tau) \sim \sqrt{3}\,\tau$ is in a sense the conservative counterpart (for $\epsilon = 0$) of the $\sqrt{\epsilon}$ law.

There is an intimate relationship between the homogeneous linear Milne equation and the non-linear Ambartsumian equation (with $\epsilon = 0$). To illustrate this, we reproduce below two formulae which, at first glance, may seem unexpected. Let α_i be the moment of order i of the conservative ($\epsilon = 0$) function $H(\mu)$:

$$\alpha_i = \int_0^1 H(\mu)\mu^i\, d\mu, \qquad i = 0,\ 1,\ 2\ldots \tag{36}$$

One can show that

$$\frac{\alpha_0}{\alpha_1} = q(0), \qquad \frac{\alpha_2}{\alpha_1} = q(\infty). \tag{37}$$

We note in passing that if one assumes gray LTE atmosphere, then $H(\mu)$ (with $\epsilon = 0$) gives brightness distribution over the stellar disk, so that $H(0) = 1$ at the limb ($\mu = 0$) and $H(1) = 2.91$ in its center ($\mu = 1$); here μ is the cosine of the angular distance from the center of the disk.

A century ago the Milne equation had played an important role not only in astrophysics but also in mathematics. In studying this equation, N. Wiener and E. Hopf developed a highly non-trivial method of solution of all the equations of the form (4) (see Hopf 1934, Chap. IV). The method is based on using complex variable theory, or more precisely, theory of analytical functions (the so called Wiener–Hopf factorization). It is still widely used in applied mathematical physics. Ironically, solutions of Eqs. (1) and (4) with the kernel functions encountered in astrophysics can be obtained using much more modest technique. This became clear, however, only much later.

To conclude this short overview of the youth of the analytical radiative transfer theory, it is appropriate to add that the Milne equation describes not only the temperature distribution in the solar atmosphere, but also multiple scattering of thermal neutrons (see, e.g., Davison 1957). In the course of the development of atomic weapons (the Manhattan project) it was found necessary to have highly accurate value of the Hopf constant: $q(\infty) = 0.710446$ (Placzek and Seidel 1947). Just for fun: recently the value of $q(\infty)$ was (twice!) published with 58 digits (Viik 1986, 2016). Equation (21) known in astrophysics as the Ambartsumian equation, first appeared several years earlier in a paper by Halpern et al. (1938). Alas, astrophysicists remained unaware of this. And Halpern et al. (1938) evidently had no idea of what had been already done in astrophysics, and started their paper by derivation of the transfer equation. This makes the results found by them even more impressive. Halpern et al. (1938) have rediscovered the Wiener–Hopf factorization, found non-linear H–equation and explicit expression for the H–function (our Eq. (65) with $\widetilde{K}(\omega)$ from Eq. (58)), obtained Hopf–Bronstein relation and found numerical value of the Hopf constant, etc. There were no references to this paper, either by astrophysicists (this might be expected), or by physicists, including those involved in atomic bomb project (and this is astounding).

4 Resonance Radiation: Lévy Flights and $\sqrt{\epsilon}$

4.1 Biberman–Holstein Equation

A real breakthrough occurred in radiative transfer theory in the 1940–1950s: in treating multiple scattering of radiation of spectral lines unrealistic assumption that photon frequency does not change upon scattering, i.e. that scattering is monochromatic, has been replaced by the opposite one—in each of the scattering events photon completely "forgets" its initial frequency and is reemitted at any frequency within the line, with probability proportional to line absorption coefficient (the so called **c**omplete **f**requency **r**edistribution, or CFR). The basic integral equation of transfer of resonance radiation in isothermal gaseous media of low density, e.g., in a stellar atmosphere, is again the Wiener–Hopf equation (1), with the kernel function

$$K(\tau) = \frac{1}{2} \int_{-\infty}^{\infty} \phi^2(x)\, E_1(\phi(x)|\tau|)\, dx, \tag{38}$$

where E_1 is the integral exponent, Eq. (25), $\phi(x)$ is the profile of line absorption coefficient normalized to unity, x is dimensionless frequency measured from line center in appropriate units, usually in Doppler widths. The probability density of transfer of excitation by a photon of resonance line (in single flight) on distance along the axis of optical depths from τ to $\tau + d\tau$ is $K(\tau)\, d\tau$.

Integral equation (1) with the kernel function (38) is known (mainly, in the physical community) as the *Biberman–Holstein equation*. They independently introduced it in the 1940s (Biberman 1947; Holstein 1947). It is clear that the $\sqrt{\epsilon}$ law holds for Eq. (1) with such a kernel, just as it holds in case of the Milne kernel.

The term "$\sqrt{\epsilon}$ law" became widely used in the 1960s–1970s in publications on line transfer theory, especially after publication of paper by Avrett and Hummer (1965). It is still widely cited. Although $\sqrt{\epsilon}$ is discussed in detail in this paper, the term "the $\sqrt{\epsilon}$ law" had not been used by Avrett and Hummer (1965).

The solution of Eq. (1) with the kernel (38) is the so called source function (in units of the Planck function). It is related to level populations as follows:

$$S(\tau) = \frac{2h\nu_0^3}{c^2}\left(\frac{g_2}{g_1}\frac{n_1}{n_2} - 1\right)^{-1} \Big/ B_{\nu_0}(T). \tag{39}$$

Here n_i and g_i, $i = 1, 2$ are populations of the levels and their statistical weights, respectively, ν_0 is frequency at which the line is located in the (planckian) continuum, $B_{\nu_0}(T)$ is the Planck function. By discarding -1 in brackets in Eq. (39) and in the denominator of the Planck function we neglect stimulated transitions (usually insignificant). Then $S(\tau)$ reduces to the ratio of level populations expressed in units of the Boltzmann population ratio. The parameter ϵ in the basic Wiener–Hopf equation (1) for the problem at hand is the photon destructure probability per scattering, i.e., the ratio of the rate of $2 \to 1$ collisional transitions (quenching collisions) $n_e C_{21}$ to the total rate of de-population of the excited level:

$$\epsilon = \frac{n_e C_{21}}{A_{21} + n_e C_{21}}\,. \tag{40}$$

In stellar atmospheres, for strong resonance lines $\epsilon \ll 1$. According to the $\sqrt{\epsilon}$ law, one has $S(0) = \sqrt{\epsilon}$, so that in outer atmospheric layers deviations of population of the upper level from the equilibrium one (i.e., Boltzmann) are large. Thus, for $\epsilon \sim 10^{-4}$ concentration of excited atoms is $\sim$ 100 times lower than that at equilibrium.

The whole class of problems of transfer of spectral line radiation is fundamentally different from the classical problems of monochromatic scattering, both isotropic and anisotropic. Under the assumption of CFR, not only the dispersion of photon path lengths but even the mean free path length is infinite. As a result, the diffusion approximation breaks down even far from the boundaries of the medium. The reason is that remote volumes effectively interact by interchanging photons in line wings. As a result of this, the kernel function $K(\tau)$ given by Eq. (38) decreases for $\tau \to \infty$ slowly, as a power law, and not exponentially, as it is the case for the Milne kernel. In particular, for the Doppler absorption coefficient (superscript D, from now on)

$$\phi^D(x) = \frac{1}{\sqrt{\pi}}\ \mathrm{e}^{-x^2} \tag{41}$$

we have

$$K^D(\tau) \sim \frac{1}{4\,|\tau|^2\sqrt{\ln(|\tau|/\sqrt{\pi})}}\,, \qquad |\tau| \to \infty. \tag{42}$$

For the Voigt absorption coefficient (superscript V)

$$\phi^V(x) = \frac{a}{\pi^{3/2}} \int\limits_{-\infty}^{\infty} \frac{\mathrm{e}^{-y^2}\,dy}{(x-y)^2 + a^2} \tag{43}$$

with $10^{-4} \le a \le 10^{-1}$ one has

$$K^V(\tau) \sim \frac{\sqrt{a}}{6\,|\tau|^{3/2}}\,, \qquad a\,|\tau| \gg 1. \tag{44}$$

Finally, for the Lorentz (L) profile

$$\phi^L(x) = \frac{1}{\pi}\,\frac{1}{1+x^2} \tag{45}$$

we have

$$K^L(\tau) \sim \frac{1}{6\,|\tau|^{-3/2}}\,, \qquad |\tau| \to \infty. \tag{46}$$

Derivation of the asymptotic forms of the kernels $K(\tau)$ and related functions is given by Ivanov (1973, §§ 2.6 and 2.7), Avrett and Hummer (1965).

Probabilistically, free path length of a resonance line photon is a random variable that is not described by the "universal" normal law. The branch of the probability theory relevant to problems of transfer of resonance radiation is the so called stable probability laws (see, e.g., Feller 1966; Ibragimov and Linnik 1965; Uchaikin 2003). The overwhelming majority of astrophysicists are unaware of their existence. Let us briefly outline the situation encountered here.

4.2 Transfer of Excitation in Scattering Media

In studying transfer of resonance radiation or, equivalently, in problems of excitation transfer by photons of resonance lines, the crucial role is played by properties of the Fourier transform of the kernel function of Eq. (1):

$$\widetilde{K}(\omega) = \int\limits_{-\infty}^{\infty} K(\tau)\,\mathrm{e}^{i\omega\tau}\,d\tau. \tag{47}$$

Let us assume that

$$1 - \widetilde{K}(\omega) \sim \varphi(\omega)\,\omega^{\alpha}, \qquad \omega \to 0, \tag{48}$$

where $\varphi(\omega)$ is a function slowly varying for $\omega \to 0$, i.e., such a function that for arbitrary $c > 0$ one has

$$\lim_{\omega \to 0} \frac{\varphi(c\,\omega)}{\varphi(\omega)} = 1. \tag{49}$$

An example of a slowly varying function is $\ln \omega$ or an arbitrary power of logarithmic function; $\varphi(\omega)$ may be a constant (and this is often the case).

The requirement (48) is quite a general one. It is satisfied by both the Milne kernel, Eq. (24), and the Biberman–Holstein kernel, Eq. (38), the latter with an arbitrary symmetric monotonically decreasing profile of line absorption coefficient $\phi(x)$. If the condition (48) is met, one says that the kernel function $K(\tau)$ is a probability density belonging to the domain of attraction of a (symmetric) stable probability law. The parameter $\alpha,\ 0 < \alpha \leq 2$, appearing in Eq. (48) is known as *the characteristic exponent* of the kernel function $K(\tau)$. For the classical random walk one has $\alpha = 2$. In this case the dispersion of lengths of single flights of walking particles is finite. If $\alpha < 2$, in physics it is usually said that we deal with *Lévy flights*. This term was first used by Mandelbrot (1982); in astrophysics, it has never been used. Lévy flights are also known as anomalous diffusion (Uchaikin 2003) or superdiffusion (Kukushkin and Sdvizhenskii 2016).

In the 1960s the author and D. I. Nagirner have undertaken detailed analytical study of problems of transfer of resonance radiation. The fundamental role of the behavior of the "tail" of the kernel $K(\tau)$ for $\tau \to \infty$ was found very soon. Somewhat later, even a more fundamental role of Eq. (48) was realized (D.I.N.). We introduced parameter $\gamma \equiv \alpha/2$ and called it the characteristic exponent. This had been done before we had learned that there are stable probability laws. We never used the term "Lévy flights" because it remained unknown to us until recently (and we are not proud of this fact).

What is the qualitative difference of trajectories of particles (photons, in our case) performing Lévy flights from the trajectories of ordinary random walk? Figure 2 clearly illustrates this. The trajectory of classical random walk (isotropic monochromatic scattering) is shown in its upper part, while lower part illustrates Lévy flights (multiple CFR scattering with Doppler absorption coefficient). The figure shows 3D trajectories projected on plane (τ_x, τ_y). The trajectories underwent by a photon in 10^4 scatterings in infinite conservative medium ($\epsilon = 0$) were modeled by the Monte Carlo method. The difference of the general view of the trajectories in the two cases is striking. The upper trajectory is the ordinary random walk of the Brownian type; the shift of the particle is proportional to the square root of the length of the trajectory. This shift is the cumulative result of many chaotic steps of not strongly differing length.

The trajectory of a spectral line photon scattered with CFR is drastically different (lower part of Fig. 2). First of all, we call attention to the difference of scales. In the classical random walk the shift in 10^4 scatterings is $\sim$100, or of the order of $\sqrt{10^4}$,

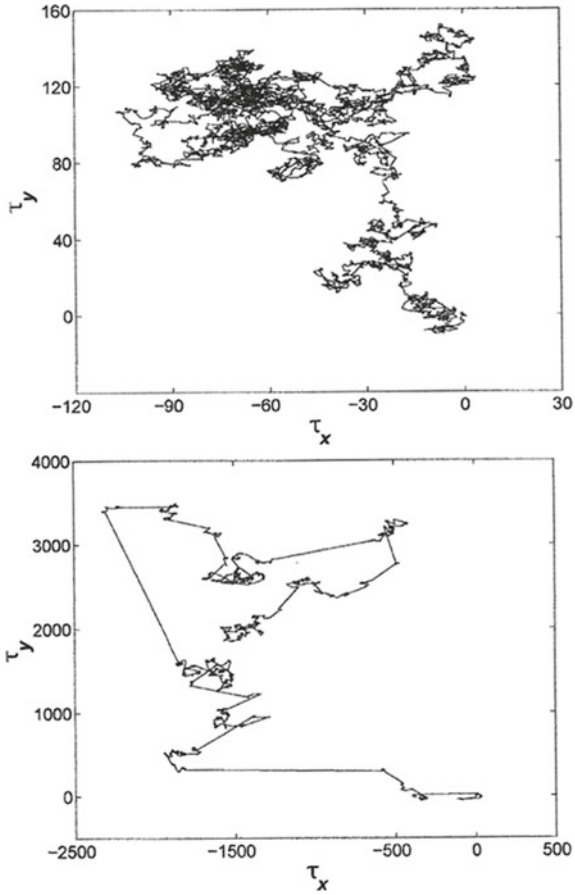

Fig. 2 Top: Brownian photon random walk (isotropic monochromatic scattering, 10^4 steps). Bottom: Doppler Lévy flights, 10^4 steps

as it should be. In the Doppler walk, as we shall briefly call Lévy flights of spectral line photons with the Doppler absorption coefficient and CFR, it is much larger, $\sim 10^4$. The main point is, however, that the shape of the trajectory is substantially different. The whole photon shift from its initial to final position is due to only a few extremely long flights. These flights occur when in the course of multiple scattering a photon is emitted far from the line center. The overwhelming fraction of steps of a random trajectory is so small that, on the scale of Fig. 2, they are indistinguishable. The photon makes no headway for a long time, until at last it is emitted far in the line wing. After a long flight it is eventually absorbed, thus causing atomic excitation. After this, the photon is again and again reemitted not far from the center of the line, and hence again makes no headway. Clearly, the displacement is caused by only several long flights.

The situation becomes even more dramatic if we continue to follow Doppler walk by giving our photon the possibility to be scattered 10^5 times (Fig. 3). Here

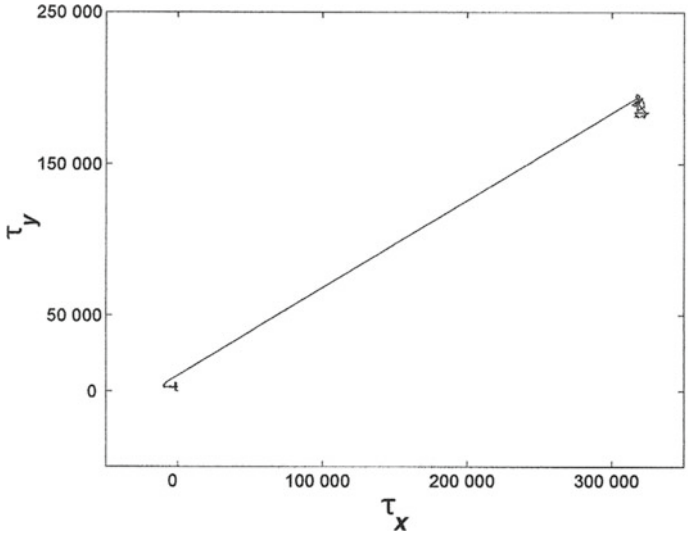

Fig. 3 Doppler Lévy flights, 10^5 steps

all the displacement in 100 000 steps is completely determined by a *single* flight of a photon emitted in a far wing of the line. This is a *radical* distinction of transfer of line radiation (and Lévy flights in general) from usual random walk of diffusion type. In astrophysics, this qualitative picture of Lévy flights was first formulated by Rybicki and Hummer (1969).

From presenting a qualitative overview of Lévy flights, let us now proceed to quantitative description of their peculiarities. The characteristic exponent α determines the asymptotic solution of homogeneous equation $S_h(\tau)$ for large τ and at the same time, as it is clear from Fig. 1, the rate of growth of $S(\tau)$ (assuming $\epsilon \ll 1$).

The result of fundamental importance for us is as follows. Solution of the homogeneous Wiener–Hopf equation with symmetric probabilistic kernel $K(\tau)$ normalized so that $S_h(0) = 1$, for large τ is (Ivanov 1973, p. 231):

$$S_h(\tau) \sim \frac{2}{\alpha\Gamma(\alpha/2)}\big(\varphi(1/\tau)\big)^{-1/2}\,\tau^{\alpha/2}, \qquad \tau \to \infty. \tag{50}$$

Here $\Gamma(\alpha/2)$ is the gamma-function. This formula gives only the leading term of the asymptotic behavior of $S_h(\tau)$. There is no universal expression for higher-order terms of the asymptotic expansion of $S_h(\tau)$ valid for arbitrary line absorption coefficient. The derivation of Eq. (50) by elementary means will be given later.

The solution of the homogeneous Wiener–Hopf equation $S_h(\tau)$ with the Milne kernel is known as the Milne problem. In astrophysics, the solution of this equation with an arbitrary probabilistic kernel $K(\tau)$ is known as the generalized Milne problem. In this case the radiation field is produced by the source in infinitely deep

layers, with no sources at finite depths. Generalized Milne problem was first formulated by Ivanov (1962) and studied in detail by Ivanov (1973, see, in particular, §§ 5.6 and 6.1), Nagirner (2007), Abramov et al. (1969), Hummer and Stewart (1966). Equation (50) is in essence a generalization of the classical Hopf–Bronstein relation $S_h(\tau) \sim \sqrt{3}\ \tau$ to the problem of scattering of spectral line photons with an arbitrary absorption profile $\phi(x)$.

The function

$$K_2(\tau) = 2\int_{\tau}^{\infty} K(\tau')\,d\tau', \qquad \tau \geq 0, \tag{51}$$

is usually called the second kernel function. Physically, it is the probability that photon displacement along optical depth axis in single flight is larger than τ. For Lévy flights (characteristic exponent $\alpha < 2$) there is a remarkably simple relation between the asymptotic form of $K_2(\tau)$ and asymptotic solution of homogeneous equation $S_h(\tau)$. The leading terms of the asymptotics of the two functions are related by

$$S_h(\tau) \sim \frac{C}{\sqrt{K_2(\tau)}}, \qquad \tau \to \infty, \tag{52}$$

where

$$C = \frac{2}{\alpha\Gamma(\alpha/2)}\left(\frac{2}{\pi}\,\Gamma(\alpha)\sin\frac{\alpha\pi}{2}\right)^{1/2}. \tag{53}$$

This formula is a variation (valid for $\alpha < 2$) of the asymptotic form (50). For Lévy flights of photons of resonance lines with infinitely extending wings one has $\alpha \in (0,\ 1]$. The coefficient C in this case is close to 1, slightly decreasing as α increases. Two particular cases are to be mentioned. For the Doppler profile we have $\alpha = 1$, so that $C = 2\sqrt{2}/\pi = 0.900$, while for the Voigt and Lorentz profiles $\alpha = 1/2$ and $C = 0.984$. In Sect. 9 it will be shown that formula (52), combined with the $\sqrt{\epsilon}$ law, may be used as the basis of constructing an approximation of $S(\tau)$.

4.3 Boundary Layer

Figure 1 shows that the smaller ϵ is, the wider is the domain where the values of $S(\tau)/\sqrt{\epsilon}$ are close to $S_h(\tau)$. If the values of ϵ up to, say, 10^{-8} were realized in nature, the domain of applicability of Eq. (52) would be very wide. Alas, in astrophysics such extremely small values of ϵ are hardly realized, otherwise residual intensities in central parts of strong absorption lines in stellar spectra would be, as we shall see shortly, ~0.01%. Nevertheless, the role played by Eqs. (52) and (53) in the theory of Lévy flights in half-space cannot be overestimated (cf. Sect. 9).

The behavior of the solution $S(\tau)$ of the non-homogeneous Wiener–Hopf Eq. (1) with probabilistic kernel $K(\tau)$ may be outlined as follows. The $\sqrt{\epsilon}$ gives the ampli-

tude of variation of $S(\tau)$, while the characteristic exponent α determines (for large τ) the slope of the curve $\lg S_h(\tau)$ as a function of $\lg \tau$. For $\epsilon \ll 1$ it is practically a segment of a straight line. To illustrate the $\sqrt{\epsilon}$ law, the ordinate on Fig. 1 has a scale. The abscissa is not scaled to make Fig. 1 universal, i.e. valid for arbitrary value of the characteristic exponent.

Order of magnitude of the thickness of the boundary layer within which $S(\tau)$ grows from $S(0) = \sqrt{\epsilon}$ to $S(\tau) \sim 1$ is found by setting $S_h(\tau)$ equal to $1/\sqrt{\epsilon}$. Let us denote this characteristic size by τ_t, so that

$$S_h(\tau_t) = \frac{1}{\sqrt{\epsilon}}\,. \tag{54}$$

Using Eq. (50) we find that within a factor of order unity, the value of τ_t in this case is

$$\tau_t \sim \epsilon^{-1/\alpha}. \tag{55}$$

In particular, for $\alpha = 2$ we have $\tau_t \sim 1/\sqrt{\epsilon}$. This value $\left(\text{more exactly, } 1/\sqrt{3\,\epsilon}\right)$ is known as the *diffusion length*. Under the assumption of CFR, for lines with infinitely extending wings the characteristic exponent is $\alpha \in (0,\ 1)$. The value of τ_t in this case is called the *thermalization length*. This term was introduced by Avrett and Hummer (1965). Thermalization length is a very important parameter. It determines the thickness of the boundary layer within which the escape of radiation causes substantial deviations from LTE.

Order-of-magnitude estimates are, for the three cases of greatest interest (assuming that $\epsilon \ll 1$):

$$\tau_t^D \sim \epsilon^{-1}, \qquad \tau_t^V \sim a\epsilon^{-2}, \qquad \tau_t^L \sim \epsilon^{-2}. \tag{56}$$

We note that if the absorption coefficient decreases in the wings $\propto |x|^{-\kappa}$, the thermalization length is $\tau_t \sim \epsilon^{-\kappa/(\kappa-1)}$.

A remarkable result is that for $\epsilon \ll 1$ one has (see Fig. 1)

$$S(\tau) \sim \sqrt{\epsilon}\, S_h(\tau), \qquad \tau \ll \tau_t\,. \tag{57}$$

Hence, **the atmosphere with $\epsilon \ll 1$ has optically thick boundary layer**. **Its structure, i.e., depth dependence of the source function**, **is universal. It is determined only by the form of the line absorption coefficient $\phi(x)$, while the thickness of this boundary layer is governed by the value of ϵ.**

Sometimes the physics of the problem being considered is lost in formulae. With this in mind, a short elucidation seems to be in order. According to Eq. (40), for $\epsilon \ll 1$ we have $\epsilon \propto n_e$. Hence, the fact that $S(\tau) \sim \sqrt{\epsilon}\, S_h(\tau)$ for $\tau \ll \tau_t$, means that everywhere within this boundary layer the population of the excited level is $\propto \sqrt{n_e}$. This seems to be somewhat unexpected—but this is what $\sqrt{\epsilon}$ tells us! The rate of primary excitations by electronic impacts is, of course, $\propto n_e$, but in the boundary layer photoexcitations by radiation born at great depths are overwhelming.

4.4 Refinements

Let us now consider the most important particular cases in more detail by presenting refinements of the asymptotic form given by Eq. (50).

For the rectangular profile

$$\begin{cases} \phi(x) = 1, & |x| \le 1/2; \\ \phi(x) = 0, & |x| > 1/2 \end{cases}$$

CFR degenerates into monochromatic scattering. Indeed, change of frequency within this profile does not lead to changes in mean photon free paths. Hence, one can assume that frequency does not change. Therefore, one deals here with the Milne kernel $K(\tau) = E_1(|\tau|)/2$. Its Fourier transform is

$$\widetilde{K}(\omega) = \frac{\arctan \omega}{\omega}, \tag{58}$$

so that

$$1 - \widetilde{K}(\omega) \sim \frac{\omega^2}{3}, \qquad \omega \to 0. \tag{59}$$

In this case $\alpha = 2$, $\varphi = 1/3$, and Eq. (50) gives $S_h(\tau) \sim \sqrt{3}\,\tau$—the result already mentioned more than once $\big($cf. Eq. (35)$\big)$.

The moments of the Milne kernel of all orders are finite. The refined asymptotic form of $S_h(\tau)$ is here

$$S_h(\tau) \sim \sqrt{3}\,\big(\tau + q(\infty)\big) + o(\mathrm{e}^{-\tau}), \qquad \tau \to \infty. \tag{60}$$

For the Doppler CFR Lévy flights one has $\alpha = 1$. Equation (42) shows that in this case the first and all higher order moments of $K^D(\tau)$ diverge. One can show (Ivanov 1970, see also Ivanov 1973, p. 234), that in this case the refined asymptotic form of $S_h(\tau)$ is

$$S_h(\tau) \sim \frac{4}{\pi}\,\tau^{1/2}\,T^{1/4} \sum_{j=0}^{\infty} \frac{s_j}{T^j}, \qquad \tau \to \infty, \tag{61}$$

where $T = \ln(\tau/\sqrt{\pi})$. The coefficients of this asymptotic expansion are defined by recursion relations ($s_0 = 1$).

We note that for Lévy flights with the asymptotics of the kernel function differing from that given by Eq. (42) only by the power of logarithm, e.g., $K(\tau) \propto \tau^{-2}\,T^{-3/2}$, the first moment of $K(\tau)$ is finite, while the characteristic exponent is the same as for the Doppler flights, i.e., $\alpha = 1$. For $\alpha < 1$ the first moment of the kernel is always divergent, for $\alpha > 1$ it is finite. For the boundary case $\alpha = 1$ both possibilities may realize.

For the Lorentz kernel (46) the refined version of the asymptotic form (50) is

$$S_h(\tau) \sim \left(\frac{2^7}{\pi}\right)^{1/4} \frac{\sqrt{3}}{\Gamma(1/4)}\ \tau^{1/4}\left(1 - \frac{3}{40}\ \frac{\ln(\tau/\pi)}{\tau} + o(1/\tau)\right), \qquad \tau \to \infty. \quad (62)$$

Thus the subleading terms in the asymptotics for the Doppler and Lorentz flights are substantially different.

We note that Eqs. (61) and (62) are essentially the counterparts of the classical Hopf's asymptotic form (60) corresponding to the cases of Doppler and Lorentz Lévy flights, respectively.

5 H–Functions, Fraunhafer Lines and $\sqrt{\epsilon}$

5.1 Emergent Radiation. H–functions

So far we discussed solutions of the equation for the source function $S(\tau)$. Let us now turn to quantities which are directly observable (at least, in principe), i.e., the line profiles. The intensity of radiation emerging from isothermal semi-infinite atmosphere is given by well known expression

$$I(0, \mu, x) = \int_0^\infty S(\tau)\exp(-\tau/z)\, d\tau/z \equiv \sqrt{\epsilon}\, H(z), \qquad z = \frac{\mu}{\phi(x)}. \quad (63)$$

Here μ is the cosine of the angle with the external normal, x is the dimensionless frequency measured from line center. From this formula it follows that $I(0, \mu, x)$ depends not on μ and x separately, but only on their combination $z \equiv \mu/\phi(x)$ and is essentially the Laplace transform of $S(\tau)$. In the limit of $\epsilon \to 0$ Eq. (63) gives, if use is made of Eq. (6),

$$H(z) = \int_0^\infty S_h(\tau)\exp(-\tau/z)\, d\tau/z\,, \qquad \epsilon = 0. \quad (64)$$

The integral appearing in Eqs. (63) and (64) is known in astrophysics as the H–function. One can get its explicit expression in terms of the Fourier transform $\widetilde{K}(\omega)$ of the kernel function $K(\tau)$ of the Wiener–Hopf Eq. (1) satisfied by $S(\tau)$. If $K(\tau)$ is an arbitrary positive symmetric function normalized to unity, i.e., if $K(\tau)$ it is a probability density, then one has

$$H(z) = \exp\left(-\frac{z}{\pi}\int_0^\infty \ln\left(1-(1-\epsilon)\widetilde{K}(\omega)\right)\frac{d\omega}{1+z^2\omega^2}\right). \tag{65}$$

This expression has been found by elementary means by Ivanov (1994). The price for simplicity of tools is a rather long and somewhat tricky derivation (see Addendum; this derivation is reproduced by Majumdar et al. 2014). By the time when this was done, the expression (65) has already been known for a long time. For the kernels exponentially decreasing as $\tau \to \infty$ (and $\epsilon = 0$) Eq. (65) appears already in Hopf's book (Hopf 1934, p. 105). However, its derivation, both by Hopf and later by many other authors (see, e.g., Chandrasekhar 1950, Sect. 40) was inevitably based on using non-elementary methods of complex variable theory.

In case of $\epsilon \neq 0$ Eq. (65) enables one to easily get the $\sqrt{\epsilon}$ law, this time appearing as $H(\infty) = 1/\sqrt{\epsilon}$. It suffices to note that the main contribution to the integral is given by the domain of small ω, and there, by virtue of Eq. (48), $1-(1-\epsilon)\widetilde{K}(\omega)$ can be replaced with ϵ. The end of the proof is evident. Similarly, if $\epsilon = 0$, for small ω argument of logarithm in Eq. (65) can be replaced with $\varphi(\omega)\,\omega^\alpha$. To calculate the integral thus appearing we use the fact that $\varphi(\omega)$ is a slowly varying function (see Eq. (49)). The result is

$$H(z) \propto \left(\varphi(1/z)\right)^{-1/2} z^{\alpha/2}, \qquad \epsilon = 0, \quad z \to \infty. \tag{66}$$

According to Eq. (64), this expression determines the behavior of the "tail" of the Laplace transform of $S_h(\tau)$. This can be used to restore the asymptotic form of $S_h(\tau)$, namely, $S_h(\tau) \propto \left(\varphi(1/\tau)\right)^{-1/2}\tau^{\alpha/2}$ for $\tau \to \infty$. The possibility of this is not so evident as it seems. A mathematician would say that here one has to appeal to a Tauberian theorem enabling one to restore the asymptotic behavior of the function from the asymptotic behavior of its Laplace transform. But astrophysicists (at least, the majority of them) have never heard about Tauber's theorems, and nevertheless got the correct results—just by trial. The calculation of proportionality coefficients is a minor technical detail, and we omit it.

It is to be stressed that in our derivation no restrictions were imposed on the properties of the kernel function $K(\tau)$, except that expressed by Eq. (48). Hence, it is valid, e.g., for the Cauchy kernel $K(\tau) = (1/\pi)\,(1+\tau^2)^{-1}$, which will appear in Sect. 9. It is not necessary for the kernel function $K(\tau)$ to be a continuous superposition of exponentials, as it is implicitly supposed if in the derivation of the asymptotic form Eq. (66) one uses the non-linear H–equation.

By introducing the integration variable $z = \mu/\phi(x)$ and changing the order of integration, the Biberman–Holstein kernel function $K(\tau)$ given by Eq. (38) can be represented as

$$K(\tau) = \int_0^\infty G(z)\,\mathrm{e}^{-|\tau|/z}dz/z, \tag{67}$$

where

$$2\int_0^\infty G(z)\,dz = 1. \tag{68}$$

The transformation of the kernel (38) to this form and the explicit expression for $G(z)$ are not given here because of space limitations. They may be found in the books of Ivanov (1973, Sect. 2.9), Nagirner (2007, Sect. 4.3.7). It seems that this simple transformation (first used by V. V. Sobolev in his pioneering paper (Sobolev 1949), to be briefly discussed below) turned out to be an insurmountable obstacle for more than one author. The detailed exposition of the derivation of Eq. (67) from Eq. (38), with an auxiliary figure, is given by Heaslet and Warming (1968).

Representation of the kernel $K(\tau)$ in the form given by Eq. (67), i.e., as a continuous superposition of exponentials with various values of z, provides the possibility for obtaining solutions of the Wiener–Hopf equations (1), (4) and related ones in explicit forms. Alas, these solutions are extremely cumbersome. These subjects are not discussed here. They are presented in Nagirner's monograph (Nagirner 2007).

However, some elements of analytical theory will be needed. In the theory of Wiener–Hopf equations a substantial role is played by the equation

$$S(\tau, z) = (1-\epsilon)\int_0^\infty K(\tau-\tau')S(\tau', z)\,d\tau' + \mathrm{e}^{-\tau/z}. \tag{69}$$

Astrophysically, $S(\tau, z)$ is the source function in the medium with exponentially distributed primary sources. Mathematically, $S(\tau, z)$ is essentially the Laplace transform of the Green function $\overline{G}$ of Eq. (1), or, more exactly, $S(\tau, z) = \overline{G}(\tau, 1/z)$ (see Eq. (16)). One can show that $S(0, z) = \overline{G}(0, 1/z) = H(z)$. The function $H(z)$ is the solution of non-linear equation

$$H(z) = 1 + (1-\epsilon)zH(z)\int_0^\infty G(z')\,H(z')\frac{dz'}{z+z'}\,. \tag{70}$$

This equation is a generalization of Ambartsumian's equation (21) for the H–function corresponding to the Milne kernel. Equation (70) is a consequence of the possibility to represent the kernel function in the form of Eq. (67). The alternative form of the H–equation is

$$H(z)\left(\sqrt{\epsilon} + (1-\epsilon)\int_0^\infty G(z')\,H(z')\frac{z'\,dz'}{z+z'}\right) = 1. \tag{71}$$

The function $H(z)$ increases monotonically from $H(0) = 1$ to

$$H(\infty) = \frac{1}{\sqrt{\epsilon}}\,. \tag{72}$$

Equation (71) is easily solved by iteration. According to (63), knowledge of $H(z)$ enables one to obtain the emergent intensity without solving the equation for the source function and finding the radiation field inside the atmosphere. That is why the H–functions attracted so much attention for decades. We note in passing that the asymptotic behavior of $S_h(\tau)$ for the Doppler Lévy flights was first found by Ivanov (1960) using the corresponding non-linear H–equation.

For the most important cases of the Doppler (Nagirner and Ivanov 1965), Lorentz (Warming 1970) and Voigt (Nagirner 1975) absorption coefficients the H–functions have been studied in detail and tabulated (see also Ivanov 1973, §§ 5.6 and 5.7). Recently, the most detailed study of the Voigt H–functions (with the continuum absorption taken into account) and related quantities was published (Grigoriev et al. 2019). In this paper the results of illustrative computations are given as well as the reference to the authors' code used in these computations which is in public domain.

5.2 Account for Continuum Absorption

In all the above discussion we ignored the fact that at line frequencies there is also continuum absorption. Let β be the continuum absorption coefficient expressed in terms of line absorption coefficient (averaged over the line and set equal to unity). Along with exit from the atmosphere, there are now two other possibilities of photon destruction in multiple scattering, i.e., "death" in a scattering event (with probability ϵ per scattering) and destruction in flights between scatterings due to continuum absorption. The probability of the second of these events is $\beta\,\delta(\beta)$, where $\delta(\beta)$ is photon mean free path between scatterings in a medium without boundaries:

$$\delta(\beta) = \int\limits_{-\infty}^{\infty} \frac{\phi(x)}{\phi(x)+\beta}\,dx. \tag{73}$$

The total probability of destruction per scattering is hence

$$\bar{\epsilon} = \epsilon + (1-\epsilon)\beta\delta(\beta). \tag{74}$$

With continuum absorption taken into account, the kernel of the basic integral equation (1) assumes the form

$$K(\tau) = \frac{A}{2}\int\limits_{-\infty}^{\infty} \phi^2(x)\,E_1\big((\phi(x)+\beta)|\tau|\big)\,dx, \tag{75}$$

where A is a factor providing normalization of $K(\tau)$ to unity:

$$A = \Big(1 - \beta\delta(\beta)\Big)^{-1}. \tag{76}$$

If we now substitute $\epsilon \Longrightarrow \bar{\epsilon}$ in the basic Wiener–Hopf Eq. (1) with the kernel function given by Eq. (75), the $\sqrt{\epsilon}$ law expressed by Eq. (3) will evidently hold, with $\bar{\epsilon}$ standing for ϵ.

If continuum absorption is taken into account, the source function $S(\tau)$ depends on two parameters, ϵ and β. If $\epsilon \gg \beta\delta(\beta)$, the role of continuum absorption is small. In this case photons are lost from multiple scattering either by destruction during scattering events or by escaping the atmosphere. In the opposite extreme case $\epsilon \ll \beta\delta(\beta)$ photons are lost mainly due to continuum absorption in flights from the place of one scattering to that of the next.

For strong lines we have $\beta \ll 1$ (up to $\sim 10^{-6}$), but the value of $\delta(\beta)$ for small β is large, and this partially compensates smallness of β. The dependence on β of the mean photon free path between successive scatterings $\delta(\beta)$ is not trivial. Let us discuss it in a little more detail. For $\beta \gtrsim 10^{-4}$, the absorption coefficient may be considered as pure Doppler, since then the Voigt wings do not significantly contribute to absorption. By assuming $\phi(x) = (1/\sqrt{\pi})\,\exp(-x^2)$ in Eq. (73), it can be easily shown that

$$\delta(\beta) \sim 2\left(\ln\frac{1}{\sqrt{\pi}\,\beta}\right)^{1/2}. \tag{77}$$

This is the leading term of the asymptotic expansion of $\delta(\beta)$ in inverse powers of $\ln\big(1/(\sqrt{\pi}\,\beta)\big)$ for the Doppler absorption coefficient. The derivation of several subleading terms that are usually given in the literature is inevitably based on the so called Sommerfeld's lemma (reproduced in Chandrasekhar 1939, Chap. X, Sect. 6). However, there is no need in Sommerfeld's lemma, since the recursive relation for the coefficients of the asymptotic expansion of $\delta(\beta)$ in inverse powers of $\ln\big(1/(\sqrt{\pi}\,\beta)\big)$ can be easily obtained by *tour de force* (see Ivanov 1973, p. 318).

As β decreases, the line becomes deeper and it develops wings. The reason is that for the Voigt absorption coefficient frequency dependence for $|x| \gtrsim (2.5 \div 3.0)$ gradually changes from $\exp(-x^2)$ to $\sim a/(\pi x^2)$, where a is the Voigt parameter $\big(a \sim (0.001 \div 0.1)\big)$. It can be easily shown that if $\beta \lesssim \big(10^{-3} \div 10^{-4}\big)$, one can simply substitute $a/(\pi x^2)$ for $\phi(x)$ in Eq. (73). This gives the correct expression of the leading term of the asymptotic form:

$$\delta(\beta) \sim \sqrt{\frac{\pi a}{\beta}}\,, \tag{78}$$

so that in this case

$$\bar{\epsilon} = \epsilon + (1-\epsilon)\big(\pi a\beta\big)^{1/2} \approx \epsilon + \big(\pi a\beta\big)^{1/2}. \tag{79}$$

In particular, if photons are lost in flights, and not in scatterings, i.e., if $\epsilon \ll \beta\delta(\beta)$, then

$$\sqrt{\bar{\epsilon}} \sim \left(\pi a \beta\right)^{1/4}. \tag{80}$$

This is an important result. The population of the excited level at the boundary of the atmosphere is less than its equilibrium value by factor of $1/\sqrt{\bar{\epsilon}}$. Therefore presence of even rather weak continuum absorption prevents large deviations from LTE. It is physically clear that for small $\bar{\epsilon}$ the emergent intensity (in units of the adjacent Planck continuum) is close to $S(0) = \sqrt{\bar{\epsilon}}$, increasing from the limb ($\mu = 0$) to the center of the disk ($\mu = 1$) (say, by a factor $1.5 \div 2$). This immediately follows from Eq. (63): the exponent in the integrand effectively dumps contribution to the emergent intensity of depths with $\tau \gtrsim z$, while in the surface layers $S(\tau)$ is close to $S(0) = \sqrt{\bar{\epsilon}}$. Hence Eq. (80) gives reliable order-of-magnitude estimate of central residual intensity of a strong line formed in an isothermal atmosphere. For $a = 0.01$ and $\beta = 10^{-6}$, Eq. (80) gives $\sim$1%, exactly as it is observed, e.g., for resonance sodium D-lines in solar spectrum. It worth mentioning that in this particular case, i.e., in the solar photosphere, continuum absorption is caused by photodetachment of electron from negative hydrogen ion.

This estimate of central residual intensities of strong Fraunhofer lines has been obtained as early as in 1949, in Sobolev's paper (Sobolev 1949, see also Sobolev 1963, Chap. VIII, where it is practically completely reproduced). In this paper V. V. Sobolev considers Milne–Eddington model atmosphere, but monochromatic scattering, which is usually assumed, is replaced with CFR. The analysis is based on rigorous methods of analytical radiative transfer theory. The main result was the estimation of central residual intensities of strong lines, which was essentially the same as that found above $\left(\approx \sqrt{\bar{\epsilon}}, \text{Eq. (80)}\right)$. This result was obtained without long calculations (it was still a pre-computer era) and not by using physical reasoning (say, of the type we have just used). Sophisticated considerations based on the so called invariance principle were used to obtain the non-linear H–equation corresponding to the problem at hand. The emergent intensity was expressed in terms of this H-function. And then, by estimating orders of magnitude of the terms appearing in the final expression, the desired result was extracted.

In case of $\beta \neq 0$ both Eqs. (54) (definition of the thermalization length τ_t) and (57) (structure of the boundary layer) as well as Eq. (56) (estimates of τ_t for Doppler, Voigt and Lorentz profiles) hold, with substitution $\bar{\epsilon} \Longrightarrow \epsilon$. In particular, if $\epsilon \ll \beta\delta(\beta) \sim (\pi a \beta)^{1/2}$, then within the whole boundary layer, i.e., for all $\tau \ll \tau_t$, the source function is $\propto \sqrt{\bar{\epsilon}} \propto \beta^{1/4}$ (for a fixed value of τ). As we have already mentioned, in case of the solar sodium D-lines continuum absorption is due to photodetachment of electrons from H^- ions, with concentration n^-. Since within the whole boundary layer $S \propto \beta^{1/4}$, this means that concentration of excited sodium atoms is proportional to $\sqrt[4]{n^-}$. The $\sqrt{\epsilon}$ law sometimes leads to seemingly strange results!

In our discussion of the situation arising when continuum is "switched on", we were (intentionally) inaccurate. The driving (free) term of the basic integral equation describes contributions to initial excitation of the upper level due to both electronic collisions (the term ϵ) and photoexcitations by continuum radiation at frequencies of

the line $\big($the term $(1-\epsilon)\beta\delta(\beta)f(\tau)\big)$. Factor $f(\tau)$ appearing here decreases from 1 in deep LTE layers, where blackbody radiation responsible for initial excitation is nearly isotropic, to 1/2 near the boundary of the atmosphere, where radiation comes only from below. So far we ignored this fact by assuming $f(\tau) \equiv 1$ and thus getting constant free term equal to $\overline{\epsilon} = \epsilon + (1-\epsilon)\beta\delta(\beta)$. This enabled us to reach our goal—to understand how the discontinuity at the boundary influences state of the gas in the non-equilibrium boundary layer thus appearing. Study of the role of depth dependence of the power of primary sources on the state of the gas and on properties of the radiation field is a different problem. However, since $f(\tau)$ varies only by a factor of 2, to obtain order-of-magnitude estimates it was legitimate to assume $f(\tau) = 1$. An accurate treatment is given by Hummer (1968) and Ivanov (1973, Chap. VII).

To summarize the astrophysical component of Sects. 4 and 5: they were devoted to describing general properties of *the non-equilibrium boundary layer*, which exists in dilute scattering atmospheres and separates hot inner layers where thermodynamic equilibrium prevails from cold outer space. To understand basic features and get rough estimates, no elaborate calculations are needed. It suffices to know two basic facts—the $\sqrt{\overline{\epsilon}}$ law and the asymptotic solution of the generalized Milne problem. Figuratively speaking, $\sqrt{\overline{\epsilon}}$ gives *height* of the jump of solution of *non-homogeneous* equation, while the asymptotic solution of the corresponding *homogeneous* equation determines *length* of this jump.

6 Finite Layer: $\sqrt{\epsilon}$ and Scaling

In this Section we consider atmospheres of finite optical thickness. It would be more appropriate to say that we deal with a plane gas layer, and not an atmosphere. Its line optical thickness is assumed large ($T \gg 1$), there is no continuum contributions to line formation. Here, the $\sqrt{\epsilon}$ is of serious help as well.

First we will give general qualitative description of the process of transfer of excitation by resonance line photons in gas of large optical size. If the medium is conservative, there are two typical sizes—one used as a unit in measuring optical distances and the other describing the size of the medium (in our case, optical thickness of gas layer T). If the second size is much larger than the first, i.e., $T \gg 1$, the radiation field in deep layers of the medium can be described by a specific approximation (so far unknown to us). This is similar to using hydrodynamic description rather than equations of gas kinetic theory everywhere except boundary layers adjacent to the walls. For optical distances from the boundary of order unity, this description breaks down, exactly as hydrodynamic equations are inapplicable near the walls (the so called Knudsen layer). Another example of similar situation—neutron transport (diffusion approximation inside + kinetic description near the boundary). Final example—theory of waveguides, with the so called correction for the open end of waveguide.

6.1 Boundary Layers

Let us first discuss the situation encountered near the boundaries of a thick layer. Assuming the gas is isothermal, we now deal not with the Wiener–Hopf equation (1), but with the Fredholm equation on a finite interval $[0,\ T]$:

$$S(\tau, T) = (1-\epsilon)\int_0^T K(\tau-\tau')\, S(\tau', T)\, d\tau' + \epsilon. \tag{81}$$

By symmetry, we have

$$S(\tau, T) = S(T-\tau, T). \tag{82}$$

It is physically obvious that in optically thick layer ($T \gg 1$) with uniformly distributed primary sources growth of the source function with the distance from each of the boundaries occurs in the same way as in the semi-infinite medium with sources in deep layers (formally, at infinity), so that

$$S(\tau, T) \sim S(0, T) S_h(\tau), \qquad \tau \ll \min(\tau_t, T/2). \tag{83}$$

This growth with τ occurs only for $\tau \ll \min(\tau_t, T/2)$, since only then the majority of photons producing excitation originates in layers that are closer to the middle of the layer. Since the solution of the Milne problem $S_h(\tau)$ is known, finding the structure of the boundary layers is thus reduced to getting the asymptotic form of $S(0, T)$ for $T \gg 1$.

If in Eq. (81) we have the Milne kernel function: $K(\tau) = E_1(|\tau|)/2$, this $K(\tau)$ is defined for all $\tau \in (-\infty, \infty)$. The Biberman–Holstein kernel (38) also is defined for all τ. But in general, the symmetric kernel function $K(\tau)$ of the Fredholm equation (81) is defined only for $\tau \in [-T,\ T]$. The kernel $K(\tau)$ in Eq. (81) is not normalized to 1 on the interval of its definition. Let us define the function $K_2(\tau)$ as follows:

$$K_2(\tau) = 1 - 2\int_0^\tau K(\tau')\, d\tau', \qquad T \geq \tau \geq 0. \tag{84}$$

We note that if $K(\tau)$ is "naturally" defined for $\tau \in (-\infty, \infty)$, as it is the case for e.g. the Biberman–Holstein kernel, the function $K_2(\tau)$ thus defined is identical to $K_2(\tau)$ used above (Eq. (51)). Let us now denote

$$K_T(\tau) \equiv K(\tau)/[1 - K_2(T)] \tag{85}$$

and

$$\epsilon_T = \epsilon + (1-\epsilon) K_2(T). \tag{86}$$

This new kernel function $K_T(\tau)$ is normalized to 1 on $[-T,\ T]$:

$$\int_{-T}^{T} K_T(\tau)\, d\tau = 1. \tag{87}$$

We now extend $K_T(\tau)$ to the whole τ semiaxis as follows: $K_T(\tau) = K(\tau)$ for $|\tau| < T$ and $K_T(\tau) = 0$ for $|\tau| > T$ and consider, along with Eq. (81), the equation on semiaxis

$$S_T(\tau) = (1 - \epsilon_T) \int_0^{\infty} K_T(\tau - \tau')\, S_T(\tau')\, d\tau' + \epsilon. \tag{88}$$

In physical terms, in *semiinfinite* medium described by Eq. (88) the direct contribution to $S_T(\tau)$ is given only by a finite layer $(\tau - T,\ \tau + T)$. According to the $\sqrt{\epsilon}$ law, the following *exact* result holds:

$$S_T(0) = \frac{\epsilon}{\sqrt{\epsilon_T}}\ , \tag{89}$$

or

$$S_T(0) = \frac{\epsilon}{\sqrt{D(T)}}\ , \qquad D(T) \equiv \epsilon + (1 - \epsilon) K_2(T). \tag{90}$$

If $T \gg 1$, it is natural to expect that, in surface layers of semiinfinite atmosphere, *indirect* contribution to $S_T(\tau)$ from layers with $\tau > T$ will be small. Neglecting of this contribution is equivalent to replacing semiinfinite atmosphere by the finite layer of thickness T. Thus, it is natural to suppose that $S(0, T) \approx S_T(0)$, or

$$S(0, T) \approx \frac{\epsilon}{\sqrt{D(T)}}\ . \tag{91}$$

As we shall see in Sect. 9, for Lévy flights described by the Wiener–Hopf equation (1), its solution can be approximated by

$$S(\tau) \approx \sqrt{\frac{\epsilon}{D(\tau)}}\ . \tag{92}$$

This high-accuracy approximation is valid for $\tau \in [0, \infty)$. The slower the kernel function $K(\tau)$ decreases for $|\tau| \to \infty$, the higher its accuracy. Comparison of Eqs. (91) and (92) reveals that

$$S(0, T) \approx \sqrt{\epsilon}\ S(T). \tag{93}$$

The domain of applicability of this approximation is wide. It holds for Lévy flights with an arbitrary characteristic exponent α; as α decreases, it becomes more accurate.

For the particular case of Doppler flights, this "remarkable approximate relation" was found by Avrett and Hummer (1965) from the analysis of numerical solutions of the corresponding integral equations. It was characterized by Avrett and Hummer (1965) as "surprising". As we have shown, this curious relation is an immediate consequence of two physically clear results, Eqs. (91) and (92).

{This comment is triggered by a recent arXiv publication of d'Eon and McCormick (2019). The relation (93) should hold for Lévy flights in spaces of arbitrary dimension d ($d = 1$ is a rod, or, in Russian publications, a one-dimensional medium; $d = 2$ is the so-called flatland; $d = 3$ is the usual three-dimensional space; $d = 4,\ 5\ldots$—d-dimensional worlds).}

The atmosphere is called effectively thick, or strongly dissipative, if $\epsilon \gg K_2(T)$. In this case $S(0, T) \approx \sqrt{\epsilon}$. Inside the medium, far from both boundaries, $S(\tau, T)$ is close to 1, i.e., thermodynamic equilibrium prevails there. In this case we have essentially two semi-infinite media fitted by their inner layers. The opposite limiting case $\epsilon \ll K_2(T)$ is much more interesting (the so called effectively thin, or weakly dissipative media). Here one has

$$S(0, T) \approx \frac{\epsilon}{\sqrt{K_2(T)}}\,, \tag{94}$$

and $S(\tau, T) \ll 1$ for all $\tau \in [0,\ T]$. In this case photon destruction in scattering events is negligible, and the process of multiple scattering is terminated by escape of radiation. If escape of photons is the only mechanism terminating their walk in the medium, one says that we deal with pure, or conservative scattering $\big(\epsilon = 0$ in the multiplier of the integral in Eq. (81)$\big)$. For this case, the asymptotically exact value of $S(0, T)$ is known (Ivanov 1973, p. 384):

$$S(0, T) \sim \epsilon\, \frac{c_1}{\sqrt{K_2(T)}}\,, \qquad T \to \infty, \tag{95}$$

where

$$c_1 = \Gamma(\alpha/2) \left(\frac{\sin(\pi\alpha/2)}{2\pi\, \Gamma(\alpha)} \right)^{1/2}. \tag{96}$$

In particular, $c_1 = 0.914$ for $\alpha = 1/2$ (Voigt and Lorentz profiles) and $c_1 = 0.707$ for $\alpha = 1$ (Doppler profile). That is what one might expect: $c_1 < 1$ and is close to 1. For non-conservative scattering, and all the more if continuum contributions to line formation are taken into account, analytical treatment becomes much more cumbersome (Ivanov 1973, Chap. VIII; substantial additions may be found in Nikoghossian 2006).

6.2 Interior Solution

Let us now discuss the scaling of the source function in the inner parts of the layer. We will consider only the simplest case of conservative scattering.

The intensity of the emergent radiation is given by the well-known formula

$$I(0,\mu,x) = I(T,\mu,x) = \int_0^T S(\tau,T)\exp\left(-\phi(x)\tau/\mu\right)\phi(x)\,d\tau/\mu. \tag{97}$$

If the primary sources are distributed uniformly and the optical thickness of the layer is large, the source function near the boundaries grows with τ approximately in the same way as for the generalized Milne problem $\big($cf. Eq. (83)$\big)$. Hence, as we shift from the center of the line, the intensity of the emergent radiation increases, because deeper layers become "visible". However, if we are far away from the line center, the whole medium is transparent, so that the exponent in Eq. (97) can be replaced with 1. The intensity becomes $\propto \phi(x)$, and hence decreases as we shift from the center of the line. One can conclude that the emergent intensity has a maximum at $\phi(x)T/\mu \sim 1$. Figuratively speaking, to look for the asymptotic form of $I(0,\mu,x)$ for a fixed $|x|$ and $T \to \infty$ is equivalent to waiting while a moving wave engulfs you. It is more appropriate to try surfing by straddling the intensity wave, i.e., by simultaneously letting $|x|$ and T to infinity in such a way that $t \equiv \phi(x)T/\mu$ remains fixed. More than half a century ago, in 1964, this trivial idea enabled to obtain the very first result in what later became known as the large-scale description of line radiation fields (Ivanov 1965). This first large-scale asymptotic formula is (conservative scattering, Doppler profile)

$$I(0,\mu,x)K_2(T) \propto \mathrm{e}^{-t/2}\, I_1(t/2),$$

$$x \to \infty, \quad T \to \infty, \quad t = \phi(x)T/\mu = \text{const}. \tag{98}$$

Here I_1 is the Bessel function of imaginary argument.

A Bessel function appearing in problems of transfer of resonance radiation? At first it looked nearly mysterious, but I had to get accustomed to it... An episode comes to my mind, historical for me. In 1956 V. V. Sobolev supervised students' astrophysical computations (we used adding machines, not computers!). I was the last-year student. Once he told me that it would be interesting to obtain asymptotic form of $I(0,\mu,x)$ for large T, and added that he tried, but failed. Needless to say, I clearly remembered this for years. In 1962 I managed to obtain asymptotics for the case of the Doppler profile and $x = \text{const},\ T \to \infty$. Soon it became clear to me that it is not the whole story. Two years later, asymptotic surfing in frequency space enabled to get Eq. (98).

One can show that in case of conservative scattering $S(T/2\,,T) \approx \epsilon/K_2(T)$. This is the so-called direct escape, or on–the–spot approximation. Asymptotically exact

expression has an additional numerical factor $(2/\alpha\pi)\,\sin(\alpha\pi/2)$, or $2/\pi$ for the Doppler profile ($\alpha = 1$) (see Ivanov 1973, p. 441). Therefore,

$$I(0,\mu,x) \approx \int_0^1 \frac{S(T\xi,T)}{S(T/2,T)}\,\mathrm{e}^{-t\xi}\,t\,d\xi \sim \mathrm{e}^{-t/2}\,I_1(t/2),$$

$$t = \phi(x)T/\mu = \text{const}, \quad T \to \infty. \tag{99}$$

By direct substitution into Eq. (99) one can verify that

$$S(\xi T,T) \sim \epsilon\,S(T/2,T)\,2\sqrt{\xi(1-\xi)}\,, \qquad T \to \infty, \quad 0 < \xi < 1, \tag{100}$$

or, taking into account the asymptotic form of the Doppler $K_2(\tau)$ (Eqs. (42) and (51)),

$$K_2(\tau) \sim \frac{1}{2\tau\ln(\tau/\sqrt{\pi})}\,, \tag{101}$$

we find

$$S(\tau,T) \sim \epsilon\,\frac{2}{T\,K_2(T)}\sqrt{\tau(T-\tau)} \propto \epsilon\left(\ln\frac{T}{\sqrt{\pi}}\right)^{1/2}\sqrt{\tau(T-\tau)}\,. \tag{102}$$

This formula describes large-scale behavior of $S(\tau,T)$ in a thick conservatively scattering layer everywhere except for boundary regions. Near the boundary $\tau = 0$ or, more exactly, within the boundary layer, $S(\tau,T)$ is given by Eq. (83). For $1 \ll \tau \ll T$ this solution is to be fitted to Eq. (102), so that it should be equal to the result given by Eq. (102). For $\tau \ll T$ the latter formula, i.e., Eq. (102), assumes the form

$$S(\tau,T) \propto \epsilon\sqrt{T}\left(\ln\frac{T}{\sqrt{\pi}}\right)^{1/2}\sqrt{\tau}\,, \tag{103}$$

whereas Eq. (83) gives

$$S(\tau,T) \propto \frac{\epsilon}{\sqrt{K_2(T)}}\,\frac{1}{\sqrt{K_2(\tau)}} \propto \epsilon\sqrt{T}\left(\ln\frac{T}{\sqrt{\pi}}\right)^{1/4}\left(\ln\frac{\tau}{\sqrt{\pi}}\right)^{1/4}\sqrt{\tau}\,. \tag{104}$$

Since logarithm is a slowly varying function, its argument $\tau = T\xi$ for $T \to \infty$ and $\xi = \text{const}$ can be replaced with T, and Eq. (104) transforms into Eq. (103), as it should be. Accurate calculation of coefficients of proportionality which is omitted for simplicity, reveals that in the right hand sides of Eqs. (103) and (104) they are identical (and equal to $4/\pi$, as can easily be verified).

Thus we managed to split the solution of the problem into two problems. One is finding the structure of the boundary layer. For a given absorption coefficient,

it is solved once and for all, and its solution $S_h(\tau)$ does not depend on the size of the region in which random walks or Lévy flights occur. This is what we called the generalized Milne problem. Another problem is elucidating structure of the inner regions. In this latter case the characteristic scale is the thickness of the layer. In case of conservative Doppler walk the solution of this second problem is given by Eq. (100). The possibility of such a splitting of the problem—boundary layer+"interior"—is of quite general nature. It is also possible for, e.g., semi-infinite atmospheres with $\epsilon \ll 1$ and $\beta \ll 1$ (see Ivanov 1973, §§ 7.7 and 8.5; Frisch and Frisch 1977).

Generalization of Eq. (99) to the case of conservative Lévy flights with an arbitrary characteristic exponent α is (Nagirner 1967; Ivanov 1973, Sect. 8.5)

$$I(0, \mu, x) \sim \epsilon \, \frac{\sqrt{\pi}}{\Gamma(1-\alpha/2)K_2(T)} \, t^{1-\alpha/2} \, \mathrm{e}^{-t/2} \, I_{(\alpha+1)/2}(t/2) \, . \tag{105}$$

It enables one to obtain from Eq. (97) that

$$S(\xi T, T)K_2(T) \sim \epsilon \, \frac{2\sin(\alpha\pi/2)}{\pi\alpha} \, \xi^{\alpha/2}(1-\xi)^{\alpha/2} \equiv \epsilon \, 2\sigma(\xi),$$
$$T \to \infty, \quad 0 < \xi < 1. \tag{106}$$

The equation satisfied by $\sigma(\xi)$ is

$$\sigma(\xi)\Big[\xi^{-\alpha} + (1-\xi)^{-\alpha}\Big] = \alpha \int_0^1 \frac{\sigma(\xi) - \sigma(\xi')}{|\xi - \xi'|^{\alpha+1}} \, d\xi + 1. \tag{107}$$

This is the large-scale asymptotic form of the basic integral equation (81) on a finite interval $[0, T]$, $T \gg 1$, from which it has been derived. An important specific feature of this equation is that there are no large or small parameters. The function $\sigma(\xi)$ given by Eq. (106) is the exact solution of Eq. (107).

If the medium is not conservative, there are two characteristic scales, thickness of the layer T and thermalization length τ_t. From the basic integral equation (81) with the probabilistic kernel $K(\tau)$ one can derive equation that determines large-scale behavior of its solution. For $\alpha < 2$, it is a counterpart of the usual diffusion equation.

The approach briefly outlined above is just the tip of the iceberg. In astrophysics, this technique appears under several names: large-scale description (Abramov et al. 1969), method of scaling (Nagirner 2007), or simply scaling (Frisch and Frisch 1977). Investigation of Lévy flights based on such an approach is now a separate branch of science, with many applications not only in physics. These phenomena are known as anomalous diffusion. They are described by the so called generalized diffusion equation. The mathematics used here is the derivatives of fractional order, and these are the integral operators of the type appearing in Eq. (107). For a review of this field, see Uchaikin (2003).

7 Methods of Derivation of the $\sqrt{\epsilon}$ Law

In this Section, the term "$\sqrt{\epsilon}$ law" means both the usual (scalar) $\sqrt{\epsilon}$ law and the asymptotic behavior of the homogeneous Wiener–Hopf equation, so that polarization is ignored. We restrict ourselves by mere mentioning of a dozen of various methods of derivation of these important results, with corresponding references. This list does not pretend to be exhaustive.

- Directly from the Milne integral equation (Hopf 1930; Bronstein 1929)
- Using the non-linear equation for the H–function (Ambartsumian 1942, 1948)
- Discretization of radiative transfer equation in angular variable + limit $n \to \infty$ (Chandrasekhar 1950)
- Probabilistic treatment of radiative transfer (Sobolev 1963)
- Trajectories of random walk in half-space (Ivanov 1973)
- Using a quadratic functional (Frisch and Frisch 1975)
- Series expansion of $\epsilon^{-1/2}$ in powers of $(1-\epsilon)^n$ + geometric interpretation of the terms of the expansion (Landi Degl'Innocenti 1979)
- Direct application of the invariance principle (Hubeny 1987)
- Using Rybicki quadratic integral (Rybicki 1977)
- Using variational formalism (Nikoghossian 2011)
- Expansion in singular eigenfunctions (Case and Zweifel 1967).

We note that the relation known in astrophysics as the $\sqrt{\epsilon}$ law is also known in probability theory, in random walk theory, at least since the 1950s. It is a particular case $\big($for a symmetric kernel: $K(\tau) = K(-\tau)\big)$ of the result known as Sparre-Andersen theorem (Sparre-Andersen 1953; see also Feller 1966, Chap. XII, Sect. 7). The result expressed by Eq. (20), with the H–function given by Eq. (65), in terminology of the probability theory, is the Spitzer–Pollaczek formula (Spitzer 1957; Pollaczek 1952).

8 Polarization: Generalizations of the $\sqrt{\epsilon}$ Law

8.1 Second Solar Spectrum

The $\sqrt{\epsilon}$ law started a second life when it was found that it also dwells in the rich realm of problems of transfer of polarized radiation.

More than 40 years ago, investigation of the wavelength dependence of the linear polarization of radiation of the solar limb resulted in the discovery of a multitude of features that may be called "lines", both in "absorption" and in "emission" (Stenflo et al. 1980). This ***second solar spectrum***, as it is now known, differs drastically from the usual Fraunhofer intensity spectrum (see its Atlas, in three volumes [sic! – VVI]—Gandorfer 2000–2005). This discovery caused a burst of interest in polarization arising in multiple resonance scattering (and somewhat later, in more

complicated situations, see below). The results of numerical modeling of polarization in spectral lines, within the framework of CFR approximation, were presented by Stenflo and Stenholm (1976), Dumont et al. (1977), Rees and Saliba (1982), Faurobert (1987), Faurobert-Scholl and Frisch (1989) and in several other publications. Strangely enough, the vector–matrix description was not used in these publications, while this technique has already been standard in studying multiple monochromatic Rayleigh and molecular scattering (e.g., Mullikin 1966; Domke 1973; Domke and Ivanov 1976; van de Hulst 1980; Viik 1990). This point is of importance for us, since without using the vector–matrix language it was difficult to suspect the existence of a vector generalization of the $\sqrt{\epsilon}$ law. This is probably the reason why it was found only in 1990 (Ivanov 1990).

8.2 Resonance Scattering. Vectors

According to the standard model, the radiation field in a plane–parallel atmosphere that is not irradiated from outside is axially–symmetric, so that the Stokes vector $\mathbf{I}(\tau, \mu, x)$ has only two components, $\mathbf{I} = (I,\ Q)^T$, where symbol ^{T} means transposition, and the polarization is linear. The reason why the polarization arises is the limb darkening. The basic assumption in treating resonance scattering is separation of angular and frequency variables in single scattering and assuming CFR for frequency redistribution (Dumont et al. 1977). The redistribution matrix (of dimension 2×2) is then

$$\hat{\mathbf{R}}(\mu, x; \mu', x') = \phi(x)\phi(x')\,\hat{\mathbf{P}}(\mu, \mu'), \tag{108}$$

where $\hat{\mathbf{P}}(\mu, \mu')$ is the phase matrix. For the rectangular profile, resonance scattering degenerates into Rayleigh (or, more precisely, molecular) scattering.

Under the assumption of Eq. (108), the calculation of the field of polarized radiation in an isothermal atmosphere reduces to solving the vector Wiener–Hopf equation

$$\mathbf{S}(\tau) = (1-\epsilon)\int_0^\infty \hat{\mathbf{K}}(\tau-\tau')\,\mathbf{S}(\tau')\,d\tau' + \epsilon\mathbf{1}, \tag{109}$$

where $\mathbf{S}(\tau) = \big(S_I(\tau), S_Q(\tau)\big)^T$ is the vector source function, with its components divided by the Planck function $B_\nu(T)$, and $\mathbf{1} = (1,\ 0)^T$. Clearly, Eq. (109) is a system of two coupled Wiener–Hopf equations.

The limiting case of Eq. (109) for $\epsilon = 0$ is the homogeneous vector equation

$$\mathbf{S}_h(\tau) = \int_0^\infty \hat{\mathbf{K}}(\tau-\tau')\,\mathbf{S}_h(\tau')\,d\tau'. \tag{110}$$

Its solution (normalized as discussed below) is the vector Milne problem.

The kernel matrix of Eqs. (109) and (110) (of dimension 2×2) can be written as

$$\hat{\mathbf{K}}(\tau) = \frac{1}{2} \int_{-\infty}^{\infty} \phi^2(x)\, dx \int_0^1 \exp\left(-\phi(x)|\tau|/\mu\right) \hat{\mathbf{\Psi}}(\mu)\, d\mu/\mu\,, \tag{111}$$

where $\hat{\mathbf{\Psi}}(\mu)$ is the so called characteristic matrix:

$$\hat{\mathbf{\Psi}}(\mu) = \hat{\mathbf{A}}^T(\mu)\hat{\mathbf{A}}(\mu), \tag{112}$$

with

$$\hat{\mathbf{A}}(\mu) = \begin{pmatrix} 1 & \sqrt{\frac{W}{8}}\,(1-3\mu^2) \\ 0 & \sqrt{\frac{W}{8}}\,3(1-\mu^2) \end{pmatrix}. \tag{113}$$

Here W is depolarization parameter, $0 < W \leq 1$. Polarization is largest for $W = 1$ (dipole scattering). The normalization of the kernel matrix is

$$\int_{-\infty}^{\infty} \hat{\mathbf{K}}(\tau)\, d\tau = \begin{pmatrix} 1 & 0 \\ 0 & 7W/10 \end{pmatrix}. \tag{114}$$

We note that the form of the equation for the vector source function is not unique. The phase matrix $\hat{\mathbf{P}}(\mu, \mu')$ appearing in the vector transfer equation

$$\mu \frac{d\mathbf{I}(\tau, \mu, x)}{dx} = -\phi(x)\mathbf{I}(\tau, \mu, x) + \frac{1-\epsilon}{2}\phi(x) \int_{-\infty}^{\infty} \phi(x')\, dx' \int_{-1}^{1} \hat{\mathbf{P}}(\mu, \mu')\, \mathbf{I}(\tau, \mu', x')\, d\mu' + \epsilon \mathbf{1},$$

can be factorized differently, i.e., represented in a different way as the product of matrices depending on one angular variable: $\hat{\mathbf{P}}(\mu, \mu') = \hat{\mathbf{A}}_1(\mu)\hat{\mathbf{A}}_2(\mu')$ (van de Hulst 1980, Chap. XVI). If one assumes the factorization

$$\hat{\mathbf{P}}(\mu, \mu') = \hat{\mathbf{A}}(\mu)\hat{\mathbf{A}}^T(\mu'), \tag{115}$$

with $\hat{\mathbf{A}}(\mu)$ given by Eq. (113), then the matrix kernel function $\hat{\mathbf{K}}(\tau)$ has the characteristic matrix of the form (112).

The vector integral equations (109) and (110) have exactly the same form as the scalar equations (1) and (4) we considered so far. This does not imply that their solutions are also of similar form. However, the scalar $\sqrt{\epsilon}$ law can easily be generalized to the vector case. This is one of only two non-trivial analytical results on the structure of solution of Eq. (109). The other result is the asymptotic behavior

of the solution of the homogeneous Eq. (110). This latter result can be looked at as a vector generalization of the classical Hopf–Bronstein relation $S(\tau) \sim \sqrt{3}\,\tau$.

The Rybicki quadratic integral (Rybicki 1977) can easily be generalized from scalars to vectors. One of the consequences of the resulting quadratic relation is the vector version of the scalar $\sqrt{\epsilon}$ law (Ivanov 1990):

$$|\mathbf{S}(0)| = \sqrt{\epsilon}, \qquad |\mathbf{S}(\infty)| = 1, \tag{116}$$

where $|\mathbf{S}|$ is the Euclidean norm of the vector $\mathbf{S}$, so that

$$|\mathbf{S}(\tau)|^2 = \mathbf{S}^T(\tau)\mathbf{S}(\tau) = S_I^2(\tau) + S_Q^2(\tau). \tag{117}$$

If one assumes that the solution of the homogeneous vector Eq. (110) is related to $\mathbf{S}(\boldsymbol{\emptyset})$ by

$$\mathbf{S}_h(\tau) = \lim_{\epsilon \to 0} \frac{\mathbf{S}(\tau)}{\sqrt{\epsilon}}\,, \tag{118}$$

then, by virtue of (116), the normalization of $\mathbf{S}_h(\tau)$ is

$$|\mathbf{S}_h(0)| = 1. \tag{119}$$

The latter two equations are obvious vector versions of Eqs. (6) and (5).

Although Eq. (116) does not enable one to get both components of $\mathbf{S}(0)$, it turned out to be a useful test of computer codes for calculating vector (and matrix, see below) source function $\mathbf{S}(\tau)$. This relation and its generalized versions have been used in many publications.

We note in passing that nearly conservative ($\epsilon \ll 1$) Rayleigh scattering in semi-infinite atmospheres, with polarization taken into account, recently has been studied by Frisch (2019). The approach used by her is similar to that described in Sect. 6 in respect to problems of scalar, i.e., neglecting polarization, conservative scattering in optically thick atmospheres. In the work of Frisch (2019) the solution is expanded in powers of a small parameter $\sqrt{\epsilon}$ and then the problem is split into two—structure of the boundary layer and structure of the interior. In case of the problem considered by Frisch (2019), the radiation field in the inner part is described by the diffusion approximation. Although nearly conservative monochromatic Rayleigh scattering had been studied long ago (in particular, by Domke 1973; Domke and Ivanov 1976), the approach of Frisch (2019) has not been used so far to solve monochromatic vector radiative transfer problems.

8.3 Resonance Scattering. Matrices

In the mid-1990s, it has been shown that by using the notion of *matrix radiative transfer equation*, one gets deeper insight into problems of multiple scattering of

polarized radiation. The matrix radiative transfer equation, with matrices of dimension 2×2, initially has been used for studying multiple Rayleigh scattering (Ivanov 1995). Somewhat later, resonance scattering with CFR has been analyzed using this technique (Ivanov et al. 1997). Not dwelling on the details, we just state that the matrix source function $\hat{\mathbf{S}}(\tau)$ satisfies the same equation as the vector $\mathbf{S}(\tau)$ does, with the vector free term $\epsilon\mathbf{1}$ replaced with the matrix $\hat{\epsilon} = \mathrm{diag}(\epsilon_I, \epsilon_Q)$, where $\epsilon_I = \epsilon$ and $\epsilon_Q = 7W/10$. The *matrix* generalization of the $\sqrt{\epsilon}$ law is

$$\hat{\mathbf{S}}^T(0)\hat{\mathbf{S}}(0) = \hat{\mathbf{E}}, \qquad \hat{\mathbf{S}}(\infty) = \hat{\epsilon}^{-1/2}. \tag{120}$$

Here $\hat{\mathbf{E}}$ is the unit matrix. According to Eq. (120), four elements of the matrix $\hat{\mathbf{S}}(0)$ obey three simple relations, and this provides a sensitive test of numerical solutions of the corresponding matrix Wiener–Hopf equations.

Detailed analytical and numerical study of polarization of resonance radiation arising in scattering atmospheres has been presented by Ivanov et al. (1997), Loskutov and Ivanov (2007), Dementiev (2008). We reproduce the main results.

In case of factorization of the phase matrix assumed above, Eqs. (115), (113), the degree of polarization of radiation emerging in grazing directions (i.e., limb polarization, $\mu = 0$) is expressed in terms of the elements of matrix $\hat{\mathbf{S}}(0)$ as follows:

$$p = \frac{3S_{21}(0)}{(8/W)^{1/2}S_{11}(0) + S_{21}(0)}\,. \tag{121}$$

Its maximum value is reached for conservative dipole scattering ($\epsilon = 0$, $W = 1$) and equals 9.443% for Doppler profile (Ivanov et al. 1997) and 5.421% for Lorentz absorption coefficient (Loskutov and Ivanov 2007). For Voigt absorption coefficient with $0 \leq a \lesssim 0.01$, the empirical formula

$$p = 9.443\exp\left(-1.387\sqrt{a}\,\right)\%\,, \qquad \epsilon = 0, \tag{122}$$

provides limb polarization with three digits (Dementiev 2008). Due to frequency redistribution upon scattering, these numbers are smaller than the Sobolev–Chandrasekhar polarization limit of 11.713% (monochromatic scattering; physically, this corresponds to Thompson scattering in purely electron stellar atmosphere of a hot star).

Somewhat unexpectedly, $\sqrt{\epsilon}$ appeared in an empirical formula that gives limb polarization ($\mu = 0$) for an atmosphere with nearly conservative ($\epsilon \ll 1$) dipole ($W = 1$) resonance scattering (CFR, Doppler absorption coefficient) (Ivanov et al. 1997):

$$p = \left(9.443 - 38.05\sqrt{\epsilon}\,\right)\%\,, \qquad W = 1. \tag{123}$$

The other result that deserves mentioning is related to the Milne problem. In case of CFR with Doppler absorption coefficient the asymptotic solution ($\tau \to \infty$) of the homogeneous Eq. (110) normalized according to (119) is (in components)

$$S_{hI}(\tau) = S_{11}(\tau) \sim \frac{4}{\pi}\,\tau^{1/2}\,T^{1/4},$$

$$S_{hQ}(\tau) = S_{21}(\tau) \sim \frac{5\pi}{64\sqrt{2}}\,\tau^{-1/2}\,T^{-9/4}, \tag{124}$$

where $T \equiv \ln(\tau/\sqrt{\pi})$. These formulae are generalizations of the scalar relation (61) or, to be more accurate, of the leading term of the expansion (61). Full asymptotic expansions of $\mathbf{S}_h(\tau)$ (and of all four elements of $\hat{\mathbf{S}}(\tau)$ for $\epsilon = 0$) in inverse powers of T similar to Eq. (61) were found by Ivanov et al. (1997). They were used as very sensitive tests of the accuracy of numerical solution of the integral equations that describe Doppler Lévy flights in the corresponding vector and matrix Milne problems.

Highly non-trivial asymptotic forms we have just briefly outlined are far descendants of the simplest Hopf–Bronstein relation $S_h(\tau) \sim \sqrt{3}\,\tau$.

8.4 Magnetic Field. Hanle Effect

Problems of line formation in atmospheres with weak magnetic field causing the so called Hanle effect are substantially more cumbersome. To learn what is the essence of the Hanle effect see, e.g., Landi Degl'Innocenti and Landolfi (2004). The Hanle effect enables one to find extremely weak magnetic fields by measuring polarization parameters of scattered resonance radiation. There are several publications where relevant versions of the $\sqrt{\epsilon}$ law have been found. The technique needed to describe radiation fields in media permeated by weak magnetic fields is not simple. It would be enough to say that here one encounters tensor source functions. There is no possibility—or need—to present here this bulky technique. Standard reference to this field is monograph of Landi Degl'Innocenti and Landolfi (2004). The derivation of a generalized $\sqrt{\epsilon}$ relation using this technique has been given by Landi Degl'Innocenti and Bommier (1994) (see also Štěpán and Bommier 2007; Frisch 1998). An illustration of using the $\sqrt{\epsilon}$ relation for checking the accuracy of calculations in Hanle problems is given by del Pino Alemán et al. (2014).

Equations describing radiation fields with the Hanle effect taken into account were cast in a more or less usual form by Grachev (2014). The magnetic field is assumed to be homogeneous and monodirectional. Its direction is characterized by angular variables (μ_B, φ_B), where μ_B is the cosine of zenith distance and φ_B is azimuth. Even in CFR approximation, the Hanle phase matrix is terrifying. We present here the structure of its complete factorization found by Grachev (2014):

$$\hat{\mathbf{P}}(\mu, \varphi; \mu', \varphi'; \mu_B, \varphi_B, \gamma_B) = \hat{\mathbf{A}}(\mu)\hat{\mathbf{R}}(\varphi_B - \varphi)\,\hat{\boldsymbol{\lambda}}\,\hat{\mathbf{M}}_B(\mu_B, \gamma_B)\hat{\mathbf{R}}(\varphi' - \varphi_B)\hat{\mathbf{E}}_{12}\hat{\mathbf{A}}^T(\mu'). \tag{125}$$

Here $\hat{\mathbf{A}}(\mu)$ is 3×6 matrix (we do not write it out here), $\hat{\mathbf{R}}(\varphi)$ is block–diagonal matrix 6×6, composed of three matrices 2×2: $\hat{\mathbf{R}}(\varphi) = \mathrm{diag}\{\hat{\mathbf{E}}, \hat{\mathbf{r}}(-\varphi), \hat{\mathbf{r}}(2\varphi)\}$, where $\hat{\mathbf{E}} =$

diag$\{1, 1\}$ and $\hat{\mathbf{r}}(\varphi)$ is rotation matrix by angle φ; matrix $\hat{\mathbf{M}}_B(\mu_B, \gamma_B)$ of dimension 6×6 describes the influence of magnetic field, γ_B is dimensionless field strength; $\hat{\mathbf{E}}_{12} =$ diag$\{1, 1, 2, 2, 2, 2\}$; finally, $\hat{\boldsymbol{\lambda}} =$ diag$\{\lambda, \lambda_p, \lambda_p, \lambda_p, \lambda_p, \lambda_p\}$ is the matrix albedo of single scattering, where $\lambda \equiv (1-\epsilon)$ is the usual albedo of single scattering and $\lambda_p = \lambda/(1+\lambda\delta^{(2)})$ is the albedo accounting of depolarizing elastic collisions.

Under the assumptions formulated above, the calculation of the radiation field can be reduced to solving of matrix integral equation for the source function $\hat{\mathbf{S}}(\tau)$ of dimension 6×6. The origin of dimension 6×6 will not be explained. This basic equation is

$$\hat{\mathbf{S}}(\tau) = \hat{\boldsymbol{\lambda}}\,\hat{\mathbf{H}}_B \int_0^\infty \hat{\mathbf{K}}(\tau-\tau')\,\hat{\mathbf{S}}(\tau')\,d\tau' + \hat{\mathbf{S}}^*, \tag{126}$$

where the kernel 6×6 matrix $\hat{\mathbf{K}}(\tau)$ is

$$\hat{\mathbf{K}}(\tau) = \frac{1}{4\pi}\,\hat{\mathbf{E}}_{12}\int_{-\infty}^{\infty}\phi^2(x)\,dx\int_0^1\frac{d\mu}{\mu}\int_0^{2\pi}\mathrm{e}^{-\phi(x)|\tau|/\mu}\,\hat{\mathbf{R}}(\varphi)\hat{\mathbf{A}}^T(\mu)\hat{\mathbf{A}}(\mu)\hat{\mathbf{R}}(-\varphi)\,d\varphi. \tag{127}$$

Here

$$\hat{\mathbf{H}}_B = \hat{\mathbf{H}}_B(\mu_B, \varphi_B, \gamma_B) = \hat{\mathbf{R}}(\varphi_B)\hat{\mathbf{M}}_B(\mu_B, \gamma_B)\hat{\mathbf{R}}(-\varphi_B) \tag{128}$$

and $\hat{\mathbf{S}}^*$ is the diagonal matrix of primary sources.

There are several versions of vector and matrix $\sqrt{\epsilon}$ law relevant to the problems we have now briefly outlined (Landi Degl'Innocenti and Bommier 1994; Frisch 1998; Štěpán and Bommier 2007; del Pino Alemán et al. 2014). To formulate them explicitly, we would need to reproduce a dozen of formulae. We restrain from this and just mention that the most general forms of the $\sqrt{\epsilon}$ law were found by Grachev (2001, 2014). They are matrix relations (matrices 6×6) similar to Eq. (120), but a little bit more complex. It is a pity that so far they have not been used in practical calculations.

Our narration about manifestation, or more exactly, about how $\sqrt{\epsilon}$ appears in theoretical investigations of the solar Hanle effect, is finished. However it is natural to add that in 2015 the space era of solar spectropolarimetry began. The project CLASP (**C**hromospheric **LA**yer **S**pectro **P**olarimeter) led to the discovery of the Hanle effect in Lyman-alpha line. This has clearly demonstrated the possibilities of using the Hanle effect for probing the structure of the transition layer between chromosphere and corona (Ballester et al. 2017; Trujillo Bueno et al. 2018).

9 Lévy Flights: Approximations Inspired by the $\sqrt{\epsilon}$ Law

Literature on Lévy flights is immense. Born in probability theory, they soon found applications in physics, economics, financial mathematics, theory of records and its applications (climate, sports, etc.). For a rather long time, astrophysicists have not heard about it. Only in the mid-1960s Petersburg's astrophysicists have discovered, first, the existence of the characteristic exponent and then, somewhat later, learned that there are stable probability laws (Ivanov and Sabashvili 1972). Investigation of Lévy frights of photons of resonance lines eventually resulted in formulation of the approximation that may be useful far beyond astrophysics. This is the subject matter of this Section.

9.1 An Illustration

We start by considering one particular, but important example. Let us consider Lévy flights on semi–axis $\tau \geq 0$ of particles that are being born at all τ with the same efficiency (Wiener–Hopf Eq. (1)). We assume that the probability density of lengths of particle steps is the Cauchy distribution:

$$K(\tau) = \frac{1}{\pi}\,\frac{1}{1+\tau^2}\,. \tag{129}$$

It may seem rather unexpected that *for small* ϵ such a simple function as

$$S^a(\tau) = \sqrt{\epsilon}\left(1-(1-\epsilon)\frac{2}{\pi}\arctan\tau\right)^{-1/2} \tag{130}$$

provides a very good approximation to the solution of the Wiener–Hopf equation (1) with the kernel function $K(\tau)$ of the form (129) (or, briefly, with the Cauchy kernel). Thus, for $\epsilon = 10^{-2}$ the maximum relative error of the approximation is $\sim$10% while the solution $S(\tau)$ increases by factor 100.

We state without proof that the leading term of the asymptotic solution of the homogeneous Wiener–Hopf Eq. (4) with the Cauchy kernel (129) (normalized so that $S_h(0) = 1$) is

$$S_h(\tau) \sim \frac{2}{\sqrt{\pi}}\,\tau^{1/2}, \qquad \tau \to \infty, \tag{131}$$

The approximation (130) gives, for the asymptotic form of the approximate solution of the homogeneous Eq. (4)

$$\lim_{\epsilon\to 0}\frac{S^a(\tau)}{\sqrt{\epsilon}} = S_h^a(\tau) \sim \sqrt{\frac{\pi}{2}}\,\tau^{1/2}, \qquad \tau \to \infty. \tag{132}$$

The coefficients of $\tau^{1/2}$ in Eqs. (132) and (131) differ by a factor close to unity, namely, $2\sqrt{2}/\pi = 0.900$.

9.2 Basic Approximation

The approximation (130) is a particular case (for the Cauchy kernel) of general expression

$$S^a(\tau) = \sqrt{\epsilon}\Big(\epsilon + (1-\epsilon)K_2(\tau)\Big)^{-1/2} \equiv \sqrt{\frac{\epsilon}{D(\tau)}}\,, \tag{133}$$

where $K_2(\tau)$ is the so called second kernel function (cf. Eq. (51)):

$$K_2(\tau) = 2\int_\tau^\infty K(\tau')\,d\tau', \qquad \tau \geq 0.$$

Properties of approximation (133) are remarkable. First, it reproduces the exact results at both ends of the range of τ values. For $\tau = 0$ we have $S^a(0) = \sqrt{\epsilon}$, while for $\tau = \infty$ Eq. (133) yields $S^a(\infty) = 1$. Thus, $S^a(\tau)$ obeys the $\sqrt{\epsilon}$ law. Second, elementary calculation shows that the exact relation which follows from Eq. (1) for $\tau = 0$,

$$S(0) = (1-\epsilon)\int_0^\infty K(\tau')\,S(\tau')\,d\tau' + \epsilon, \tag{134}$$

is satisfied if $S^a(\tau)$ is substituted here for $S(\tau)$. An immediate consequence of this is the relation

$$\int_0^\infty K(\tau)\Big(S(\tau) - S^a(\tau)\Big)\,d\tau = 0. \tag{135}$$

It is obtained if we subtract from Eq. (134), term by term, the same equation with S^a substituted for S. Equation (135) states that, globally, positive and negative deviations of the approximate solution from the exact one are exactly compensated if averaged with the weight $K(\tau)$. The third—and the most important—feature of the approximation (133) is as follows. Figure 1 clearly shows that, for $\epsilon \ll 1$, there is a wide domain of τ values where $S(\tau)$ is close to $\sqrt{\epsilon}\,S_h(\tau)$. If we deal with Lévy flights (characteristic exponent $\alpha < 2$), the kernel function has "thick tails", i.e., decreases for $|\tau| \to \infty$ so slowly that the second moment of $K(\tau)$ diverges. As we mentioned in Sect. 5, in this case the leading term of the asymptotic solution of the homogeneous Eq. (4) normalized so that $S_h(0) = 1$ is

$$S_h(\tau) \sim \frac{C}{\sqrt{K_2(\tau)}}\,, \qquad \tau \to \infty,$$

where the factor C is close to unity. It decreases monotonically as the tails of $K(\tau)$ become thicker, i.e., as the characteristic exponent α decreases. Thus, for Doppler and Cauchy flights $\alpha = 1$ and $C = 0.900$, while for Lorentz flights one has $\alpha = 1/2$

and $C = 0.984$. Hence, in the whole domain where $S(\tau) \ll 1$ one has, apart from a factor close to unity, $S^a(\tau) \approx \sqrt{\epsilon}\, S_h(\tau) \approx \sqrt{\epsilon}/\sqrt{K_2(\tau)}$.

Approximation (133) was initially introduced as an interpolation formula incorporating all these features (Ivanov 1971; see also Ivanov 1973, §§ 5.5 and 6.3). The slower the kernel function $K(\tau)$ decreases for $|\tau| \to \infty$, the higher the accuracy of this approximation.

9.3 Discussion

Simple probabilistic significance of all the quantities appearing in Eq. (133) strongly suggests that this approximation is amenable to direct physical interpretation. This is indeed the case. Specific features of trajectories of Lévy flights discussed in Sect. 5 enable one to conjecture that the essence of the approximation is probably just replacing the whole zig–zag trajectory with only one of its links, namely, the largest one. For an *infinite* medium this approximation—the so called **L**ongest **F**lght **A**pproximation (LFA)—was formulated by Rybicki and Hummer (1969). Later it was shown by Ivanov (1985) that $S^a(\tau)$ is indeed LFA for *semi–infinite* medium (walks on half–line), and not just a useful interpolation formula.

The proof of the fact that Eq. (133) is the half–space LFA is not difficult in principle, but needs rather long considerations of the type we used in deriving the expression of the Green function $G(\tau, \tau_1)$ of Eq. (1) in terms of the surface Green function $G_0(\tau)$ (Eq. (9)). We do not reproduce this proof here.

The accuracy provided by Eqs. (133) and (136) in problems of transfer of resonance radiation with Doppler and Voigt absorption coefficients has been studied in detail by Ivanov and Serbin (1984). For the Doppler case it is of the order of accuracy of CFR approximation. For the Voigt absorption coefficient, as it is well known, CFR breaks down in line wings. However, if one assumes the applicability of CFR in this case, it turns our that the approximation (133) works perfectly.

To summarize this subsection: at the base of the approximation (133) is the specific feature of Lévy flights—the decisive role of largest steps. Combined with the universal scale of variation of the solution of the Wiener–Hopf equation (1) with a probabilistic kernel as given by the $\sqrt{\epsilon}$ law, it provides the approximation with properties seldom appearing together—simplicity, high accuracy and wide domain of applicability.

9.4 Notes

Two points are to be added. First, the derivative of the approximate form $S^a(\tau)$ provides a perfect approximation to non-singular part of the surface Green function $G_0(\tau)$:

$$G_0^a(\tau) = \frac{1}{\sqrt{\epsilon}} \frac{(1-\epsilon)K(\tau)}{9D^{3/2}(\tau)} + \delta(\tau). \tag{136}$$

We note that this approximation satisfies the $\sqrt{\epsilon}$ law (cf. Eq. (15)):

$$\int_0^\infty G_0^a(\tau)\, d\tau = \epsilon^{-1/2}. \tag{137}$$

As it has been shown in Sect. 2, the Green function $G(\tau, \tau_1)$ of the Wiener–Hopf equation (1) is explicitly expressed (in quadratures) in terms of $G_0(\tau)$. This implies that we got an approximate solution of the whole class of Wiener–Hopf equations with an arbitrary free term and an arbitrary symmetric probabilistic kernel $K(\tau)$, slowly decreasing for $|\tau| \to \infty$ (i.e., as a power law, apart from, possibly, a slowly varying factor). The only needed information is the kernel functions $K(\tau)$ and $K_2(\tau)$.

The second point to be mentioned is that the assumptions imposed on the kernel function $K(\tau)$ are mild. No information specific to problems of transfer of resonance radiation has been used. Hence the approximation we discuss is applicable to all symmetric Lévy flights on semi-axis. This was illustrated at the beginning of this Section by considering Lévy flights with Cauchy kernel.

Although the approximation (133) is known presumably not only in radiative transfer, but also in general random walk theory, we failed to find any traces of this. However, in Feller's treatise (Feller 1966) there is a result which is close to LFA for Lévy flights in full space. Namely, it states that for symmetric Lévy flights with characteristic exponent $\alpha < 1$ the mean value of the ratio of the sum of n random steps to the value of the largest one tends, for $n \to \infty$, to $1/(1-\alpha)$. This means that, for $\alpha < 1$, the main contribution to the sum is given by the largest of the terms (Problem 20 in Sect. 11 of Chap. XIII of Feller 1966). For the Doppler random walk and for flights with Cauchy kernel we have $\alpha = 1$, so that contribution of the largest step is not absolutely dominant. Numerical tests have shown that even in this extreme case the approximation (133) still works. One can conjecture that the sufficient condition of its applicability is divergence of the *first* moment of $K(\tau)$. The author is unaware whether the approximation (133) remains reasonable for Lévy flights with $\alpha \in (1,\ 2)$, i.e., what is the accuracy it provides for kernels with $\alpha > 1$.

9.5 Finite Layer

A generalization of the approximation (133) to the case of a layer of final thickness T is possible (Ivanov 1973, Sect. 8.11; Serbin 1985; Castor 2004). An approximate solution of the integral equation (81) with positive symmetric kernel $K(\tau)$ is given by

$$S^a(\tau, T) = \frac{\epsilon}{\sqrt{D(\tau)D(T-\tau)}}. \tag{138}$$

This is an interpolation formula, seemingly devoid of direct probabilistic interpretation. Nevertheless its properties are remarkable. For boundary values of $S(0, T)$ Eq. (138) gives

$$S^a(0, T) = \frac{\epsilon}{\sqrt{D(T)}}\,. \tag{139}$$

In particular, for effectively thick layer $\big(\epsilon \gg K_2(T)\big)$ we get $S^a(0, T) = \sqrt{\epsilon}$, as it should be. In the opposite case of (nearly) conservative scattering

$$S^a(0, T) = \frac{\epsilon}{\sqrt{K_2(T)}}\,, \tag{140}$$

while the exact asymptotic result ($T \to \infty$) has an extra factor c_1 close to unity (Eq. (96)). The large–scale solution of Sect. 6 (conservative scattering, Doppler flights) is correctly reproduced by the approximation we discuss now:

$$\frac{S^a(\xi T, T)}{S^a(T/2, T)} = \frac{K_2(T/2)}{\sqrt{K_2(\xi T) K_2(T - \xi T)}} \sim 2\sqrt{\xi(1-\xi)},$$

$$T \to \infty, \quad 0 < \xi < 1. \tag{141}$$

With all of this in mind, one might expect that Eq. (138) is a reasonable approximation valid for a wide range of values of parameters T and ϵ. Thus, for photon Lévy flights with Doppler absorption profile (characteristic exponent $\alpha = 1$) the ratio $S^a(\tau, T)/S(\tau, T)$ is within a factor of less than 2 for all $\epsilon \in (0, 1]$ and $T \in (0, \infty)$, while for large T and small ε the values of $S(\tau, T)$ vary with τ by orders of magnitude.

10 Conclusion

Analytical **R**adiative **T**ransfer, or ART, is an art, and the $\sqrt{\epsilon}$ law is a well known piece of this art. Historically, the $\sqrt{\epsilon}$ law was first established for the case of the Wiener–Hopf equation (1) with the Milne kernel. This result and the asymptotic solution of the corresponding homogeneous Wiener–Hopf equation (4) were the very first exact ART results. They were found around 1930. Later it became clear that these results admit generalizations in several directions. They provided a key for understanding non-LTE effects in problems of line formation in scattering stellar atmospheres. The $\sqrt{\epsilon}$ law enabled understanding of scaling in problems of line formation in atmospheres of finite optical thickness. Several generalized forms of the $\sqrt{\epsilon}$ law are the only non-trivial rigorous analytical results known in problems of transfer of polarized radiation. They provide sensitive tests of numerical solutions of multiple Rayleigh and resonance scattering problems as well as problems of line formation in atmospheres permeated by weak magnetic fields causing Hanle effect.

Finally, the $\sqrt{\epsilon}$ law combined with the asymptotic solution of the generalized Milne problem formed a starting point in developing a high–accuracy approximate solution of a wide class of problems of symmetrical Lévy flights on semi-axis. As of today, this is the end of the glorious history of the $\sqrt{\epsilon}$ law.

Acknowledgements The author is indebted to A. V. Dementiev for calculations and preparing figures.

Addendum

In this Appendix the Wiener–Hopf integral equation for the source function $S(\tau)$ with the free term $Q = Q(\tau)$ and parameter $\lambda \equiv 1 - \epsilon$, i.e., the equation

$$S(\tau) = \lambda \int_0^\infty K(\tau - \tau')\, S(\tau')\, d\tau' + Q(\tau) \tag{A.1}$$

will be written in short as

$$S = \lambda \Lambda S + Q. \tag{A.2}$$

The Green function $G(\tau, \tau_1)$ of Eq. (A.1)

$$G = \lambda \Lambda G + \delta(\tau - \tau_1) \tag{A.3}$$

provides the solution of Eq. (A.2) for an arbitrary $Q(\tau)$:

$$S(\tau) = \int_0^\infty G(\tau, \tau_1)\, Q(\tau_1)\, d\tau_1. \tag{A.4}$$

Now, let $G_\infty(\tau)$ be the Green function for an infinite medium, i.e., the solution of

$$G_\infty = \lambda \Lambda_\infty G_\infty + \delta(\tau), \tag{A.5}$$

where Λ_∞ is the operator of the same form as Λ is, but with integration with respect to τ' from $-\infty$ to ∞, and not $(0, \infty)$.

The aim of this Addendum is to show, following Ivanov (1994), how the explicit expression for the H–function given by Eq. (65) can be derived by elementary means. First of all, we note that $H(z)$ is essentially the Laplace transform of the surface Green function $\overline{G}_0$, or, to be more accurate,

$$H(1/s) = \overline{G}_0(s) \equiv \int_0^\infty G_0(\tau)\, \mathrm{e}^{-s\tau}\, d\tau, \tag{A.6}$$

so that we want to show that

$$\ln \overline{G}_0(s) = -\frac{s}{2\pi} \int_{-\infty}^{\infty} \ln\left(1 - \lambda \widetilde{K}(\omega)\right) \frac{d\omega}{s^2 + \omega^2}\,. \tag{A.7}$$

Here $\widetilde{K}(\omega)$ is the Fourier transform of the kernel function $K(\tau)$ (Eq. (47).

To get a hint on how we can get the desirable result, let us compare (A.7) with the expression for the Green function G_∞ for the whole space

$$G_\infty(\tau) = \Phi_\infty(\tau) + \delta(\tau) = \frac{1}{2\pi} \int_{-\infty}^{\infty} \frac{\lambda \widetilde{K}(\omega)}{1 - \lambda \widetilde{K}(\omega)}\, \mathrm{e}^{-i\tau\omega}\, d\omega + \delta(\tau), \tag{A.8}$$

which is easily obtained by applying the Fourier transform to the convolution equation (A.5) for G_∞ for the whole space. The comparison enables one to reveal that

$$\lambda \frac{\partial \ln \overline{G}_0(s)}{\partial \lambda} = \overline{\Phi}_\infty(s), \tag{A.9}$$

where $\overline{\Phi}_\infty(s)$ is the Laplace transform of the non-singular part of $G_\infty(\tau)$.

Hence to get (A.7), it suffices to prove (A.9). And this is a non-linear relation between the Laplace transforms of the Green functions for full space and for half-space. Somewhat unexpectedly, it involves the derivative with respect to the parameter λ. This derivative with respect to λ is the key in obtaining Eq. (A.7) by elementary means.

Now it is easily seen how we have to proceed. Using the equation that defines the half-space surface Green function

$$G_0 = \lambda \Lambda G_0 + \delta(\tau) \tag{A.10}$$

one gets

$$\frac{\partial G_0}{\partial \lambda} = \lambda \Lambda \frac{\partial G_0}{\partial \lambda} + \Lambda\, G_0. \tag{A.11}$$

By (A.10), the term $\Lambda\, G_0$ in the **r**ight **h**and **s**ide (RHS) of (A.11) equals $\lambda^{-1}\big(G_0(\tau) - \delta(\tau)\big)$. Thus, Eq. (A.11) may be looked at as the equation of our usual form (A.2) for the function $\partial G_0/\partial\lambda$ with the free term

$$Q(\tau) = \lambda^{-1}\big(G_0(\tau) - \delta(\tau)\big). \tag{A.12}$$

Substituting this expression for Q into (A.4) and using the symmetry of $G(\tau, \tau_1)$, we obtain

$$\lambda \frac{\partial G_0(\tau)}{\partial \lambda} = \int_0^\infty G(\tau_1, \tau)\big[G_0(\tau_1) - \delta(\tau_1)\big]\, d\tau_1. \tag{A.13}$$

In the RHS of this equation there is a product of *three* functions G_0 (see Eq. (9) for $G(\tau, \tau_1)$). Now, we make the Laplace transformation in τ (with the parameter of the transformation s) and substitute for $\overline{G}(\tau_1, s)$ in the RHS the expression

$$\overline{G}(\tau_1, s) = \overline{G}_0(s) \int_0^{\tau_1} G_0(\tau_1 - t)\, \mathrm{e}^{-st}\, dt. \tag{A.14}$$

This expression for $\overline{G}(\tau_1, s)$ is obtained from Eq. (9) by applying the Laplace transformation in τ. As a result, we get the double integral. By first changing the order of integration and then putting $\tau_1 = \tau + t$ we obtain

$$\lambda \frac{\partial \overline{G}_0(s)}{\partial \lambda} = \overline{G}_0(s) \int_0^\infty \int_0^{\tau_1} G_0(\tau_1 - t) \Big[G_0(\tau_1) - \delta(\tau_1)\Big] \mathrm{e}^{-st}\, dt\, d\tau_1 \tag{A.15}$$

$$= \overline{G}_0(s) \int_0^\infty \int_t^\infty \Big(G_0(\tau_1 - t) \Big[G_0(\tau_1) - \delta(\tau_1)\Big] d\tau_1 \Big) \mathrm{e}^{-st}\, dt$$

$$= \overline{G}_0(s) \int_0^\infty \Big(\int_0^\infty G_0(\tau)\, G_0(\tau + t)\, d\tau - \delta(t) \Big) \mathrm{e}^{-st}\, dt. \tag{A.16}$$

Using Eq. (13) (p. 5) and taking into account that $G_\infty(t) = \Phi_\infty(t) + \delta(t)$, we find

$$\lambda \frac{\partial \overline{G}_0(s)}{\partial \lambda} = \overline{G}_0(s) \int_0^\infty \Phi_\infty(t)\, \mathrm{e}^{-st}\, dt,$$

and this is identical to (A.9). Equation (A.7) is thus proved.

References

Abramov YY, Dykhne AM, Napartovich AP (1969) Stationary problems of radiative transfer of excitation. Inst Atomic Energy, Report IAE-1804 (in Russian)

Ambartsumian VA (1942) The scattering of light by planetary atmospheres. Astron Zhurn 19:30–41 (reprinted in: Ambartsumian VA (1960) Scientific works, vol I. Armenian Academy of Sciences Publications, Erevan, pp. 206–222 (in Russian), English transl. in: Ambartsumian RV (1998), A life in astrophysics. Selected papers of Viktor A. Ambartsumian. Allerton Press, New York, pp. 67–82)

Ambartsumian VA (1948) On the number of scatterings at the diffusion of photons in turbid medium. Dokl Acad Nauk Arm SSR 8:101–104 (reprinted in: Ambartsumian VA (1960) Scientific works, vol I. Armenian Academy of Sciences Publications, Erevan, pp. 282–285 (in Russian))

Avrett E, Hummer DG (1965) Non-coherent scattering. II. Line formation with a frequency independent source function. Month Not Roy Astron Soc 130:295–331

Ballester EA, Beluzzi L, Trujillo Bueno J (2017) The transfer of resonance line polarization with partial frequency redistribution in the general Hanle-Zeeman regime. Astrophys J 836:6

Biberman LM (1947) On theory of the diffusion of resonance radiation. Zhurn Eksperim Theor Phys 17:416–426

Bronstein M (1929) Zum Strahlungsgleichgewichtsproblem von Milne. Z Phys 58:696–699; Über das Verhältnis des effektiven Temperatur der Sterne zur Temperatur ihrer Oberfläche. ibid 59:144–148

Case KM, Zweifel PF (1967) Linear transport theory. Addison-Wesley, Reading

Castor JI (2004) Radiation hydrodynamics. Cambridge University Press, Cambridge

Chandrasekhar S (1939) Introduction to the study of stellar structure. University of Chicago Press, Chicago

Chandrasekhar S (1947) On the radiative equilibrium of a stellar atmosphere. XX. Astrophys J 106:145–151

Chandrasekhar S (1950) Radiative transfer. Clarendon Press, Oxford

Chwolson OD (1889) Grundzüge einer mathematischen Theorie der inneren Diffusion des Lichtes. Bull l'Acad Imp Sci St-Petersb 13:83–113

Davison B (1957) Neutron transport theory. Oxford University Press, London

del Pino Alemán T, Manso Sainz R, Trujillo Bueno J (2014) Non coherent continuum scattering as a line polarization mechanism. Astrophys J 784:46

Dementiev AV (2008) Polarization of resonance lines in the case of a Voigt absorption profile. Astron Lett 34:574–580

d'Eon E, McCormick J (2019) Radiative transfer in half spaces of arbitrary dimension. arXiv:1905.07825v1

Domke H (1973) Multiple scattering of polarized light in a semiinfinite atmosphere with small true absorption. Sov Astron 17:81–87

Domke H, Ivanov VV (1976) Asymptotics of Green's function of the transfer equation for polarized radiation. Sov Astron 19:624–626

Dumont S, Omont A, Pecker J-C, Rees D (1977) Resonance line polarization: the line core. Astron Astrophys 654:675–681

Eddington AS (1926) The internal constitution of the stars. Cambridge University Press, Cambridge

Eddington AS (1929) The formation of absorption lines. Mon Not R Astron Soc 89:620–636

Faurobert M (1987) Linear polarization of resonance lines in the absence of magnetic fields. I. Slabs of finite optical thickness. Astron Astrophys 178:269–276; (1988) Linear polarization of resonance lines in the absence of magnetic fields. II. Semi-infinite atmospheres. ibid 194:268–278

Faurobert-Scholl M, Frisch H (1989) Asymptotic analysis of resonance polarization and escape probability approximation. Astron Astrophys 219:338–351

Feller W (1966) An introduction to probability theory and its applications, vol II. Wiley, New York

Frisch H (1998) The Hanle effect. The density matrix and scattering approaches to the protect sqrt epsilon-law. Astron Astrophys 338:683–693

Frisch H (2019) Nonconservative Rayleigh scattering. A perturbation approach. Astron Astrophys 625:A125

Frisch U, Frisch H (1975) Non-LTE transfer. $\sqrt{\epsilon}$ revisited. Mon Not R Astron Soc 173:167–182

Frisch U, Frisch H (1977) Non-LTE transfer. III. Asymptotic expansion for small epsilon. Mon Not R Astron Soc 181:273–280

Grachev SI (2001) Transfer of polarized radiation: nonlinear integral equations for I-matrices in the general case and for resonance scattering in a weak magnetic field. Astrophys 44:369–381

Grachev SI (2014) The formation of polarized lines: factorization of the Hanle phase matrix and $\sqrt{\epsilon}$ law in the most general form. Vestn St Petersburg Univ 59:632–639 (in Russian)

Gandorfer A (2000–2005) The second solar spectrum. vdf Hochschulverlag AG an der ETH, Zurich (vol. I, 2000, vol. II, 2002, vol. III, 2005)

Grigoriev VV, Nagirner DI, Grachev SI (2019) H-functions in radiative transfer theory: calculation of Voigt functions and justification of a model for formation of cyclotron lines in the spectra of neutron stars. Astrophys 62:129–146

Halpern O, Lueneburg RK, Clark O (1938) On multiple scattering of neutrons. I. Theory of the albedo of a plane boundary. Phys Rev 53:173–183, (1939) ibid 56, 1068; (1949) Multiple scattering of neutrons. II. Diffusion in a plate of finite thickness. ibid 76:1811–1819

Heaslet MA, Warming RF (1968) Theoretical predictions of spectral line formation by noncoherent scattering. J Quant Spectrosc Radiat Transfer 8:1101–1146

Holstein T (1947) Imprisonment of resonance radiation in gases. Phys Rev 72:1212–1233

Hopf E (1930) Remarks on the Schwarzschild-Milne model of the outer layers of a star. Mon Not R Astron Soc 90:287–293

Hopf E (1934) Mathematical problems of radiative equilibrium. Cambridge University Press, Cambridge

Hubeny I (1987) Probabilistic interpretation of radiative transfer. I. The square root of epsilon law. II. Rybicki equation. Astron Astrophys 185:332–342

Hubeny I, Mihalas D (2015) Theory of stellar atmospheres. Princeton University Press, Princeton

Hummer DG (1968) Non-coherent scattering. III. The effect of continuous absorption on the formation of spectral lines. Mon Not R Astron Soc 138:73–108

Hummer DG, Stewart JC (1966) Thermalization lengths and the homogeneous transfer equation in line formation. Astrophys J 146:290–294

Ibragimov IA, Linnik YV (1965) Independent and linearly connected variables. Nauka Publ, Moscow (in Russian)

Ivanov VV (1960) On diffusion of radiation with frequency redistribution in one-dimensional medium. Vestn LGU #19:117–123 (in Russian)

Ivanov VV (1962) Diffusion of resonance radiation in stellar atmospheres and nebulae I. Semi-infinite medium. Sov Astron 6:793–801

Ivanov VV (1965) Scattering of light in an atmosphere of finite optical thickness. Sov Astron 8:874–881

Ivanov VV (1970) Transfer of resonance radiation in purely scattering media. I. Semi-infinite medium. J Quant Spectrosc Radiat Transf 10:665–680 (in Russian)

Ivanov VV (1971) Transfer of radiation in a spectral line. In: Ivanov AP (ed) Theoretical and applied problems of light scattering. Nauka i Tekhnika Publ. Co., Minsk, pp 93–113 (in Russian)

Ivanov VV (1973) Transfer of radiation in spectral lines. NBS Special Publ #385. US Gov Print Office, Washington

Ivanov VV (1985) The transfer of line radiation. IV. A long-standing puzzle. Sov Astron 29:162–167

Ivanov VV (1990) Nonmagnetic polarization of the Doppler cores of Fraunhofer resonance lines. Sov Astron 34:621–625

Ivanov VV (1994) Resolvent method: exact solutions of half-space transport problems by elementary means. Astron Astrophys 286:328–337

Ivanov VV (1995) Generalized Rayleigh scattering. I. Basic theory. Astron Astrophys 303:609–620

Ivanov VV, Sabashvili ShA (1972) Transfer of resonance radiation and photon random walks. Astrophys Space Sci 17:13–22

Ivanov VV, Serbin VM (1984) The transfer of line radiation. II. Approximate solutions for semi-infinite atmospheres. Sov Astron 28:524–531

Ivanov VV, Grachev SI, Loskutov VM (1997) Polarized line formation by resonance scattering. I. Basic formalism. Astron Astrophys 318:315–326; Polarized line formation by resonance scattering. II. Conservative case. ibid 321:968–984

Kukushkin AB, Sdvizhenskii PA (2016) Automodel solutions for Levy flight-based transport on a uniform background. J Phys A: Math Theor 49:255002

Landi Degl'Innocenti E (1979) Non-LTE transfer. An alternative derivation for $\sqrt{\epsilon}$. Mon Not R Astron Soc 186:369–375

Landi Degl'Innocenti E, Bommier V (1994) Resonance line polarization for arbitrary magnetic fields in optically thick media. III. A generalization of the $\sqrt{\epsilon}$-law. Astron Astrophys 284:865–873

Landi Degl'Innocenti E, Landolfi H (2004) Polarization in spectral lines. Kluwer Academic Publishers, New York

Lommel E (1889) Die Photometrie der diffusen Zuruckwefung. Ann Phys U Chem 36:473–502

Loskutov VM, Ivanov VV (2007) Polarized line formation by resonance scattering: Lorentz profile. Astrophys 50:157–174

Majumdar SN, Mounaix Ph, Schehr G (2014) On the gap and time interval between the first two maxima of long random walks. J Stat Mech P09013

Mandelbrot BB (1982) The fractal geometry of nature. WH Freeman, New York

Milne EA (1921) Radiative equilibrium in the outer layers of a star. Mon Not R Astron Soc 81:361–375

Milne EA (1930) Thermodynamics of the stars. In: Handbuch der Astrophysik, vol III, part I. Springer, Berlin, pp. 70–172 (reprinted in Menzel D (ed) (1966) Selected papers on the transfer of radiation. Dover Publications, New York, pp. 77–269)

Mullikin TW (1966) The complete Rayleigh-scattered field within a homogeneous plane-parallel atmosphere. Astrophys J 145:886–931

Nagirner DI (1967) Asymptotic formulas for the X and Y functions in the theory of multiple scattering of radiation within a line. Astrophys 3:133–139

Nagirner DI (1975) The calculation of the profiles of spectral lines formed in a scattering atmosphere. Trudi Astron Obs LGU 31:3–99 (in Russian)

Nagirner DI (2007) Analytical methods in radiative transfer theory. Astrophys Space Sci Rev 13:1–440

Nagirner DI, Ivanov VV (1965) H-functions in the theory of resonance radiation transfer. Astrophys 1:86–101

Nikoghossian AG (2006) Statistical description of the radiation field in a homogeneous medium of finite optical thickness. Astrophys 49:228–239

Nikoghossian AG (2011) Bilinear integrals of the radiative transfer equation. Astrophys 54:242–249

Placzek G, Seidel W (1947) Milne's problem in transport theory. Phys Rev 72:550–556

Pollaczek F (1952) Fonctions caracteristiques de certaines repartitions definies au moyen de la notion d'ordre. Application a la theorie des attentes. Comptes Rendus Acad Sci Paris, Ser IV 234:2334–2336

Rees DE, Saliba GJ (1982) Non-LTE resonance line polarization with partial redistribution effects. Astron Astrophys 115:1–7

Rybicki GB (1977) Integrals of the transfer equation. I. Quadratic integrals for monochromatic, isotropic scattering. Astrophys J 213:165–176

Rybicki GB, Hummer DG (1969) Non-coherent scattering. V. Thermalization distance and their distribution function. Mon Not R Astron Soc 144:313–323

Serbin VM (1985) The transfer of line radiation. III. Approximate solutions for finite-thickness atmospheres. Sov Astron 29:155–161

Sobolev VV (1949) Non-coherent light scattering in stellar atmospheres. Astron Zhurn 26:129–137 (in Russian)

Sobolev VV (1963) A treatise on radiative transfer. Van Nostrand, Princeton

Sparre-Andersen E (1953) On the fluctuations of sums of random variables. Math Scand 1:263–285; (1954) On the fluctuations of sums of random variables II. ibid 2:195–223

Spitzer F (1957) The Wiener-Hopf equation whose kernel is a probability density. Duke Math J 24:327–343

Stenflo JO, Stenholm L (1976) Resonance-line polarization. II. Calculations of linear polarization in solar UV emission lines. Astron Astrophys 46:69–79

Stenflo JO, Baur TG, Elmore DF (1980) Resonance-line polarization: IV. Observations of non-magnetic line polarization and its center-to-limb variations. Astron Astrophys 84:60–67

Štěpán J, Bommier V (2007) A generalized $\sqrt{\epsilon}$-law. The role of unphysical source terms in resonance line polarization transfer and its importance as an additional test of NLTE radiative transfer codes. Astron Astrophys 468:797–801

Trujillo Bueno J, Štěpán J, Belluzzi L et al. (2018) CLASP constraints on the magnetization and geometrical complexity of the chromosphere-corona transition region. Astrophys J 866:L15

Uchaikin VV (2003) Self-similar anomalous diffusion and Levy-stable laws. Sov Phys Usp 46:821–849

van de Hulst HC (1980) Multiple light scattering. Academic, New York

Viik T (1986) An efficient method to calculate Ambarzumian/Chandrasekhar's and Hopf's functions. Astrophys Space Sci 127:285–307

Viik T (1990) Rayleigh-Cabannes scattering in planetary atmospheres. III. The Milne problem in conservative atmospheres. Earth Moon Planets 49:163–175

Viik T (2016) On the planetary and Milne problems in complex radiative transfer. J Quant Spectrosc Radiat Transf 183:162–167

Warming RF (1970) The direct calculation of the H-function for completely noncoherent scattering. Astrophys J 159:593–604

Solar Heating of the Cryosphere: Snow and Ice Sheets

Leonid A. Dombrovsky and Alexander A. Kokhanovsky

1 Introduction

Polar regions of our planet are undergoing rapid changes, including warming of both atmosphere and underlying surface (Kokhanovsky and Tomasi 2020) and decrease of snow/ice extent/albedo (Tedesco 2015) with corresponding impacts on polar environments (Barry and Hall-McKim 2018). The behavior of massive ice sheets and snowpack under regular summer heating by solar radiation is one of the problems which are not well understood because of interaction of a variety of physical processes.

There are many research papers concerning the spectral properties of pure and polluted snow fields and also ice sheets containing gas bubbles and some particulate inclusions (Warren 1982; Kokhanovsky and Zege 2004; Tedesco 2015; Warren et al. 2019). However, only few publications are focused on modeling the combined radiative and conductive heat transfer in a snowpack or ice sheet. One should recall the interesting findings of the study by Brandt and Warren (1993) on a relatively deep penetration of shortwave solar radiation in a snowpack and night radiative cooling by emission of thermal infrared radiation to space occurring at the very top surface of the snow. The term "solid-state greenhouse" was suggested for the first of these interesting phenomena. Deep penetration of heat into the snowpack was discussed also by Liston and Winther (2005). In particular, they reported that about seven times more meltwater is produced subsurface compared to the surface for snow-covered areas in near coastal Antarctica.

The main objective of the present paper is to present an approximate but complete and reliable computational model for both the transfer of solar radiation and the

L. A. Dombrovsky (✉)
Joint Institute for High Temperatures, Krasnokazarmennaya Str. 17A, Moscow 111116, Russia
e-mail: ldombr@yandex.ru

A. A. Kokhanovsky
VITROCISET Belgium SPRL, A Leonardo Company, Bratustrasse 7, Darmstadt D-64293, Germany

© The Author(s), under exclusive license to Springer Nature Switzerland AG 2021

A. Kokhanovsky (ed.), *Springer Series in Light Scattering*, Springer Series in Light Scattering, https://doi.org/10.1007/978-3-030-71254-9_2

related transient heat transfer in a snowpack and also in a light-scattering ice sheet. Our consideration is based on recently published journal papers by Dombrovsky et al. (2019) and Dombrovsky and Kokhanovsky (2019, 2020a, b, c).

The physical models, analytical solutions, and computational procedures developed by the authors are quite general and can be employed in solving a wide range of problems associated with solar heating of snow and ice sheets. The methodological part of the work is expected to be more interesting for potential readers than an overview of the particular physical results which have been already obtained by the authors. Therefore, a theoretical part of the paper is considered in the first place and this consideration contains all the important details. The materials of the monograph by Dombrovsky and Baillis (2010) and more recent review paper by Dombrovsky (2019) are used in the first part of the paper.

It should be noted that solar radiation not only heats snow and ice, but is also responsible for other important physical processes. In other words, not only the spectrally integrated power of the absorbed radiation is important, but also the spectral composition of the radiation, which penetrates to some depth in snow or ice must be accounted for. In particular, the life cycle of microalgae, as well as the formation of gas bubbles in a surface layer of ice sheets and snow microstructure, are naturally associated with the penetrating solar radiation. Moreover, generally speaking, there is a physical feedback between the spectral composition of the absorbed radiation and the formation of one or another morphology of snow or light-scattering ice. The foregoing means that the spectral radiative transfer is the main problem which should be solved first of all. After this, one can focus, for example, on the transient heat transfer problem, as is done in the present paper, or, for example, on the study of photosynthesis or, say, the process of formation and growth of gas bubbles in ice layer.

Therefore, the methods of radiative transfer analysis are considered in the beginning of the methodological part of the paper, before the study of the transient heat transfer problem. We are taking into account time variation of external conditions, such as the zenith angle of the Sun, temperature of air and wind speed. The main results of the computational studies on solar heating of snow and ice at conditions of polar summer on our planet are presented in the second part of the paper.

2 Differential Models for Radiative Transfer in Light Scattering Media

In the present paper, as in many other studies, the differential models are derived from the traditional continuum approach and the radiative transfer equation (RTE) which describes the radiative transfer in an absorbing and scattering medium. In the problems under consideration, the volumetric emission of thermal radiation is negligible and the RTE for the isotropic medium can be written as follows (Dombrovsky and Baillis 2010; Modest 2013; Howell et al. 2015):

$$\vec{\Omega}\nabla I_\lambda\left(\vec{r},\vec{\Omega}\right)+\beta_\lambda(\vec{r})I_\lambda\left(\vec{r},\vec{\Omega}\right)=\frac{\sigma_\lambda(\vec{r})}{4\pi}\int\limits_{(4\pi)} I_\lambda\left(\vec{r},\vec{\Omega}'\right)\Phi_\lambda\left(\vec{r},\vec{\Omega}'\cdot\vec{\Omega}\right)\mathrm{d}\vec{\Omega}' \quad (1)$$

where I_λ is the spectral radiation intensity at point $\vec{r}$ in direction $\vec{\Omega}$, $\beta_\lambda=\alpha_\lambda+\sigma_\lambda$ is the extinction coefficient, α_λ and σ_λ are the coefficients of absorption and scattering, respectively, and Φ_λ is the scattering phase function. The physical meaning of Eq. (1) is evident: variation of the radiation intensity takes place due to extinction and the scattering from other directions.

Note that in many other problems of radiative heat transfer, the thermal radiation of a semi-transparent medium should be taken into account. In this case, on the right-hand side of Eq. (1) there is one more term, usually written as the product of the absorption coefficient by the Planck function: $\alpha_\lambda(\vec{r})I_{\mathrm{b},\lambda}(T(\vec{r}))$ or in a more complex form for a multi-temperature composite medium (Dombrovsky 2007, 2009b; Dombrovsky and Baillis 2010).

The thermal emission of snow and ice should also be taken into account, but only in the middle and far infrared part of the spectrum, outside the near-infrared range. Both snow and ice are opaque media in the middle-infrared and thermal radiation is emitted only by the surface of the snow cover or ice sheet. Therefore, the intrinsic thermal radiation of the medium does not appear in the radiative transfer equation.

The most general form of the RTE, the so-called vector RTE (VRTE), which fully accounts for the polarization nature of electromagnetic radiation, is formulated for the Stokes column vector instead of the radiation intensity, and the scattering matrix is used instead of the scattering phase function in the VRTE integral term (Mishchenko et al. 2006). The polarization effects are important in some problems of remote sensing and also in the microwave spectral range. However, one can ignore polarization of the visible and infrared radiation in most of radiative heat transfer problems. Moreover, the details of scattering phase function are usually not important and it is sufficient to know the asymmetry factor of scattering or the average cosine of scattering angle (Dombrovsky and Baillis 2010):

$$\bar{\mu}_\lambda(\vec{r})=\frac{1}{4\pi}\int\limits_{(4\pi)}\left(\vec{\Omega}'\cdot\vec{\Omega}\right)\Phi_\lambda\left(\vec{r},\vec{\Omega}'\cdot\vec{\Omega}\right)\mathrm{d}\vec{\Omega}'. \quad (2)$$

2.1 Transport Approximation

In the detailed modeling of single scattering, one can consider an expansion of the scattering phase function in a series of the Legendre functions or description of the main maxima of this function by several delta-functions with some weight coefficients. The combinations of these two approaches are also employed (Özişik 1973; Dombrovsky 1996a; Dombrovsky and Baillis 2010; Modest 2013). The simplest

approximations of these approaches are well known. If one is restricted to two terms in expansion on Legendre functions, as it was done in early studies, the result is the linear-anisotropic approximation:

$$\Phi_\lambda(\mu_0) = 1 + 3\bar{\mu}_\lambda \mu_0, \;\; \mu_0 = \vec{\Omega}' \cdot \vec{\Omega}. \tag{3}$$

However, the linear approximation loses any physical sense with $\bar{\mu}_\lambda > 1/3$, i.e., at large anisotropy of scattering, since $\Phi_\lambda(\mu_0)$ becomes negative when $\mu_0 < -1/(3\bar{\mu}_\lambda)$. The other drawback of approximation (3) should also be noted: the linear dependence on the cosine of the scattering angle is too far from the typical scattering functions of disperse systems (Dombrovsky 1996a). If one takes into account only the forward and backward scattering, presenting the scattering function as a linear combination of the Dirac delta-functions $\delta(1 + \mu_0)$ and $\delta(1 - \mu_0)$, the simplest "back-scattering" model is derived. This approximation, in which the integral term in the RTE disappears, has been employed in early solutions to some 1-D problems (Belov 1982).

On the contrary, the so-called transport approximation discussed by Davison (1957) is a highly successful method to solve many present-day applied problems (Dombrovsky 1996a, b, 2012, 2019; Dombrovsky and Baillis 2010). According to this approximation, the scattering phase function is replaced by a sum of the isotropic component and the term describing the peak of forward scattering (the independent variable $\vec{r}$ is hereafter omitted for brevity):

$$\Phi_\lambda(\mu_0) = (1 - \bar{\mu}_\lambda) + 2\bar{\mu}_\lambda \delta(1 - \mu_0). \tag{4}$$

With the use of transport approximation, the RTE can be written in the same way as that for isotropic scattering, i.e., with $\Phi_\lambda \equiv 1$:

$$\vec{\Omega} \nabla I_\lambda\left(\vec{r}, \vec{\Omega}\right) + \beta_\lambda^{tr} I_\lambda\left(\vec{r}, \vec{\Omega}\right) = \frac{\sigma_\lambda^{tr}}{4\pi} G_\lambda(\vec{r}), \;\; G_\lambda(\vec{r}) = \int\limits_{(4\pi)} I_\lambda\left(\vec{r}, \vec{\Omega}\right) \mathrm{d}\vec{\Omega}, \tag{5}$$

where G_λ is the irradiation function and the transport scattering and extinction coefficients are introduced as follows:

$$\sigma_\lambda^{\mathrm{tr}} = \sigma_\lambda(1 - \bar{\mu}_\lambda), \;\; \beta_\lambda^{\mathrm{tr}} = \alpha_\lambda + \sigma_\lambda^{\mathrm{tr}} = \beta_\lambda - \sigma_\lambda \bar{\mu}_\lambda. \tag{6}$$

The transport approximation has been widely used in neutron transport and radiative transfer. The accuracy of this approach has been analyzed in early papers by Pomraning (1965), Bell et al. (1967), Potter (1970), and Crosbie and Davidson (1985). In the case of strong forward and backward scattering, one can introduce an additional delta-function in the backward direction (Sjöstrand 2001). According to Williams (1966) this scattering function was used already by Fermi.

2.2 The Simplest Differential Approximations

An accurate numerical solution to the RTE in scattering media is a complicated task even in the case of transport approximation. One can find a number of studies in the literature on specific numerical methods developed to obtain more accurate spatial and angular characteristics of the radiation intensity field. Several modifications of the discrete ordinates method (DOM), the finite-volume method (FVM), and statistical Monte Carlo (MC) methods are the most popular tools employed by many authors. However, simple and physically clear differential approximations are widely used for solving the radiative transfer problems in scattering media, particularly in combined heat transfer problems (Özişik 1973; Rubtsov 1984; Viskanta 2005; Dombrovsky 1996a, 2012, 2019; Dombrovsky and Baillis 2010).

The angular dependence of the radiation intensity is the main difficulty in solving the RTE. Fortunately, this angular dependence is rather simple in many applied problems. This enables one to derive the so-called differential approximations. These approximations have a long history. The latter is reflected in their well-known names such as the Milne–Eddington method (Milne 1930; Eddington 1959), the Schuster–Schwarzschild method (Schuster 1905; Schwarzschild 1906), etc. It should be emphasized that all the differential approximations are based on one or another simple presentation of angular dependence of the radiation intensity. As a result, it is sufficient to consider a limited number of coordinate functions and turn to the coupled ordinary differential equations (ODE) by the integration of RTE. The same result can be obtained if the integral term of the RTE is expressed in the form of the Gaussian quadrature (Case and Zweifel 1967). Particularly, through the use of the DOM one can derive the same ODEs as those by expansion of radiation intensity on the spherical functions. Differential approximations are suitable for calculations at arbitrary optical depth, but their possibilities to account for real scattering phase functions are very limited. For example, the mathematical formulations of P_1, the first approximation of the spherical harmonics method (Davison 1957) for linear and transport scattering functions are identical.

The simplest differential approximations, brought together by Adrianov (1972), Dombrovsky (1996a), and Dombrovsky and Baillis (2010) by the general term "diffusion approximation", give the following representation of the spectral radiative flux:

$$\vec{q}_\lambda = -D_\lambda \nabla G_\lambda \tag{7}$$

and differ only by the expression for the radiation diffusion coefficient D_λ. Sometimes, the term "diffusion approximation" is related only to the case when $D_\lambda = 1\big/\left(3\beta_\lambda^{\mathrm{tr}}\right)$ (Zeldovich and Raizer 1966). This case corresponds to the Eddington approximation. It is known that Eq. (7) can be also derived based on some assumptions concerning the angular dependence of radiation intensity. Substituting Eq. (7) into the radiation energy balance

$$\nabla \vec{q}_\lambda = -\alpha_\lambda G_\lambda \tag{8}$$

we obtain the modified Helmholtz equation for the spectral irradiance:

$$-\nabla(D_\lambda \nabla G_\lambda) + \alpha_\lambda G_\lambda = 0. \tag{9}$$

Note that the radiation power absorbed in a medium can be expressed as follows:

$$P(\vec{r}) = \int p_\lambda(\vec{r})\, \mathrm{d}\lambda, \;\; p_\lambda = \alpha_\lambda G_\lambda. \tag{10}$$

To clarify the physical sense of the diffusion approximation, consider the linear angular dependence of radiation intensity in the popular P_1 approximation:

$$I_\lambda\left(\vec{r}, \vec{\Omega}\right) = \frac{1}{4\pi}\left[G_\lambda(\vec{r}) + 3\vec{\Omega}\vec{q}_\lambda(\vec{r})\right]. \tag{11}$$

By multiplying the transfer Eq. (1) by $\vec{\Omega}$ and integrating it over a solid angle, one can find that the spectral radiative flux is simply related to the spectral irradiation:

$$\vec{q}_\lambda = -D_\lambda \nabla G_\lambda, \;\; D_\lambda = 1\big/\left(3\beta_\lambda^{\mathrm{tr}}\right). \tag{12}$$

Note that Eq. (12) is obtained for an arbitrary scattering function but it is the same as that for transport approximation. In other words, the asymmetry factor of scattering $\bar{\mu}_\lambda$ is the only characteristics of scattering anisotropy taken into account in this approach.

The two-flux approximation is also often used to solve 1-D radiative transfer problems including those considered in the present paper. Consider the transport RTE:

$$\mu \frac{\partial I_\lambda}{\partial z} + \beta_\lambda^{\mathrm{tr}} I_\lambda = \frac{\sigma_\lambda^{\mathrm{tr}}}{2} G_\lambda, \;\; \mu = \cos\theta \tag{13}$$

where $0 < z < d$ is the coordinate across the medium layer and θ is the angle measured from the z-axis direction. The spectral radiative flux is derived as

$$q_\lambda = \left(G_\lambda^+ - G_\lambda^-\right)\big/2, \;\; G_\lambda^\pm(\vec{r}) = \pm 2\pi \int_0^{\pm 1} I_\lambda(z, \mu)\, \mathrm{d}\mu \tag{14}$$

in this approximation. Note that it follows: $G_\lambda = G_\lambda^- + G_\lambda^+$. With the use of two-flux approximation, the radiation intensity is assumed to be constant over the backward and forward hemispheres:

$$I_\lambda(z,\mu) = \begin{cases} \frac{1}{2\pi} G_\lambda^-(z) \text{ when } -1 < \mu < 0 \\ \frac{1}{2\pi} G_\lambda^+(z) \text{ when } 0 < \mu < 1 \end{cases} \tag{15}$$

The integration of RTE over the hemispheres leads to the following coupled ODEs:

$$-\frac{1}{2}\frac{\mathrm{d}G_\lambda^-}{dz} + \beta_\lambda^{\mathrm{tr}} G_\lambda^- = \frac{\sigma_\lambda^{\mathrm{tr}}}{2} G_\lambda, \ \frac{1}{2}\frac{\mathrm{d}G_\lambda^+}{\mathrm{d}z} + \beta_\lambda^{\mathrm{tr}} G_\lambda^+ = \frac{\sigma_\lambda^{\mathrm{tr}}}{2} G_\lambda. \tag{16}$$

These equations and the expression for the spectral radiative flux can be written as follows:

$$-\frac{d}{dz}\left(D_\lambda \frac{dG_\lambda}{dz}\right) + \alpha_\lambda G_\lambda = 0, \ q_\lambda = -D_\lambda \frac{dG_\lambda}{dz} \tag{17}$$

where $D_\lambda = 1\big/\left(4\beta_\lambda^{\mathrm{tr}}\right)$. One can see that two-flux approximation leads to the typical relations of the diffusion approximation. We will not discuss the boundary conditions for the P_1 and two-flux equations. The details of these approaches including the accuracy analysis based on a comparison with reference solutions for the model problems can be found in monograph by Dombrovsky and Baillis (2010). However, it is important to recall that P_1 approximation does not produce accurate results at the boundaries of turbid media in the case of discontinuous angular dependence of radiation intensity. Therefore, the two-flux approximation is preferable when the solar light irradiates a snowpack or ice sheet. By the way, it has been shown by Dombrovsky et al. (2013) that the same choice can be recommended to analyze the laser-induced hyperthermia of superficial human tumors.

2.3 Propagation of Solar Radiation in Snow

The solution considered in this section is applicable to the snowpack irradiated by collimated solar radiation and also by diffuse radiation from the sky. In the case of oblique solar irradiation, the radiation field in a snow layer is three-dimensional. However, the distribution of the absorbed power over the thickness of a light scattering layer depends only on the solar zenith angle and it does not matter which side of the normal the Sun is located.

Let us imagine that the radiative flux is uniformly distributed over the surface of a cone with the same zenith angle at the vertex. Of course, in this case the power profile of the absorbed radiation will be the same. In other words, the original problem is equivalent to the 1-D axisymmetric problem of the oblique irradiation along the cone surface. This idea has been used by Dombrovsky et al. (2011e, 2019) and Dombrovsky and Randrianalisoa (2018). The axial symmetry of the equivalent problem enables one to integrate the original transport RTE over the azimuthal angle. The resulting equations can be written as follows (Dombrovsky 1996a, b; Dombrovsky and Baillis 2010; Modest 2013; Howell et al. 2015):

$$\mu \frac{\partial I_{\lambda,\mathrm{i}}}{\partial z} + \beta_\lambda^{\mathrm{tr}} I_{\lambda,\mathrm{i}} = \frac{\sigma_\lambda^{\mathrm{tr}}}{2} G_{\lambda,\mathrm{i}},\ G_{\lambda,\mathrm{i}}(z) = \int_{-1}^{1} I_{\lambda,\mathrm{i}}(z,\mu)\,\mathrm{d}\mu,\ \mu = \cos\theta,\ 0 < z < d, \tag{18a}$$

$$I_{\lambda,\mathrm{i}}(0,\mu) = I_\lambda^{\mathrm{sol}}(\mu_\mathrm{i})\,\delta(\mu_\mathrm{i} - \mu) + I_\lambda^{\mathrm{sky}},\ I_{\lambda,\mathrm{i}}(d,-\mu) = 0,\ \mu, \mu_\mathrm{i} > 0, \tag{18b}$$

where $\mu_\mathrm{i} = \cos\theta_\mathrm{i}$ corresponds to the direction of incident collimated light, I_λ^{sol} is the intensity of solar radiation transmitted through the atmosphere, I_λ^{sky} is the intensity of diffuse radiation from the sky, d is the thickness of a layer. The solar irradiation depends on current time, t, but the value of t is just a parameter of the radiative transfer problem.

The linearity of the RTE makes possible a separate consideration of additive contribution of the direct solar radiation and radiation from the sky. Consider first the transfer of direct solar radiation using the dimensionless form of Eqs. (18a) and (18b):

$$\mu \frac{\partial \bar{I}_{\lambda,\mathrm{i}}}{\partial \tau_\lambda^{\mathrm{tr}}} + \bar{I}_{\lambda,\mathrm{i}} = \frac{\omega_\lambda^{\mathrm{tr}}}{2} \bar{G}_{\lambda,\mathrm{i}},\ \bar{G}_{\lambda,i}\left(\tau_\lambda^{\mathrm{tr}}\right) = \int_{-1}^{1} \bar{I}_{\lambda,i}\left(\tau_\lambda^{\mathrm{tr}},\mu\right)\mathrm{d}\mu, \tag{19a}$$

$$\bar{I}_{\lambda,\mathrm{i}}(0,\mu) = \delta(\mu_\mathrm{i} - \mu),\ \bar{I}_{\lambda,\mathrm{i}}(\infty,-\mu) = 0,\ \mu, \mu_\mathrm{i} > 0. \tag{19b}$$

There are some simplifications in these equations: the boundary condition at $z = d$ is replaced by the same condition at $\tau_\lambda^{\mathrm{tr}} \to \infty$ (this can be done for optically thick layers) and the following dimensionless variables are introduced: the ratio of $\bar{I}_{\lambda,\mathrm{i}} = I_\lambda \big/ I_\lambda^{\mathrm{sol}}(\mu_\mathrm{i})$, the current optical thickness $\tau_\lambda^{\mathrm{tr}} = \int_0^z \beta_\lambda^{\mathrm{tr}}(z)\,\mathrm{d}z$, and transport albedo of single scattering $\omega_\lambda^{\mathrm{tr}}(z) = \sigma_\lambda^{\mathrm{tr}}(z) \big/ \beta_\lambda^{\mathrm{tr}}(z)$.

Following the usual technique (Sobolev 1975), the radiation intensity is represented as a sum of the diffuse component $\bar{J}_{\lambda,\mathrm{i}}$ and the term corresponding to the direct solar radiation:

$$\bar{I}_{\lambda,\mathrm{i}}\left(\tau_\lambda^{\mathrm{tr}},\mu\right) = \bar{J}_{\lambda,\mathrm{i}}\left(\tau_\lambda^{\mathrm{tr}},\mu\right) + E_\lambda^{\mathrm{i}}\delta(\mu - \mu_\mathrm{i}),\ E_{\lambda,\mathrm{i}} = \exp\left(-\tau_\lambda^{\mathrm{tr}} \big/ \mu_\mathrm{i}\right). \tag{20}$$

The spectral irradiance can be also written as a sum of two components:

$$\bar{G}_{\lambda,\mathrm{i}}\left(\tau_\lambda^{\mathrm{tr}}\right) = \bar{G}_{\lambda,\mathrm{i}}^{\mathrm{diff}}\left(\tau_\lambda^{\mathrm{tr}}\right) + E_{\lambda,\mathrm{i}},\ \bar{G}_{\lambda,i}^{\mathrm{diff}} = \int_{-1}^{1} \bar{J}_\lambda\, d\mu. \tag{21}$$

The mathematical problem statement for the diffuse component of radiation intensity is as follows:

$$\mu \frac{\partial \bar{J}_{\lambda,\mathrm{i}}}{\partial \tau_\lambda^{\mathrm{tr}}} + \bar{J}_{\lambda,\mathrm{i}} = \frac{\omega_\lambda^{\mathrm{tr}}}{2}\left(\bar{G}_{\lambda,\mathrm{i}}^{\mathrm{diff}} + E_{\lambda,\mathrm{i}}\right), \tag{22a}$$

$$\bar{J}_{\lambda,\mathrm{i}}(0,\mu) = \bar{J}_{\lambda,\mathrm{i}}(\infty,-\mu) = 0\ ,\ \mu > 0 \tag{22b}$$

The source term on the right of Eq. (22a) does not depend on the angular variable μ. This enables further simplification of the problem with the use of two-flux approximation.

For the diffuse radiation from the sky, one should use another normalization, $\bar{I}_\lambda = I_\lambda \big/ q_\lambda^{\mathrm{sky}}$, and replace the term $\delta(\mu_\mathrm{i} - \mu)$ by 1 in Eq. (19b). As a result, the following equations are true:

$$\mu \frac{\partial \bar{J}_\lambda}{\partial \tau_\lambda^{\mathrm{tr}}} + \bar{J}_\lambda = \frac{\omega_\lambda^{\mathrm{tr}}}{2} \bar{G}_\lambda^{\mathrm{sky}}, \tag{23a}$$

$$\bar{J}_\lambda(0,\mu) = 1,\ \ \bar{J}_\lambda(\infty,-\mu) = 0,\ \mu > 0. \tag{23b}$$

The spectral component of the absorbed radiation power taking into account both the direct solar radiation and the diffuse radiation of the sky, can be written as follows:

$$p_\lambda(z) = \alpha_\lambda(z)\left[\bar{G}_{\lambda,\mathrm{i}}(z)\, q_{\lambda,\mathrm{i}}^{\mathrm{sol}} + \bar{G}_\lambda^{\mathrm{sky}}(z)\, q_\lambda^{\mathrm{sky}}\right]. \tag{24}$$

According to the two-flux method, the following approximation of the diffuse component of radiation intensity is considered:

$$\bar{J}_{\lambda,\mathrm{i}}\left(\tau_\lambda^{\mathrm{tr}},\mu\right) = \begin{cases} \bar{J}_{\lambda,\mathrm{i}}^{-}\left(\tau_\lambda^{\mathrm{tr}}\right) \text{ when } -1 < \mu < 0 \\ \bar{J}_{\lambda,\mathrm{i}}^{+}\left(\tau_\lambda^{\mathrm{tr}}\right) \text{ when } 0 < \mu < 1 \end{cases}. \tag{25}$$

Integrating Eq. (22a) separately over the intervals $-1 < \mu < 0$ and $0 < \mu < 1$, one can obtain the boundary-value problem for the diffuse irradiance $\bar{G}_{\lambda,\mathrm{i}}^{\mathrm{diff}} = \bar{J}_{\lambda,\mathrm{i}}^{-} + \bar{J}_{\lambda,\mathrm{i}}^{+}$:

$$-\left(\bar{G}_{\lambda,\mathrm{i}}^{\mathrm{diff}}\right)'' + \xi_\lambda^2 \bar{G}_{\lambda,\mathrm{i}}^{\mathrm{diff}} = 4\omega_\lambda^{\mathrm{tr}} E_{\lambda,\mathrm{i}},\ \ \xi_\lambda = 2\sqrt{1-\omega_\lambda^{\mathrm{tr}}}, \tag{26a}$$

$$\left(\bar{G}_{\lambda,\mathrm{i}}^{\mathrm{diff}}\right)'(0) = 2\bar{G}_{\lambda,\mathrm{i}}^{\mathrm{diff}}(0),\ \left(\bar{G}_{\lambda,\mathrm{i}}^{\mathrm{diff}}\right)'(\infty) = 0. \tag{26b}$$

The above equations are true at arbitrary variations of ξ_λ and $\omega_\lambda^{\mathrm{tr}}$ with the current optical thickness $\tau_\lambda^{\mathrm{tr}}$, and the problem (26a, b) can be easily solved numerically. However, it is interesting to obtain an analytical solution of the problem in the case of vertically homogeneous snow layers. The analytical solution to Eqs. (26a, b) at $\xi_\lambda \neq 1\big/\mu_\mathrm{i}$ can be written as follows (Dombrovsky and Randrianalisoa 2018; Dombrovsky et al. 2019):

$$\bar{G}_{\lambda,\mathrm{i}}^{\mathrm{diff}} = \frac{4\omega_\lambda^{\mathrm{tr}}}{\xi_\lambda^2 - 1\big/\mu_\mathrm{i}^2}\left(E_{\lambda,\mathrm{i}} - \frac{2 + 1\big/\mu_\mathrm{i}}{2+\xi_\lambda} E_\lambda^{\mathrm{diff}}\right),\ E_\lambda^{\mathrm{diff}} = \exp\left(-\xi_\lambda \tau_\lambda^{\mathrm{tr}}\right). \tag{27}$$

where μ_{i} should be considered as a parameter. There are two different exponential functions in Eq. (27). The first one, $E_{\lambda,\mathrm{i}}$, is related with a contribution of the collimated solar radiation, whereas the second one, $E_{\lambda}^{\mathrm{diff}}$, corresponds to the diffuse component of the radiation field.

The following simple expression can be easily obtained for the diffuse radiation of the sky:

$$\bar{G}_{\lambda}^{\mathrm{sky}}\left(\tau_{\lambda}^{\mathrm{tr}}\right) = 2E_{\lambda}^{\mathrm{diff}}. \tag{28}$$

It is interesting to compare the propagation depth values for the collimated and diffuse radiation. The propagation depth can be defined as a distance from the snow surface at which the irradiance decreases e times. In the case of normal incidence, a comparison of functions $E_{\lambda,\mathrm{i}}\left(\tau_{\lambda}^{\mathrm{tr}}\right)$ and $E_{\lambda}^{\mathrm{diff}}\left(\tau_{\lambda}^{\mathrm{tr}}\right)$ indicates that the propagation depth of collimated radiation is less than that of diffuse radiation when $\omega_{\lambda}^{\mathrm{tr}} > 0.75\,(\xi_{\lambda} < 1)$.

2.4 Modified Solution for Refracting Host Medium

In the case of a semi-transparent scattering ice sheet, the above radiative transfer model should be modified to take into account the refraction of solar light in bulk ice. The generalized boundary condition leads to the following equations for the direct solar radiation instead of Eqs. (18a, b):

$$\mu\frac{\partial \bar{I}_{\lambda,\mathrm{i}}}{\partial \tau_{\lambda}^{\mathrm{tr}}} + \bar{I}_{\lambda,\mathrm{i}} = \frac{\omega_{\lambda}^{\mathrm{tr}}}{2}\bar{G}_{\lambda,\mathrm{i}},\ \ \bar{G}_{\lambda,\mathrm{i}}\left(\tau_{\lambda}^{\mathrm{tr}}\right) = \int_{-1}^{1} \bar{I}_{\lambda,\mathrm{i}}\left(\tau_{\lambda}^{\mathrm{tr}},\mu\right)\mathrm{d}\mu, \tag{29a}$$

$$\begin{aligned}\bar{I}_{\lambda,\mathrm{i}}(0,\mu) &= r_{\lambda,\mathrm{i}}\bar{I}_{\lambda,\mathrm{i}}(0,-\mu) + \left(1 - r_{\lambda,\mathrm{i}}\right)\delta\left(\mu_{\mathrm{j}} - \mu\right),\\ \bar{I}_{\lambda,\mathrm{i}}(\infty,\mu) &= \bar{I}_{\lambda,\mathrm{i}}(\infty,-\mu) = 0,\ \mu,\mu_{\mathrm{j}} > 0,\end{aligned} \tag{29b}$$

where $\bar{I}_{\lambda,\mathrm{i}} = I_{\lambda,\mathrm{i}}/I_{\lambda,\mathrm{i}}^{\mathrm{inc}}$, $\bar{G}_{\lambda,\mathrm{i}} = G_{\lambda,\mathrm{i}}/I_{\lambda,\mathrm{i}}^{\mathrm{inc}}$, $I_{\lambda,\mathrm{i}}^{\mathrm{inc}}$ is the incident radiation intensity in direction μ_{i}, $r_{\lambda,\mathrm{i}} = r_{\lambda}(n,\mu_{\mathrm{i}})$ is the Fresnel reflection coefficient (Born and Wolf 1999), μ_{j} is the directional cosine of the angle of refraction. The refraction leads to the change of direction of the incident solar radiation at the medium boundary. The new direction of the refracted solar light under the horizontal surface of a refracting medium is $\mu_{\mathrm{j}} = \sqrt{1 - \left(1 - \mu_{\mathrm{i}}^{2}\right)/n^{2}}$. In particular, sunlight propagates in a plane-parallel layer of refracting and non-scattering medium along the surface of a cone with a half-angle at the apex $\theta = \arccos\left(1 - 1/n^{2}\right)$. Note that simple equation of $r_{\lambda,\mathrm{i}} = r_{\lambda,\mathrm{n}} = (n-1)^{2}/(n+1)^{2}$ can be used instead of the general Fresnel equations in the case of normal irradiation ($\mu_{\mathrm{i}} = 1$) of a weakly absorbing host medium, when $\kappa << n$.

As before, the radiation intensity is presented as a sum of the diffuse and collimated components:

$$\bar{I}_{\lambda,\mathrm{i}} = \bar{J}_{\lambda,\mathrm{i}} + \left(1 - r_{\lambda,\mathrm{i}}\right) E_{\lambda,\mathrm{j}} \delta\left(\mu_{\mathrm{j}} - \mu\right),\ E_{\lambda,\mathrm{j}} = \exp\left(-\tau_{\lambda}^{\mathrm{tr}} / \mu_{\mathrm{j}}\right), \tag{30}$$

and the problem statement for the diffuse component is as follows:

$$\mu \frac{\partial \bar{J}_{\lambda,\mathrm{i}}}{\partial \tau_{\lambda}^{\mathrm{tr}}} + \bar{J}_{\lambda,\mathrm{i}} = \frac{\omega_{\lambda}^{\mathrm{tr}}}{2} \bar{G}_{\lambda,\mathrm{i}},\ \bar{G}_{\lambda,\mathrm{i}} = \bar{G}_{\lambda,\mathrm{i}}^{\mathrm{diff}} + \left(1 - r_{\lambda,\mathrm{i}}\right) E_{\lambda,\mathrm{j}}, \tag{31a}$$

$$\bar{J}_{\lambda,\mathrm{i}}(0, \mu) = r_{\lambda,\mathrm{i}} \bar{J}_{\lambda,\mathrm{i}}(0, -\mu),\ \bar{J}_{\lambda,\mathrm{i}}(\infty, -\mu) = \bar{J}_{\lambda,\mathrm{i}}(\infty, -\mu),\ \mu, \mu_{\mathrm{i}} > 0. \tag{31b}$$

According to the modified two-flux approximation (Dombrovsky et al. 2005, 2006) the angular dependence of the radiation intensity takes into account the total internal reflection at the upper boundary ($\tau_{\lambda}^{\mathrm{tr}} = 0$):

$$\bar{J}_{\lambda,\mathrm{i}}\left(\tau_{\lambda}^{\mathrm{tr}}, \mu\right) = \begin{cases} \bar{J}_{\lambda,\mathrm{i}}^{-}\left(\tau_{\lambda}^{\mathrm{tr}}\right) \text{ when } -1 \le \mu < -\mu_{\mathrm{c}} \\ \bar{J}_{\lambda,\mathrm{i}}^{0}\left(\tau_{\lambda}^{\mathrm{tr}}\right) \text{ when } -\mu_{\mathrm{c}} < \mu < \mu_{\mathrm{c}} \\ \bar{J}_{\lambda,\mathrm{i}}^{+}\left(\tau_{\lambda}^{\mathrm{tr}}\right) \text{ when } \mu_{\mathrm{c}} < \mu \le 1 \end{cases},\ \mu_{\mathrm{c}} = \sqrt{1 - \frac{1}{n^2}}. \tag{32}$$

Clearly, the interval $-\mu_{\mathrm{c}} < \mu < \mu_{\mathrm{c}}$ does not contribute to the radiative flux. It should be recalled that the same idea (but with variable boundaries of the intermediate angular range) has been used in the modified differential approximation developed by Dombrovsky (2000, 2002b) for the radiative transfer in large spherical particles. After the confirmation of good quality of this approximation (by comparison with the exact numerical solution for RTE), this approach was employed to solve several engineering problems (Dombrovsky and Ignatiev 2003; Dombrovsky 2004b; Dombrovsky and Dinh 2008).

Integrating Eq. (29a) over the angles, one can obtain the boundary-value problem for the normalized diffuse irradiance:

$$-\left(\bar{G}_{\lambda,\mathrm{i}}^{\mathrm{diff}}\right)'' + \xi_{\lambda}^{2} \bar{G}_{\lambda,\mathrm{i}}^{\mathrm{diff}} = \xi_{\lambda}^{2} \chi_{\mathrm{i}} E_{\lambda,\mathrm{j}}, \tag{33a}$$

$$\tau_{\lambda}^{\mathrm{tr}} = 0,\ (1 + \mu_{\mathrm{c}})\left(\bar{G}_{\lambda,\mathrm{i}}^{\mathrm{diff}}\right)' = 2\gamma\, \bar{G}_{\lambda,\mathrm{i}}^{\mathrm{diff}},\ \tau_{\lambda}^{\mathrm{tr}} = \infty,\ \bar{G}_{\lambda,\mathrm{i}}^{\mathrm{diff}} = 0, \tag{33b}$$

$$\xi_{\lambda}^{2} = \frac{4}{(1 + \mu_{\mathrm{c}})^2} \frac{1 - \omega_{\lambda}^{\mathrm{tr}}}{1 - \omega_{\lambda}^{\mathrm{tr}} \mu_{\mathrm{c}}},\ \chi_{\mathrm{i}} = \frac{\omega_{\lambda}^{\mathrm{tr}}}{1 - \omega_{\lambda}^{\mathrm{tr}}}\left(1 - r_{\lambda,\mathrm{i}}\right),\ \gamma = \frac{1 - \bar{r}_{\lambda}}{1 + \bar{r}_{\lambda}}, \tag{33c}$$

where $\bar{r}_{\lambda}$ is the angle-averaged reflectance for the diffuse radiation at the interface ($\tau_{\lambda}^{\mathrm{tr}} = 0$).

The analytical solution to the above problem at $\xi_{\lambda} \neq 1 / \mu_{\mathrm{j}}$ is:

$$\bar{G}^{\mathrm{diff}}_{\lambda,\mathrm{i}} = \frac{\xi_\lambda^2 \chi_\mathrm{i}}{\xi_\lambda^2 - 1\big/\mu_\mathrm{j}^2}\left(E_{\lambda,\mathrm{j}} - \frac{2\gamma + (1+\mu_\mathrm{c})\big/\mu_\mathrm{j}}{2\gamma + (1+\mu_\mathrm{c})\xi_\lambda} E^{\mathrm{diff}}_{\lambda,\mathrm{i}}\right). \tag{34}$$

In the case of a non-refracting medium ($r_{\lambda,\mathrm{i}} = 0$, $\mu_\mathrm{j} = \mu_\mathrm{i}$, and $\gamma = 1$), Eqs. (33a–c) and (34) are reduced to the solution derived by Dombrovsky and Randrianalisoa (2018) and employed by Dombrovsky et al. (2019) and Dombrovsky and Kokhanovsky (2019) for solar radiation transfer in a snowpack.

It should be recalled that a comparison with the exact numerical results obtained using the high-order composite discrete ordinates method (CDOM) when the integral over directions is split into integrals over three subintervals by the critical angle, and each subinterval uses a set of quadrature points (Liou and Wu 1996; Muresan et al. 2004) performed by Dombrovsky et al. (2006) and also a comparison with the Monte Carlo simulation (Dombrovsky et al. 2012a, 2013; Ganesan et al. 2013) showed that the modified two-flux approximation can be used to retrieve the main optical properties of absorbing and scattering materials from the experimental data for the normal-hemispherical reflectance and transmittance of flat samples of these materials (Baillis-Doermann and Sacadura 2000; Sacadura 2011). This method has been successfully employed in studies of spectral radiative properties of various dispersed materials with not too high values of the refraction index (Dombrovsky et al. 2005, 2007b, 2010, 2011a, b, c, 2018a; Hakoume et al. 2014). The same method was recently used in a heat transfer model for photothermal hyperthermia of superficial tumors (Dombrovsky et al. 2011d, 2015a).

The differential approximations for radiative transfer cannot give reliable parameters of the radiation field in the case of complex angular dependence of the radiation intensity. There are two important cases when the error of these approximations is too large. First of all, one should recall diverse multi-dimensional problems. Even in the case of large optical thickness of a medium, one can expect large errors of differential approximations in the regions of sharp spatial variation of the medium properties and near the corners of a complex region (Dombrovsky 1996a, 1997; Dombrovsky and Baillis, 2010). Nevertheless, the diffusion approximation is usually a good approach for estimating the irradiance field. With the use of transport approximation, the irradiance field is sufficient to obtain the source function (the right-hand side) of RTE. As a result, there is a possibility to improve the solution using the second iterative step of a computational procedure. It is sufficient to solve the RTE with the known source function using one of the ray-tracing procedures. In the hypothetic case of a medium with isotropic scattering, this idea was realized for the first time by Edwards and Bobcôo (1967) and Bobcôo (1967) who used the diffusion (P_1) approximation as an initial approach. The modification of this method for the case of anisotropic scattering with the use of transport approximation was then suggested in the early papers by Adzerikho et al. (1979) and Dombrovsky and Barkova (1986). A study of applicability and accuracy of the combined two-step procedure with the use of Monte Carlo method at the second step of the iterative solution has been reported by Dombrovsky and Lipiński (2010). It was shown that the method is rather accurate excluding the case of the so-called searchlight effect. The details can be found in

the book by Dombrovsky and Baillis (2010). The two-step method has been recently used to solve quite different applied problems of radiative transfer in scattering media (Dombrovsky and Randrianalisoa 2018; Dombrovsky et al. 2016, 2018b).

We do not consider 2-D problems of radiative transfer (with two spatial variables) in the present paper. However, the two-step method enables one to improve significantly the approximate 1-D solution for the normal-hemispherical reflectance of an absorbing, scattering and refracting medium. The ordinary or modified two-flux approximation can be used at the first step of this solution. In the case of a uniform layer of the medium (when absorption and scattering properties are constant across the layer) the analytical solution of the problem can be obtained, as it was done by Dombrovsky et al. (2011b) for the normal emissivity of isothermal layer.

3 Computational Model for Combined Heat Transfer

Generally speaking, there are various combined thermal or related processes in a snowpack or scattering ice sheet and many of these processes should be involved in a complete transient computational model for snow heating. As an example, one should recall the processes of ice sublimation and diffusion of water vapor through a snow layer. These processes appear to be important for the snow microstructure, which determines macroscopic snow properties. The related problems are analyzed in detail by Kaempfer and Plapp (2009) and Pinzer et al. (2012). Strictly speaking, a contribution of both sublimation and diffusion processes to the combined heat transfer in deep layers of snow should be also taken into account (Haussener et al. 2012; Riche and Schneebeli 2013; Ebner et al. 2016, 2017). However, a study of these processes is beyond the scope of the present paper.

The 1-D transient energy equation for temperature, $T(t, z)$, in a layer of snow or ice and the accompanying initial and boundary conditions can be written as follows:

$$\rho c \frac{\partial T}{\partial t} = \frac{\partial}{\partial z}\left(k \frac{\partial T}{\partial z}\right) + P,\ t > 0\ , 0 < z < d_{\text{th}}, \tag{35a}$$

$$T(0, z) = T_0(z), \tag{35b}$$

$$z = 0,\ -k \frac{\partial T}{\partial z} = h\,(T_{\text{air}} - T) - \varepsilon\,\pi \int_{\lambda_{\text{w1}}}^{\lambda_{\text{w2}}} I_{\text{b}}(T, \lambda)\,\mathrm{d}\lambda,\ z = d_{\text{th}},\ \frac{\partial T}{\partial z} = 0, \tag{35c}$$

where z is the coordinate measured from the irradiated surface of the layer, ρ, c, and k are the density, the specific (per unit mass) heat capacity, and the thermal conductivity of snow or ice, respectively, $T_{\text{air}}(t)$ is the temperature of ambient air, and $h(t)$ is the convective heat transfer coefficient. The adiabatic condition at the conventional boundary $z = d_{\text{th}} >> d$ (the last of conditions (2.35c)) means that

we neglect heat transfer at $z > d_{\mathrm{th}}$. Of course, the value of d_{th} increases with time and should be estimated using additional calculations. The time dependence of heat transfer coefficient is determined by a wind speed.

The last term in the right-hand side of the boundary condition at $z = 0$ (see Eq. (35c)) is the mid-infrared radiative cooling due to thermal radiation of snowpack or ice sheet surface in the atmospheric window of $\lambda_{\mathrm{w1}} < \lambda < \lambda_{\mathrm{w2}}$ ($\lambda_{\mathrm{w1}} = 8$ μm, $\lambda_{\mathrm{w2}} = 13$ μm) (Raman et al. 2014; Chen et al. 2016; Hossain and Gu 2016). The radiative cooling is limited during the night time when it is not compensated by solar mid-infrared radiation. Therefore, the coefficient ε varies from zero in the day time to the unity at night. The absorbed radiation power, $P(z)$, at arbitrary conditions of solar irradiation should be recalculated time by time during the combined problem solution.

Of course, the large value of the latent heat of ice melting, $L = 0.34$ MJ/kg, should be taken into account. This can be done using an equivalent additional heat capacity, Δc, in narrow temperature range of $T_{\mathrm{m}} - \Delta T < T < T_{\mathrm{m}} + \Delta T$ (where $T_{\mathrm{m}} = 273$ K is the ice melting temperature, $\Delta T << T_{\mathrm{m}} - T_0$) as it was done by Dombrovsky and Dinh (2008), Dombrovsky (2009a, 2017), and Dombrovsky et al. (2015b) for physically similar melting and solidification problems. The following simple variant of this approach was used by Dombrovsky et al. (2019):

$$\Delta c = \frac{L}{\Delta T}\left(1 - |T_{\mathrm{m}} - T| \big/ \Delta T\right) \tag{36}$$

A correct choice of ΔT value is determined by the interval of the computational grid and the time step of numerical solution to problem (35a)–(35c). Obviously, it is difficult to choose a realistic initial profile of temperature, $T_0(z)$, for the heat transfer calculations. Fortunately, the effect of this temperature profile decreases with time. It was shown by the authors that the choice of $T_0(z)$ makes no difference for the snow temperature after about four hours from the conventional initial time moment. An implicit finite-difference scheme of the second order of spatial approximation can be recommended for numerical calculations. The specific combination of a strong decrease of heat generation rate with the distance from the irradiated surface and rather deep propagation of heat in the snow or ice layer due to long-time conduction makes it necessary to use a detailed and strongly non-uniform computational grid and double precision calculations.

According to the ordinary procedure, the following finite-difference approximation of Eq. (35a) is used in the calculations:

$$(\rho c)_{\mathrm{i}} \frac{T_{\mathrm{i}}^{\mathrm{j}} - T_{\mathrm{i}}^{\mathrm{j}-1}}{\tau_{\mathrm{j}}} = \frac{2}{h_{\mathrm{i}} + h_{\mathrm{i}-1}} \left(k_{\mathrm{i}+1/2} \frac{T_{\mathrm{i}+1}^{\mathrm{j}} - T_{\mathrm{i}}^{\mathrm{j}}}{h_{\mathrm{i}}} - k_{\mathrm{i}-1/2} \frac{T_{\mathrm{i}}^{\mathrm{j}} - T_{\mathrm{i}-1}^{\mathrm{j}}}{h_{\mathrm{i}-1}} \right) + P_{\mathrm{i}}, \tag{37a}$$

where

$$\tau_j = t_j - t_{j-1},\ h_i = z_{i+1} - z_i,\ k_{i\mp 1/2} = (k_i + k_{i\mp 1}) \tag{37b}$$

After transformations, the finite-difference equation can be written as follows:

$$T^{\mathrm{j}}_{\mathrm{i}+1} - B_{\mathrm{i}} T^{\mathrm{j}}_{\mathrm{i}} + C_{\mathrm{i}} T^{\mathrm{j}}_{\mathrm{i}-1} = -A_{\mathrm{i}}, \tag{38a}$$

$$B_{\mathrm{i}} = 1 + C_{\mathrm{i}} + D_{\mathrm{i}},\ C_{\mathrm{i}} = \frac{k_{\mathrm{i}-1/2}}{k_{\mathrm{i}+1/2}} \frac{h_{\mathrm{i}-1}}{h_{\mathrm{i}}},\ D_{\mathrm{i}} = \frac{(\rho c)_{\mathrm{i}}}{k_{\mathrm{i}+1/2}} \frac{h_{\mathrm{i}}(h_{\mathrm{i}} + h_{\mathrm{i}-1})}{2\tau_{\mathrm{j}}},$$
$$A_{\mathrm{i}} = D_{\mathrm{i}} \left(T^{\mathrm{j}-1}_{\mathrm{i}} + \frac{P_{\mathrm{i}} \tau_{\mathrm{j}}}{(\rho c)_{\mathrm{i}}} \right), \tag{38b}$$

For better approximation of the boundary conditions one should use the expansion of temperature into Taylor series in the neighborhood of the boundary nodes of the mesh:

$$T^{\mathrm{j}}_2 = T^{\mathrm{j}}_1 + \left.\frac{\partial T^{\mathrm{j}}}{\partial z}\right|_1 h_1 + \left.\frac{\partial^2 T^{\mathrm{j}}}{\partial z^2}\right|_1 \frac{h_1^2}{2} + O\left(h_1^3\right),$$
$$T^{\mathrm{j}}_N = T^{\mathrm{j}}_{N+1} + \left.\frac{\partial T^{\mathrm{j}}}{\partial z}\right|_{N+1} h_N + \left.\frac{\partial^2 T^{\mathrm{j}}}{\partial z^2}\right|_{N+1} \frac{h_N^2}{2} + O\left(h_N^3\right), \tag{39}$$

where $\frac{\partial^2 T^{\mathrm{j}}}{\partial z^2}$ is determined through T^{j} and $\frac{\partial T^{\mathrm{j}}}{\partial z}$ according to the differential Eq. (35a). As a result, one can find the coefficients in the following equations:

$$T^{\mathrm{j}}_2 = a_1 + b_1 T^{\mathrm{j}}_1,\ T^{\mathrm{j}}_N = a_2 + b_2 T^{\mathrm{j}}_{N+1}. \tag{40}$$

In accordance with the factorization method, the relation between the neighboring nodal values of temperature is

$$T^{\mathrm{j}}_{\mathrm{i}} = \psi_{\mathrm{i}} + \phi_{\mathrm{i}} T^{\mathrm{j}}_{\mathrm{i}+1}, \tag{41}$$

where ϕ_{i} and ψ_{i} are the factorization coefficients. From the finite-difference form of the boundary condition at $z = 0$ we find

$$\phi_1 = 1 \big/ b_1,\ \psi_1 = -a_1 \phi_1. \tag{42}$$

The formulas of upward factorization

$$\phi_{\mathrm{i}} = 1 \big/ (B_{\mathrm{i}} - C_{\mathrm{i}} \phi_{\mathrm{i}-1}),\ \psi_{\mathrm{i}} = \phi_{\mathrm{i}} (C_{\mathrm{i}} \psi_{\mathrm{i}-1} + A_{\mathrm{i}}) \tag{43}$$

allow obtaining all the values of ϕ_{i} and ψ_{i} up to $i = N$. After that, one can calculate the value of T^{j}_{N+1} from the boundary condition at $z = d_{\mathrm{th}}$:

$$T^{\mathrm{j}}_{N+1} = (\psi_N - a_2) \big/ (b_2 - \phi_N) \tag{44}$$

and all the others T_i^j are determined by Eq. (41).

Note that the above model of heat transfer is incomplete in the case of a considerable melting of snow because water penetrates downward through porous snow and solidifies there. This process should be taken into account in more general physical and computational model. The accompanying variation of optical properties of a non-uniform snowpack should be also analyzed on the basis of more sophisticated models.

It is important that the heat transfer problem considered here differs from the classical problem of radiative-conductive heat transfer, when the temperature of the medium is not only formed due to the combined action of radiative heat transfer and heat conduction, but the radiative transfer substantially depends on the temperature field (Dombrovsky and Baillis 2010). In the case of solar heating of a snow cover, the snow temperature does not directly affect the radiative transfer, which greatly simplifies the solution of the problem, since a single spectral calculation of the radiative transfer is sufficient. In this regard, the problem solved in the present study is methodologically very similar to the infrared heating of biological tissues used in thermal treatment of superficial tumors (Dombrovsky et al. 2011d, 2012b, 2013, 2015a). Otherwise, in the case of a considerable volumetric emission of thermal radiation by the medium, solving the transient energy equation would require systematic calculations of radiation absorption field at the selected time steps of the numerical solution (Siegel 1998; Dombrovsky and Baillis 2010; Modest 2013).

4 Heating of a Snowpack by Solar Radiation

This section in based on the computational study reported recently by Dombrovsky et al. (2019). We are focused on the main results, which are physically sound and expected to be interesting for potential readers.

4.1 Spectral Optical Properties of Pure Snow

4.1.1 Optical Constants of Ice in the Visible and Near-Infrared

The complex refractive index $m(\lambda) = n(\lambda) - i\kappa(\lambda)$, where n is the index of refraction, κ is the index of absorption, determines the peculiarities of light absorption, transmission, and reflectance by both homogeneous and inhomogeneous media (Born and Wolf 1999). Spectral behavior of the indices of refraction and absorption are not independent of each other but satisfy the Kramers–Krönig relation (Lucarini et al. 2005). Particularly, the index of refraction is almost constant in the spectral ranges of a very low absorption as that for water ice in the visible range. The spectral optical constants of ice are plotted in Fig. 1 (Warren and Brandt 2008). The wavelength range

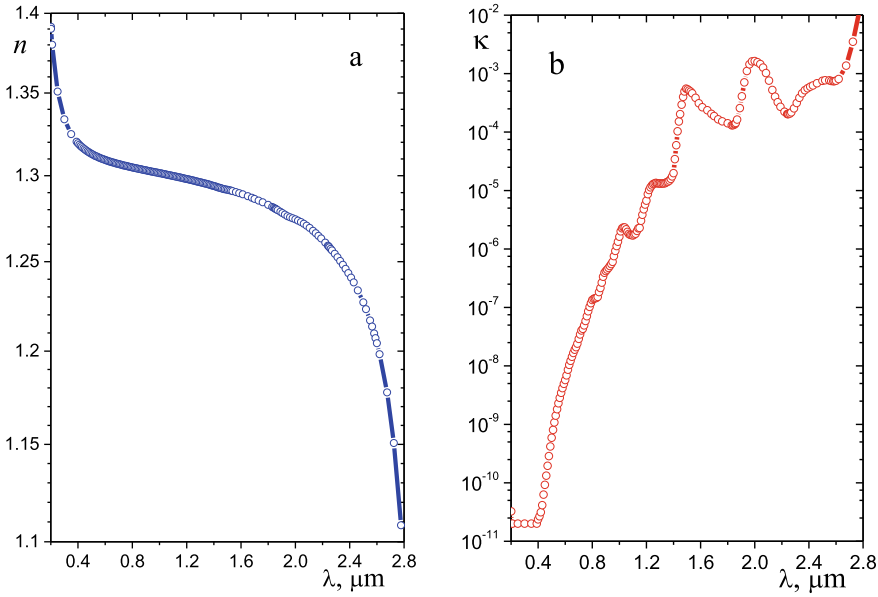

Fig. 1 Spectral optical constants of ice: **a**—index of refraction, **b**—index of absorption. Adopted from (Dombrovsky et al. 2019)

shown in this figure is the most important one for the radiative heating problem under consideration.

The extremely low value of κ in the visible and a significant increase of absorption index in the near-infrared range determine the specific spectral properties of ice grains and snow. In particular, the known high value of snow albedo is a result of almost perfect spectral transparency of pure ice (Wiscombe and Warren 1980; Warren 1982; Kokhanovsky and Zege 2004). Obviously, even very small amount of impurities such as atmospheric aerosol particles may increase significantly the light absorption in snow leading to the decrease of the observed spectral and broadband albedo of snow (Warren and Wiscombe 1980; Chýlek et al. 1983; Warren and Clarke 1990; Tedesco 2015). We also recommend more recent papers on the specific problem of snow albedo (Aoki et al. 2000; Gardner and Sharp 2010; Brandt et al. 2011; Malinka et al. 2016; Wang et al. 2017; Kokhanovsky et al. 2018; Picard et al. 2020).

4.1.2 Local Optical Properties of Snow

Theoretical modeling of optical properties of various turbid media is often based on the classical Mie theory for spherical particles (Van de Hulst 1981; Bohren and Huffman 1983; Hergert and Wriedt 2012). The size of snow particles is much greater that the wavelength of solar radiation, and the shape of these particles can be very complex. Therefore, the geometrical optics (GO) approximation and some other

advanced methods are used to calculate optical properties of single particles and the resulting properties of snow (Bi et al. 2011; Borovoi et al. 2014; Lindqvist et al. 2018). Alternative approaches for studies of optical properties of ice grains of complex shape can be found in papers (Grenfell and Warren 1999; Neshyba et al. 2003; Libois et al. 2013; Räisänen et al. 2015; Ishimoto et al. 2018). However, for the sake of simplicity, one should not forget about physically sound analytical approximations suggested in early papers by Irvine (1963, 1964), Kokhanovsky and Zege (1995, 1996), and Dombrovsky (1996a, b).

In the present paper, the spherical ice grains of various sizes are considered instead of ice particles of complex shape and orientation. The calculations are performed for ice spheres of radius $a = 50\ \mu\text{m}$, $100\ \mu\text{m}$, and $200\ \mu\text{m}$. These variants can be treated as those corresponding to different snow morphology. The case of nonspherical particles can be treated as well. However, the present study is focused on snowpack heating and the problem of nonsphericity of ice grains is of a secondary importance.

The most general solution for the optical properties of homogeneous spherical particles is given by the rigorous Mie theory. However, the ice grains considered are much larger in size that the wavelength. This makes reasonable to consider the GO approximation as the main tool in this work. At the same time, the Mie theory with the use of computer code published in (Dombrovsky 1996a) and described also by Dombrovsky and Baillis (2010) is used for the reference calculations.

With the use of transport approximation, only two dimensionless characteristics of absorption and scattering of single particles are necessary: the absorption efficiency factor, Q_a, and the transport efficiency factor of scattering, $Q_s^{tr} = Q_\text{s} \cdot (1 - \bar{\mu})$. The values of transport efficiency factor of extinction, $Q_\text{tr} = Q_\text{a} + Q_s^{tr}$, and transport albedo of the particle, $\omega_\text{tr} = Q_s^{tr} \big/ Q_\text{tr}$ are also considered. The above mentioned characteristics depend on spectral optical constants and also on the diffraction parameter $x = 2\pi a \big/ \lambda$ introduced in the Mie theory.

The results of calculations using the GO solution obtained by Kokhanovsky and Zege (1995) are compared with calculations based on the Mie theory in Fig. 2. One can see that GO can be used to calculate both Q_a and ω_tr for ice grains of various sizes. As a result, the value of transport extinction efficiency factor, $Q_\text{tr} = Q_\text{a} \big/ (1 - \omega_\text{tr})$, can be also obtained using the GO solution for the case of $\kappa << n$ (Kokhanovsky and Zege 1995):

$$Q_\text{a} = 2 - Q_\text{s},\ Q_\text{s} = 1 + \tilde{Q}_\text{s},\ \bar{\mu} = (1 + y) \Big/ \left(1 + \tilde{Q}_\text{s}\right), \tag{45a}$$

$$\tilde{Q}_\text{s} = \frac{1}{2} \sum_{\text{j}=1}^{2} \int_0^{\pi/2} f_\text{j}(\zeta) \sin 2\zeta \ \text{d}\zeta,\ \ y = \frac{1}{2} \sum_{\text{j}=1}^{2} \int_0^{\pi/2} \frac{\varphi_\text{j}(\zeta) \sin 2\zeta \ \text{d}\zeta}{1 - 2R_\text{j}\tilde{E} + R_\text{j}^2 \tilde{E}^2}, \tag{45b}$$

where

$$\varphi_\text{j}(\zeta) = \tilde{E}\left(1 - R_\text{j}\right)^2 \cos 2\left(\zeta - \tilde{\zeta}\right) + R_\text{j}\left(1 - \tilde{E}^2\right) \cos 2\zeta + 2R_\text{j}^2\left(\tilde{E} - \cos 2\tilde{\zeta}\right)\tilde{E} \cos 2\zeta, \tag{45c}$$

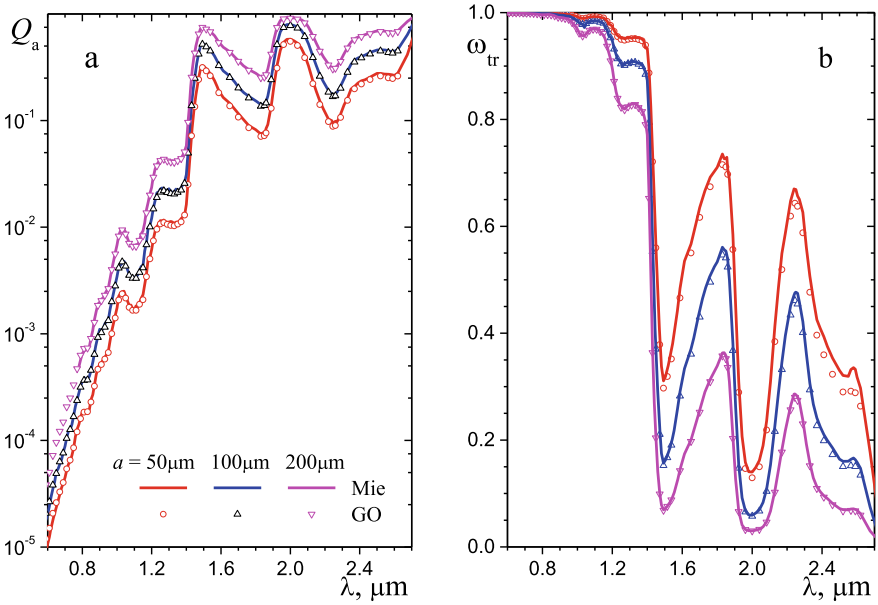

Fig. 2 Optical properties of ice grains: **a**—efficiency factor of absorption, **b**—transport albedo of single scattering

$$f_j(\zeta) = R_j + \tilde{E}(1 - R_j)^2 \Big/ \left(1 - R_j \tilde{E}\right), \tag{45d}$$

$$R_1 = \frac{\tan^2\left(\zeta - \tilde{\zeta}\right)}{\tan^2\left(\zeta + \tilde{\zeta}\right)},\ R_2 = \frac{\sin^2\left(\zeta - \tilde{\zeta}\right)}{\sin^2\left(\zeta + \tilde{\zeta}\right)},\ \tilde{E} = \exp\left(-4\kappa x\sqrt{1 - \tilde{\zeta}^2}\right),\ \tilde{\zeta} = \frac{\cos\zeta}{n}, \tag{45e}$$

To avoid numerical errors of direct calculations by Eqs. (45a)–(45e) at $Q_a < 10^{-5}$, one can use the following approximation which is correct in the case of $\kappa x << 1$:

$$Q_a = 4\nu\kappa x,\ \nu = \frac{2}{3}\left[n^3 - \left(n^2 - 1\right)^{3/2}\right]. \tag{46}$$

An approximation suggested by Dombrovsky (2002a) for arbitrary values of x is also appropriate.

It follows from Fig. 2b that GO provides very accurate results. Also one can see that light scattering highly predominates very weak absorption in the visible spectral range. This results in a strong reflection of visible solar radiation from the snow surface and relatively small contribution of this spectral range to the heating of snow surface layer. At the same time, the remaining (not reflected) visible part

of the collimated solar radiation forms almost diffuse radiation field in the snow. As a result, the visible light is absorbed relatively far from the snow surface, and its contribution to heating deep layers of snow is considerable. On the contrary, the reflection of near-infrared solar radiation from the snow surface is relatively small and this spectral range contribute strongly to the radiation power absorbed in the surface layer.

It is assumed that the hypothesis of independent scattering by single ice grains in snow is true. It means that each particle absorbs and scatters the radiation in exactly the same manner as if other particles do not exist. In addition, there is no systematic phase relation between partial waves scattered by individual particles during the observation time interval, so that the intensities of the partial waves can be added without regard to phase. In other words, each particle is in the far-field zones of all other particles and scattering by individual particles is incoherent.

4.1.3 Analytical Estimations and Numerical Results

Let us consider first a model problem to understand the main special features of solar radiation transfer in a snowpack. Obviously, a contribution of the direct solar radiation to the snowpack heating is predominant as compared with the sky radiation. Therefore, it is sufficient to consider the absorbed power of solar radiation at various values of zenith angle θ_{sol}. It is assumed that the spectrum of the incident solar radiation is similar to the blackbody radiation at temperature $T_{\mathrm{sol}} = 6000$ K. The calculated relative values of the integral (over the spectrum) radiation power, $\bar{P}_{\mathrm{t}} = \int_0^{\infty} P(z)\,\mathrm{d}z \Big/ \int_{\lambda_{min}}^{\lambda_{max}} I_{\mathrm{b}}(T_{\mathrm{sol}}, \lambda)\,\mathrm{d}\lambda$ (I_{b} is the Planck function), absorbed in a snowpack containing ice grains of different sizes are presented in Fig. 3.

As one can expect, the main part of solar radiation is reflected from the snowpack because of a strong reflection of the visible radiation. One can see that $\bar{P}_{\mathrm{t}}$ decreases

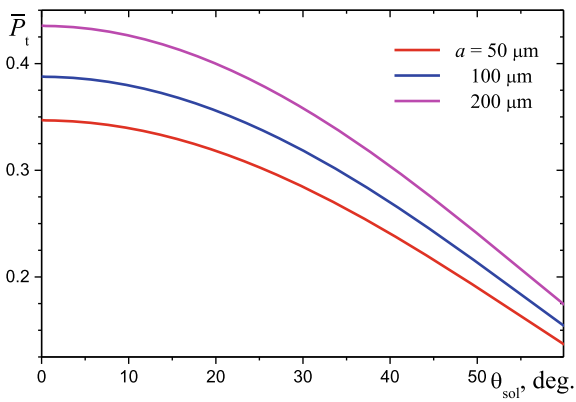

Fig. 3 The normalized integral (over the spectrum) radiative power absorbed in optically thick snowpack. Adopted from (Dombrovsky et al. 2019)

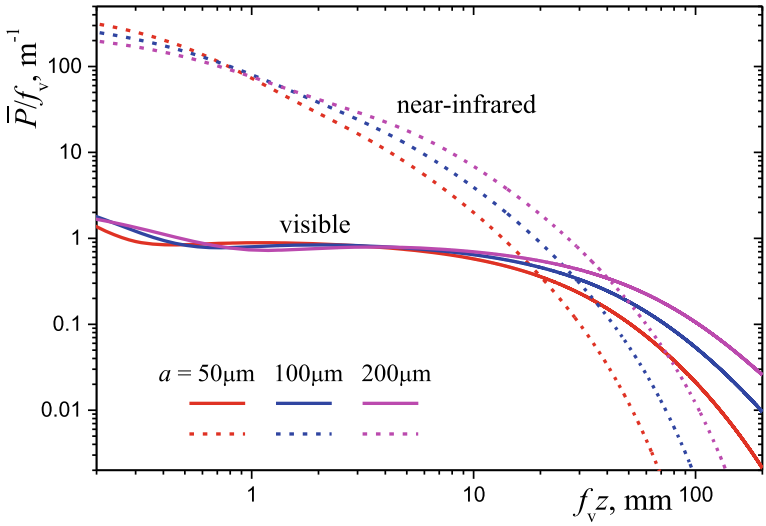

Fig. 4 Contributions of the visible range ($\bar{P}_{\text{vis}}$) and near-infrared range ($\bar{P}_{\text{ni}}$) to the profiles of normalized absorbed radiation power in a snowpack

considerably with the zenith angle, whereas the effect of ice grain size is insignificant. It should be also recalled that the calculations by Dombrovsky et al. (2019) for polydisperse spherical ice grains showed that one can use the monodisperse approximation with an equivalent mean radius of the grains to obtain the spectral properties of snow.

The depth of the radiation propagation into the snowpack can be illustrated by calculations at normal incidence (see Fig. 4). The contributions of the visible range ($\lambda < 0.78$ μm) and the near-infrared range to the absorbed radiation power are calculated separately:

$$\bar{P}(z) = \bar{P}_{\text{vis}}(z) + \bar{P}_{\text{ni}}(z),\ \left\{\bar{P}_{\text{vis}},\ \bar{P}_{\text{ni}}\right\} = \{P_{\text{vis}},\ P_{\text{ni}}\} \Big/ \int_{\lambda_{min}}^{\lambda_{max}} I_{\text{b}}(T_{\text{sol}}, \lambda)\, \mathrm{d}\lambda. \qquad (47)$$

The universal coordinates $f_{\text{v}} z$ and $\bar{P} \big/ f_v$ are used in Fig. 4 to present simultaneously the results for various values of f_{v} (the ratio of snow density to ice density). At realistic value of $f_{\text{v}} = 0.33$, the near-infrared radiation is absorbed mainly in a thin surface layer of snowpack, whereas the visible radiation is absorbed almost uniformly in the layer of thickness about 60 mm and its contribution to heating deep layers of snowpack is expected to be considerable. This result agrees well with the conclusion by Munneke et al. (2009) about an important role of the deep penetration of short-wave solar radiation in heat balance of a snowpack. The effect of grain size on this effect is not strong. Therefore, the subsequent calculations are performed at $a = 100$ μm.

It is interesting to analyze the results obtained at realistic parameters of the problem. The wide range of snow density variation from $\rho = 100\,\mathrm{kg/m^3}$ to $550\,\mathrm{kg/m^3}$ leads to the corresponding variations in thermal properties of snow. Obviously, the volumetric heat capacity, ρc, is directly proportional to the density, whereas the thermal conductivity of snow exhibits more strong increase with the snow density. In addition, at the same snow density, variations in snow microstructure can change thermal conductivity by a factor of two. Thermal conductivity of snow has been studied in many papers (Fukusako 1990; Sturm and Johnson 1992; Sturm et al. 1997, 2002; Schneebeli and Sokratov 2004; Calonne et al. 2011; Shertzer and Adams 2011; Riche and Schneebeli 2013; Löwe et al. 2013; Oldroyd et al. 2013; Osokin et al. 2017). The most of the results obtained are discussed in review paper by Arenson et al. (2015). It was shown that thermal conductivity is almost directly proportional to the square of density and varies from $k = 0.04$ W/(m K) to 1 W/(m K). The temperature variations of thermal properties of snow are relatively small and the effect of temperature on snow density and thermal properties is neglected. The constant values of $k = 0.2$ W/(m K) and $\rho c = 0.6$ MJ/(m^{3}K) corresponding to the volume fraction of ice grains of $f_\mathrm{v} = 0.33$ are used in the calculations.

In the midsummer (summer solstice), the current declination of the Sun is equal to $\delta = 23.44$. This value of δ is used to determine the solar zenith angle:

$$\cos\theta_\mathrm{sol} = \sin\phi\sin\delta + \cos\phi\cos\delta\cos\chi\,, \tag{48}$$

where ϕ is the local latitude and χ is the hour angle. The value of $\phi = 70°$ is considered in the calculations. The following relation is used to determine the value of χ for the current time, t, measured in hours from the midnight:

$$\chi = \pi\left|1 - t_1/12\right|, \qquad t_1 = t - 24\lfloor t/24 \rfloor, \tag{49}$$

where symbol $\lfloor\ \rfloor$ denotes the floor function. The resulting variation of θ_sol with the local solar time is shown in Fig. 5. The effect of a sloping surface of snow is also considered below. There are many possible orientations of the sloping surface with respect to the visible path of the Sun. The simplest orientation can be treated as a variation of the declination angle. Time variation of the solar zenith angle for such a surface with a sloping angle $\vartheta_\mathrm{sl} = 10°$ is also shown in Fig. 5.

The spectral radiative flux from the Sun and clear sky at the horizontal underlying surface are presented in Fig. 6. The spectral dependences were calculated using the SBDART code (Ricchiazzi et al. 1998). The choice of solar zenith angles is determined by the case problem parameters. Generally speaking, a contribution of direct solar radiation is much greater than that of diffuse radiation from the sky. However, it is not the case for visible light at solar zenith angles $\theta_\mathrm{sol} > 60°$. Therefore, the sky radiation is taken into account in the calculations.

According to (Dombrovsky et al. 2019), the following analytical expressions for the daily variation of coefficients of convective heat transfer and radiative cooling are considered:

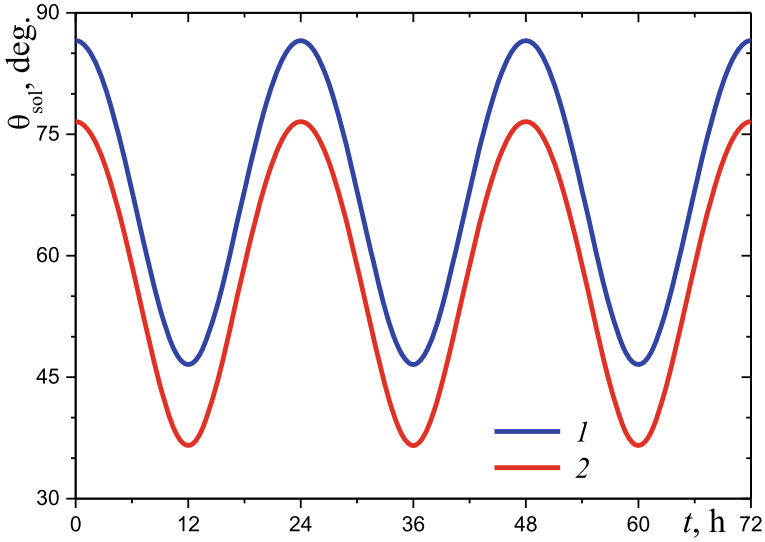

Fig. 5 Time variation of solar zenith angle considered in the case problem: *1*—horizontal surface, *2*—sloping surface at $\vartheta_{sl} = 10°$. Adopted from (Dombrovsky et al. 2019)

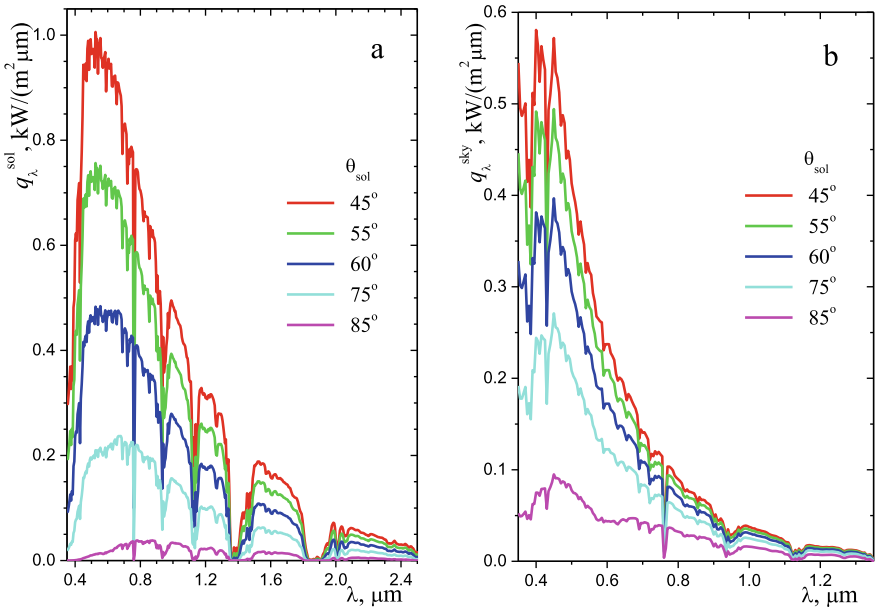

Fig. 6 The spectral radiative flux at the earth surface: **a**—direct radiation from the Sun, **b**—diffuse (scattered) radiation from the clear sky. Adopted from (Dombrovsky et al. 2019)

$$h = h_{\min} + \left(h_{\max} - h_{\min}\right)\psi(\theta_{\text{sol}}),\ \varepsilon = 1 - F(\theta_{\text{sol}}) \tag{50a}$$

$$\psi(\theta_{\text{sol}}) = \begin{cases} 1,\ 0 \le \theta_{\text{sol}} < 4\pi/9 \\ 0.5 - 0.5\sin\left(18\theta_{\text{sol}} - 8.5\pi\right),\ 4\pi/9 \le \theta_{\text{sol}} < \pi/2 \end{cases} \tag{50b}$$

It is assumed in Eqs. (50a) and (50b) that the midnight conditions approach gradually starting from $\theta_{\text{sol}} = 80°$. Note that the values of $h_{\max} = 10$ W/(m^2 K) and 15 W/(m^2 K) correspond to a weak wind (with a speed less that about 1–2 m/s) and to a moderate wind of speed about 3 m/s, respectively (Defraeye et al. 2011; Mirsadeghi et al. 2013), whereas $h_{\min} = 6$ W/(m^2 K) can be used for the windless weather.

The temperature profiles in a snowpack calculated for the first day at $T_0 = T_{air}(z) = -10$ °C are presented in Fig. 7. One can see that snowpack is heated rather fast in the morning and the melting temperature is reached at noon. A further evolution of the snowpack temperature depends strongly on wind speed. In the afternoon, the maximum temperature of snow is predicted at the distance about 15 mm from the snow surface at 6 pm and $h_{\max} = 15$ W/(m^2 K). The evening and night cooling of snowpack takes place for the surface layer of thickness from 15 mm to about 120 mm, whereas a continuous heat conduction leads to further heating of deep layers of the snowpack.

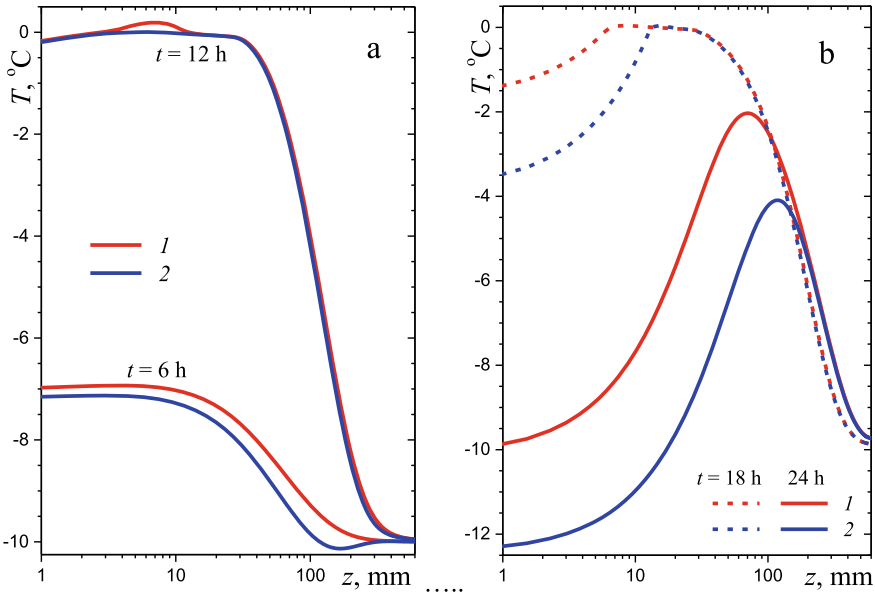

Fig. 7 Typical profiles of temperature in snowpack (**a**) before the noon and (**b**) after the noon at various values of the maximum heat transfer coefficient: *1* – $h_{\max} = 10$ W/(m^2 K), *2* – *15* W/(m^2 K). Adopted from (Dombrovsky et al. 2019)

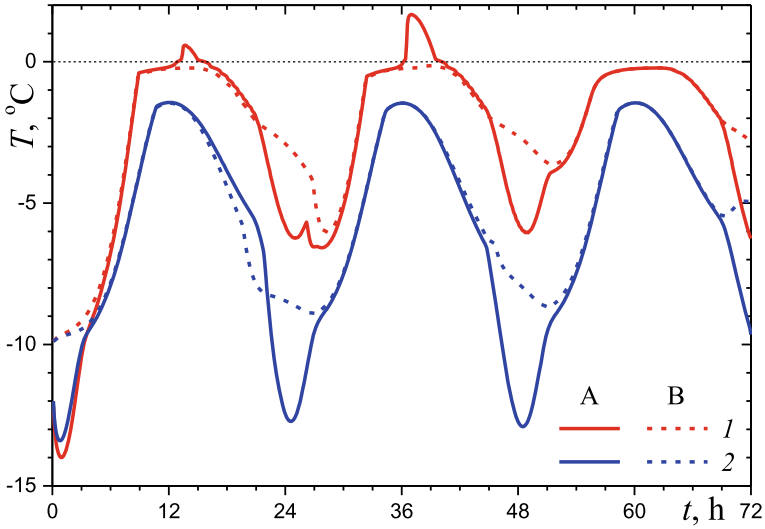

Fig. 8 The effect of wind on snow surface temperature: *1*—$h_{\max} = 8$ W/(m^2 K) (weak wind), *2*—*15* W/(m^2 K) (moderate wind); A—complete calculation, B—without radiative cooling

The computational results for the three-day variation of snow surface temperature presented in Fig. 8 show an almost periodic variation of the temperature with a great difference between the day and the night. The effects of both the convective heat transfer in windy weather and the radiative cooling of a snowpack surface are significant. It is interesting that radiative cooling is partially compensated by a relatively long convective heating. The latter may lead to the unexpectedly strong surface heating and even melting as compared with the computational predictions ignoring the radiative cooling. This physical result of combined transient heat transfer in a snowpack was obtained by Dombrovsky et al. (2019) for the first time. Note that the details of temperature behavior near the melting temperature are explained by the finite value of $\Delta T = 0.1$ K used in the calculations.

Similar calculations for the better irradiated sloping surface of snowpack with $\vartheta_{\rm sl} = 10°$ can be easily calculated by multiplying the directional radiative flux at solar zenith angle $\theta_{\rm sol}(t)$ by the ratio of $\cos\left(\theta_{\rm sol}^{\rm sl}\right) / \cos(\theta_{\rm sol})$. According to Eq. (32), the conventional night-time conditions including the radiative cooling do not take place for the sloping surface considered. The overall effect of snow surface sloping on time variation of snow pack surface temperature is shown in Fig. 9. Obviously, the snow surface turned to the Sun exhibits a higher temperature, especially in the time of large zenith angle of the Sun. It means that specific conditions of solar irradiation cannot be ignored even at sloping angle of $\vartheta_{\rm sl} = 10°$.

The results obtained make clear a contribution of the visible and near-infrared solar radiation as well as the role of convective cooling or heating of snow, mid-infrared radiative cooling of snow surface, and continuous heating of deep snow layers due to heat conduction. The numerical analysis indicates a deep heating of snowpack

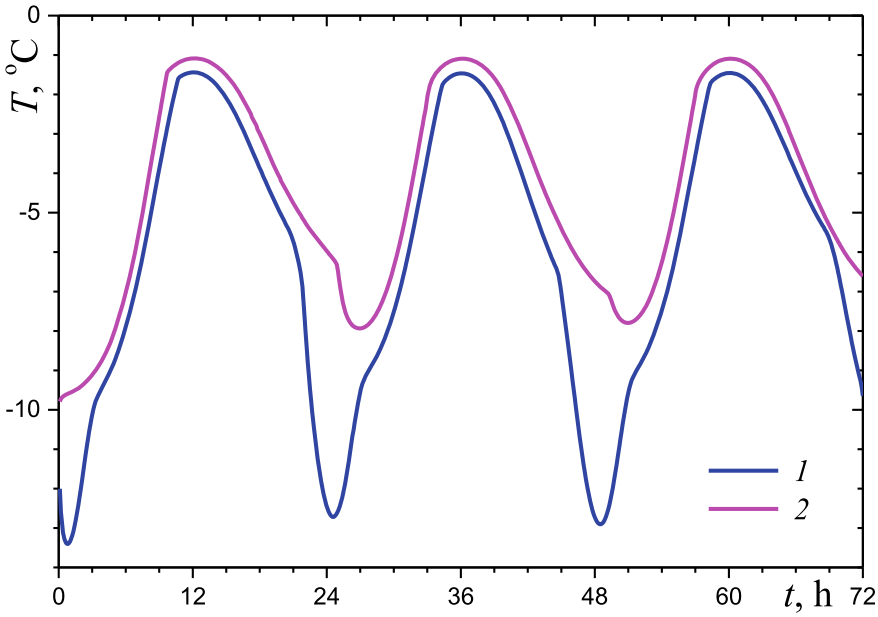

Fig. 9 Effect of sloping of snowpack surface on the time variation of surface temperature: *1*—horizontal surface, *2*—sloping surface ($\vartheta_{sl} = 10°$). Calculations at $h_{max} = 15$ W/(m^2 K). Adopted from (Dombrovsky et al. 2019)

and relatively strong effect of wind and radiative cooling on surface temperature of snow. The calculations for the studied problem demonstrated the main possibilities of the computational model, which is expected to be a convenient and useful tool in further studies of snowpack solar heating.

5 Effect of Snow Pollution on Radiative Heating of Snowpack

A combination of physical processes of snow formation in the atmosphere and periodic partial melting of snow cover can lead to various morphologies of contaminated snow. Therefore, both the internal mixing of soot in ice grains and the external mixing when soot is between the grains should be considered. Following the work (Dombrovsky and Kokhanovsky 2020b), the geometrical optics approximation for ice grains, the Rayleigh theory for small soot particles, the Maxwell-Garnett theory for the effective optical constants of ice containing soot, and the Mie theory generalized for the case of by two-layered spherical particles are employed in this section.

5.1 Internal Versus External Mixture of Soot

Due to very weak absorption of visible light by pure ice, even very small amounts of various impurities significantly affect the absorption of light in the snow cover composed of ice grains. This effect is especially important in the Arctic regions located close to pollution sources, where the snow load should be taken into account to understand the features of sunlight reflection and heating of the snow cover (Doherty et al. 2010). The effect of various impurities on the spectral albedo of snow has been studied in detail since the early paper by Warren and Wiscombe (1980), as well as in many relatively recent studies (Flanner et al. 2007, 2012; Brandt et al. 2011; Aoki et al. 2011; Liou et al. 2011, 2014; Kokhanovsky 2013; Qian et al. 2015; Dang et al. 2015; Wang et al. 2017; He et al. 2017, 2018; Warren 2019a). We restrict ourselves to considering the most important effect of soot, also called "black carbon," but the results are expected to be qualitatively correct for other impurities (Kuchiki et al. 2015).

Two variants of location of soot particles are considered in the literature as well as in recent studies by Dombrovsky and Kokhanovsky (2019, 2020a, b): inside the ice grains ("internally mixed") and between the grains ("externally mixed"). The case of externally mixed soot particles is simpler for direct modeling (Flanner et al. 2007; Aoki et al. 2011; Liou et al. 2011; Kokhanovsky 2013; Dang et al. 2015; Wang et al. 2017; Kokhanovsky et al. 2018). However, some researchers consider the internally mixed soot as a very realistic case (Liou et al. 2011, 2014; Flanner et al. 2012; He et al. 2017, 2018). The physical processes which lead to soot inclusion in ice particles were discussed by Liou et al. (2011) and Flanner et al. (2012). It was estimated by Flanner et al. (2012) that 32–73% of soot particles in the snow are internally mixed with ice grains.

Usually the uniform/random distribution of soot particles inside the ice grains is considered. However, it is physically clear that contribution of soot particles positioned in the central part or near the surface of an ice grain to the absorption of incident light is different (Dombrovsky 2000, 2002b, 2004b; Dombrovsky and Baillis 2010). The main objective of this section of the present paper is to estimate the effect of a non-uniform distribution of soot in ice grains on absorption coefficient of the polluted snow. The schematic of various spatial distributions of soot is presented in Fig. 10.

5.1.1 External Mixing Model

The simplest model of external mixing of soot particles is often used to estimate the pollution effect of soot on absorption coefficient of snow. In this case, the absorption coefficient is additive: $\alpha_\lambda = \alpha_\lambda^{\text{pure}} + \alpha_\lambda^{\text{soot}}$. According to recent paper by Dombrovsky and Kokhanovsky (2020b), we focus on light absorption by snow in the visible range and in the short-wavelength part of the near infrared. It is known that the index of absorption of ice in this range is very small (Warren and Brandt 2008) and the analytical solution by Kokhanovsky and Zege (1995) for spherical ice grains based on the geometrical optics approximation (GO) can be employed to calculate the optical

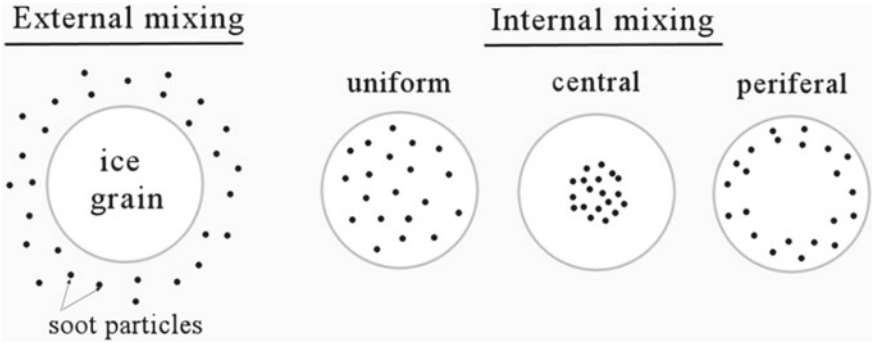

Fig. 10 The schematic of various mixing of ice grains and soot particles. Adopted from (Dombrovsky and Kokhanovsky 2020b)

properties of pure snow (Grenfell and Warren 1999; Libois et al. 2013; Räisänen et al. 2015). It was shown by Dombrovsky et al. (2019) that the GO can be used instead the rigorous Mie theory to calculate the values of absorption efficiency factor and transport albedo of single scattering for large spherical ice grains in the spectral range of interest.

As usually, our model is based on the hypothesis of independent scattering of light by single particles (Tien and Drolen 1987; Tien 1988; Kokhanovsky 2004; Mishchenko et al. 2006; Mishchenko 2014, 2018). The error of this approach is expected to be negligible because both the size of randomly positioned ice grains and the distances between them are much greater that the radiation wavelength. It should be noted that absorption coefficient of snow in the spectral range under consideration does not depend on size of equivalent ice grains. It is known that nonsphericity of ice grains leads to the slight increase in absorption (Kokhanovsky 2004), but this secondary effect is not considered in the present work.

Soot particles are produced usually as a result of incomplete combustion of hydrocarbon fuels. Soot consists of nearly monodisperse spherical primary particles that collect into fractal aggregates having broad size distribution. By combustion of gaseous or liquid fuel, the diameters of primary soot particles are usually in the range between 5 and 80 nm. Much larger particles can be observed in a fuel oil flame. These large particles are considered as a result of thermal decomposition of fuel droplets (Blokh 1988; Xu et al. 2004). The primary soot particles in gas flames are nearly spherical, but these particles grow by agglomeration forming chain-like aggregates.

Soot contains not only carbon but also hydrocarbons and other substances (Wagner 1981). As a result, the optical constants of soot may vary and do not coincide with optical constants of pure amorphous carbon. However, the effect of this difference on absorption coefficient of soot is insignificant (Dombrovsky and Baillis 2010). The airborne soot is an important component of the atmosphere and it is considered as the main component of the snow pollution.

As a rule, atmospheric soot particles are characterized by a strong absorption in the visible spectral range, but the radiation scattering by soot particles is relatively small (Liu et al. 2008; Doner and Liu 2017; Wang et al. 2019). The calculation of radiation absorption by soot containing complex aggregates of primary soot particles is not a simple task. The great uncertainty in the morphology of soot aggregates makes reasonable the use of a simple approximation for physical estimates. Therefore, the Rayleigh approximation for spherical soot particles is employed and the absorption coefficient of soot is calculated as follows (Dombrovsky and Baillis 2010):

$$\alpha_\lambda^{\text{soot}} = B\gamma_\lambda^{\text{soot}} f_{\text{v}}^{\text{soot}},\ B = \frac{9n_{\text{soot}}}{\left(n_{\text{soot}}^2 - \kappa_{\text{soot}}^2 + 2\right)^2 + 4n_{\text{soot}}^2\kappa_{\text{soot}}^2}. \tag{51}$$

where $\gamma_\lambda^{\text{soot}} = 4\pi\kappa_{\text{soot}}/\lambda$ is the bulk absorption coefficient of soot, $f_{\text{v}}^{\text{soot}} = \rho_{\text{soot}}^{\text{cloud}}/\rho_{\text{soot}}$ is the volume fraction of soot ($\rho_{\text{soot}}^{\text{cloud}}$ is the density of the soot cloud, ρ_{soot} is the density of the soot particle substance), n_{soot} and κ_{soot} are the spectral indices of refraction and absorption of soot. The dispersion relation suggested by Dalzell and Sarofim (1969) for the optical constants of soot is used in subsequent calculations.

According to Doherty et al. (2010, 2013), the local value of the mass fraction of soot far from populated areas is less than $s = 0.1$ ppm (or 100 ng/g). However, the value of $s = 0.5$ ppm is also used below to estimate the role of a relatively high pollution.

5.1.2 Internal Mixing Model

The effective medium approximation based on the theory by Maxwell-Garnett (1904) can be employed to determine the effective optical constants of ice containing small soot particles. According to this approach, the complex permittivity of a composite medium in ice grains is calculated in terms of particle polarizability by applying the Lorentz–Lorenz formula (Koledintseva et al. 2009; Markel 2016). The following relations are used to calculate the effective complex index of refraction $m_{\text{eff}} = n_{\text{eff}} - i\kappa_{\text{eff}}$ at the known values of $m = n - i\kappa$ for pure ice and $m_{\text{soot}} = n_{\text{soot}} - i\kappa_{\text{soot}}$ for soot:

$$m_{\text{eff}}^2 = m^2 \frac{2\delta_{\text{soot}}\left(m_{\text{soot}}^2 - m^2\right) + m_{\text{soot}}^2 + 2m^2}{2m^2 + m_{\text{soot}}^2 - \delta_{\text{soot}}\left(m_{\text{soot}}^2 - m^2\right)} \tag{52}$$

where δ_{soot} is the local volume fraction of soot in the ice grain. This designation is used to emphasize that the volume fraction of soot is usually very small. The latter enables us to rewrite Eq. (52) as follows:

$$m_{\text{eff}}^2 = m^2\left(1 + 3\delta_{\text{soot}}\frac{1 - \bar{m}^2}{1 + 2\bar{m}^2}\right),\ \bar{m} = m/m_{\text{soot}} \tag{53}$$

Equation (53) is free of the obvious drawback of Eq. (52) in the case of a combination of two very small values: δ_{soot} and κ. Note that a similar approach based on effective medium approximations was used by Flanner et al. (2012) to determine the optical constants of ice contaminated by soot particles. One cannot exclude that sizes of some soot particles are near the boundary of the Rayleigh region after aging process in the atmosphere (Schwarz et al. 2013; Lim et al. 2014). In this case, one should consider more accurate approach to determine the effective optical properties of the polluted ice (Mishchenko et al. 2000).

In all variants of the spatial distribution of soot particles in snow, the mass concentration of soot is assumed to be the same. It means that the local volume fraction of soot may be different. Let us consider a spherical ice grain with uniform distribution of soot. In this case, the volume fraction of soot in the ice grain is determined as:

$$\delta_{\text{soot}}^{0} = \frac{s}{f_{\text{v}}} \frac{\rho_{\text{ice}}}{\rho_{\text{soot}}} \tag{54}$$

where ρ_{ice} and ρ_{soot} are the densities of ice and soot, $f_{\text{v}} = \rho_{\text{snow}} / \rho_{\text{ice}}$ is the volume fraction of ice in snow (ρ_{snow} is the density of snow). The values of $\rho_{\text{ice}} = 916.7$ kg/m^3, $\rho_{\text{soot}} = 2050$ kg/m^3, and $f_{\text{v}} = 0.33$ are used in subsequent calculations. The physical sense of Eq. (54) is quite clear because the ratio of s / f_{v} is the mass fraction of soot in the ice grain.

It is interesting to consider two cases of nonuniform distribution of soot in a spherical ice grain illustrated in Fig. 10: (1) The same mass of soot is uniformly distributed in the central part, $0 < r < a_{\text{c}}$ ($a_{\text{c}} \leq a$), of the ice grain with radius a; (2) All the soot is in the surface layer of the grain: $a - \Delta < r \leq a$. In these cases, the local value of δ_{soot} increases as follows:

$$\delta_{\text{soot}} = \delta_{\text{soot}}^{0} / \psi \quad \psi = \begin{cases} \bar{a}_{\text{c}}^{3}, & \text{central pollution} \\ 1 - \left(1 - \bar{\Delta}\right)^{3}, & \text{peripheral pollution} \end{cases} \tag{55}$$

where $\bar{a}_{\text{c}} = a_{\text{c}} / a$ and $\bar{\Delta} = \Delta / a$. The values of $\bar{a}_{\text{c}} = 1$ and $\bar{\Delta} = 1$ correspond to the case of the uniformly distributed soot, when $\psi = 1$ and $\delta_{\text{soot}} = \delta_{\text{soot}}^{0}$. In other cases, $\psi < 1$ and $\delta_{\text{soot}} > \delta_{\text{soot}}^{0}$. Obviously, the soot particles increase the effective index of absorption of the polluted parts of ice grains, whereas the effective index of refraction is insensitive to the presence of soot.

5.1.3 Absorption Coefficient of Snow Composed of Ice Grains Containing Soot Particles

The computational estimates have shown that scattering properties of snow containing a small amount of soot are almost the same as those of pure snow, whereas the effect of soot on absorption coefficient of snow in the visible spectral range is significant (Dombrovsky and Kokhanovsky 2019).

It seems natural to begin the analysis from the efficiency factor of absorption of single particles. However, the value of Q_a is directly proportional to the radius a of homogeneous weakly absorbing particles of arbitrary size (Dombrovsky and Baillis 2010). This makes convenient to work with the ratio of Q_a/a. In the case of snow composed of monodisperse spherical grains the spectral absorption coefficient of snow is determined as follows:

$$\alpha_\lambda = 0.75 f_\mathrm{v} Q_\mathrm{a}/a \tag{56}$$

where Q_a can be calculated not only for homogeneous spherical particles considered in the classical Mie theory, but also for centrally symmetric inhomogeneous particles (Bohren and Huffman 1983; Prishivalko et al. 1984; Dombrovsky 1996a; Babenko et al. 2003). To solve a particular problem of the present paper, it is sufficient to consider two-layered spherical particles. It should be recalled that the general analytical solution to the electromagnetic scattering problem for concentric core-mantle spherical particles was derived in 1951 by Aden and Kerker (1951). Practically simultaneously with Aden and Kerker, similar solutions were published by Shifrin (1952) and Güttler (1952). The corresponding analytical solution and computer code can be found also in the monograph by Bohren and Huffman (1983). Some modifications of this code are also freely available. The computer code by Dombrovsky (1996a) was used in subsequent calculations. It should be recalled that a general solution for a multi-layered spherical particle was obtained by Mackowski et al. (1990).

The results of calculations for ice grains containing soot uniformly distributed in the central part or in the concentric surface layer of the grain at the wavelength of $\lambda = 0.5\ \mu\mathrm{m}$ and $s = 0.5$ ppm are presented in Fig. 11. One can see some wave effects at $a = 20\ \mu\mathrm{m}$ and a fast transfer to the geometrical optics limit at $a \approx 50\ \mu\mathrm{m}$ with the universal (independent of a) monotonic dependences of absorption coefficient for the ice grains with $a \geq 50\ \mu\mathrm{m}$. The latter is important because the effective radius of ice grains in a snowpack satisfies usually this condition. As a result, the spectral absorption coefficient of snow containing polydisperse ice grains can be obtained using the above results for the monodisperse model.

It is interesting that α_λ does not depend on $\bar{a}_\mathrm{c}$ in the range of $\bar{a}_\mathrm{c} < 0.75$ and decreases almost linearly at larger values of $\bar{a}_\mathrm{c}$ (Fig. 11a). An effect of a predominant absorption in the central part of symmetrically illuminated large weakly absorbing spherical particles was studied in early papers (Tuntomo et al. 1991; Lai et al. 1991; Choudhury et al. 1992; Lage and Rangel 1993; Velesco et al. 1997). The kick in the absorption profiles at radius of $r = a/n$ was explained by the geometrical optics effects. Moreover, the analysis of evolution of angular distribution of radiation intensity in the particle enabled to suggest a modified differential approximation used in some problems of nonuniform heating or cooling of semi-transparent particles (Dombrovsky 2002b, 2004b; Dombrovsky and Lipiński 2007; Dombrovsky and Dinh 2008).

The monotonic increase in the absorption coefficient with the relative thickness of the polluted surface layer of ice grains is also significant (Fig. 11b). In the case under consideration, we have $\alpha_\lambda = 1.6\ \mathrm{m}^{-1}$ when soot is in a thin surface layer of

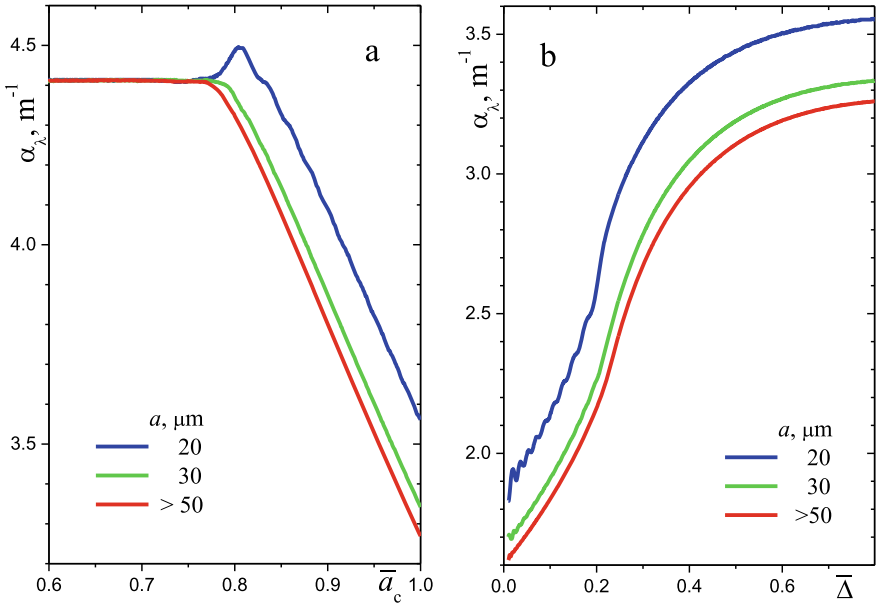

Fig. 11 Absorption coefficient of snow with ice grains containing soot particles (**a**) in the central part or (**b**) in the surface layer of the grain. Adopted from (Dombrovsky and Kokhanovsky 2020b)

the ice grain, $\alpha_\lambda = 3.3\ \mathrm{m}^{-1}$ for the uniform distribution of soot in the grain, and $\alpha_\lambda = 4.4\ \mathrm{m}^{-1}$ when soot is uniformly distributed in the central region of ice particle with radius $a_c < 0.75a$. The difference between the above values should not be ignored in an analysis of absorption of visible radiation in the polluted snow cover.

The above calculations are based on the assumption of a symmetric irradiation of ice grains. Strictly speaking, this assumption is incorrect for the optically thin surface layer of snow. The asymmetric illumination of ice grains can be taken into account using the method developed by Dombrovsky (2004b). However, this more accurate consideration is not necessary because of multiple scattering of visible solar radiation in snow and the resulting transformation of collimated solar radiation to the diffuse radiation in a very thin surface layer of the snow cover.

Let us consider the spectral variation of the absorption coefficient of snow at various assumptions on distribution of soot in the ice grain. The results of calculations in the visible range and in the adjacent part of the near-infrared, where the effect of impurities is also considerable, are presented in Fig. 12. The values of α_λ in this figure are calculated for the volume fraction of ice in snow $f_v = 0.33$, but one can easily determine the absorption coefficient at another value of f_v. It is interesting that Mie theory calculations for ice grains containing soot in a thin surface layer ($\bar{\Delta} = 0.01$) give almost the same absorption coefficient as that obtained for the external mixing of soot. This particular case should be taken into account while using the general statement by Liou et al. (2011) that "light-absorbing particles can absorb more radiation when they are mixed or coated with weakly-absorbing material". At

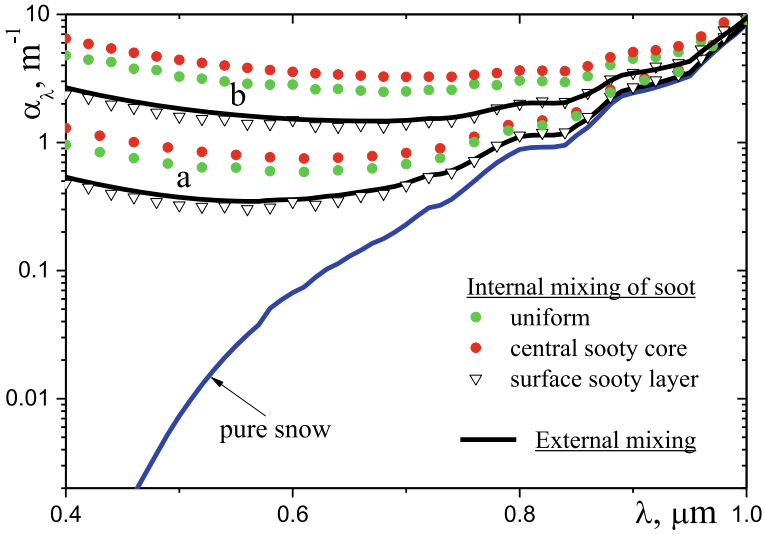

Fig. 12 Effect of soot on absorption coefficient of snow: **a**—s = 0.1 ppm, **b**—s = 0.5 ppm. Adopted from (Dombrovsky and Kokhanovsky 2020b)

the same time, the latter statement is quite correct in the simplest variant of uniform distribution of soot in the ice grain.

5.1.4 Effect of Pollution on Solar Heating and Melting of Snowpack

The effect of vertically inhomogeneous polluted snow (say, due to buried polluted snow layers) on solar heating and possible melting of a snowpack has been studied by Dombrovsky and Kokhanovsky (2019). It seems obvious that an additional solar heating due to absorption of solar radiation in a thin surface layer of not very polluted snow is partially compensated by the convective cooling. However, the additional solar heating may be significant when the layer of a dirty snow is sufficiently thick or positioned at a distance under the surface because of partial thermal protection of deep layers from the convective cooling due low thermal conductivity of snow. It is interesting that some observations in Greenland reported by Doherty et al. (2010, 2013) showed the sharp maximum in concentration of BC positioned at distance of 10 cm under the snowpack surface.

5.1.5 Radiative Transfer in Non-Uniformly Polluted Snowpack

As compared with the general problem of radiative transfer considered in Sect. 2.4, we use two simplifications: the relatively small diffuse radiation from the sky is neglected and the snowpack is assumed to be horizontal (the sloping surface effect is not

considered). These simplifications are physically not important but the authors prefer to focus on computational study of the effect of possible non-uniform impurity of snow on heating and melting of a snowpack. Of course, the analytical solution derived for the uniform snowpack cannot be used. Instead, the numerical procedure based on the finite-difference scheme and factorization method is employed (Dombrovsky and Baillis 2010). This method is applicable for not too optically thick computational region only, but cannot be used over the whole spectrum. To solve the problem, Dombrovsky and Kokhanovsky (2019) suggested a combined computational method based on dividing the whole spectrum in two parts. The numerical solution for a thick layer of snow containing one or several layers of snow with impurities is necessary in the wavelength range of $\lambda < \lambda_* \approx 1$ μm because of the expected absorption of solar radiation in the deep layers. On the contrary, the infrared radiation at $\lambda > \lambda_*$ is absorbed in a thin surface layer even in the case of pure snow. The latter enables us to use the analytical solution for the uniform snowpack of pure snow by ignoring the impurities at larger wavelengths, where absorption is mostly due to bulk ice and not due to the snow impurities.

Of course, one should choose an appropriate value of λ_* and verify the suggested spectral splitting the computational procedure in the combined "two-band" spectral method. The verification can be made using the case of a uniform layer of pure snow. The model heat transfer problem is exactly the same as that considered in Sect. 2.4 for the summer solstice at the local latitude of 70°. It should be noted only that thermal conductivity of snow is taken equal to $k = 0.2$ W/(m K) and the maximum convective heat transfer coefficient in the middle of the day $h_{\max} = 10$ W/(m^2 K), which corresponds to a weak wind of speed less that about 1–2 m/s (Mirsadeghi et al. 2013). The periodic heating and cooling of snow during the day and night may lead to some changes in snow morphology and the resulting changes in both optical properties and thermal conductivity of snow. These effects have been studied by Kaempfer and Plapp (2009), Pinzer et al. (2012), Löwe et al. (2013), and Oldroyd et al. (2013) and we do not consider them in the calculations. It is also assumed that effect of soot on thermal conductivity of snow can be neglected.

The calculated temperature profiles at different time moments during the first day are plotted in Fig. 13 and the three-day variation of the snow surface temperature is presented in Fig. 14. The zenith angle of the sun is less that 90° even in the midnight (at 12 am) because we consider the polar summer conditions. The external mixing of soot with the high value of $s = 1$ ppm is considered. The value of $\lambda_* = 1$ μm was used in the combined model calculations. One can see that the combined "two-band" spectral computational model is sufficiently accurate and can be used to estimate the thermal effects of layered impurities in a snowpack.

The effect of thin but highly polluted ($s = 1$ ppm) layers of snow on profiles of absorbed radiation power in the of $\lambda < \lambda_*$ is illustrated in Fig. 15. The universal coordinates $f_v z$ and P / f_v are used in this figure to present simultaneously the results for various values of f_v. The local increase in absorption coefficient of snow leads to considerable variation of absorbed radiation power in the polluted layers of snow and also in the deeper part of the snowpack.

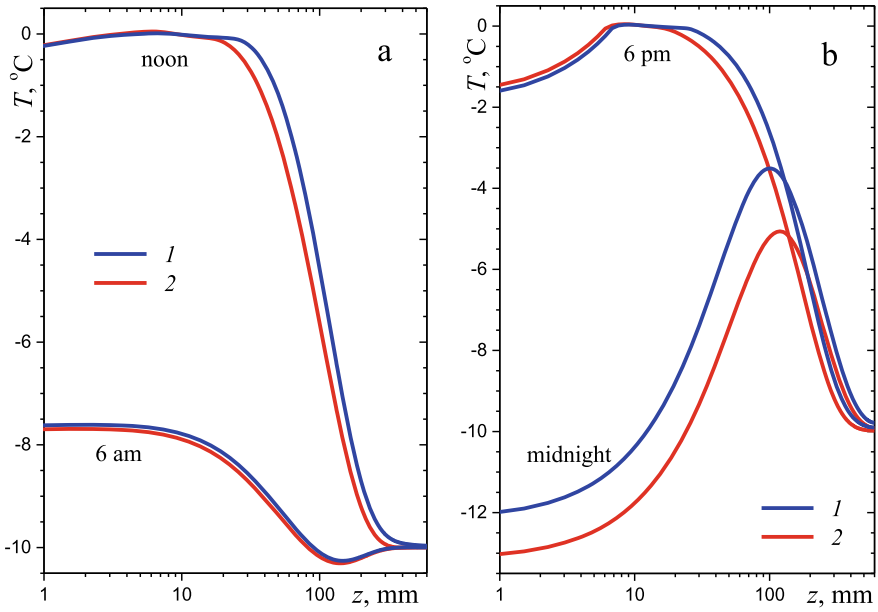

Fig. 13 Typical profiles of temperature in snowpack (**a**) before the noon and (**b**) after the noon: *1*—analytical solution, *2*—combined computational model. Adopted from (Dombrovsky and Kokhanovsky 2019)

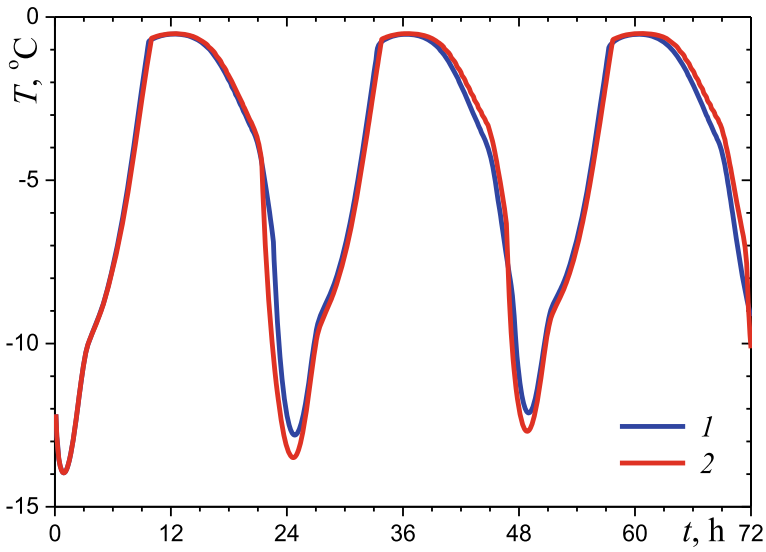

Fig. 14 Time variation of surface temperature of a snowpack: *1*—analytical solution, *2*—combined computational model. Adopted from (Dombrovsky and Kokhanovsky 2019)

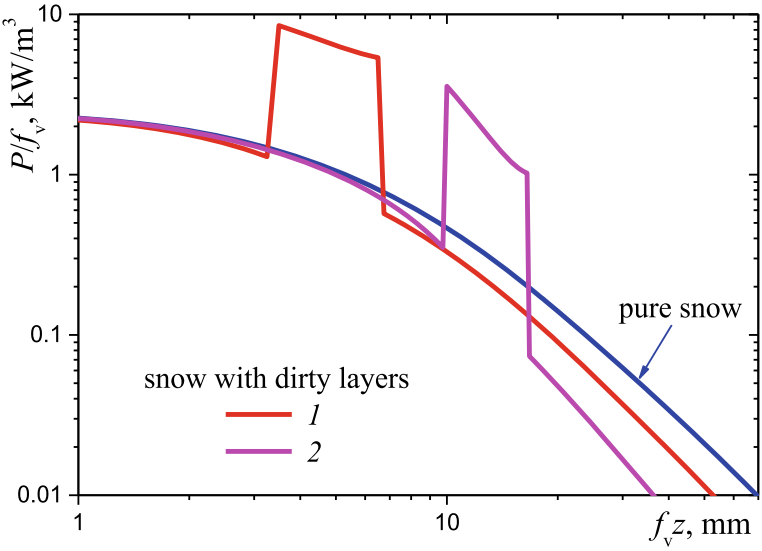

Fig. 15 Effect of single layers of polluted snow on absorbed radiation power in the wavelength range of $\lambda < \lambda_*$ at various positions of the polluted layers: *1*—$3.3 < f_v z < 6.6$ mm, *2*—$9.9 < f_v z < 13.2$ mm

The effect of a single layer of soot-containing snow at $s = 1$ ppm on profiles of temperature in a snowpack at $f_v = 0.33$ is shown in Fig. 16. To minimize the effect of initial conditions, the second day from the beginning of heating is considered.

The calculations show the melting of snow in the internal region of a snowpack at noon and also at 6 pm. The temperature profiles with a deeply positioned maximum at $z \approx 200$ mm are observed at 6 pm. The temperature maximum at the midnight due to intense surface cooling is stronger in the case of a polluted snow.

Note that a similar effect of the periodic formation of relatively warm and, at the same time, sufficiently thick layers in the ice cover leads to significant tensile thermal stresses on the cold surface of ice. As a result, cracks and even large crevices are formed on the surface of glaciers (Lachenbrush 1961; Sanderson 1978). It is interesting to mention that internal absorption of concentrated solar radiation in semi-transparent particles in a solar thermochemical reactor leads also to tensile stresses which may destroy the particle (Dombrovsky and Lipiński 2007).

It should be noted that the latent heat of ice melting results in a considerable delay in snow melting and the so-called mushy zone at the melting temperature is formed during the melting (Huppert 1990; Feltham and Worster 2000; McKenzie et al. 2007). It is also important that heat is accumulated in a snowpack with time and the internal temperature increases day by day.

It would be interesting to validate the above suggested model by comparison with the measurements for both the irradiation and temperature profiles in a snowpack.

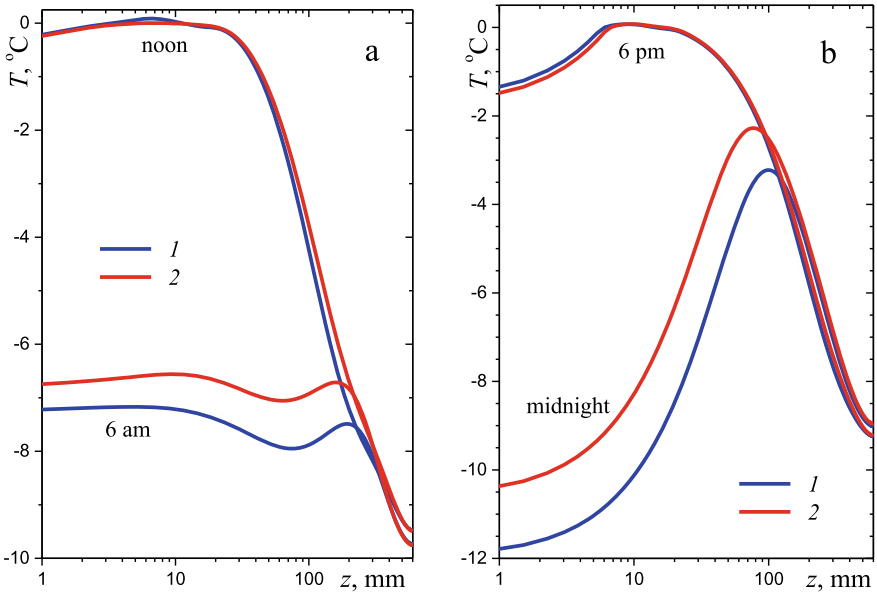

Fig. 16 Effect of internal dirty layer of snow on temperature profiles in a snowpack before the noon and (**b**) after the noon: *1*—pure snow; *2*—snow with polluted layer of $10 < z < 20$ mm

Perhaps, the method of spectral irradiance measurements developed recently by Tuzet et al. (2019) can be used in the experimental work.

The results obtained showed that both the distribution of soot in ice grains and layered pollution of a snowpack affect the absorption of solar radiation and snowpack albedo in the visible range. The local layered impurities of snow may lead to considerable additional heating of deep layers of snow and the resulting accumulation of heat inside the snowpack.

6 Solar Heating of Ice Containing Gas Bubbles

Numerous and diverse gas bubbles, often found in the volume of ice, continue to attract the attention of researchers for many years (Bader 1950; Carte 1961; Carras and Macklin 1975; Schwander and Stauffer 1984; Bender et al. 1997). These bubbles are clearly visible due to intense scattering of visible light. At the same time, the multiple scattering of light by gas bubbles significantly affects the absorption of solar light in semi-transparent ice layers. The study of the resulting increase in surface layer heating of ice sheets containing gas bubbles is one of the important tasks of geophysics. The radiative transfer in light-scattering ice have been studied in detail for more than four past decades (Gilpin et al. 1977; Seki et al. 1979; Perovich and Grenfell 1982; Grenfell 1983,1991; Mobley et al. 1998; McGuinness et al. 2001;

Timofeev 2018; Sleptsov and Savvinova 2019). The ice heating and even melting due to absorbed external radiation was also considered in some of these papers. The volumetric absorption of solar light is sometimes characterized by non-monotonic profiles of radiative heating of ice sheets. In some cases, this internal heating may lead to strong tensile stresses and the resulting big cracks at the surface of ice sheets.

It should be recalled that the presence of gas bubbles in various semi-transparent media affects the optical and thermal properties of such two-phase systems and hence the transport phenomena. One can mention the influence of bubbles on scattering of light in the near-surface layer of the ocean (Zhang et al. 1998; Yan et al. 2002; Soloviev and Lukas 2014; Stamnes et al. 2017), the effect of bubbles generated by chemical reactions during the glass melting in the industrial furnaces (Shelby 2005; Van der Schaaf and Beerkens 2006; Hrma 2009), and the optical properties of solid glass containing bubbles (Pilon and Viskanta 2003; Dombrovsky et al. 2005). Aerogels or other materials with numerous bubbles or hollow microspheres in semi-transparent host media are considered as advanced thermal insulations (Richter et al. 1995; German and Grinchuk 2002; Papadopoulos 2005; Dombrovsky 2005; Dombrovsky et al. 2007a; Thapliyal and Singh 2014). In some cases, the pores in low-porous ceramics can be modeled as spherical gas bubbles (Manara et al. 1999; Lisitsyn et al. 2016). It was shown by Dombrovsky (2004a) that the role of steam bubbles is considerable in radiative heating of boiling water. In this regard, it should be recalled that the problem of the fuel-coolant interaction (FCI) in a hypothetical severe accident of nuclear reactors involves the near-infrared radiative heating of water containing numerous bubbles (Dombrovsky 2007, 2009; Dombrovsky et al. 2009; Dombrovsky and Davydov 2010).

The methodological basis of recent study by Dombrovsky and Kokhanovsky (2020c) on ice containing gas bubbles includes three physical problems: (1) determination of the optical properties of ice containing gas bubbles, (2) spectral calculation of solar radiation transfer in a layer of the light scattering ice (Seki et al. (1979) called this ice as "cloudy ice"), and (3) the solution to heat transfer problem to determine the transient temperature profile in the ice sheet. The above problems can be solved using the known analytical or numerical methods, so that the construction of a general computational model does not require special methodological developments. At the same time, the choice of particular approaches is limited by the main objective of the work, which is a qualitative analysis of the influence of the size and volume fraction of gas bubbles on heating of ice at a large distance under the surface, when the volumetric solar heating becomes insensitive to conditions of convective heat transfer at the ice sheet surface.

The computational study is significantly simplified by using an analytical solution for the absorbed radiation power, since the numerical solution of the radiative transfer problem in an optically thick layer of the scattering medium is associated with mathematical difficulties. Therefore, the physical problem statement contains a number of assumptions concerning both the optical properties of "cloudy ice" and the solar radiation transfer in ice sheets.

The most important simplification is associated with multiple scattering of light in ice sheets in the spectral range of semi-transparency. In addition, the large optical

thickness of the medium leads to a relatively simple angular dependence of the radiation intensity, which allows a transition from the RTE to one of the differential approximations, as was done, for example, in (Gilpin et al. 1977; Perovich and Grenfell 1982; Sleptsov and Savvinova 2019; Dombrovsky and Kokhanovsky 2020c). However, one should take into account the effect of total internal reflection on the ice/air interface.

Strictly speaking, even for the conditions of the polar summer, the time variation of solar zenith angle should not be ignored. Such calculations were carried out by Dombrovsky et al. (2019) and Dombrovsky and Kokhanovsky (2019) in more detailed computational analysis of solar heating of a snowpack. In the case of ice sheet containing gas bubbles, we restrict ourselves to calculations for the Sun at its zenith. Moreover, instead of a complex spectrum of solar radiation transmitted through the atmosphere, for a qualitative study of this work, the smooth Planck spectrum is considered.

6.1 Optical Properties of Ice Containing Numerous Gas Bubbles

The spectral properties of pure ice without any inclusions were discussed in the present paper (see Fig. 1). Note that the near-ultraviolet range may be also important for the phytoplankton growth beneath sea ice (Hill et al. 2018) and the data by Warren et al. (2006) for index of absorption in the near-ultraviolet should be also considered.

The geometrical optics can be used to study the optical properties of gas bubbles and other spherical inclusions with large diffraction parameter also in the case of the relative refractive index below unity. One should mention the early paper by Davis (1955) and the recent study by Malinka et al. (2018) on this subject.

Small gas bubbles in ice are usually spherical. The elongated bubbles are also observed in ice sheets. However, these bubbles elongated by strain return to their spherical shape by diffusive processes (Alley and Fitzpatric 1999). Therefore, only spherical bubbles are considered below. Moreover, for simplicity, it is assumed that all the bubbles have the same size. The radius of bubbles is assumed to be much greater than the wavelength (the diffraction parameter $x >> 1$). The absorption coefficient and transport scattering coefficient of ice containing such bubbles can be calculated as follows (Dombrovsky 2004a):

$$\alpha_\lambda = (1 - f_\mathrm{v})\alpha_\lambda^0, \;\; \sigma_\lambda^\mathrm{tr} = \sigma_\lambda(1 - \bar{\mu}_\lambda) = 0.75 f_\mathrm{v} Q_\mathrm{s}^\mathrm{tr} \big/ a \tag{57}$$

where f_v is the volume fraction of bubbles, $\alpha_\lambda^0 = 4\pi\kappa \big/ \lambda$ is the absorption coefficient of ice without bubbles. It is interesting to note that the above equations agree totally with a simple physical approach applicable to many optically soft semi-transparent materials of different nature. This approach is based on the following principles formulated by Dombrovsky and Baillis (2011) and Dombrovsky et al. (2011a):

1. The absorption coefficient is independent of the material morphology. It is directly proportional to the volume fraction of the absorbing substance in a porous material: $\alpha_\lambda = \alpha_\lambda^0(1-p)$, where α_λ^0 is the absorption coefficient of bulk material of the same chemical composition and p is the porosity.
2. The scattering is insensitive to a weak absorption and can be predicted by an analysis of the material morphology.

There are many materials which optical properties satisfy the above principles. Some examples can be found in (Dombrovsky et al. 2005, 2007a, 2011a; c, 2018a; Ganesan et al. 2013; Baillis et al. 2013; Hakoume et al. 2014; Lisitsyn et al. 2016; Bashkatov et al. 2016; Tuchin 2017).

A relative mutual independence of absorption and scattering is not a specific property of semi-transparent porous materials. This is a general behavior of disperse systems containing optically soft particles satisfying the conditions of the Rayleigh–Gans theory (Van de Hulst 1981; Bohren and Huffman 1983). However, it was demonstrated by Dombrovsky et al. (2010) that there are some cases when scattering really depends on absorption. Of course, the spatially uniform absorption cannot lead to the radiation scattering. On the contrary, appearance of strongly absorbing regions comparable in size with the wavelength may lead to an additional scattering. In all cases, the different physical nature of absorption and scattering makes reasonable a separate analysis of the experimental data for absorption coefficient and transport scattering coefficient. Some researchers prefer to use the sum of these values (transport extinction coefficient) in combination with the single-scattering transport albedo of the medium instead of the mentioned physical quantities. This approach makes it difficult to analyze important physical effects such as the so-called "scattering by absorption" (Dombrovsky et al. 2010; Hakoume et al. 2014).

Obviously, $f_\mathrm{v} << 1$ in the case of ice containing small bubbles and one can consider α_λ^0 instead of α_λ in this particular problem. The absorption coefficient of ice is very small in the near-ultraviolet and visible ranges but increases strongly with the wavelength. So, the ice layer of thickness more than 1–2 mm is almost opaque in the wavelength range of $\lambda > 1.4\ \mu\mathrm{m}$.

Let us consider the effect of bubbles on the transport efficiency factor of scattering of gas bubbles in ice at the wavelength $\lambda < 0.8\ \mu\mathrm{m}$, where the scattering is expected to be more important. The index of refraction of ice in this spectral range is not close to unity. Therefore, the approximation of optically soft host medium (when $n-1 << 1$) considered in some papers is not appropriate. A series of the Mie theory calculations reported by Dombrovsky (2004a) and Dombrovsky et al. (2005) showed that absorption has almost no effect on scattering of radiation by bubbles in a weakly absorbing host medium, and it is sufficient to consider the dependences of $Q_\mathrm{s}^\mathrm{tr}(x)$ for $\kappa = 0$.

The calculations at indices of refraction from $n = 1.2$ to 1.5 showed that Q_s^tr is approximately constant when $x > 20$ and its value in the range of geometrical optics can be estimated as follows:

$$Q_\mathrm{s}^\mathrm{tr} = 0.9\,(n-1) \tag{58}$$

The resulting equations for the absolute and relative scattering coefficients are:

$$\sigma_\lambda^{\mathrm{tr}} = 0.675\,(n-1)\,f_{\mathrm{v}}\big/a,\;\; \sigma_\lambda^{\mathrm{tr}}\big/\alpha_\lambda = 0.3375\,f_{\mathrm{v}}(n-1)\big/(\kappa x), \tag{59}$$

Obviously, the radiation scattering is predominant at $f_{\mathrm{v}} > 10\kappa x$. Note that the asymmetry factor of scattering is the same for all large bubbles and this value can be approximated as:

$$\bar{\mu}_\lambda = 1 - 0.45(n-1) \tag{60}$$

The above results for radiation scattering by bubbles and the effect of bubbles on radiation absorption have been used by Dombrovsky et al. (2005) for fused quartz containing gas bubbles, in radiative heat transfer analysis for water containing steam bubbles (Dombrovsky 2004a, 2007, 2009; Dombrovsky et al. 2009; Dombrovsky and Davydov 2010), and as a limiting solution for thin-wall glass microspheres in a polymer matrix (Dombrovsky 2005; Dombrovsky et al. 2007a).

As a verification of the above analytical approximation, one can consider the results of more accurate calculations ("without the phase interferences") at $n = 4\big/3$ reported by Wu et al. (2007):

$$Q_{\mathrm{s}} = 1.9997\;\bar{\mu}_\lambda = 0.8444 \tag{61}$$

Note that the above value of $\bar{\mu}_\lambda$ is exactly the same as that obtained analytically by Warren et al. (2006) and one can obtain $Q_{\mathrm{s}}^{\mathrm{tr}} = 0.311$, whereas Eq. (59) gives $Q_{\mathrm{s}}^{\mathrm{tr}} = 0.3$. At the same index of refraction, Eq. (60) gives $\bar{\mu}_\lambda = 0.85$ which is also close to the exact value.

As was noted above, the solution under consideration is applicable only in the spectral ranges where the host medium is semi-transparent. In the opacity range, where the medium is strongly absorbing, the radiative transfer problem degenerates and there is no any reason to study the volumetric radiative characteristics of the medium containing bubbles. It means that heat transfer modeling should be based on quite different approaches for the spectral regions of the medium semi-transparency and opacity.

Coming back to the particular problem of pure ice containing gas bubbles, consider some results of spectral calculations using the Mie theory for very small bubbles. The value of $\bar{Q}_{\mathrm{s}}^{\mathrm{tr}}$, which is a ratio of $Q_{\mathrm{s}}^{\mathrm{tr}}$ to the approximate value given by Eq. (58), is presented in Fig. 17a. Most likely, Eq. (58) is applicable in the wavelength range of $\lambda < 0.8$ μm for all the bubbles with radius of $a > 10$ μm. Moreover, the error of this equation is less than 5% even at $a = 5$ μm. It is interesting also to consider the ratio of $\sigma_\lambda^{\mathrm{tr}}\big/\alpha_\lambda$ for more realistic radius of gas bubbles. The results of calculations at $a = 50$ μm and two different volume fractions of gas bubbles are shown in Fig. 17b. In the near-ultraviolet and in the main part of the visible range, the transport scattering coefficient of ice with bubbles is greater than the absorption coefficient.

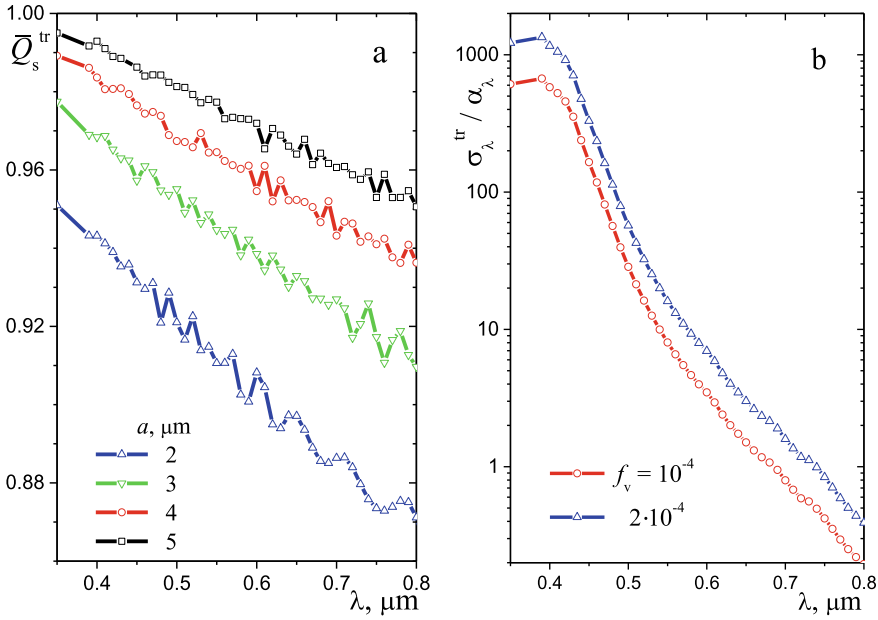

Fig. 17 Mie theory calculations of for ice containing bubbles with radius 50 μm: **a**—the correction factor to the transport efficiency factor of scattering, **b**—the ration of the transport scattering coefficient to the absorption coefficient. Adopted from (Dombrovsky and Kokhanovsky 2020c)

Note that the above optical model for gas bubbles in ice is based on the hypothesis of independent scattering of light by single particles. The error of this approach is expected to be negligible when both the size of randomly positioned bubbles and the distances between them are much greater that the wavelength of solar light.

6.2 Absorption of Solar Radiation in Scattering Ice Sheet

According to Eq. (2.59), the only parameter of gas bubbles that affects the light scattering in ice is the "scattering parameter" $S = f_v / a$ measured in m^{-1}. This simplifies the analysis of computational results. The calculated profiles of $\bar{p}(z, \lambda) = \alpha_\lambda(z)\bar{G}_\lambda(z)$ at several wavelengths in the visible range are presented in Fig. 18. The strong increase in the index of absorption of ice with the wavelength is responsible for the absorption of radiation even in the range of $0.6 < \lambda < 0.7$ μm. The increase in both the wavelength and scattering parameter leads to a smaller penetration depth of incident radiation.

Relative contributions of different spectral ranges to the solar radiation absorption in ice with bubbles can be estimated assuming that the spectrum of solar radiation is similar to that of the blackbody at temperature $T_{sol} = 6000$ K. It is sufficient to

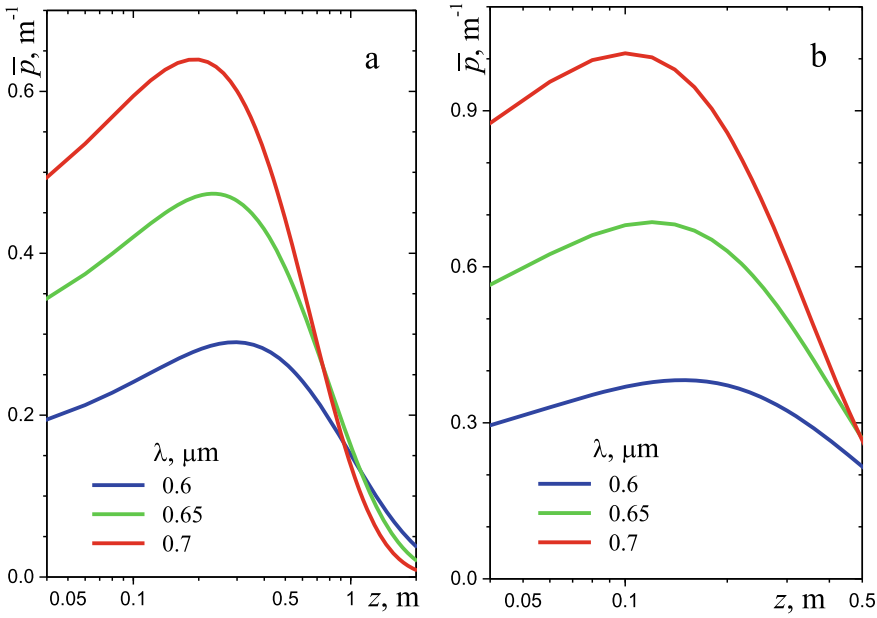

Fig. 18 Normalized profiles of absorbed spectral radiation power: **a**—$S = 20$ m^{-1}, **b**—50 m^{-1}. Adopted from (Dombrovsky and Kokhanovsky 2020c)

compare the following two profiles:

$$\bar{P}_1(z) = \frac{1}{P_0}\int_{\lambda_{11}}^{\lambda_{12}} \bar{p}(z,\lambda)\, I_{\lambda,\mathrm{b}}(T_{\mathrm{sol}})\, \mathrm{d}\lambda \quad \bar{P}_2(z) = \frac{1}{P_0}\int_{\lambda_{12}}^{\lambda_{22}} \bar{p}(z,\lambda)\, I_{\lambda,\mathrm{b}}(T_{\mathrm{sol}})\, \mathrm{d}\lambda \tag{62}$$

where $P_0 = \int_{\lambda_{11}}^{\lambda_{22}} I_{\lambda,\mathrm{b}}(T_{\mathrm{sol}})\, \mathrm{d}\lambda$, $\lambda_{11} = 0.35$ μm, $\lambda_{12} = 0.8$ μm, $\lambda_{22} = 2.778$ μm. The function $\bar{P}_1(z)$ corresponds to a contribution of the near-ultraviolet and visible ranges, whereas $\bar{P}_2(z)$ characterizes a contribution of the near-infrared range. The results of calculations presented in Fig. 19a indicate that infrared radiation contributes strongly to the absorption of solar radiation in a thin surface layer of the ice sheet, whereas the volumetric absorption of radiation at distances more than about 25 cm from the surface is determined by a contribution of the short-wavelength range. As one can expect, the latter effect depends strongly on the scattering parameter. Note that the absolute values of the absorbed radiation power presented in Fig. 19b were calculated at the approximate value of $q_0 = 1$ kW/m^2 for the incident radiative flux at the ice sheet surface.

The calculations show that the radiation at $\lambda = 1.4$ μm is almost totally absorbed in the surface layer of thickness $d_{\mathrm{surf}} = 1$ mm, whereas $d_{\mathrm{surf}} = 1/\alpha_\lambda \approx 0.1$ mm at $\lambda = 2.5$ μm. It means that the heat transfer analysis can be based on the assumption that the infrared radiation in the range of $\lambda > 1.4$ μm is absorbed just on the surface

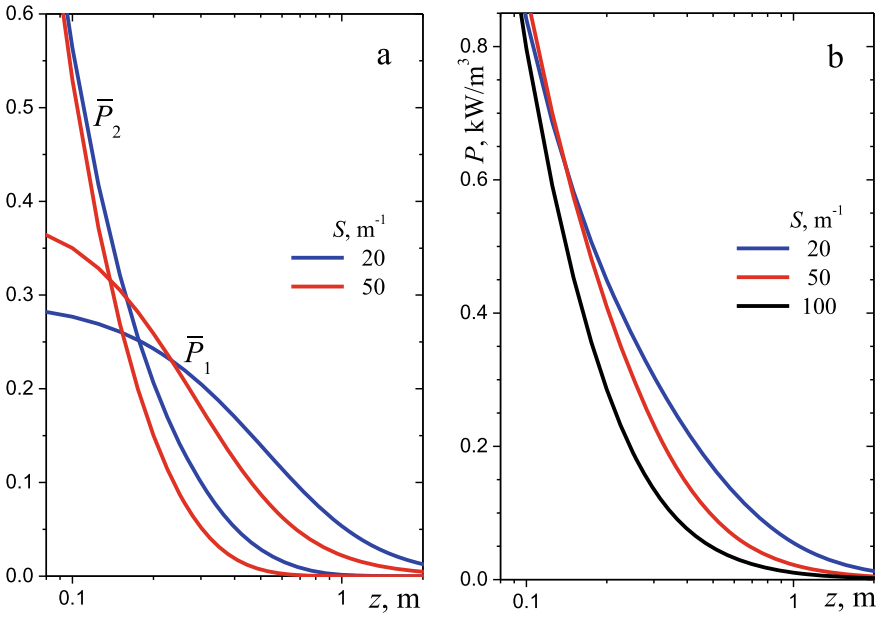

Fig. 19 Absorption of solar radiation in ice sheet containing gas bubbles: **a**—relative contribution of two spectral ranges, **b**—profiles of total absorbed power. Adopted from (Dombrovsky and Kokhanovsky 2020c)

of ice sheet. This will be taken into account in mathematical formulation of heat transfer problem by a separate consideration of the radiative flux absorbed at the surface and the radiation power absorbed in the volume of ice sheet.

It was found in recent paper by Dombrovsky and Kokhanovsky (2020c) that specific spectral properties of ice containing gas bubbles affect considerably the normal-hemispherical reflectance, R_{n-h}, of an ice sheet. First of all, it should be noted that the spectral dependences of R_{n-h} in the visible range are strong and quite different from those for albedo of pure and polluted snow. It is also interesting that the scattering parameter of a thick ice sheet not covered by snow can be estimated using the measurements of R_{n-h} in the wavelength range of $0.5 < \lambda < 0.65$ μm. In addition, one to distinguish the colors of ice sheets with quite different values of scattering parameter. The color of ice sheet observed from above is expected to change from the violet to blue with the increase of scattering parameter. In connection with the discussed change in the colour of ice due to light scattering, the recent papers by Warren et al. (2019) and Warren (2019b) should be mentioned. However, the observed green colour of icebergs has received another physical explanation.

6.3 The Case Study for Solar Heating of Ice Sheet

The 1-D transient energy equation for temperature, $T(t, z)$, in the ice layer of thickness d and the accompanying initial and boundary conditions can be written as follows:

$$\rho c \frac{\partial T}{\partial t} = \frac{\partial}{\partial z}\left(k \frac{\partial T}{\partial z}\right) + (1-\zeta)P, \ t > 0, \ 0 < z < d \tag{63a}$$

$$T(0, z) = T_0, \ z = 0, \ -k\frac{\partial T}{\partial z} = h\,(T_\mathrm{e} - T) + \zeta q_0, \ z = d, \ \frac{\partial T}{\partial z} = 0 \tag{63b}$$

where ρc and k are the specific volumetric heat capacity and the thermal conductivity of ice, $T_\mathrm{e}(t)$ is the temperature of air flow outside the thermal boundary layer, $h(t)$ is the convective heat transfer coefficient. The condition of thermal insulation at the boundary $z = d$ means that we neglect heat transfer by conduction at $z > d$. The value of ζq is the radiative flux of the infrared solar radiation absorbed in a thin surface layer, whereas the term $(1-\zeta)P(z)$ is the absorbed power of the short-wave radiation, where the coefficient $\zeta < 1$ is determined as:

$$\zeta(\lambda_*) = \int_{\lambda_*}^{\lambda_{22}} I_{\lambda,\mathrm{b}}(T_\mathrm{sol})\,\mathrm{d}\lambda \Bigg/ \int_{\lambda_{11}}^{\lambda_{22}} I_{\lambda,\mathrm{b}}(T_\mathrm{sol})\,\mathrm{d}\lambda \tag{64}$$

The values of $\lambda_* = 1.4$ μm and $\zeta = 0.118$ are used in subsequent calculations.

When solving the model problem, the calculations can be carried out at constant values of thermal properties of ice from the literature (Fukusako 1990): $k = 2.3$ W/(m K) and $\rho c = 1.84$ MJ/(m^{3}K). Strictly speaking, the temperature dependences of these properties should be taken into account in numerical calculations, but this is not important for the qualitative analysis of the problem. In the case problem, the following parameters are considered: $T_0 = -10$ °C, $T_\mathrm{e} = -20$ °C, and the heat transfer coefficient of $h = 20$ W/(m^2 K) which corresponds to a moderate wind of speed about 4 m/s (Defraeye et al. 2011; Mirsadeghi et al. 2013). The calculations using the implicit finite-difference procedure were performed for the solar irradiation of ice sheet of thickness $d = 1$ m during three hours. The numerical results obtained at various values of the scattering parameter are presented in Fig. 20. The convective cooling of ice sheet by a wind of relatively cold air leads to the fact that the maximum temperature is not on the surface of irradiated ice sheet, but at a distance of about 6–7 cm below the surface. The position of this maximum of temperature is weakly sensitive to the scattering parameter, but the value of T_max increases considerably with S and may reach the melting temperature in about 7 h at $S = 50$ m^{-1}.

Figure 20 indicates that gas bubbles in ice affect considerably the internal overheating of an ice sheet. At the same time, it should be mentioned that the model problem considered is very simplified. The most important simplification is the absence of a snow layer at the ice sheet surface. The highly scattering snow cover

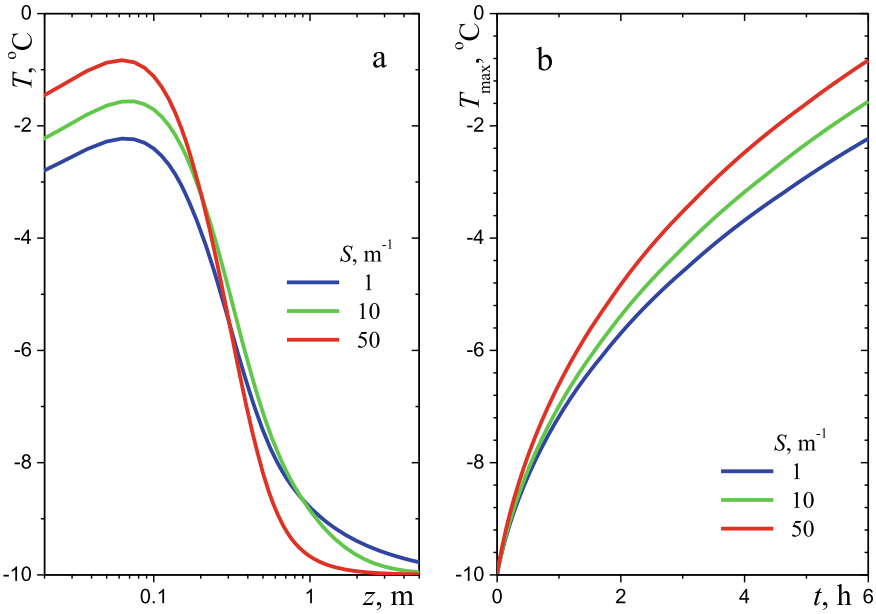

Fig. 20 Effect of scattering parameter on (**a**) temperature profiles in ice sheet at $t = 6$ h and (**b**) the maximum temperature of ice. Adopted from (Dombrovsky and Kokhanovsky 2020c)

will prevent penetration of visible radiation to the ice sheet. It this case, the effect of gas bubbles on solar heating of ice will be not as strong as that in the above model problem.

It is known that a collimated irradiation of semi-transparent scattering media leads to considerable volumetric absorption of the radiation. Moreover, the maximum of the radiation absorption can be observed at a distance from the irradiated surface. This effect is explained by a relatively strong absorption of the diffuse radiation formed due to multiple scattering in the medium. In particular, non-monotonic profiles of absorbed radiative power can be observed in the case of weakly absorbing media like atmospherics clouds or mists in the visible range or some dry biological tissues in the visible and near-infrared ranges.

In the case of a scattering ice sheet, the maximum temperature at a distance from the ice-air interface leads to tensile stresses at the open surface of the sheet. A similar effect has been predicted and estimated even for small particles under concentrated solar irradiation in solar thermochemical reactors (Dombrovsky and Lipiński 2007). There are several cases when the relatively warm ice layers may lead to surface cracks on the ice sheet surface. The known example is the cracking of sea ice when the air temperature drops below the water temperature under the floating ice sheet (Evans and Untersteiner 1971). The optical properties of light-scattering ice affect the periodic heating and cooling of a surface layer of glaciers that is important for their complex behaviour.

The theoretical estimates showed that small gas bubbles may lead to a considerable additional heating of ice at several centimeters below the ice-sheet surface. Both the computational model and the reported numerical analysis are considered by the authors as a basis of more comprehensive modeling of solar heating of various ice sheets with account for the effect of a snow cover and specific optical and thermal properties of continental ice and sea ice. In particular, in some cases one also needs to account for other absorbing and scattering particulate matter in ice such as brine, microalgae, soot particles, and dust inclusions (Light 2010; Cook et al. 2017; Courville et al. 2020; Di Mauro et al. 2020; Williamson et al. 2020).

7 Conclusion

The computational model based on the approximate analytical solution of the spectral radiative transfer equation and also on the numerical solution of the transient heat transfer problem enables the authors to obtain some new physically sound results for solar heating and possible melting of pure and polluted snow and also ice sheets as applied to summer conditions in polar regions of our planet. The numerical analysis indicated a deep heating of snowpack by combined action of the visible solar light and heat conduction. At the same time, the near-infrared solar heating of snow surface is partially compensated by the cooling effect of a cold wind. A contribution of middle-infrared radiative cooling to the surface temperature of snow appears to be also important. It is interesting that possible nonuniform pollution of ice grains may lead to significantly different values of absorption coefficient of snow cover in the visible range. The maximum absorption is predicted in the case of soot positioned in the central part of ice grains. The calculations showed that the main solar heating of ice containing gas bubbles takes place at a distance of several centimetres below the ice-sheet surface and the maximum heating increases with the scattering parameter which is a ratio of volume fraction of gas bubbles to their mean size.

The authors hope that both the developed methods and particular findings reported in this work will be useful for the researchers involved in studies of solar light interaction with snow and ice sheets.

Acknowledgements Leonid Dombrovsky is grateful to the Russian Foundation for Basic Research (Grant No. 19-08-00238a) for the financial support of the present work. The work of Alexander Kokhanovsky has been supported by the European Space Agency (ESRIN contracts 4000118926/16/I-NB and 4000125043 - ESA/AO/1-9101/17/I-NB).

References

Aden AL, Kerker M (1951) Scattering of electromagnetic waves from two concentric spheres. J Appl Phys 22(10):1242–1246

Adrianov VN (1972) Fundamentals of radiative and combined heat transfer. Energiya, Moscow (in Russian)

Adzerikho KS, Antsulevich VI, YaK Lapko, Nekrasov VP (1979) Luminescence of two-phase inhomogeneous media of cylindrical geometry. Int J Heat Mass Trans 22(1):131–136

Alley RB, Fitzpatric JJ (1999) Conditions for bubble elongation in cold ice-sheet ice. J Glaciol 45(149):147–153

Aoki T, Aoki T, Fukabori M, Hachikibo A, Tashibana Y, Nishio F (2000) Effects of snow physical parameters on spectral albedo and bidirectional reflectance of snow surface. J Geophys Res Atmos 105(D8):10219–10236

Aoki T, Kuchiki K, Kodama Y, Hosaka M, Tanaka T (2011) Physically based snow albedo model for calculating broadband albedos and the solar heating profile in snowpack for general circulation models. J Geophys Res Atmos 116:D11114

Arenson LU, Colgan W, Marshall HP (2015) Physical, thermal, and mechanical properties of snow, ice, and permafrost, Chapter 2 in "Snow and Ice-Related Hazards, Risk and Disasters", 35–75

Babenko VA, Astafieva LG, Kuzmin VN (2003) Electromagnetic Scattering in Disperse Media. Inhomogeneous and Anisotropic Particles. Praxis, New York

Bader H (1950) The significance of air bubbles in glacier ice. J Glaciol 1(8):443–451

Baillis-Doermann D, Sacadura J-F (2000) Thermal radiation properties of dispersed media: Theoretical prediction and experimental characterization. J Quant Spectrosc Radiat Trans 67(5):327–363

Baillis D, Coquard R, Randrianalisoa JH, Dombrovsky LA, Viskanta R (2013) Thermal radiation properties of highly porous cellular foams. Special Topics & Reviews Porous Media 4(2):111–136

Barry RG, Hall-McKim EA (2018) Polar environments and global change. Cambridge University Press, Cambridge (UK)

Bashkatov AN, Genina EA, Tuchin VV (2016) Tissue optical properties. In: Boas DA, Pitris C, Ramanujam N (eds) "Handbook of Biomedical Optics", Chapter 5. CRC Press, New York, pp 67–100

Belov GYa (1982) Effectiveness of backward scattering model in the radiation transfer theory in media with axisymmetrical scattering functions. High Temper 20(6):1102–1109

Bell GI, Hansen GE, Sandmeier HA (1967) Multitable treatment of anisotropic scattering in SN multigroup transport calculations. Nucl Sci Eng 28(3):376–383

Bender M, Sowers T, Brook E (1997) Gases in ice cores. Proc Natl Acad Sci USA 94(16):8343–8349

Bi L, Yang P, Kattawar GW, Hu Y, Baum BA (2011) Scattering and absorption of light by ice particles: solution by a new physical-geometrical optics hybrid method. J Quant Spectrosc Radiat Trans 112(9):1492–1508

Blokh AG (1988) heat transfer in steam boiler furnaces. Hemisphere, New York

Bobcôo RP (1967) Directional emissivities from a two-dimensional, absorbing-scattering medium: the semi-infinite slab. ASME J Heat Trans 89(4):313–320

Bohren CF, Huffman DR (1983) Absorption and scattering of light by small particles. Wiley, New York

Born M, Wolf E (1999) Principles of optics, Seventh (expanded) edition. Cambridge University Press, New York

Brandt RE, Warren SG (1993) Solar-heating rates and temperature profiles in Antarctic snow and ice. J Glaciol 39(131):99–110

Brandt RE, Warren SG, Clarke AD (2011) A controlled snow-making experiment testing the relation between black carbon content and reduction of snow albedo. J Geophys Res Atmos 116(D8):D08109

Borovoi A, Konoshonkin A, Kustova N (2014) The physical-optics approximation and its application to light backscattering by hexagonal ice crystals. J Quant Spectrosc Radiat Trans 146:181–189

Calonne N, Flin F, Morin S, Lesaffre B, du Roscoat SR, Geindreau C (2011) Numerical and experimental investigations of the effective thermal conductivity of snow. Geophys Res Lett 38(23):L23501

Carras JN, Macklin WC (1975) Air bubbles in accreted ice. Quart J Royal Met Soc 101(427):127–146

Carte AE (1961) Air bubbles in ice. Proc Phys Soc 77(3):757–67

Case KM, Zweifel PF (1967) Linear transport theory. Addison-Wesley, Reading, MA

Chen Z, Zhu L, Raman A, Fan S (2016) Radiative cooling to deep sub-freezing temperatures through a 24-h day-night cycle. Nat Commun 7:13729

Choudhury DQ, Barber PW, Hill SC (1992) Energy-density distribution inside large nonabsorbing spheres by using Mie theory and geometrical optics. Appl Opt 31:3518–3523

Chýlek P, Ramaswamy V, Srivastava V (1983) Albedo of soot-containing snow. J Geophys Res Oceans 88(C15):10837–10843

Cook JM, Hodson AJ, Taggart AJ, Mernild SH, Tranter M (2017) A predictive model for the spectral "bioalbedo" of snow. J Geophys Res Earth Surf 122(1):434–454

Courville ZR, Lieblappen RM, Thurston AK, Barbato RA, Fegyveresi JM, Farnsworth LB, Derry J, Jones RM, Doherty SJ, Rosten SA (2020) Microorganisms associated with dust on Alpin snow. Front Earth Sci 8:122

Crosbie AL, Davidson GW (1985) Dirac-delta function approximation to the scattering phase function. J Quant Spectrosc Radiat Trans 33(4):391–409

Dalzell WH, Sarofim AP (1969) Optical constants of soot and their application to heat-flux calculations. ASME J Heat Trans 91(1):100–104

Dang C, Brandt RE, Warren SJ (2015) Parametrization for narrowband and broadband albedo of pure snow and snow containing mineral dust and black carbon. J Geophys Res Atmos 120(11):5446–5468

Davis GE (1955) Scattering of light by an air bubble in water. J Opt Soc Am 45(7):572–581

Davison B (1957) Neutron transport theory. Oxford University Press, London

Defraeye T, Blocken B, Carmeliet J (2011) Convective heat transfer for exterior building surfaces: Existing correlations and CFD modelling. Energy Convers Manag 52(1):512–522

Di Mauro B, Garzonio R, Baccolo G, Franzetti A, Pittino F, Leoni B, Remias D, Colombo R, Rossini M (2020) Glacier algae foster ice-albedo feedback in the European Alps. Sci Rep 10(1):4739

Doherty SJ, Warren SG, Grenfell TC, Clarke AD, Brandt RE (2010) Light-absorbing impurities in Arctic snow. Atmos Chem Phys 10(23):11647–11680

Doherty SJ, Warren SG, Forsström S, Hegg DL, Brandt RE, Warren SG (2013) Observed vertical redistribution of black carbon and other insoluble light-absorbing particles in melting snow. J Geophys Res Atmos 118(11):1–17

Dombrovsky LA (1996a) Radiation heat transfer in disperse systems. Begell House, New York

Dombrovsky LA (1996b) Approximate methods for calculating radiation heat transfer in dispersed systems. Therm Eng 43(3):235–243

Dombrovsky LA (1997) Evaluation of the error of the P1 approximation in calculations of thermal radiation transfer in optically inhomogeneous media. High Temper 35(4):676–679

Dombrovsky LA (2000) Thermal radiation from nonisothermal spherical particles of a semitransparent material. Int J Heat Mass Trans 43(9):1661–1672

Dombrovsky LA (2002a) Spectral model of absorption and scattering of thermal radiation by droplets of diesel fuel. High Temper 40(2):242–248

Dombrovsky LA (2002b) A modified differential approximation for thermal radiation of semitransparent nonisothermal particles: application to optical diagnostics of plasma spraying. J Quant Spectrosc Radiat Trans 73(2–5):433–441

Dombrovsky LA (2004a) The propagation of infrared radiation in a semitransparent liquid containing gas bubbles. High Temper 42(1):133–139

Dombrovsky LA (2004b) Absorption of thermal radiation in large semi-transparent particles at arbitrary illumination of the polydisperse system. Int J Heat Mass Trans 47(25):5511–5522

Dombrovsky LA (2005) Modeling of thermal radiation of a polymer coating containing hollow microspheres. High Temper 43(2):247–258
Dombrovsky LA (2007) Large-cell model of radiation heat transfer in multiphase flows typical for fuel–coolant interaction. Int J Heat Mass Trans 50(17–18):3401–3410
Dombrovsky LA (2009a) Approximate model for break-up of solidifying melt particles due to thermal stresses in surface crust layer. Int J Heat Mass Trans 52(3–4):582–587
Dombrovsky LA (2009b) Thermal radiation modeling in multiphase flows typical of melt-coolant interaction, Chapter 4 in the book "Advances in multiphase flow and heat transfer", Cheng L, Mewes D (eds), Bentham Sci. Publ. 1, pp 114–57
Dombrovsky LA (2012) The use of transport approximation and diffusion-based models in radiative transfer calculations. Comput Therm Sci 4(4):297–315
Dombrovsky LA (2017) Steam explosion in nuclear reactors: droplets of molten steel vs core melt droplets. Int J Heat Mass Trans 107:432–438
Dombrovsky L.A. (2019) Scattering of radiation and simple approaches to radiative transfer in thermal engineering and bio-medical applications, Chapter 2 in the book "Springer Series in Light Scattering", Kokhanovsky A (ed) Springer. 4, pp 71–127
Dombrovsky LA, Baillis D (2010) Thermal radiation in disperse systems: an engineering approach. Begell House, New York
Dombrovsky LA, Baillis D (2011) A simple physical approach to model spectral radiative properties of semi-transparent dispersed materials. Proc ASME/JSME 8th Therm Eng Conf, Honolulu, Hawaii, USA, 44011
Dombrovsky LA, Barkova LG (1986) Solving the two-dimensional problem of thermal-radiation transfer in an anisotropically scattering medium using the finite element method. High Temper 24(4):585–592
Dombrovsky LA, Davydov MV (2010) Thermal radiation from the zone of melt-water interaction. Comput Therm Sci 2(6):535–547
Dombrovsky LA, Dinh TN (2008) The effect of thermal radiation on the solidification dynamics of metal oxide melt droplets. Nucl Eng Design 238(6):1421–1429
Dombrovsky LA, Ignatiev MB (2003) An estimate of the temperature of semitransparent oxide particles in thermal spraying. Heat Trans Eng 24(2):60–68
Dombrovsky LA, Kokhanovsky AA (2019) The influence of pollution on solar heating and melting of a snowpack. J Quant Spectrosc Radiat Trans 233:42–51
Dombrovsky LA, Kokhanovsky AA (2020a) Corrigendum to "The influence of pollution on solar heating and melting of a snowpack [JQSRT 233 (2019) 42–51]". J Quant Spectrosc Radiat Trans 241:106733
Dombrovsky LA, Kokhanovsky AA (2020b) Light absorption by polluted snow cover: Internal versus external mixture of soot. J Quant Spectrosc Radiat Trans 242C:106799
Dombrovsky LA, Kokhanovsky AA (2020c) Solar heating of ice sheets containing gas bubbles. J Quant Spectrosc Radiat Trans 250:106991
Dombrovsky LA, Lipiński W (2007) Transient temperature and thermal stress profiles in semi-transparent particles under high-flux irradiation. Int J Heat Mass Trans 50(11–12):2117–2123
Dombrovsky LA, Lipiński W (2010) A combined P1 and Monte Carlo model for multi-dimensional radiative transfer problems in scattering media. Comput Therm Sci 2(6):549–560
Dombrovsky LA, Randrianalisoa JH (2018) Directional reflectance of optically dense planetary atmosphere illuminated by solar light: An approximate solution and its verification. J Quant Spectrosc Radiat Trans 208:78–85
Dombrovsky L, Randrianalisoa J, Baillis D, Pilon L (2005) Use of Mie theory to analyze experimental data to identify infrared properties of fused quartz containing bubbles. Appl Opt 44(33):7021–7031
Dombrovsky LA, Randrianalisoa J, Baillis D (2006) Modified two-flux approximation for identification of radiative properties of absorbing and scattering media from directional-hemispherical measurements. J Opt Soc Am A 23(1):91–98

Dombrovsky L, Randrianalisoa J, Baillis D (2007a) Infrared radiative properties of polymer coatings containing hollow microspheres. Int J Heat Mass Trans 50(7–8):1516–1527

Dombrovsky LA, Tagne HK, Baillis D, Gremillard L (2007b) Near-infrared radiative properties of porous zirconia ceramics. Infrared Phys Techn 51(1):44–53

Dombrovsky LA, Davydov MV, Kudinov P (2009) Thermal radiation modeling in numerical simulation of melt–coolant interaction. Comput Therm Sci 1(1):1–35

Dombrovsky L, Lallich S, Enguehard F, Baillis D (2010) An effect of "scattering by absorption" observed in near-infrared properties of nanoporous silica. J Appl Phys 107(8):083106

Dombrovsky LA, Baillis D, Randrianalisoa JH (2011a) Some physical models used to identify and analyze infrared radiative properties of semi-transparent dispersed materials. J Spectr Dynam 1:1–20

Dombrovsky LA, Randrianalisoa JH, Lipiński W, Baillis D (2011b) Approximate analytical solution to normal emittance of semi-transparent layer of an absorbing, scattering, and refracting medium. J Quant Spectrosc Radiat Trans 112(12):1987–1994

Dombrovsky LA, Rousseau B, Echegut P, Randrianalisoa JH, Baillis D (2011c) High temperature infrared properties of YSZ electrolyte ceramics for SOFCs: Experimental determination and theoretical modelling. J Amer Ceram Soc 94(12):4310–4316

Dombrovsky LA, Timchenko V, Jackson M, Yeoh GH (2011d) A combined transient thermal model for laser hyperthermia of tumors with embedded gold nanoshells. Int J Heat Mass Trans 54(25–26):5459–5469

Dombrovsky LA, Solovjov VP, Webb BW (2011e) Attenuation of solar radiation by water mist and sprays from the ultraviolet to the infrared range. J Quant Spectrosc Radiat Trans 112(7):1182–1190

Dombrovsky L, Ganesan K, Lipiński W (2012a) Combined two-flux approximation and Monte Carlo model for identification of radiative properties of highly scattering dispersed materials. Comput Therm Sci 4(4):365–378

Dombrovsky LA, Timchenko V, Jackson M (2012b) Indirect heating strategy of laser induced hyperthermia: an advanced thermal model. Int J Heat Mass Trans 55(17–18):4688–4700

Dombrovsky LA, Randrianalisoa JH, Lipiński W, Timchenko V (2013) Simplified approaches to radiative transfer simulations in laser induced hyperthermia of superficial tumors. Comput Therm Sci 5(6):521–530

Dombrovsky LA, Timchenko V, Pathak C, Piazena H, Müller W, Jackson M (2015a) Radiative heating of superficial human tissues with the use of water-filtered infrared-A radiation: a computational modeling. Int J Heat Mass Trans 85:311–320

Dombrovsky LA, Nenarokomova NB, Tsiganov DI, Zeigarnik YuA (2015b) Modeling of repeating freezing of biological tissues and analysis of possible microwave monitoring of volumetric phase changes. Int J Heat Mass Trans 89:894–902

Dombrovsky LA, Reviznikov DL, Sposobin AV (2016) Radiative heat transfer from supersonic flow with suspended particles to a blunt body. Int J Heat Mass Trans 93:853–861

Dombrovsky L, Henry J-F, Lorreyte C, Pron H, Randrianalisoa J (2018a) Optical properties of oakwood in the near-infrared range of semi-transparency. Appl Opt 57(23):6657–6663

Dombrovsky LA, Dembele S, Wen JX, Sikic I (2018b) Two-step method for radiative transfer calculations in a developing pool fire at the initial stage of its suppression by a water spray. Int J Heat Mass Trans 127B:717–726

Dombrovsky LA, Kokhanovsky AA, Randrianalisoa JH (2019) On snowpack heating by solar radiation: A computational model. J Quant Spectrosc Radiat Trans 227:72–85

Doner N, Liu F (2017) Impact of morphology on the radiative properties of fractal soot aggregates. J Quant Spectrosc Radiat Trans 187:10–19

Ebner PP, Schneebeli M, Steinfeld A (2016) Metamorphism during temperature gradient with undersaturated advective airflow in a snow sample. Cryosphere 10(2):791–797

Ebner PP, Steen-Larsen HC, Stenni B, Schneebeli M, Steinfeld A (2017) Experimental observation of transient δ18O interaction between snow and advection airflow under various temperature gradient conditions. Cryosphere 11(4):1733–1743

Eddington AS (1959) The internal constitution of the stars. Dover Publications, New York
Edwards RN, Bobcôo RP (1967) Radiant heat transfer from isothermal dispersion with isotropic scattering. ASME J Heat Trans 89(4):300–308
Evans RJ, Untersteiner N (1971) Thermal cracks in floating ice sheets. J Geophys Res Oceans Atmos 76(3):694–703
Feltham DL, Worster MG (2000) Similarity solutions describing the melting of a mushy layer. J Cryst Growth 208:746–756
Flanner MG, Zender CS, Randerson JT, Rasch PJ (2007) Present-day climate forcing and response from black carbon in snow. J Geophys Res Atmos 112(11):D11202
Flanner MG, Liu X, Zhou C, Penner JE, Jiao C (2012) Enhanced solar energy absorption by internally-mixed black carbon in snow grains. Atmos Chem Phys 12(10):4699–4721
Fukusako S (1990) Thermophysical properties of ice, snow, and sea ice. Int J Thermophys 11(2):353–372
Ganesan K, Dombrovsky LA, Lipiński W (2013) Visible and near-infrared optical properties of ceria ceramics. Infrared Phys Techn 57:101–109
Gardner AS, Sharp MJ (2010) A review of snow and ice albedo and the development of a new physically based broadband albedo parameterization. J Geophys Res Earth Surf 115(F1):F01009
German ML, Grinchuk PS (2002) Mathematical model for calculating the heat-protection properties of the composite coating "ceramic microspheres – binder". J Eng Phys Thermophys 75(6):1301–1313
Gilpin RR, Robertson RB, Singh B (1977) Radiative heating in ice. ASME J Heat Trans 99(2):227–232
Grenfell TC (1983) A theoretical model of the optical properties of sea ice in the visible and near infrared. J Geophys Res Oceans 88(C14):9723–9735
Grenfell TC (1991) A radiative transfer model for sea ice with vertical structure variations. J Geophys Res Oceans 96(C9):16991–7001
Grenfell T, Warren S (1999) Representation of a nonspherical ice particle by a collection of independent spheres for scattering and absorption of radiation. J Geophys Res Atmos 104(D24):31697–31709
Güttler A (1952) Die Miesche Theorie der Beugung durch dielektrische Kugeln mit absorbierendem Kern und ihre Bedeutung für Probleme der interstellaren Materie und des atmospherischen Aerosols. Ann Phys 11(2–3):65–98
Hakoume D, Dombrovsky LA, Delaunay D, Rousseau B (2014) Spectroscopic diagnostics of morphological changes arising in thermal processing of polypropylene. Appl Opt 53(12):2702–2710
Haussener S, Gergely M, Schneebeli M, Steinfeld A (2012) Determination of the macroscopic optical properties of snow based on exact morphology and direct pore-level heat transfer modeling. J Geophys Res Earth Surf 117(F3):F03009
He C, Takano Y, Liou K-N, Yang P, Li Q, Chen F (2017) Impact of grain shape and black-carbon snow internal mixing on snow optical properties: parametrization for climate models. J Climate 30:10019–10036
He C, Liou K-N, Takano Y, Yang P, Qi L, Chen F (2018) Impact of grain shape and multiple black carbon internal mixing on snow albedo: parametrization and radiative effect analysis. J Geophys Res Atmos 123(2):1253–1268
Hergert W, Wriedt T (2012) The Mie theory: basics and applications. Springer, Berlin
Hill VJ, Light B, Steele M, Zimmerman RC (2018) Light availability and phytoplankton growth beneath Arctic sea ice: integrating observations and modeling. J Geophys Res Oceans 123(5):3651–3667
Hossain MM, Gu M (2016) Radiative cooling: principles, progress, and potentials. Adv Sci 3(7):1500360
Howell JR, Mengüç MP, Siegel R (2015) Thermal radiation heat transfer, 6th edn. CRC Press, New York

Hrma P (2009) Effect of heating rate on glass foaming: transition to bulk foam. J Non-Cryst Solids 355(4–5):257–63
Huppert HE (1990) The fluid dynamics of solidification. J Fluid Mech 212:209–240
Irvine WM (1963) The asymmetry of the scattering diagram of a spherical particle. Commun Observ Leiden 17(3):176–184
Irvine WM (1964) Light scattering by spherical particles: radiation pressure, asymmetry factor, and extinction cross section. J Opt Soc Am 55(1):16–21
Ishimoto H, Adachi S, Yamaguchi S, Tanikawa T, Aoki T, Masuda K (2018) Snow particles extracted from X-ray computed microtomography imagery and their single-scattering properties. J Quant Spectrosc Radiat Trans 209:113–128
Kaempfer TU, Plapp M (2009) Phase-field modelling of dry snow metamorphism. Phys Rev E 79(2, pt1):031502
Kokhanovsky AA (2004) Optics of light scattering media: problems and solutions, 3rd edn. Praxis, Chichester, UK
Kokhanovsky A (2013) Spectral reflectance of solar light from dirty snow: a simple theoretical model and its validation. Cryosphere 7(4):1325–1331
Kokhanovsky AA, Zege EP (1995) Local optical parameters of spherical polydispersions: simple approximations. Appl Opt 34(24):5513–5519
Kokhanovsky AA, Zege EP (1996) Optical properties of aerosol particles: a review of approximate analytical solutions. J Aerosol Sci 28(1):1–21
Kokhanovsky AA, Zege EP (2004) Scattering optics of snow. Appl Opt 43(7):1589–1602
Kokhanovsky A, Lamare M, Di Mauro B, Picard G, Arnaud L, Dumont M, Tuzet F, Brockmann C, Box JE (2018) On the reflectance spectroscopy of snow. Cryosphere 12(7):2371–2382
Kokhanovsky AA, Tomasi C (eds) (2020) Physics and chemistry of the arctic atmosphere. Springer, Cham
Koledintseva MY, DuBroff RE, Schwartz RW (2009) Maxwell Garnett rule for dielectric mixtures with statistically distributed orientations of inclusions. Prog Electromag Res 99:131–148
Kuchiki K, Aoki T, Niwano M, Matoba S, Kodama Y, Adachi K (2015) Elemental carbon, organic carbon, and dust concentrations in snow measured with thermal optical and gravimetric methods: Variations during the 2007-2013 winters at Sapporo, Japan. J Geophys Res Atmos 120(2):868–882
Lachenbrush AH (1961) Depth and spacing of tension cracks. J Geophys Res 66(12):4273–4292
Lage PLC, Rangel PH (1993) Total thermal radiation absorption by a single spherical droplet. AIAA J Thermophys Heat Trans 7(1):101–109
Lai HM, Leung PT, Poon KL, Young K (1991) Characterization of the internal energy density in Mie scattering. J Opt Soc Am A 8(10):1553–1558
Libois Q, Picard G, France JL, Arnaud L, Dumont M, Carmagnola CM, King MD (2013) Influence of grain shape on light penetration in snow. Cryosphere 7(6):1803–1818
Light B (2010) Theoretical and observational techniques for estimating light scattering in first-year arctic sea ice. In: Kokhanovsky A (ed) Light scattering reviews 5: single light scattering and radiative transfer. Springer, pp 331–391
Lim S, Faïn X, Zanatta M, Cozik J, Jaffrezo J-L, Ginot P, Laj P (2014) Refractory black carbon mass concentrations in snow and ice: method evaluation and inter-comparison with elemental carbon measurement. Atmos Meas Tech 7(4):3307–3324
Lindqvist H, Martikainen J, Räbinä J, Penttilä A, Muinonen K (2018) Ray optics for absorbing particles with application to ice crystals at near-infrared wavelengths. J Quant Spectrosc Radiat Trans 217:329–337
Liou B-T, Wu C-Y (1996) Radiative transfer in a multilayer medium with Fresnel interfaces. Heat Mass Trans 32(1–2):103–107
Liou KN, Takano Y, Yang P (2011) Light absorption and scattering by aggregates: application to black carbon and snow grains. J Quant Spectrosc Radiat Trans 112(10):1581–1594
Liou KN, Takano Y, He C, Yang P, Leung LR, Gu Y, Lee WL (2014) Stochastic parametrization for light absorption by internally mixed BC/dust in snow grains for application to climate models. J Geophys Res Atmos 119(2):7616–7632

Liu L, Mishchenko MI, Arnott WP (2008) A study of radiative properties of fractal soot aggregates using the superposition T-matrix method. J Quant Spectrosc Radiat Trans 109(15):2656–2663

Lisitsyn AV, Dombrovsky LA, Mendeleyev VYa, Grigorenko AV, Vlaskin MS, Zhuk AZ (2016) Near-infrared optical properties of a porous alumina ceramics produced by hydrothermal oxidation of aluminum. Infrared Phys Techn 77:162–70

Liston GE, Winther J-G (2005) Antarctic surface and subsurface snow and ice melt fluxes. J Climate 18(10):1469–1481

Löwe H, Riche F, Schneebeli M (2013) A general treatment of snow microstructure exemplified by an improved relation for thermal conductivity. Cryosphere 7(5):1473–1480

Lucarini V, Saarinene JJ, Peiponen K-E, Vartainen EM (2005) Kramers–Krönig relations in optical material research, Springer Series in Optical Sciences. Springer, Berlin

Mackowski DW, Altenkirch RA, Mengüç MP (1990) Internal absorption cross section in a stratified sphere. Appl Opt 29(10):1551–1559

Malinka A, Zege E, Istomina L, Heygster G, Spreen G, Perovich D, Polashenski C (2018) Reflective properties of melt ponds on sea ice. Cryosphere 12(6):1921–1937

Malinka A, Zege E, Heygster G, Istomina L (2016) Reflective properties of white sea ice and snow. Cryosphere 10(6):2541–2557

Manara J, Caps R, Raether F, Fricke J (1999) Characterization of the pore structure of alumina ceramics by diffuse radiation propagation in the near infrared. Opt Commun 168(1–4):237–250

Markel VA (2016) Introduction to the Maxwell Garnett approximation: tutorial. J Opt Soc Am A 33(7):1244–1256

Maxwell-Garnett JC (1904) Colours in metal glasses and in metallic films. Phil Trans Royal Soc London A 203:385–420

McGuinness MJ, Landman KA, Trodahl HJ, Pantoja AE (2001) Solar radiative heating in first-year sea ice. Annals Glaciol 33:261–266

McKenzie M, Voss CI, Siegel DI (2007) Groundwater flow with energy transport and water-ice phase change: Numerical simulations, benchmarks, and application to freezing in peat bogs. Adv Water Resour 30(4):966–983

Milne FA (1930) Thermodynamics of the stars. Handbook der Astrophysik. Springer-Verlag, OHG, Berlin, pp 65–255

Mirsadeghi M, Cóstola D, Blocken B, Hensen JLM (2013) Review of external convective heat transfer coefficient models in building energy simulation programs: Implementation and uncertainty. Appl Therm Eng 56(1–2):134–151

Mishchenko MI (2014) Electromagnetic scattering by particles and particle groups: an introduction. Cambridge University Press, Cambridge, UK

Mishchenko MI (2018) "Independent" and "dependent" scattering by particles in a multi-particle group. OSA Continuum 1(1):243–260

Mishchenko MI, Hovenier JV, Travis LD (eds) (2000) Light scattering by nonspherical particles—theory, measurements, and applications. Academic Press, New York

Mishchenko MI, Travis LD, Lacis AA (2006) Multiple scattering of light by particles: radiative transfer and coherent backscattering. Cambridge University Press, Cambridge, UK

Mobley CD, Cota GF, Grenfell TC, Maffione RA, Pegau WS, Perovich DK (1998) Modelling light propagation in sea ice. IEEE Trans Geosci Remote Sens 36(5):1743–1749

Modest MF (2013) Radiative heat transfer, 3rd edn. Academic Press, New York

Munneke PK, van den Broeke MR, Reijmer CH, Helsen MM, Boot W, Schneebeli M, Steffen K (2009) The role of radiation penetration in the energy budget of the snowpack at Summit, Greenland. Cryosphere 3(2):155–165

Muresan C, Vaillon R, Menezo C, Morlot R (2004) Discrete ordinates solution of coupled conductive radiative heat transfer in a two-layer slab with Fresnel interfaces subject to diffuse and obliquely collimated irradiation. J Quant Spectrosc Radiat Trans 84(4):551–562

Neshyba SP, Grenfell TC, Warren SG (2003) Representation of a nonspherical ice particle by a collection of independent spheres for scattering and absorption of radiation: 2. Hexagonal columns and plates. J Geophys Res Atmos 108(D15):4448

Oldroyd HJ, Higgins CW, Huwald H, Selker JS, Parlange MB (2013) Thermal diffusivity of seasonal snow determined from temperature profiles. Adv Water Resour 55:121–130
Osokin NI, Sosnovskiy AV, Chernov RA (2017) Effective thermal conductivity of snow and its variations. Earth's Cryosph 21(3):55–61
Özişik MN (1973) Radiative transfer and interaction with conduction and convection. Wiley, New York
Papadopoulos AM (2005) State of the art in thermal insulation materials and aims for future developments. Energy Build 37(1):77–86
Perovich DK, Grenfell TC (1982) A theoretical model of radiative transfer in young sea ice. J Glaciol 28(99):341–356
Picard G, Dumont M, Lamare M, Tuzet F, Larue F, Pirazzini R, Arnaud L (2020) Spectral albedo measurements over snow-covered slopes: theory and slope effect corrections. Cryosphere 14(5):1497–1517
Pilon L, Viskanta R (2003) Radiation characteristics of glass containing bubbles. J Am Ceram Soc 86(8):1313–1320
Pinzer BR, Schneebeli M, Kaempfer TU (2012) Vapor flux and recrystallization during dry snow metamorphism under a steady temperature gradient as observed by time-lapse micro-tomography. Cryosphere 6(5):1141–1155
Pomraning GC (1965) A flexible numerical approach to linear transport problems. Trans Am Nucl Soc 8:488–489
Potter JF (1970) The delta function approximation in radiative transfer theory. J Atmos Sci 27(6):943–949
Prishivalko AP, Babenko VA, Kuzmin VN (1984) Scattering and absorption of light by inhomogeneous and anisotropic spherical particles. Nauka i Tekhnika, Minsk (in Russian)
Qian Y, Yasunari TJ, Doherty SJ, Flanner MG, Lau WKM, Jing M, Wang H, Wang M, Warren SG, Zhang R (2015) Light-absorbing particles in snow and ice: Measurement and modeling of climatic and hydrological impact. Adv Atmos Sci 32(1):64–91
Raman AP, Anoma MA, Zhu L, Rephaeli E, Fan S (2014) Passive radiative cooling below ambient air temperature under direct sunlight. Nature 515:540–544
Räisänen P, Kokhanovsky A, Guyot G, Jourdan O, Nousiainen T (2015) Parametrization of single-scattering properties of snow. Cryosphere 9(3):1277–1301
Ricchiazzi P, Yang S, Gautier C, Sowle D (1998) SBDART: a research and teaching software for plane-parallel radiative transfer in the earth atmosphere. Bull Am Meteorol Soc 79(10):2101–2114
Riche F, Schneebeli M (2013) Thermal conductivity of snow measured by three independent methods and anisotropy considerations. Cryosphere 7(1):217–227
Richter K, Norris PM, Tien C-L (1995) Aerogels: applications, structure and heat transfer phenomena. Ann Rev Heat Trans 6:61–114
Rubtsov NA (1984) Radiation heat transfer in continuous media. Nauka, Novosibirsk (in Russian)
Sacadura J-F (2011) Thermal radiative properties of complex media: Theoretical prediction versus experimental identification. Heat Trans Eng 32(9):754–770
Sanderson TJO (1978) Thermal stresses near the surface of a glacier. J Glaciol 20(83):257–283
Schneebeli M, Sokratov S (2004) Tomography of temperature gradient metamorphism of snow and associated changes in heat conductivity. Hydrol Processes 18(18):3655–3665
Schuster A (1905) Radiation through a foggy atmosphere. Astrophys J 21:1–22
Schwander J, Stauffer B (1984) Age difference between polar ice and the air trapped in its bubbles. Nature 311(6):45–47
Schwarz JP, Gao RS, Perring AS, Spackman JR, Fahey DW (2013) Black carbon aerosol size in snow. Sci Rep 3(1):1356
Schwarzschild K (1906) Über das Gleichgewicht der Sonnenatmosphären (Equilibrium of the Sun's atmosphere). Akad Wiss Göttingen, Math-Phys Kl Nachr 195:41–53
Seki N, Sugawara M, Fukusako S (1979) Radiative melting of ice layer adhering to a vertical surface. Wärme– und Stoffübertragung 12(2):137–44

Shelby JE (2005) Introduction to glass science and technology, 2nd edn. The Royal Soc Chem, Cambridge (UK)
Shertzer RH, Adams EE (2011) Anisotropic thermal conductivity model for dry snow. Cold Reg Sci Techn 69(2–3):122–128
Shifrin KS (1952) Scattering of light by two-layer particles. Trans USSR Acad Sci Geophys 2:15–21 (in Russian)
Siegel R (1998) Transient effects of radiative transfer in semitransparent materials. Int J Eng Sci 36(12–14):1701–1739
Sjöstrand NG (2001) On an alternative way to treat highly anisotropic scattering. Annals Nucl Energy 28(4):351–355
Sleptsov SD, Savvinova NA (2019) Ice melting under irradiation by a selective heat source. Thermophys Aeromech 26(5):761–768
Sobolev VV (1975) Light scattering in planetary atmospheres. Pergamon Press, Oxford
Soloviev A, Lukas R (2014) The near-surface layer of the ocean: structure, dynamics and applications, Second Edition (Atmospheric and Oceanographic Sciences Library, v. 48). Springer, New York
Stamnes K, Thomas GE, Stamnes JJ (2017) Radiative transfer in the atmosphere and ocean, Second Revised edn. Cambridge University Press, Cambridge (UK)
Sturm M, Johnson J (1992) Thermal conductivity measurements of depth hoar. J Geophys Res Solid Earth 97(B2):2129–2139
Sturm M, Holmgren J, König M, Morris K (1997) The thermal conductivity of seasonal snow. J Glaciol 43(143):26–41
Sturm M, Perovich DK, Holmgren J (2002) Thermal conductivity and heat transfer through the snow on the ice of the Beaufort Sea. J Geophys Res Oceans 107(C21):8043
Tedesco M (ed) (2015) Remote sensing of the cryosphere. Wiley Blackwell, Chichester
Thapliyal PC, Singh K (2014) Aerogels as promising thermal insulating materials: an overview. J Mater 2014:127049
Tien CL (1988) Thermal radiation in packed and fluidized beds. ASME J Heat Trans 110(4):1230–1242
Tien CL, Drolen BL (1987) Thermal radiation in particulate media with dependent and independent scattering. In: Annual review of numerical fluid mechanics and heat transfer, vol 1, pp 1–32. Hemisphere, New York
Timofeev AM (2018) Simulation of radiative heating of snow and ice coating. Thermophys Aeromech 25(5):765–772
Tuchin VV (2017) Tissue optics: light scattering methods and instruments for medical diagnostics. SPIE Press, Bellingham, WA
Tuntomo A, Tien CL, Park SH (1991) Internal distribution of radiant absorption in a spherical particle. ASME J Heat Trans 113(2):407–412
Tuzet F, Dumont M, Arnaud L, Voisin D, Lamare M, Larue F, Revuelto J, Picard G (2019) Influence of light absorbing particles on snow spectral irradiance profiles. Cryosphere 13(8):2169–2187
Van de Hulst HC (1981) Light scattering by small particles. Dover, New York
Van der Schaaf J, Beerkens RGC (2006) A model for foam formation, stability, and breakdown in glass-melting furnaces. J Colloid Interf Sci 295(1):218–229
Velesco N, Kaiser T, Schweiger G (1997) Computation of the internal field of a large spherical particle by use of the geometrical optics approximation. Appl Opt 36(33):8724–8728
Viskanta R (2005) Radiative transfer in combustion systems: fundamentals and applications. Begell House, New York
Wagner HG (1981) Soot formation—An overview. Proc Int Symp Part Carbon, Plenum Press. 1981:1–29
Wang X, Pu W, Ren Y, Zhang X, Zhang X, Shi J, Jin H, Dai M, Chen Q (2017) Observations and model simulations of snow albedo reduction in seasonal snow due to insoluble light-absorbing particles during 2014 Chinese survey. Atmos Chem Phys 17(3):2279–2296

Wang Y-F, Huang Q-X, Wang F, Chi Y, Yan J-H (2019) A feasible and accurate method for calculating the radiative properties of soot particle ensembles in flames. J Quant Spectrosc Radiat Trans 224:222–232

Warren SG (1982) Optical properties of snow. Rev Geophys Space Phys 20(1):67–89

Warren SG (2019a) Light-absorbing impurities in snow: A personal and historical account. Front Earth Sci 6:250

Warren SG (2019b) Optical properties of ice and snow. Phil Trans Royal Soc A 377:20180161

Warren SG, Brandt RE (2008) Optical constants of ice from the ultraviolet to the microwave: a revised compilation. J Geophys Res Atmos 113(D14):D14220

Warren SG, Clarke AD (1990) Soot in the atmosphere and snow surface of Antarctica. J Geophys Res Atmos 95(D2):1811–1816

Warren SG, Wiscombe WJ (1980) A model for the spectral albedo of snow, II: snow containing atmospheric aerosols. J Atmos Sci 137(12):2734–2745

Warren SG, Brandt RE, Grenfell TC (2006) Visible and near-ultraviolet absorption spectrum of ice from transmission of solar radiation into snow. Appl Opt 45(21):5320–5334

Warren SG, Roesler CS, Brandt RE, Curran M (2019) Green icebergs revisited. J Geophys Res Oceans 124(2):925–938

Williams MMR (1966) The slowing down and thermalization of neutrons. North-Holland Publ. Co., Amsterdam

Williamson CJ, Cook J, Tedstone A, Yallop M, McCutcheon J, Poniecka E, Campbell D, Irvine-Fynn T, McQuaid J, Tranter M, Perkins R, Anesio A (2020) Algal photophysiology drives darkening and melt of Greenland Ice Sheet. Proc Nat Acad Sci 117(11):5694–5705

Wiscombe WJ, Warren SG (1980) A model for the spectral albedo of snow, I: pure snow. J Atmos Sci 37(12):2712–2733

Wu L, Yang H, Li X, Yang B, Li G (2007) Scattering by large bubbles: Ccomparisons between geometrical optics theory and Debye series. J Quant Spectrosc Radiat Trans 108(1):54–64

Xu G, Ikegami M, Honma S, Ikeda K, Dietrich DL, Struk PM (2004) Sooting characteristics of isolated droplet burning in heated ambient under microgravity. Int J Heat Mass Trans 47(26):5807–5821

Yan B, Chen B, Stamnes K (2002) Role of oceanic air bubbles in atmospheric correction of ocean color imagery. Appl Opt 41(12):2202–2212

Zhang X, Lewis M, Johnson B (1998) Influence of bubbles on scattering of light in the ocean. Appl Opt 37(27):6525–6536

Zeldovich YaB, Raizer YuP (1966) Physics of shock waves and high-temperature hydrodynamic phenomena. Academic Press, New York

Stereological Methods in the Theory of Light Scattering by Nonspherical Particles

Aleksey Malinka

1 Introduction

Stereology is a part of probability theory that deals with geometrical statistics. Since, in classical sense, light scattering is the interaction of electromagnetic waves with a medium that contains the refractive index inhomogeneities arranged in a stochastic manner, stereology seems to be a suitable way to describe scattering media. Particularly, it can be very useful in interpreting the microphysical properties of densely packed media, widespread both in nature—snow, sand, sea foam, or planetary regoliths—and among artificial products—ceramics, pharmaceutical pills, etc.

The key concept in stereology is a random chord. The random medium is considered as a stochastic mixture of two components: material and gap. (In general, the number of components is not limited, but in this work we will restrict ourselves to these two.) Any random straight line inside the medium has a number of intercepts, lying either in the material or in the void. These intercepts are called random chords. Chord length ξ is a random value, characterized by some distribution density called the chord length distribution (CLD): $f(\xi)$ with mean a for material and $g(\xi)$ with mean h for gaps. Here is what Roberts and Torquato (1999) write about the CLD in the multi-component mixture and its conceptual meaning (we have changed symbols to align with our notation):

"One reason for the usefulness of the chord function is that $f_i(\xi)$ can be directly interpreted in terms of observable microstructure features. First, if $f_i(0) \neq 0$ then, at the resolution at which it is measured, phase i contains sharp corners. Second, the value at which $f_i(\xi)$ takes a maximum value provides an estimate of the length scale associated with phase i.

A. Malinka (✉)
Institute of Physics, National Academy of Sciences of Belarus, pr. Nezavisimosti 68-2, 220072 Minsk, Belarus
e-mail: aleksey.malinka@gmail.com

© The Author(s), under exclusive license to Springer Nature Switzerland AG 2021

A. Kokhanovsky (ed.), *Springer Series in Light Scattering*, Springer Series in Light Scattering, https://doi.org/10.1007/978-3-030-71254-9_3

Another is provided by the average chord length $\langle\xi\rangle$. Third, if $f_i(\xi) \neq 0$ for large ξ, connected regions in phase i at scale ξ exist. This 'connectedness' information (along a lineal path) is clearly important if long-range phenomena (like macroscopic properties) are to be studied. The direct relationship between $f_i(\xi)$ and morphology shows that the chord functions give a strong 'signature' of microstructure and are therefore an important tool in the characterization of porous and composite media."

We will consider here the isotropic case only, i.e., when the normals to the interface surface are distributed isotropically and the CLD is independent of the direction. Another important feature of the random mixture is that because of its stochastic nature the distance the ray goes between two refractions/reflections does not depend on the refraction angle (in contrast to the case of a regular shape, e.g. sphere, where the length of a ray inside a particle is unambiguously determined by the refraction angle); so these two (angle and distance) are independent random values.

If the process of the intersection of the material–gap interface has the Markov property, the CLDs are exponential:

$$f(\xi) = \frac{1}{a}\exp\left(-\xi/a\right), \quad g(\xi) = \frac{1}{h}\exp\left(-\xi/h\right). \tag{1}$$

The possibility of a plane dissection into a random mosaic with Markov properties, to our knowledge, was first supposed by Pielou (1964). A year later, Switzer (1965) constructed such a model and proved its Markov properties. Debye et al. (1957), however, had considered scattering in a random medium with similar, but weaker requirements (the exponential correlation function), several years earlier. We will come back to Debye's consideration a bit later.

The Switzer model is very simple and clear. A number of random straight lines dissect a plane into convex polygons. Each polygon is considered as belonging to component 1 with the predefined probability β and to component 2 with probability $1-\beta$. An example of such a mosaic is presented in Fig. 1. It can be easily generalized to 3 or more dimensions. This model is also sometimes called the Poisson mosaic or 'Poisson cells' (Jeulin 2000; Gommes et al. 2020); however, it should not to be confused with the Poisson–Voronoi tessellation, which is also often called the Poisson cells, where the cell nuclei are distributed in space at random by a Poisson process and a point belongs to cell i if it is closer to nucleus i than to any other nucleus $j \neq i$ (Meijering 1953; Gilbert 1962; Miller 1969). The latter model is also widely used in various applications including light scattering (see, e.g., Ishimoto et al. 2010).

The random mosaic—or its 3-dimensional generalization—has been widely used in a range of different fields: investigation of vegetation (Pielou 1964; Norrisa et al. 1997) or drumlins distribution (Boors and Burns 1984), neutron transport in reactors (Sahni 1989), radiative transfer thought broken clouds (Pomraning 1988, 1991; Lane et al. 2002).

Such a mosaic with the Markov property is the simplest example of the two-phase mixture, for which one can find strict analytical solutions to many problems of light scattering. Often it is sufficient to describe light scattering properties of a medium; however, if higher accuracy is required, the difference of the CLD from

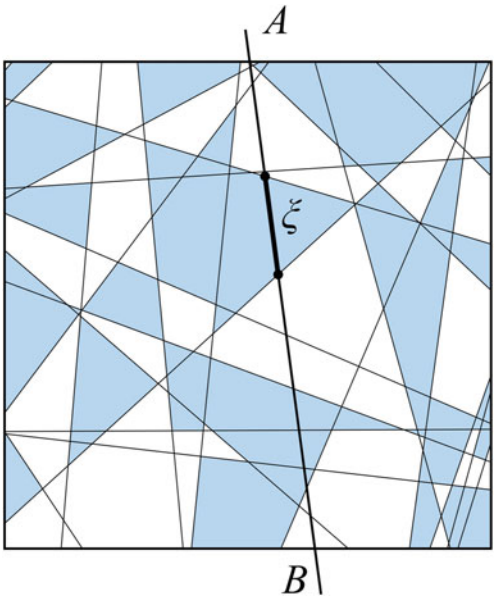

Fig. 1 Example of the random mosaic with $\beta = 1/2$. AB is a random straight line with a random chord ξ

the exponential form given by Eq. (1) may be significant, e.g., as was mentioned, if the interface is smooth, i.e., with no sharp corners or edges, then $f(0) = 0$. We will use the functions given by Eq. (1) as an important particular case and in examples of numerical calculations, giving, however, the general formulae for CLDs of any kind. A number of CLDs and some related quantities for bodies of various shapes are given by Coleman (1981), Mäder (1980), and Kellerer (1971, 1984).

Independently of the CLD, the following statements hold true (Meijering 1953; Debye et al. 1957; Gille 2000; Gille et al. 2002).

The material fraction β, the porosity ϕ, the bulk density ρ_b, and the material density ρ_m are related to the mean chords:

$$\beta = 1 - \phi = \frac{\rho_b}{\rho_m} = \frac{a}{a+h}. \tag{2}$$

Here the densities can be either surface or volume ones, depending on whether 2- or 3-dimensional case is considered.

Consider the indicator function $\eta(\mathbf{r})$ that gives 1 in the material phase and 0 in voids. The two-point covariance $C_2(\mathbf{r})$ is the function given by

$$C(\mathbf{r}) = \left\langle \eta(\mathbf{r}')\eta(\mathbf{r}' + \mathbf{r}) \right\rangle_{\mathbf{r}'}, \tag{3}$$

where the sign $\langle\rangle_{\mathbf{r}'}$ denotes averaging over the coordinate $\mathbf{r}'$.

For any isotropic mixture, the two-point covariance depends on the module of $\mathbf{r}$ only:

$$C_2(\mathbf{r}) = C_2(r). \tag{4}$$

It is obvious that

$$\begin{aligned} \langle \eta \rangle &= \beta, \\ C_2(0) &= \langle \eta^2 \rangle = \beta. \end{aligned} \tag{5}$$

Let us introduce the auto-correlation function $\gamma(r)$ as

$$\gamma(r) = \frac{\langle [\eta(\mathbf{r}') - \langle \eta \rangle][\eta(\mathbf{r}' + \mathbf{r}) - \langle \eta \rangle] \rangle_{\mathbf{r}'}}{\langle [\eta(\mathbf{r}') - \langle \eta \rangle]^2 \rangle_{\mathbf{r}'}}. \tag{6}$$

It is easy to see that

$$C_2(r) = \beta(1-\beta)\gamma(r) + \beta^2. \tag{7}$$

By definition, the correlation length l_c is

$$l_c = -\frac{1}{\gamma'(0)}. \tag{8}$$

Debye et al. (1957) showed that the auto-correlation function $\gamma(r)$ has the exponential form in quite a general case:

$$\gamma(r) = e^{-r/l_c}. \tag{9}$$

It is to be noted though that the exponential form of $\gamma(r)$ doesn't demand the same for CLDs $f(\xi)$ and $g(\xi)$.

One of the fundamental relations in stereology is represented by Cauchy's formulas that link the mean chords with the specific area s_V—the interface surface per volume of a 3D mixture—or the specific perimeter l_A—the interface perimeter per area of a 2D mosaic:

$$\begin{aligned} s_V &= \frac{4\beta(1-\beta)}{l_c} = \frac{4}{a+h} \qquad \text{for } 3D, \\ l_A &= \frac{\pi\beta(1-\beta)}{l_c} = \frac{\pi}{a+h} \qquad \text{for } 2D. \end{aligned} \tag{10}$$

It follows for both 2D and 3D cases that

$$l_c = \frac{ah}{a+h}. \tag{11}$$

The very close characteristic—specific surface area (*SSA*) per sample mass—is very often used to characterize porous materials like snow (Domine et al. 2008;

Picard et al. 2009):

$$SSA = \frac{\text{interface area}}{\text{sample mass}} = \frac{s}{\rho_{bulk}} = \frac{4}{(a+h)\rho_{solid}\beta} = \frac{4}{\rho_{solid}a}. \tag{12}$$

Thus, *SSA* is determined by only one mixture characteristic: the mean chord of the material phase.

It is necessary to note that the stereological approach is valid not only for the random mixture, but also for any ensemble of independent particles. E.g., Eq. (12) holds true and relates the mean chord a to the average particle volume $\langle V \rangle$ and its projection area $\langle S_\perp \rangle$:

$$a = \frac{\langle V \rangle}{\langle S_\perp \rangle}. \tag{13}$$

A 2D analogue of Eq. (13) is

$$a = \frac{\langle S \rangle}{\langle D \rangle}, \tag{14}$$

where $\langle S \rangle$ is the mean obstacle area and $\langle D \rangle$ is its average diameter.

For any convex particle the average projection area equals one-fourth its surface area:

$$\langle S_\perp \rangle = S/4, \tag{15}$$

and for any convex obstacle the average diameter equals its perimeter L divided by π:

$$\langle D \rangle = L/\pi. \tag{16}$$

Equation (13), up to a constant factor 4/3, matches the standard definition of the effective size of snow grains (Grenfell and Warren 1999: Kokhanovsky and Zege 2004; Zege et al. 2008, 2011) and the effective radius r_{32} of polydispersed aerosol and cloud particles (Dobbins and Jizmagian 1966; Naumenko 1971; Hansen and Travis 1974; Schmidt et al. 2013). Equation (12), however, is more general that Eq. (13), as the stochastic mixture does not require the grain convexity and can be densely packed.

A lot of useful information on geometrical probabilities can also be found in the fundamental monograph of Kendall and Moran (1963).

In this work, the stereological approach is applied to the classical approximations of the theory of light scattering: Fraunhofer diffraction, the Rayleigh–Gans and Wentzel–Kramers–Brillouin approximations, anomalous diffraction, and geometrical optics. These results were originally published in (Malinka 2011a, b, 2014a, b, 2015a) and were applied to the description of phytoplankton (Malinka 2015b), snow

and sea ice optical properties (Malinka et al. 2016a, 2018; Zege et al. 2015a, 2018), as well as to remote sensing of the sea ice cover (Heygster et al. 2012; Zege et al. 2013, 2015b, 2019; Istomina et al. 2015a, b).

2 Fraunhofer Diffraction

Fraunhofer diffraction is a well-known tool to describe light scattering in the near-forward directions. Light diffraction by obstacles of a regular shape or by a screen with regularly placed gaps is a classical problem of physical optics. However, a lot of scatterers in nature, such as cirrus cloud crystals or volcanic ashes, are far from spheres or have a random irregular shape. A monolayer of such particles represents the case where obstacles and gaps are distributed stochastically. In this regard, the problem arises: how to describe Fraunhofer diffraction by a random screen, where obstacles and gaps have a random irregular shape and are distributed randomly over the screen plane. The stereological approach gives a clue.

2.1 Single Obstacle Approximation

Let us first apply the stochastic approach to describe Fraunhofer diffraction in the single obstacle approximation. This approximation means that the interference between different obstacles can be neglected, so it can be used if the medium is sparse enough (the distance between particles is large, e.g., in aerosols or clouds). Although the obstacles may have an arbitrary shape, the whole ensemble is considered as azimuthally isotropic, i.e., the particles do not have a preferable orientation in the plane, perpendicular to the incident beam.

The amplitude of Fraunhofer diffraction of a plane wave by a single obstacle is (see, e.g., Hulst 1957; Born and Wolf 1968)

$$u = \frac{1}{\lambda} \int_S e^{i\,\Delta\mathbf{k}\cdot\mathbf{r}} d^2\mathbf{r}, \tag{17}$$

where the integral is taken over the obstacle area S and $\Delta\mathbf{k}$ is a change of the wave vector due to diffraction:

$$\begin{aligned} &\Delta\mathbf{k} = \mathbf{k} - \mathbf{k}_0, \\ &|\Delta\mathbf{k}| = \Delta k = \frac{2\pi}{\lambda}\theta, \end{aligned} \tag{18}$$

$\mathbf{k}$, the wavevector of the diffracted wave, $\mathbf{k}_0$, the wavevector of the incident wave, θ, the diffraction angle (assumed to be small), λ, the wavelength.

The differential cross-section is

$$\frac{dC_{sca}}{d\Omega} = \langle |u|^2 \rangle = \left\langle \frac{1}{\lambda^2} \iint\limits_S e^{i\,\Delta\mathbf{k}\cdot(\mathbf{r}-\mathbf{r}')} d^2\mathbf{r}\, d^2\mathbf{r}' \right\rangle, \tag{19}$$

where the sign $\langle\rangle$ denotes averaging over an ensemble, which can include averaging over orientations if the obstacles are identical and randomly oriented, over shape for irregular particles, and over size for polydispersions.

To do the integration, let us take a point O inside the obstacle and make the following coordinates transformation:

$$\begin{aligned} x &= \chi \sin\varphi + \rho\cos\varphi \qquad & y &= -\chi\cos\varphi + \rho\sin\varphi \\ x' &= \chi' \sin\varphi + \rho\cos\varphi \qquad & y' &= -\chi'\cos\varphi + \rho\sin\varphi, \end{aligned} \tag{20}$$

where ρ is the distance from point O to line $(\mathbf{r}, \mathbf{r}')$, φ is the angle between $\Delta\mathbf{k}$ and OP—the perpendicular, dropped from O to this line—χ and χ' are distances from P to $\mathbf{r}$ and $\mathbf{r}'$, respectively (see Fig. 2 for geometrical interpretation).

In these coordinates integral becomes

$$\frac{dC_{sca}}{d\Omega} = \left\langle \frac{1}{\lambda^2} \int\limits_{-\pi/2}^{\pi/2} d\varphi \int\limits_{D(\varphi)} d\rho \int\limits_A^B \int\limits_A^B e^{i\,\Delta k|\chi-\chi'|\sin(\varphi'-\varphi)} |\chi-\chi'| d\chi\, d\chi' \right\rangle, \tag{21}$$

where $D(\varphi)$ is the obstacle diameter in direction OP (see Fig. 3).

Averaging over azimuth φ' gives

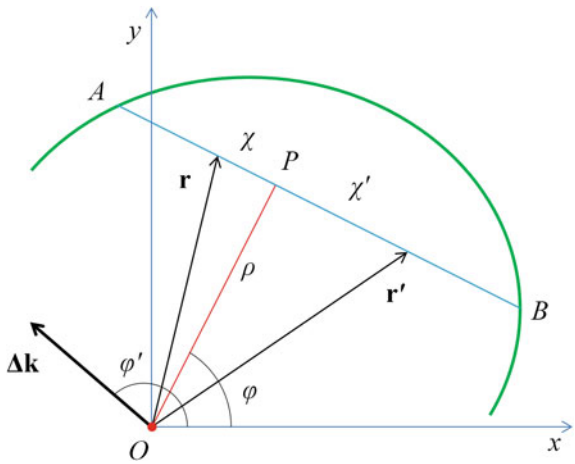

Fig. 2 Geometric interpretation of transformation (20)

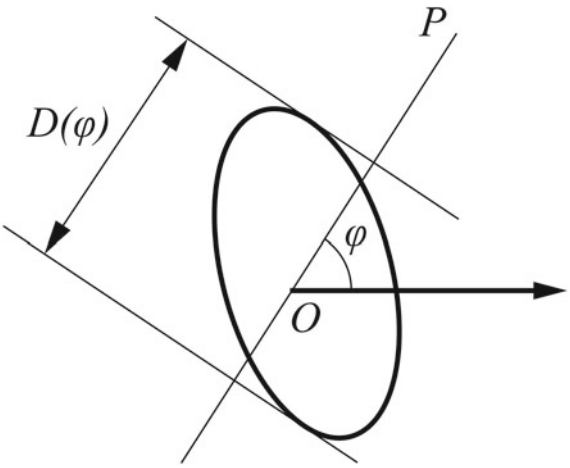

Fig. 3 Definition of the diameter in direction *OP*

$$\frac{dC_{sca}}{d\Omega} = \frac{1}{\lambda^2} \int\limits_{-\pi/2}^{\pi/2} d\varphi \int\limits_{D(\varphi)} d\rho \int\limits_{A}^{B} \int\limits_{A}^{B} J_0\big(\Delta k|\chi - \chi'|\big)|\chi - \chi'| d\chi d\chi'. \tag{22}$$

Chord AB (and its length ξ) of a given contour is completely determined by the variables φ and ρ. Therefore, integration over element $d\varphi d\rho$ is averaging over all possible chords AB of an obstacle (Kendall and Moran 1963). Thus, we have

$$\int\limits_{-\pi/2}^{\pi/2} d\varphi \int\limits_{D(\varphi)} v(AB) d\rho = \pi \langle D \rangle \int\limits_{0}^{\infty} v(AB) f(\xi) d\xi, \tag{23}$$

where $v(AB)$ is any function, defined on the set of chords.

Therefore, for the integral in Eq. (21) we get (doing integration of $\sin\varphi$ inside)

$$\frac{dC_{sca}}{d\Omega} = \frac{\pi \langle D \rangle}{\lambda^2} \int\limits_{0}^{\infty} f(\xi) d\xi \int\limits_{0}^{\xi} \int\limits_{0}^{\xi} J_0\big(\Delta k|\chi - \chi'|\big)|\chi - \chi'| d\chi d\chi', \tag{24}$$

$J_k(x)$ is the Bessel function of the kth order.

The integral over $d\chi d\chi'$ in Eq. (24) equals

$$\int\limits_{0}^{\xi} \int\limits_{0}^{\xi} J_0\big(\Delta k|\chi - \chi'|\big)|\chi - \chi'| d\chi d\chi' = \frac{2}{\Delta k^3} \mathrm{Ker}(\Delta k \xi), \tag{25}$$

where $\mathrm{Ker}(x)$ denotes the following function

$$\mathrm{Ker}(x) = \int_0^x J_1(t)tdt = \frac{\pi}{2}x[J_1(x)\,H_0(x) - J_0(x)\,H_1(x)], \tag{26}$$

where $H_k(x)$ is the Struve function.

Thus, the diffraction pattern is the integral transformation of the CLD with kernel:

$$\frac{dC_{sca}}{d\Omega} = \frac{2\pi S}{\lambda^2 \Delta k^3 a} \int_0^\infty \mathrm{Ker}(\Delta k\xi) f(\xi) d\xi. \tag{27}$$

Kernel is quite complex, so it could be more convenient to rewrite integral by making integration by parts and introducing the probability function $\Phi(\xi)$—the probability that a randomly taken chord is longer than ξ:

$$\Phi(\xi) = \int_\xi^\infty f(\xi')d\xi'. \tag{28}$$

Integration by parts gives

$$\int_0^\infty \mathrm{Ker}(\Delta k\xi) f(\xi) d\xi = \Delta k^2 \int_0^\infty \Phi(\xi) J_1(\Delta k\xi)\xi d\xi, \tag{29}$$

so the diffraction pattern happens to be a simple Hankel transform from the probability function $\Phi(\xi)$:

$$\frac{dC_{sca}}{d\Omega} = \frac{2\pi S}{\lambda^2 \Delta k\, a} \int_0^\infty \Phi(\xi) J_1(\Delta k\xi)\xi d\xi. \tag{30}$$

Equation (30) gives a simple expression for Fraunhofer diffraction pattern by an ensemble of chaotically oriented obstacles of arbitrary shape (strictly speaking, the shape variability is restricted here with the demand of convexity). As a case in point, let us consider a circular obstacle with diameter D. In this case the CLD is

$$\Phi(\xi) = \begin{cases} \frac{1}{D}\sqrt{D^2 - \xi^2}, & \xi \le D, \\ 0, & \xi > D, \end{cases} \tag{31}$$

and the mean chord is

$$a = \frac{\pi}{4} D. \tag{32}$$

Integration in Eq. (30) gives

$$\frac{dC_{sca}}{d\Omega} = \frac{D^2}{4\theta^2} J_1^2\left(\frac{\pi\,\theta}{\lambda} D\right), \tag{33}$$

which is the well-known function of Fraunhofer diffraction by a circle disk of diameter D(see, e.g., Hulst 1957).

This result shows that the Fraunhofer diffraction pattern is determined by the obstacle CLD rather than by its shape itself.

2.2 Diffraction by a Screen

Now we consider the screen, i.e., the case where the interference between different obstacles cannot be neglected. Generally speaking, as we consider the random screen, we cannot define a single obstacle or a single gap. Rather we can only talk about the chord statistics: distribution functions $f(\xi)$ and $g(\xi)$. The diffraction cross-section given by Eq. (19) in the case of a screen, perpendicular to the direction of incidence, is

$$\frac{dC_{sca}}{d\Omega} = \frac{1}{\lambda^2} \iint\limits_{\Sigma\,\Sigma'} \overline{\eta}(\mathbf{r})\overline{\eta}(\mathbf{r}') e^{i\,\Delta\mathbf{k}\cdot(\mathbf{r}-\mathbf{r}')} d^2\mathbf{r}\, d^2\mathbf{r}', \tag{34}$$

where $\overline{\eta}(\mathbf{r}) = 1 - \eta(\mathbf{r})$ is the complementary indicator function (1 for a gap, 0 for an obstacle) and Σ is the screen area, which is much greater than the mean obstacle or gap area, with infinity as a limit. Taking the complementary covariance $\overline{C}_2(\mathbf{r})$, analogous to that given by Eq. (3), and the auto-correlation function given by Eq. (7), we get

$$\frac{dC_{sca}}{d\Omega} = \frac{\Sigma}{\lambda^2} \int \overline{C}_2(\mathbf{r}) e^{i\,\Delta\mathbf{k}\cdot\mathbf{r}} d^2\mathbf{r} = \frac{\Sigma}{\lambda^2}\left[\phi(1-\phi)\int \gamma(\mathbf{r}) e^{i\,\Delta\mathbf{k}\cdot\mathbf{r}} d^2\mathbf{r} + \phi^2 \int e^{i\,\Delta\mathbf{k}\cdot\mathbf{r}} d^2\mathbf{r}\right], \tag{35}$$

where ϕ is the area fraction of gaps. The integral in the second term of Eq. (35) gives the Dirac delta-function:

$$\int e^{i\,\Delta\mathbf{k}\cdot\mathbf{r}} d^2\mathbf{r} = (2\pi)^2 \delta(\Delta\mathbf{k}) = \left(\frac{2\pi}{k}\right)^2 \delta(\boldsymbol{\theta}), \tag{36}$$

where $\boldsymbol{\theta}$ is the diffraction vector: $\boldsymbol{\theta} = (\theta_x, \theta_y) = (\theta\cos\varphi, \theta\sin\varphi)$. So the differential cross-section is

$$\frac{dC_{sca}}{d\Omega} = \phi(1-\phi)\frac{\Sigma}{\lambda^2}\int \gamma(\mathbf{r}) e^{i\,\Delta\mathbf{k}\cdot\mathbf{r}} d^2\mathbf{r} + \phi^2 \delta(\boldsymbol{\theta})\Sigma. \tag{37}$$

Expression (37) means that because of the interference between different parts of the screen, the part of incident light with weight $\phi^2 = (1-\beta)^2$, where β is the fraction of shadowing, is transmitted through the screen without any changes in the phase or direction. This conclusion is in complete agreement with the result obtained by Borovoi (2006) for a monolayer of optically hard particles. From now on, talking about diffraction, we will refer to the first term of Eq. (37) only. So, the diffraction efficiency Q^d (the diffraction cross-section per unit screen area) is

$$Q^d = \phi(1-\phi) = \beta\phi = \beta(1-\beta) = \frac{l_A l_c}{\pi}, \tag{38}$$

where we used Cauchy's formula Eq. (10). The brightness B of the screen, diffracting a wave of unit flux density, is

$$B = \frac{\beta(1-\beta)}{\lambda^2}\int \gamma(\mathbf{r})e^{i\,\Delta\mathbf{k}\cdot\mathbf{r}}d^2\mathbf{r}. \tag{39}$$

If the screen is azimuthally symmetric,

$$B = \frac{\beta(1-\beta)}{\lambda^2}2\pi\int_0^\infty \gamma(r)J_0(k\theta r)rdr. \tag{40}$$

The diffraction angular pattern (the phase function) is

$$p(\theta) = \frac{2\pi}{C_{sca}}\frac{dC_{sca}}{d\Omega} = k^2\int_0^\infty \gamma(r)J_0(k\theta r)rdr, \tag{41}$$

(it is normalized as $\int_0^\infty p(\theta)\theta d\theta = 1$).

For the exponential correlation function (Eq. (9)), the angular pattern is given by

$$p(\theta) = \frac{k^2 l_c^2}{\left(1+\Delta k^2 l_c^2\right)^{3/2}} = \frac{x^2}{\left(1+x^2\theta^2\right)^{3/2}}. \tag{42}$$

Equation (42) is the well-known function given by Wells (1973), which is a small-angle analog of the widely used Henyey–Greenstein function (Henyey and Greenstein 1941) and is used in the theory of small-angle light scattering, especially often in hydro-optics (e.g.,McLean and Voss 1991; Zege et al. 2006).

Now, we are going to express the diffraction pattern in terms of the screen CLDs. Making coordinates transformation (20), let us write Eq. (19) as

$$\frac{dC_{sca}}{d\Omega} = \frac{1}{\lambda^2}\int_{-\pi/2}^{\pi/2} d\varphi \int_{-X}^{X} d\rho \int_{-X}^{X}\int_{-X}^{X} \overline{\eta}(\rho,\varphi,\chi)\overline{\eta}(\rho,\varphi,\chi')e^{i\,\Delta k|\chi-\chi'|\sin\varphi}|\chi-\chi'|d\chi d\chi', \tag{43}$$

where we assume that coordinates ρ, χ, and χ' take values from $-X$ to X, which is much greater then $a+h$, with infinity as a limit.

Let straight line AB (defined by variables ρ and φ) intersects the obstacle-gap boundary at points ξ_n. Let points with an even index ξ_{2n} stand for the transition from gaps to obstacles when moving along the line in the direction from A to B and points with an odd index ξ_{2n+1} vice versa (see Fig. 4).

As function $\overline{\eta}(\rho, \varphi, \chi)$ is equal to 1 if χ belongs to interval (ξ_{2n-1}, ξ_{2n}) and equal to 0 for $\chi \in (\xi_{2n}, \xi_{2n+1})$, integral (43) becomes

$$\frac{dC_{sca}}{d\Omega} = \frac{1}{\lambda^2} \int\limits_{-\pi/2}^{\pi/2} d\varphi \int\limits_{-X}^{X} d\rho \sum_{n,m} \int\limits_{\xi_{2n-1}}^{\xi_{2n}} \int\limits_{\xi_{2m-1}}^{\xi_{2m}} e^{i\,\Delta k|\chi-\chi'|\sin\varphi} |\chi-\chi'| d\chi d\chi'. \tag{44}$$

As the screen is assumed to be azimuthally isotropic, integration over $d\rho$ provides averaging over different chords, so we have

$$\frac{dC_{sca}}{d\Omega} = \frac{2X}{\lambda^2} \int\limits_{-\pi/2}^{\pi/2} d\varphi \left\langle \sum_{n,m} \int\limits_{\xi_{2n-1}}^{\xi_{2n}} \int\limits_{\xi_{2m-1}}^{\xi_{2m}} e^{i\,k_y|\chi-\chi'|} |\chi-\chi'| d\chi d\chi' \right\rangle, \tag{45}$$

where we introduce the new variable

$$k_y = \Delta k \sin\varphi. \tag{46}$$

For integration, let us write

$$\begin{aligned} \frac{dC_{sca}}{d\Omega} &= \frac{2X}{\lambda^2} \int\limits_{-\pi/2}^{\pi/2} d\varphi \frac{\partial}{i\partial k_y} \left\langle \sum_{n,m} \int\limits_{\xi_{2n-1}}^{\xi_{2n}} \int\limits_{\xi_{2m-1}}^{\xi_{2m}} e^{i\,k_y|\chi-\chi'|} d\chi d\chi' \right\rangle \\ &= \frac{2X}{\lambda^2} \int\limits_{-\pi/2}^{\pi/2} d\varphi \frac{\partial}{i\partial k_y} \sum_{n=-\infty}^{\infty} \langle Sum_n \rangle \end{aligned}, \tag{47}$$

where

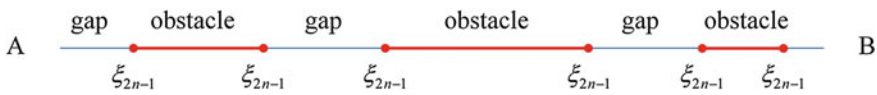

Fig. 4 Intersections of line AB with the obstacle-gap boundary

$$Sum_n = \int_{\xi_{2n-1}}^{\xi_{2n}} \int_{\xi_{2n-1}}^{\xi_{2n}} e^{i\,k_y|\chi-\chi'|} d\chi d\chi' + \sum_{m=n+1}^{\infty} \int_{\xi_{2n-1}}^{\xi_{2n}} \int_{\xi_{2m-1}}^{\xi_{2m}} e^{i\,k_y|\chi-\chi'|} d\chi d\chi'$$
$$+ \sum_{m=-\infty}^{n-1} \int_{\xi_{2n-1}}^{\xi_{2n}} \int_{\xi_{2m-1}}^{\xi_{2m}} e^{i\,k_y|\chi-\chi'|} d\chi d\chi' \tag{48}$$

It is obvious that all terms $\langle Sum_n \rangle$ are equal. For the summation with infinite limits, we assume

$$\sum_{n=-\infty}^{\infty} = \lim_{X\to\infty} \sum_{n=-X/(a+h)}^{X/(a+h)}, \tag{49}$$

so the summation over n in Eq. (47) gives

$$\sum_{n=-\infty}^{\infty} \langle Sum_n \rangle = \frac{2X}{a+h} \langle Sum_n \rangle, \tag{50}$$

and Eq. (47) becomes

$$\frac{dC_{sca}}{d\Omega} = \frac{4X^2}{\lambda^2(a+h)} \int_{-\pi/2}^{\pi/2} d\varphi \frac{\partial}{i\partial k_y} \langle Sum_n \rangle. \tag{51}$$

The expression for the screen brightness due to diffraction is then:

$$B = \frac{1}{(2X)^2} \frac{dC}{d\Omega} = \frac{1}{\lambda^2(a+h)} \int_{-\pi/2}^{\pi/2} d\varphi \frac{\partial}{i\partial k_y} \langle Sum_n \rangle. \tag{52}$$

To calculate the integrals in Eq. (48) we introduce the Fourier transforms of functions $f(\xi)$ and $g(\xi)$:

$$F = \int_0^{\infty} \exp\big(ik_y\xi\big) f(\xi)\, d\xi, \quad G = \int_0^{\infty} \exp\big(ik_y\xi\big) g(\xi)\, d\xi. \tag{53}$$

These transforms F and G are the characteristic functions for random variables $\xi_{2n+1} - \xi_{2n}$ and $\xi_{2n} - \xi_{2n-1}$, respectively. In the vicinity of point $k_y = 0$, these functions have the series expansion

$$F \approx 1 + ik_y a, \quad G \approx 1 + ik_y h. \tag{54}$$

According to our statistical approach, difference $\xi_{2n+1} - \xi_{2n}$ is an independent random variable with distribution $f(\xi)$ and mean a; difference $\xi_{2n} - \xi_{2n-1}$ is an independent random variable with distribution $g(\xi)$ and mean h. This means that averaging expressions $\exp\big(ik_y(\xi_{2n+1} - \xi_{2n})\big)$ and $\exp\big(ik_y(\xi_{2n} - \xi_{2n-1})\big)$ gives

$$\begin{aligned}\big\langle \exp\big(ik_y(\xi_{2n+1} - \xi_{2n})\big)\big\rangle &= F,\\ \big\langle \exp\big(ik_y(\xi_{2n} - \xi_{2n-1})\big)\big\rangle &= G.\end{aligned} \tag{55}$$

Difference $\xi_{2n+2} - \xi_{2n}$ is a random variable, which is the sum of two independent variables: $\xi_{2n+1} - \xi_{2n}$ and $\xi_{2n+2} - \xi_{2n+1}$; therefore, its distribution is the convolution of functions $f(\xi)$ and $g(\xi)$ ($\int_0^\xi f(\xi - \xi')g(\xi')\,d\xi'$) and its characteristic function is equal to product FG. More general, variable $\xi_{2m+1} - \xi_{2n+1}$ is the sum of $m - n$ independent variables with distribution $f(\xi)$ and $m - n$ variables with distribution $g(\xi)$ (we put $m > n$ for definiteness). Therefore, its characteristic function is $(FG)^{m-n}$. In the same way, for averaging expressions of the kind $\exp\big(ik_y(\xi_k - \xi_n)\big)$ we have

$$\begin{aligned}\big\langle \exp\big(ik_y(\xi_{2m-1} - \xi_{2n-1})\big)\big\rangle &= (FG)^{m-n},\\ \big\langle \exp\big(ik_y(\xi_{2m} - \xi_{2n})\big)\big\rangle &= (FG)^{m-n},\\ \big\langle \exp\big(ik_y(\xi_{2m-1} - \xi_{2n})\big)\big\rangle &= F(FG)^{m-n-1},\\ \big\langle \exp\big(ik_y(\xi_{2m} - \xi_{2n-1})\big)\big\rangle &= G(FG)^{m-n}.\end{aligned} \tag{56}$$

Let us come back to Eq. (48). The first term equals

$$\begin{aligned}\int_{\xi_{2n-1}}^{\xi_{2n}}\int_{\xi_{2n-1}}^{\xi_{2n}} e^{i\,k_y|\chi-\chi'|}d\chi d\chi' &= 2\int_0^{\xi_{2n}-\xi_{2n-1}} dx \int_0^x e^{i\,k_y x'}dx' \\ &= 2\frac{1-\exp\big(ik_y(\xi_{2n}-\xi_{2n-1})\big)}{k_y^2} + 2i\,\frac{(\xi_{2n}-\xi_{2n-1})}{k_y}\end{aligned}, \tag{57}$$

and after averaging it gives

$$\left\langle \int_{\xi_{2n-1}}^{\xi_{2n}}\int_{\xi_{2n-1}}^{\xi_{2n}} e^{i\,k_y|\chi-\chi'|}d\chi d\chi' \right\rangle = 2\left(\frac{1-G}{k_y^2} + i\,\frac{h}{k_y}\right). \tag{58}$$

The second and third terms in Eq. (48) describe the interference of the different parts of the screen. For the second term in Eq. 48, we have $m > n$ and the integral equals

$$\int_{\xi_{2n-1}}^{\xi_{2n}}\int_{\xi_{2m-1}}^{\xi_{2m}} e^{i\,k_y|\chi-\chi'|}d\chi d\chi'\Bigg|_{m>n} = \frac{1}{k_y^2}\exp\big(i\,k_y(\xi_{2m}-\xi_{2n}\big) + \frac{1}{k_y^2}\exp\big(i\,k_y(\xi_{2m-1}-\xi_{2n-1}\big)$$

$$-\frac{1}{k_y^2}\exp\big(i\,k_y(\xi_{2m-1}-\xi_{2n})-\frac{1}{k_y^2}\exp\big(i\,k_y(\xi_{2m}-\xi_{2n-1})\big). \tag{59}$$

And averaging Eq. 59, according to Eqs. (56), gives

$$\left\langle \int\limits_{\xi_{2n-1}}^{\xi_{2n}} \int\limits_{\xi_{2m-1}}^{\xi_{2m}} e^{i\,k_y|\chi-\chi'|} d\chi d\chi' \right\rangle \Bigg|_{m>n} = -\frac{(1-G)^2 F}{k_y^2}(FG)^{m-n-1}. \tag{60}$$

The third term in Eq. (48) is obviously equal the second one. So, we have for Eq. (48)

$$\langle Sum_n \rangle = \frac{2}{k_y^2}\left(1-G+ik_y h-(1-G)^2 F\sum_{m=0}^{\infty}(FG)^m\right). \tag{61}$$

The sum in Eq. (61) converges for $|FG| < 1$ and equals

$$\sum_{m=0}^{\infty}(FG)^m = \frac{1}{1-FG}. \tag{62}$$

However, for $k_y \to 0$, expression (62) diverges as (see expansion (54))

$$\frac{1}{1-FG} \approx \frac{1}{-ik_y(a+h)}, \tag{63}$$

so the entire integral in Eq. (51) also diverges. Note that this divergence takes place not only for the strictly forward direction but also for all angles of scattering because $k_y = 0$ not only for $\Delta k = 0$ but also for $\sin\varphi = 0$.

To treat this divergence correctly let us note that the sum in Eqs. (61) and (62) is treated as a limit

$$\sum_{m=0}^{\infty}(FG)^m = \lim_{X\to\infty}\sum_{m=0}^{X/(a+h)}(FG)^m = \lim_{X\to\infty}\frac{1-(FG)^{X/(a+h)}}{1-FG}. \tag{64}$$

Value $(FG)^{X/(a+h)}$ is unit at $FG = 1$ and zero at $|FG| < 1$, i.e.,

$$\lim_{X\to\infty}(FG)^{X/(a+h)} = \begin{cases} 1, & \text{if } k_y = 0, \\ 0, & \text{if } k_y > 0. \end{cases} \tag{65}$$

Using expansion (54), we can write

$$\lim_{\substack{X\to\infty\\ k_y\to 0}} (FG)^{X/(a+h)} = \lim_{\substack{X\to\infty\\ k_y\to 0}} \big(1 + ik_y(a+h)\big)^{X/(a+h)} = \lim_{X\to\infty} e^{ik_yX}. \tag{66}$$

So, let us add and subtract the principal term regarding k_y (Eq. 63) in the third term of Eq. (61)

$$-\frac{(1-G)^2F}{k_y^2}\sum_{m=0}^{\infty}(FG)^m = -\frac{(1-G)^2F}{k_y^2}\frac{1}{1-FG} - \frac{h^2}{-ik_y(a+h)} + h^2\lim_{X\to\infty}\frac{1-e^{ik_yX}}{-ik_y(a+h)}. \tag{67}$$

So, for Eq. (61) we have

$$\langle Sum_n\rangle = \frac{2}{k_y^2}\left(\frac{(1-F)(1-G)}{1-FG} + ik_y\frac{ah}{(a+h)}\right) + i\frac{2h^2}{(a+h)}\lim_{X\to\infty}\frac{1-e^{ik_yX}}{k_y}. \tag{68}$$

The second term in Eq. (68) gives

$$\begin{aligned}
&\frac{1}{\lambda^2(a+h)}\int_{-\pi/2}^{\pi/2} d\varphi\frac{\partial}{i\partial k_y}2i\frac{h^2}{(a+h)}\lim_{X\to\infty}\frac{1-\exp(ik_yX)}{k_y}\\
&= \frac{2h^2}{\lambda^2(a+h)^2}\lim_{X\to\infty}\int_{-\pi/2}^{\pi/2} d\varphi\frac{\partial}{\partial k_y}\frac{1-\exp(ik_yX/2)}{k_y}\\
&= \frac{2\phi^2}{\lambda^2}\lim_{X\to\infty}\pi X\frac{J_1(\Delta kX)}{\Delta k} = \frac{2\pi\phi^2}{\lambda^2}\frac{\delta(\Delta k)}{\Delta k} = \phi^2\frac{\delta(\theta)}{2\pi\theta},
\end{aligned} \tag{69}$$

where $\delta(\theta)$ is the Dirac delta-function.

Expression gives the portion of the directly transmitted light in complete agreement with Eq. (37).

Substituting only the first term of Eq. (68) into Eq. (52), we get the mathematically correct expression for the diffracted light brightness

$$B = \frac{1}{\lambda^2(a+h)}\int_{-\pi/2}^{\pi/2} d\varphi\frac{\partial}{i\partial k_y}\frac{2}{k_y^2}\left(\frac{(1-F)(1-G)}{1-FG} + ik_yl_c\right). \tag{70}$$

Equation (70) describes the diffraction itself. Let us denote the function under the differential operator in Eq. (70) as $W(k_y)$:

$$W(k_y) = \frac{2}{k_y^2}\left(\frac{(1-F)(1-G)}{1-FG} + ik_yl_c\right), \tag{71}$$

and consider it as the Fourier transform of $w(r)$ defined for $r \geq 0$. Then Eq. (70) becomes

$$B = \frac{1}{\lambda^2(a+h)} \int_{-\pi/2}^{\pi/2} d\varphi \frac{\partial}{i\partial k_y} W(k_y) = \frac{1}{\lambda^2(a+h)} \int_0^\infty w(r)dr \int_{-\pi/2}^{\pi/2} d\varphi \frac{\partial}{i\partial k_y} e^{ik_y r}$$
$$= \frac{1}{\lambda^2(a+h)} \int_0^\infty w(r)dr \int_{-\pi/2}^{\pi/2} d\varphi\, r\, e^{ik_y r} = \frac{\pi}{\lambda^2(a+h)} \int_0^\infty w(r) J_0(\Delta k\, r) r dr. \tag{72}$$

Comparing it with Eq. (40), we get

$$\gamma(r) = \frac{w(r)}{2l_c}, \tag{73}$$

or

$$k_y \Gamma(k_y) = \frac{1}{k_y l_c} \frac{(1-F)(1-G)}{1-FG} + i, \tag{74}$$

where $\Gamma(k_y)$ is the Fourier transform of the auto-correlation function γ(r).

Equation (74) expresses the auto-correlation function—and, as a consequence, the diffraction pattern—in terms of the screen characteristic functions, or the CLDs in Fourier space. This relation was derived by several authors in completely different ways. Roberts and Torquato (1999) expressed the Laplace transform of the two-point covariance $C_2(r)$. Gille (2000) gave this relation in the initial space coordinates, using multiple convolutions. (His expression corresponds to ours except for the last term containing the delta function, though.)

2.3 Discussion

We defined the diffraction efficiency Q^d as the diffraction cross-section per unit screen area. A more common way, especially when dealing with sparsely packed ensembles, is to define it as the diffraction cross-section per obstacle area, i.e., Q^d/β. In the limit of a sparse ensemble of obstacles this value is equal to unit:

$$\frac{Q^d}{\beta} = 1 - \beta \xrightarrow[\beta \to 0]{} 1. \tag{75}$$

Equation (75) demonstrates, however, that in the case of a densely packed ensemble it is less than unit because of the interference between obstacles.

The diffraction pattern of a random screen is expressed in terms of the auto-correlation function (Eqs. (40) and (41)), which in its turn is expressed in terms of the CLDs. These expressions are symmetric regarding a and h (F and G). This is in accordance to Babinet's principle: if we exchange obstacles and gaps, the diffraction pattern (and also the diffraction efficiency Q^d) will remain the same.

If there are no free spaces between obstacles ($h = 0$ and, consequently, $G = 1$) or there are no obstacles ($a = 0$ and $F = 1$), then the correlation function goes to 0: the screen is fully blind or open and there is no diffracted light.

In contrast, if the obstacles are far from each other—a sparse ensemble—so that $h \to \infty$ and, consequently, $G = 0$, the correlation function is determined by distribution $f(\xi)$ only and expression (41) is equivalent to Eq. (30) for an ensemble of non-coherent scatterers. In this case $l_c = a$ and

$$k_y^2 a\Gamma(k_y) = 1 - F + ik_y a. \tag{76}$$

Given that the Fourier image of the second derivative of the correlation function is

$$\mathbf{F}\{\gamma''(r)\} = -\gamma'(0) + ik_y\gamma(0) - k_y^2\Gamma = \frac{1}{l_c} + ik_y - k_y^2\Gamma, \tag{77}$$

we find:

$$f(\xi) = a\gamma''(\xi), \tag{78}$$

which is the well-known expression for the CLD of a single particle in terms of its correlation function derived in the classical works of Guinier and Fournet (1955), Porod (1982), or Feigin and Svergun (1987). It is necessary to note that the relationships between the auto-correlation function and the CLD given by Eqs. (74), (76), and (78) are independent of the number of dimensions, so they remain valid also for three-dimensional space. However, the convexity of a particle, the requirement that any line intersecting a particle has only one segment within it, is a necessary requirement for Eq. (78) at any dimensionality.

It is of interest also to compare the obtained solution (42) with the approximating formula found in (Malinka 2010), where the scattering function of an azimuthally symmetric sparse ensemble of arbitrary shaped obstacles is written in the form

$$p(\theta) = \frac{1}{2\nu}\exp\left(-\frac{\theta^2}{2\nu}\right) + \frac{\rho^2}{2\left(1+\rho^2\theta^2\right)^{3/2}}, \tag{79}$$

where ν^{-1} is proportional to value $\langle S^2\rangle / \langle S\rangle$, the average square of the obstacle area per average area, and ρ is determined by value $\langle L\rangle / \langle S\rangle$, the average obstacle perimeter per average area. This approximating formula was derived through completely different reasons. However, the more strict investigation performed here leads to

a similar result. The average square of the obstacle area per average area approaches infinity for the case of a screen, and parameter v goes to zero, so the first term in Eq. (79) transforms to the delta-function, being an analog of Eqs. (37) or (69). Ratio $\langle L\rangle / \langle S\rangle$ is equal (see Eq. (10)) to

$$\frac{\langle L\rangle}{\langle S\rangle} = \frac{\pi}{a+b}\frac{1}{\beta} = \frac{\pi}{a}, \tag{80}$$

that is, determined only by the mean chord a, which is the limit of l_c for $h \to \infty$.

3 Rayleigh–Gans Approximation

The Rayleigh–Gans (RG) approximation implies that the field inside a particle is approximately equal to the incident field and every point inside the particle is a secondary source for the scattered field. This condition is met when both $n - 1$ and the phase shift inside the particle are negligible:

$$n - 1 \ll 1 \tag{81}$$

$$(n - 1)x \ll 1, \tag{82}$$

where n is the particle refractive index and x is the particle dimensionless size. Perhaps because of its widespread use in quantum mechanics, where it is called the first Born approximation, the stereological approach, as for our knowledge, was first applied exactly to this approximation (Dirac 1943). Since then, the stereological approach has been widely applied to small-angle scattering of X-rays and neutrons (Guinier and Fournet 1955; Porod 1982; Feigin and Svergun 1987; Gille 2000; Gille et al. 2002). The popularity of the stereological approach to these problems is due not only to its simplicity but also to the validity of the Rayleigh–Gans–Born approximation for this kind of problems, given the high accuracy of Eqs. (81) and (82) for X-ray and neutron scattering. In contrast, its applications to light scattering problems are rather limited because scattering particles are usually much larger than the wavelength ($x \gg 1$) and this condition is rarely met simultaneously with Eq. (82).

3.1 Solution for a Single Particle

Although the demand given by Eq. (82) is opposite to that of Fraunhofer diffraction—which is $(n-1)x \gg 1$—mathematically these approaches are completely analogous. The amplitude matrix elements in the RG approximations are (Hulst 1957; Bohren and Huffman 1983)

$$S_1 = -i\frac{k^3}{2\pi}(m-1)\int\limits_V \exp(i\Delta\mathbf{k}\cdot\mathbf{r})d^3\mathbf{r}, \quad S_2 = S_1\cos\theta, \tag{83}$$

where $m = n + i\kappa$ is the complex refractive index of the particle and $\Delta\mathbf{k}$ is the change of the wavevector due to scattering:

$$\begin{aligned} &\Delta\mathbf{k} = \mathbf{k} - \mathbf{k}_0, \\ &|\Delta\mathbf{k}| = \Delta k = 2k\sin\frac{\theta}{2}, \end{aligned} \tag{84}$$

where θ is the scattering angle. The integral is taken over the particle volume V. The differential cross-section is

$$\frac{dC_{sca}}{d\Omega} = \frac{|S_1|^2 + |S_2|^2}{2k^2} = \frac{1+\cos^2\theta}{2k^2}|S_1|^2. \tag{85}$$

Substituting Eq. (83) into Eq. (85), we get the equation, analogous to Eq. (19):

$$\frac{dC_{sca}}{d\Omega} = \frac{1+\cos^2\theta}{8\pi^2}k^4|m-1|^2\left\langle \iint\limits_{V\,V'} e^{i\,\Delta\mathbf{k}\cdot(\mathbf{r}-\mathbf{r}')}d^3\mathbf{r}\,d^3\mathbf{r}' \right\rangle. \tag{86}$$

To take the integral in Eq. (86), let us make the coordinates transformation, analogous to Eq. (20):

$$\begin{aligned} x &= \chi(\cos\varphi\cos\vartheta\cos\psi - \sin\varphi\sin\psi) + \rho\cos\varphi\sin\vartheta \\ y &= \chi(-\sin\varphi\cos\vartheta\cos\psi - \cos\varphi\sin\psi) - \rho\sin\varphi\sin\vartheta, \\ z &= \chi\sin\vartheta\cos\psi + \rho\cos\vartheta \end{aligned} \tag{87}$$

and the same for $\mathbf{r}'$ with χ' in place of χ. Here $(\varphi, \vartheta, \psi)$ are Euler's rotational angles. The geometrical interpretation is shown in Fig. 5.

The z-axis matches the direction of vector $\Delta\mathbf{k}$.Two points inside the particle with radius-vectors $\mathbf{r}$ and $\mathbf{r}'$ define a straight line (AB), which is taken as the new z'-axis. Its direction is given by (θ, φ), the polar and azimuth angles. Radius-vector $\boldsymbol{\rho}$ is perpendicular to line AB and has polar coordinates (ρ, ψ) in the $x'y'$-plane. χ and χ' are the distances form point $\boldsymbol{\rho}$ to points $\mathbf{r}$ and $\mathbf{r}'$, respectively.

The Jacobian determinant of transformation (87) is

$$\frac{D(x, y, z, x', y', z')}{D(\chi, \chi', \rho, \psi, \theta, \varphi)} = |\chi - \chi'|^2\rho\sin\theta, \tag{88}$$

so the integral in Eq. (86) in coordinates $(\chi, \chi', \rho, \psi, \theta, \varphi)$ has the form

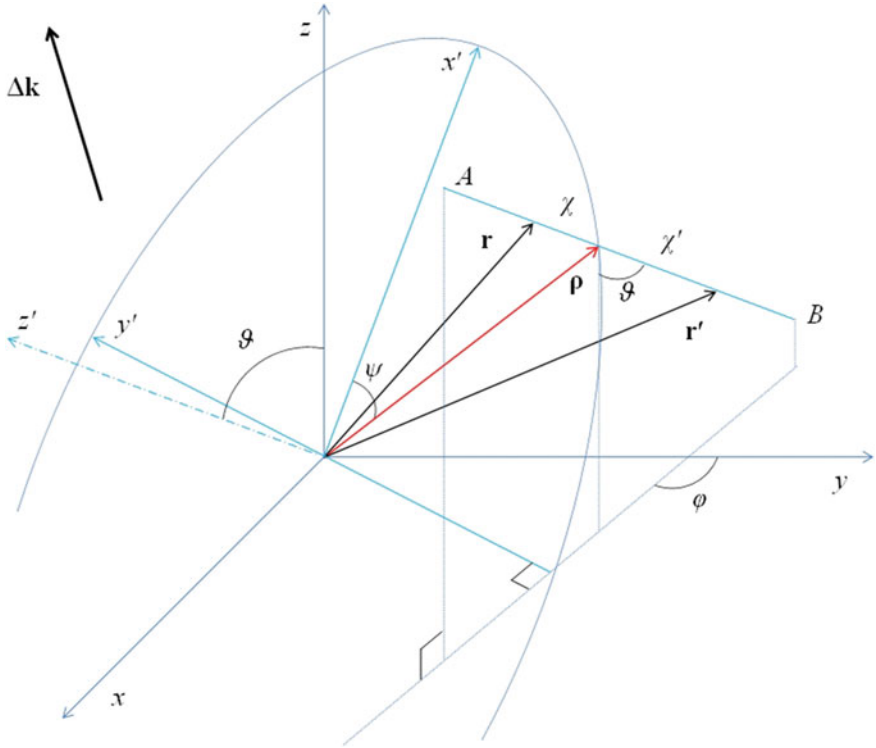

Fig. 5 Geometrical interpretation of transformation (87)

$$\iint\limits_{V\,V'} e^{i\,\Delta\mathbf{k}\cdot(\mathbf{r}-\mathbf{r}')} d^3\mathbf{r}\, d^3\mathbf{r}' = \int\limits_{2\pi} \sin\theta d\theta d\varphi \int\limits_{S_\perp(\theta,\varphi)} \rho d\rho d\psi \int\limits_A^B \int\limits_A^B e^{i\,\Delta k|\chi-\chi'|\cos\alpha} |\chi-\chi'|^2 d\chi d\chi'. \tag{89}$$

Here the integration over $d\chi d\chi'$ gives a function of ξ, the length of chord AB, the integration over $\rho d\rho d\psi$ means averaging over $S_\perp(\theta,\varphi)$, the area of the particle projection in the direction (θ,φ), and the integration over $\sin\theta d\theta d\varphi$ yields averaging over the direction of line AB (the integration is taken over the hemisphere because the opposite directions of line AB are identical).

For an ensemble of chaotically oriented particles, we should average Eq. (89) over α, the angle between $\Delta\mathbf{k}$ and line AB:

$$\left\langle \iint\limits_{V\,V'} e^{i\,\Delta\mathbf{k}\cdot(\mathbf{r}-\mathbf{r}')} d^3\mathbf{r}\, d^3\mathbf{r}' \right\rangle = \frac{1}{2}\int\limits_0^\pi \sin\alpha d\alpha \iint\limits_{V\,V'} e^{i\,\Delta k|\mathbf{r}-\mathbf{r}'|\cos\alpha} d^3\mathbf{r}\, d^3\mathbf{r}' = \iint\limits_{V\,V'} \frac{\sin\Delta k|\mathbf{r}-\mathbf{r}'|}{\Delta k|\mathbf{r}-\mathbf{r}'|} d^3\mathbf{r}\, d^3\mathbf{r}'$$

$$= 2\pi\langle S_\perp\rangle \int\limits_0^\infty f(\xi) d\xi \int\limits_0^\xi \int\limits_0^\xi \frac{\sin\Delta k|\chi-\chi'|}{\Delta k} |\chi-\chi'| d\chi d\chi'$$

$$=4\pi\langle S_\perp\rangle\int_0^\infty \frac{2-2\cos\Delta k\xi-\Delta k\xi\sin\Delta k\xi}{\Delta k^4}f(\xi)d\xi. \tag{90}$$

Finally, the differential cross-section is

$$\frac{dC_{sca}}{d\Omega}=\frac{1+\cos^2\theta}{2\pi}|m-1|^2k^4\langle S_\perp\rangle\int_0^\infty \frac{2-2\cos\Delta k\xi-\Delta k\xi\sin\Delta k\xi}{\Delta k^4}f(\xi)d\xi. \tag{91}$$

Introducing the Fourier transform $F$of the CLD, we get

$$\frac{dC_{sca}}{d\Omega}=\frac{1+\cos^2\theta}{2\pi}|m-1|^2k^4\langle S_\perp\rangle\frac{2-2\mathrm{Re}F(\Delta k)+\Delta k\mathrm{Re}F'(\Delta k)}{\Delta k^4}. \tag{92}$$

The total scattering cross-section is

$$C_{sca}=2\pi\int_0^\pi \frac{dC_{sca}}{d\Omega}\sin\theta d\theta=2|m-1|^2\langle S_\perp\rangle\int_0^\infty \mathrm{Ker}(k\xi)f(\xi)d\xi, \tag{93}$$

with the integral kernel

$$\mathrm{Ker}(x)=\frac{x^2}{2}-\ln 2x+\mathrm{Ci}(2x)+\frac{1}{2x^2}+\left(\frac{1}{4}-\frac{1}{2x^2}\right)\cos 2x-\frac{\sin 2x}{x}+\frac{3}{4}-\gamma, \tag{94}$$

where $\mathrm{Ci}(x)$ is the cosine integral and γ is Euler's constant.

As was mentioned earlier, the case when particles are much larger than the wavelength ($ka\gg 1$) is of great practical interest. In this case, the first term in Eq. (94) ($\sim\xi^2$) is leading and the scattering cross-section approximately equals

$$C_{sca}=k^2|m-1|^2\langle\xi^2\rangle\langle S_\perp\rangle. \tag{95}$$

The scattering efficiency Q_{sca} is the scattering cross-section per mean projection area:

$$Q_{sca}=2|m-1|^2\langle\mathrm{Ker}(k\xi)\rangle, \tag{96}$$

or for large particles

$$Q_{sca}=|m-1|^2k^2\langle\xi^2\rangle. \tag{97}$$

Equation (97) was derived in (Malinka, 2020) by the asymptotic method of stationary phase, which required rather cumbersome calculations, while the stereological approach gives it immediately as a leading term for large particles.

The CLD in a spherical particle of diameter R is

$$f(\xi) = \begin{cases} \frac{\xi}{2R^2}, \xi \leq 2R, \\ 0, \quad \xi > 2R. \end{cases} \tag{98}$$

In this case, Eqs. (91) and (92) gives

$$\frac{dC_{sca}}{d\Omega} = \frac{1+\cos^2\theta}{2}|m-1|^2 k^4 \frac{4(\sin\Delta kR - \Delta kR\cos\Delta kR)^2}{\Delta k^6}, \tag{99}$$

which is the well-known expression for a spherical scatterer with the refractive index close to 1 in the RG approximation (Hulst 1957; Bohren and Huffman 1983).

Here are some quantities, useful in radiative transfer calculations, obtained in a limit of large particles, i.e., as the asymptotic behavior at $\xi \to \infty$. The average cosine of the scattering angle

$$g = 1 - \frac{2}{k^2\langle\xi^2\rangle}\int_{1/k}^{\infty}(\ln 2k\xi - 1 + \gamma)f(\xi)d\xi, \tag{100}$$

the fraction of scattering into the backward hemisphere

$$b = \frac{1-\ln 2}{k^2\langle\xi^2\rangle}, \tag{101}$$

and the lidar backscattering efficiency

$$Q_b = \frac{4\pi}{\langle S_\perp\rangle}\frac{dC_{sca}(\pi)}{d\Omega} = \frac{|m-1|^2}{2}. \tag{102}$$

The last quantity determines a lidar backscattering signal. As seen, in the RG approximation, it depends on the refractive index only.

It is interesting to compare these formulas with the results obtained in (Malinka 2011b, 2020) by the asymptotic method of stationary phase.

3.2 Densely Packed Random Medium

For the case of porous material with the refractive index close to unit, Eq. (83) takes the form

$$S_1 = -i\frac{k^3}{2\pi}(m-1)\int \eta(\mathbf{r})\exp(i\,\Delta\mathbf{k}\cdot\mathbf{r})d^3\mathbf{r}, \tag{103}$$

and the scattering cross-section is given by

$$\frac{dC_{sca}}{d\Omega} = \frac{1+\cos^2\theta}{8\pi^2}k^4|m-1|^2\left\langle \iint\limits_{V\,V'} \eta(\mathbf{r})\eta(\mathbf{r}')e^{i\,\Delta\mathbf{k}\cdot(\mathbf{r}-\mathbf{r}')}d^3\mathbf{r}\,d^3\mathbf{r}'\right\rangle. \tag{104}$$

As the integral in Eq. (104) is completely analogous to that in Eq. (34), we can write immediately

$$\frac{dC_{sca}}{d\Omega} = \frac{1+\cos^2\theta}{8\pi^2}k^4|m-1|^2 V\beta(1-\beta)\int \gamma(\mathbf{r})e^{i\,\Delta\mathbf{k}\cdot\mathbf{r}}d^3\mathbf{r}, \tag{105}$$

where V is the sample volume, which is much larger than the typical cell volume $(a+h)^3$. In Eq. (105), we have omitted the term with the delta-function, which is indistinguishable from the incident beam.

The differential cross-section per unit volume is the differential scattering coefficient $\beta(\theta)$ also called the volume scattering function, particularly in hydrooptics (see, e.g., Jerlov 1968; Kopelevich 1983). In our problem, it equals

$$\beta(\theta) = \frac{1}{V}\frac{dC_{sca}}{d\Omega} = \frac{1+\cos^2\theta}{8\pi^2}k^4|m-1|^2\beta(1-\beta)\int \gamma(\mathbf{r})e^{i\,\Delta\mathbf{k}\cdot\mathbf{r}}d^3\mathbf{r}. \tag{106}$$

Given the azimuthal symmetry, we can write

$$\beta(\theta) = \frac{1+\cos^2\theta}{2\pi}k^4|m-1|^2\beta(1-\beta)\int \gamma(r)\frac{\sin\Delta kr}{\Delta kr}r^2dr. \tag{107}$$

For exponential correlation function, Eq. (107) becomes:

$$\begin{aligned}\beta(\theta) &= \frac{1+\cos^2\theta}{2\pi}k^4|m-1|^2\beta(1-\beta)\frac{2l_c^3}{\left(1+\Delta k^2 l_c^2\right)^2}\\ &= \frac{1+\cos^2\theta}{4\pi}|m-1|^2 s_V\frac{k^4 l_c^4}{\left(1+\Delta k^2 l_c^2\right)^2}.\end{aligned} \tag{108}$$

the result obtained by Debye et al. (1957). The scattering pattern in terms of the CLD is still given by relationship (74).

4 Wentzel–Kramers–Brillouin Approximation and Anomalous Diffraction

In the framework of the Wentzel–Kramers–Brillouin (WKB) approximation, the electric field inside a particle $\mathbf{E}_{in}$ is given by the following equation (Wentzel 1926; Kramers 1926; Brillouin 1926):

$$\mathbf{E}_{in} = \mathbf{E}_0 \frac{1}{\sqrt{m(\mathbf{r})}} \exp\left[ik \int m(\mathbf{r}) dz\right], \tag{109}$$

where $\mathbf{E}_0$ is the initial field amplitude (we omit the term $e^{-i\omega t}$) and $m = n + i\kappa$ is the complex refractive index, which, in general, depends on the coordinate $\mathbf{r}$. The z-axis matches the wave propagation direction.

The WKB approximation is valid for particles with the refractive index close to 1 and accounts correctly for the phase shift, regardless of its magnitude. This means that its range of applicability defined by the condition

$$|m - 1| \ll 1, \tag{110}$$

is much wider than that of the RG approximation because the requirement given by Eq. (82) is much stronger than Eq. (110). Many particles of practical interest have the refractive index close to that of a surrounding medium and at the same time the size far exceeding the wavelength of visible light. Cases in point are cells in biological tissues like erythrocytes in blood (Duck 1990), phytoplankton in sea waters (Kopelevich 1983), brine inclusions in sea ice (Light 2010), liquid crystals in polymers (Loiko et al. 2016), and so on.

Physically, Eq. (109) describes a wave that does not change its direction and propagates with the phase corresponding to the optical path length in the substance; thus, the WKB approximation is closely related to the eikonal approximation (see, e.g., Born and Wolf 1968). Also such acknowledged approaches as the RG approximation, van de Hulst anomalous diffraction, and Fraunhofer diffraction, follow from the WKB approximation in various limiting cases (Klett and Sutherland 1992; Lopatin and Shepelevich 1996).

In optics, some authors use factor $2/(m+1)$ instead of $1/\sqrt{m}$ (Ishimaru 1978; Klett and Sutherland 1992). These two factors are equal under assumption (110) to the first order of $(m-1)$, and factor $2/(m+1)$ can be treated as the Fresnel transmission coefficient at normal incidence.

4.1 Single Particle

In what follows we will only consider homogeneous particles with $n > 1$. For the homogeneous particle, the integral in Eq. (109) takes the form

$$\mathbf{E}_{in} = \mathbf{E}_0 \frac{1}{\sqrt{m}} \exp[i\,k\,m\,(z - z_1(\mathbf{r}_\perp)) + i\,k\,z_1(\mathbf{r}_\perp)], \tag{111}$$

where the sign $\perp$ denotes the projection of a vector onto the xy-plane, and function $z_1(\mathbf{r}_\perp)$ determines the lower part of the particle surface (see Fig. 6).

The strict expression for the amplitude scattering function $\mathbf{f}$ is (Ishimaru 1978)

$$\mathbf{f} = \frac{1}{4\pi} \int\limits_V \left\{-\mathbf{k} \times \left[\mathbf{k} \times \mathbf{E}_{in}(\mathbf{r}) / E_0\right]\right\} \left[m^2(\mathbf{r}) - 1\right] e^{-i\,\mathbf{k}\cdot\mathbf{r}} dV, \tag{112}$$

where the integral is taken over the particle volume V. So, the amplitude scattering matrix in the WKB approximation is

$$S_1 = -i \frac{k^3}{2\pi}(m-1) \int\limits_V \exp\left[i\,k\,m\,(z - z_1) + i\,k\,z_1 - i\,k\,z\,\mu - i\,\mathbf{k}_\perp \cdot \mathbf{r}_\perp\right] dV, \quad S_2 = S_1\,\mu\,, \tag{113}$$

where $\mu = \cos\theta$ is the cosine of the scattering angle θ.

The RG approximation follows from the WKB approximation as the first term of the order $|m - 1|\,x$, where x is the dimensionless particle size. Formally, if we put $m = 1$ in the integrand in Eq. (113), we will get the expression for the RG approximation given by Eq. (83).

Doing integration over z in Eq. (113), we have

$$S_1 = \frac{k^2}{2\pi} \frac{m-1}{m-\mu} \int\limits_{S_\perp} \left(1 - e^{i\,k\,(m-\mu)\xi(\mathbf{r}_\perp)}\right) e^{i\,k\,z_1(\mathbf{r}_\perp)(1-\mu) - i\,\mathbf{k}_\perp \cdot \mathbf{r}_\perp} dx dy, \tag{114}$$

where $\xi(\mathbf{r}_\perp) = z_2(\mathbf{r}_\perp) - z_1(\mathbf{r}_\perp)$.

Van de Hulst (1957)anomalous diffraction appears as a small-angle limit of the WKB approximation, i.e., if one put $\mu = 1$ in Eq. (114):

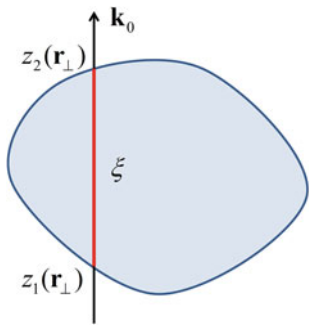

Fig. 6 Diagram of a scattering particle

$$S_1 = \frac{k^2}{2\pi} \int\limits_{S_\perp} \left(1 - e^{i\,k\,(m-1)\xi(\mathbf{r}_\perp)}\right) e^{-i\,\mathbf{k}_\perp \cdot \mathbf{r}_\perp} dx dy. \tag{115}$$

Fraunhofer diffraction follows from Eq. (115) if a particle is optically hard. Indeed, if $k\,(m-1)\xi \gg 1$, the first term in the integrand in Eq. (115) vanishes because of the fast oscillations of the exponential function, and Eq. (115) turns into Eq. (17).

We can easily get the extinction cross-section in the WKB approximation from Eq. (114) through the optical theorem:

$$C_{ext} = \frac{4\pi}{k^2} \mathrm{Re}[S_1(\theta = 0)] = 2\mathrm{Re} \int\limits_{S_\perp} (1 - \exp[ik(m-1)\xi])d^2\mathbf{r}_\perp. \tag{116}$$

Considering an ensemble of particles, we get

$$C_{ext} = 2\langle S_\perp \rangle \mathrm{Re}[1 - F(k(m-1))], \tag{117}$$

where F is the characteristic function. For the extinction efficiency Q_{ext} we have:

$$Q_{ext} = \frac{C_{ext}}{\langle S_\perp \rangle} = 2\mathrm{Re}[1 - F(k(m-1))]. \tag{118}$$

Thus, we see that, with the use of the stereological approach, the analytical expression (118) for the extinction efficiency follows from the WKB approximation straightforwardly.

The expression for absorption is just as easy to get. The strict formula for the absorption cross-section C_{abs} is (Ishimaru 1978)

$$C_{abs} = 2k \int\limits_V n(\mathbf{r})\kappa(\mathbf{r}) \left|\mathbf{E}_{in}(\mathbf{r}) \big/ E_0\right|^2 dV. \tag{119}$$

Putting the inner field from Eq. (111) into Eq. (119), we get

$$C_{abs} = 2k \frac{n\kappa}{|m|} \int\limits_V \exp[-2k\kappa(z - z_1)]dV. \tag{120}$$

The absolute value of the complex refractive index $|m|$ is equal to its real part to the first order of $|m-1|$:

$$|m| = \sqrt{m^* m} = \sqrt{[1 + (m-1)^*][1 + (m-1)]} = \sqrt{1 + 2\mathrm{Re}(m-1) + |m-1|^2} \approx 1 + \mathrm{Re}(m-1) = n. \tag{121}$$

Thus, we can reduce factor $n \big/ |m|$ in Eq. (120):

$$C_{abs} = 2k\kappa \int\limits_{S_\perp} d^2\mathbf{r}_\perp \int\limits_{z_1}^{z_2} \exp[-2k\kappa(z - z_1)]dz = \int\limits_{S_\perp} (1 - \exp[-2k\kappa\xi])d^2\mathbf{r}_\perp. \tag{122}$$

Taking the average over an irregular shape or random orientation, we have, analogously to Eq. (117)

$$C_{abs} = \langle S_\perp \rangle \int \left(1 - e^{-2k\kappa\xi}\right) f(\xi)d\xi = \langle S_\perp \rangle (1 - F(i\alpha)), \tag{123}$$

where α is the absorption coefficient of the substance,

$$\alpha = 2k\kappa, \tag{124}$$

and $F(i\alpha)$ coincides with the Laplace transform of the CLD. The absorption efficiency Q_{abs} is

$$Q_{abs} = \frac{C_{abs}}{\langle S_\perp \rangle} = 1 - F(i\alpha). \tag{125}$$

The approximation of anomalous diffraction leads to the similar results as the WKB one. Indeed, Eq. (123) gives the absorption in terms of the electric field within the particle, which is the same in both approximations, while the different expressions for S_1—Eqs. (114) and (115)—coincide in the strictly forward direction, which determines extinction.

In the Rayleigh-Gans limit, for $|m - 1|\, x \ll 1$, the Fourier transform have the expansion

$$F(p) = 1 + ipa - \frac{1}{2}p^2\langle\xi^2\rangle + \cdots. \tag{126}$$

Up to the first non-vanishing terms in $n - 1$ and κ (i.e., to the 2nd and 1st orders, respectively), Eqs. (118) and (125) take the form

$$\begin{aligned} Q_{ext} &= \alpha a + (n-1)^2 k^2 \langle\xi^2\rangle, \\ Q_{abs} &= \alpha a. \end{aligned} \tag{127}$$

Given Eq. (13), the second equation here is the well-known expression for the absorption efficiency in the RG approximation (see, e.g., Bohren and Huffman 1983), which means that if the inner field is equal to the incident one, then the absorption cross-section is proportional to the particle volume, regardless of its shape:

$$C_{abs} = \alpha V. \tag{128}$$

The first expression in Eq. (127) should be interpreted as the sum of the absorption and scattering efficiencies, the latter coinciding to the first non-vanishing terms with Eq. (97) obtained in the RG approximation for large particles.

On the other hand, in contrast to the GR approximation, the WKB approximation demonstrates the correct behavior at $x \to \infty$ because, as mentioned above, it has no restrictions on the particle size. Indeed, if $n > 1$, F approaches zero in the limit $x \to \infty$ regardless of absorption because of the fast oscillations of the exponential function $e^{i(n-1)x}$. Thus, for Eq. (118) we have

$$\lim_{x\to\infty} Q_{ext} = 2, \tag{129}$$

which is the well-known limit of the extinction efficiency in the classical theory of light scattering (see, e.g., Bohren and Huffman 1983). If the particle is absorbing, $\kappa > 0$, then F approaches zero because of the factor $e^{-\alpha\xi}$. Thus, the absorption efficiency approaches unit:

$$\lim_{x\to\infty} Q_{abs} = 1, \tag{130}$$

which means that all the energy of radiation that hits the particle is completely absorbed.

The very similar expression for the scattering cross-section of clusters of non-absorbent spheres was derived by Jacquier and Gruy (2008) via anomalous diffraction:

$$C_{sca} = 2\langle S_\perp\rangle \int (1 - \cos[k(n-1)\xi])\, f(\xi)\, d\xi, \tag{131}$$

where n is a real refractive index.

Unfortunately, the angular pattern cannot be expressed analytically in terms of the CLD in the WKB approximation. However, the approximate analytical expression was found by Malinka (2015a, 2020) for large particles.

4.2 Comparison with the Discrete-Dipole Approximation

It is interesting to compare numerically the formulas derived in the WKB approximation with the results given by a more strict method, namely, the discrete-dipole approximation (DDA). The description of the DDA can be found in (Yurkin and Hoekstra 2011), and the code is available at https://github.com/adda-team/adda.

As an object of comparison, we took the ensembles of randomly oriented spheroids, prolate (with the axes ratio of 4:1) and oblate (with the axes ratio of 1:4), both with maximum dimensionless size $kD_{\max} = 100$. Figure 7 presents the extinction and absorption efficiencies of both ensembles for different refractive indices. It

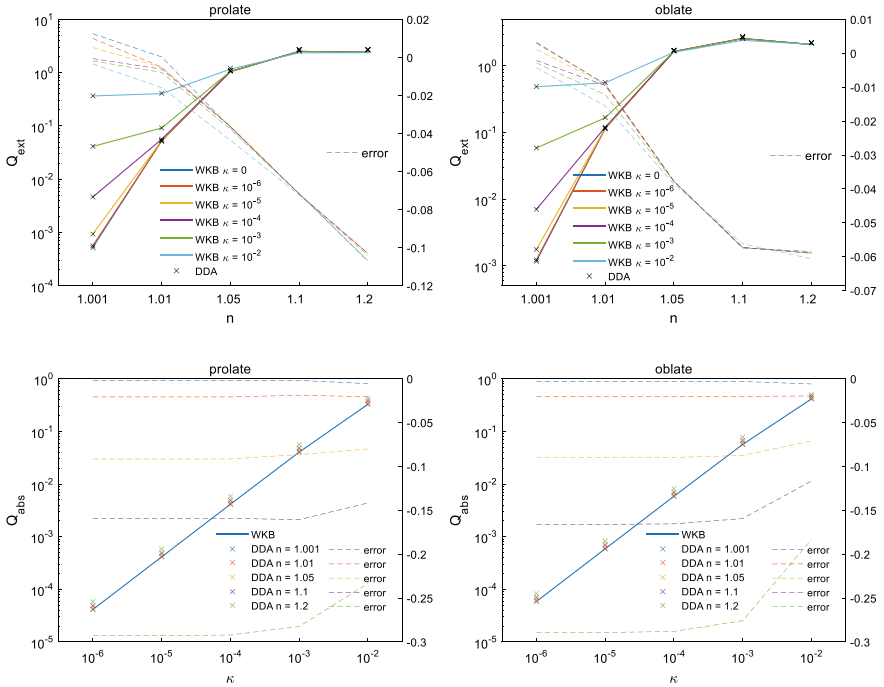

Fig. 7 Extinction (upper) and absorption (lower) efficiencies of prolate (left) and oblate (right) spheroids with the maximal dimension $x = 100$ for different refractive indices

is seen that although the refractive indices of 1.1 and 1.2 hardly satisfy Eq. (110), the WKB approximation provides good estimations of the efficiencies even for these cases. The error increases as expected with the real part of the refractive index and is nearly independent of its imaginary part. Both extinction and absorption efficiencies are slightly underestimated. The WKB approximation is more precise for extinction. In the range $n \leq 1.05$, the error is a few percent for extinction and less than 10% for absorption. For $n \leq 1.2$ it is not greater than 10% and 30% for extinction and absorption, respectively.

4.3 Discussion

The problem of light scattering in the WKB approximation turns out to be related closely to the geometrical statistics. The extinction and absorption efficiencies of light scattering by randomly oriented or irregularly shaped particles are expressed in terms of the characteristic functions (Fourier transforms of the CLD). The concept of CLD has been investigated well by mathematicians. The CLD functions or their moments are expressed analytically or semi-analytically for different particle shapes.

In practice, it is more convenient, though, to make a direct numerical calculation of the Fourier transforms, which only takes a few seconds on a standard PC.

It is important to note that the numerical example given above considers the convex particles (spheroids), but the case of nonconvex particles has its own features. First, for convex particles, the surface area S and the average projection area $\langle S_\perp \rangle$ are related with the well-known equality $S = 4\langle S_\perp \rangle$. For nonconvex particles, this relation does not hold true: $S > 4\langle S_\perp \rangle$. Second, if a particle is nonconvex (or hollowed), a straight line can intersect it more than one time. In this case, the two types of CLD appear: the one chord distribution (OCD), when the chord length is defined as a sum of lengths for all intersection intervals, and the multiple chord distribution (MCD), when each interval is considered separately. The mean chords, calculated with these two distributions, obviously differ, the MCD averaged chord $\langle \xi \rangle_{MCD}$ being less than or equal to the OCD averaged chord $\langle \xi \rangle_{OCD}$. Equation (13) is then modified as

$$V = \langle \xi \rangle_{OCD} \langle S_\perp \rangle = \langle \xi \rangle_{MCD} \frac{S}{4}. \tag{132}$$

Because in the WKB approximation the total optical path length matters, the OCD should be used when calculating efficiencies with Eqs. (118) and (125).

5 Geometrical Optics

The RG and WKB approximations deal with optically soft materials, whose refractive index is close to unit (or to that of a surrounding medium, in general). At the same time, plenty of materials, such as ceramics, pharmaceutical pills, seafoam, snowpacks, or planetary regoliths, have the refractive index that notably differs from unit. As a result, these materials scatter light strongly. In particular, snow covers and regoliths affect the albedo of a planet and thus form its energy budget.

The characteristic grain size in such materials is usually large compared with the wavelength. Together with the fact that the refractive index differs notably from unit, this means that phase shifts in grains are large. If in addition the imaginary part of the refractive index is small—which is the case of dielectric materials—this allows us to apply the laws of geometrical optics to light scattering in such a medium.

5.1 Extinction and Absorption

The extinction coefficient in the classical light scattering theory is

$$\varepsilon = C_{ext} N, \tag{133}$$

where C_{ext} is the extinction cross-section and N is the particle number concentration, which can be written in terms of the stereological quantities as

$$N = \frac{1}{\langle V \rangle}\beta = \frac{1}{a\langle S_\perp \rangle}\frac{a}{a+h} = \frac{1}{\langle S_\perp \rangle (a+h)}. \tag{134}$$

Substituting Eq. (134) into Eq. (133), we have

$$\varepsilon = \frac{Q_{ext}}{a+h}. \tag{135}$$

In the approximation of geometrical optics, the extinction efficiency is equal to unit:

$$Q_{ext} = 1. \tag{136}$$

We do not consider the diffraction part here; otherwise, the extinction efficiency would be twice as great. We suppose that relationships (135)–(136) hold true in a more general case of the stochastic mixture, i.e.

$$\varepsilon = \frac{1}{a+h}. \tag{137}$$

In order to find the absorption efficiency Q_{abs}, we will follow Bohren and Huffman (1983), who derived the formula for absorption by a sphere using geometrical optics. If the imaginary part κ of the complex refractive index $n + i\kappa$ is much less than its real part, then one can consider the ray refraction process in the same manner as it occurs with the real refractive index n. In this case, the refractive angle is real, and the ray inside the medium is attenuated by the exponential law with the absorption coefficient

$$\alpha = \frac{4\pi}{\lambda}\kappa. \tag{138}$$

Let an incident ray of unit intensity be reflected and refracted by the boundary (see Fig. 8).

The intensity of the ray refracted into the grain equals $T_{out}(\theta)$, the Fresnel transmittance of the boundary for the ray, coming with incident angle θ from the outside into the grain. The refracted ray passes through the grain at distance ξ_1 to the boundary. Its intensity at the boundary equals $T_{out}(\theta)\ \exp(-\alpha\xi_1)$. The fraction of energy absorbed along chord 1 is:

$$W^1_{abs} = T_{out}(\theta)\,(1 - \exp(-\alpha\xi_1)). \tag{139}$$

Then, the ray undergoes refraction and internal reflection with the Fresnel reflectance $R_{in}(\beta_1)$ at internal incidence angle β_1. The fraction of energy, absorbed

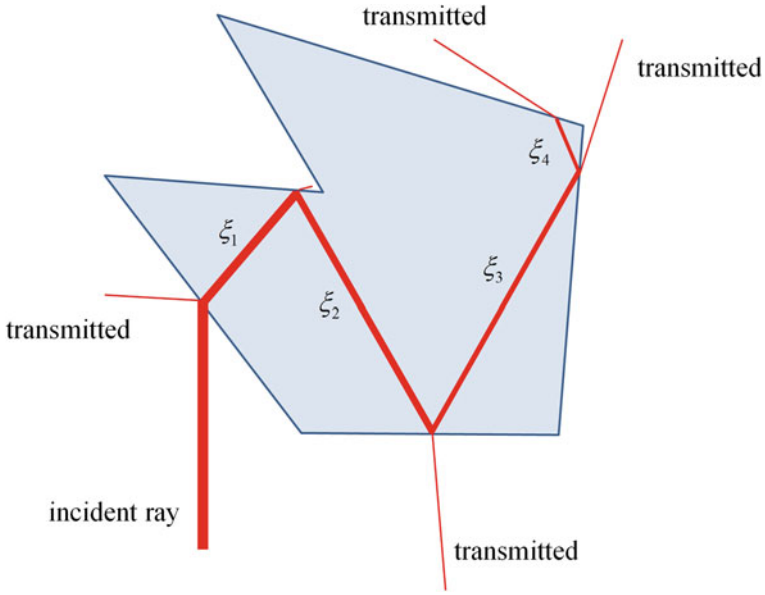

Fig. 8 Ray reflection/refraction by a random irregular grain

while the ray propagates along chord 2, is:

$$W_{abs}^2 = T_{out}(\theta)\exp(-\alpha\xi_1)R_{in}(\beta_1)\,(1-\exp(-\alpha\xi_2)). \tag{140}$$

Going on with the process, we get that the fraction of energy, absorbed along the kth chord, is:

$$W_{abs}^k = T_{out}(\theta)\prod_{j=0}^{k-1}\exp(-\alpha\xi_j)R_{in}(\beta_j)\,(1-\exp(-\alpha\xi_k)). \tag{141}$$

As the grain shape is random and irregular, we average Eq. (141) over all incident angles and chord lengths. All these variables, as were mentioned above, are statistically independent, so we have:

$$\left\langle W_{abs}^k\right\rangle = \langle T_{out}(\theta)\rangle\left[\langle\exp(-\alpha\xi)\rangle\langle R_{in}(\beta)\rangle\right]^{k-1}\left[1-\langle\exp(-\alpha\xi)\rangle\right]. \tag{142}$$

Angular averaging implies that all facets are oriented isotropically, that is

$$\langle T_{out}(\theta)\rangle = 2\int_0^{\pi/2} T_{out}(\theta)\cos\theta\sin\theta\,d\theta = T_{out},$$

$$\langle R_{in}(\beta)\rangle = 2\int_0^{\pi/2} R_{in}(\beta)\cos\beta\sin\beta\, d\beta = R_{in}, \tag{143}$$

where T_{out} and R_{in} are the Fresnel transmittance and internal reflectance of the boundary for diffuse light.

These values (T_{out} and R_{in}) are related to T_{in} and R_{out} (the transmittance for internal diffuse incidence and reflectance for external diffuse incidence, respectively) as follows:

$$\begin{aligned} R_{out} &= 1 - T_{out}, \\ T_{in} &= T_{out}/n^2, \\ R_{in} &= 1 - \frac{1}{n^2} + \frac{R_{out}}{n^2} = 1 - T_{in} = 1 - \frac{T_{out}}{n^2}. \end{aligned} \tag{144}$$

In Eq. (144), $1 - 1/n^2$ is the fraction of light flux subjected to the total internal reflection.

These values depend on the refractive index only (in the considered case on its real part): transmittance T_{out} equals (Gershun 1937)

$$T_{out} = \frac{2(5n^6 + 8n^5 + 6n^4 - 5n^3 - n - 1)}{3(n^3 + n^2 + n + 1)(n^4 - 1)} + \frac{n^2(n^2-1)^2}{(n^2+1)^3}\ln\frac{n+1}{n-1} - \frac{8n^4(n^4+1)}{(n^4-1)^2(n^2+1)}\ln n, \tag{145}$$

and the others (T_{in}, R_{out}, and R_{in}) can be found through Eq. (144).

Averaging over chord length ξ, we get for the absorbed energy

$$Q_{abs} = \sum_{k=1}^{\infty}\left\langle W_{abs}^k\right\rangle = T_{out}(1 - F(i\alpha))\sum_{k=1}^{\infty}[R_{in}F(i\alpha)]^{k-1} = T_{out}\frac{1 - F(i\alpha)}{1 - R_{in}F(i\alpha)}. \tag{146}$$

Formula (146) is completely general, of course, under the assumption that the geometrical optics laws are valid. For weak absorption ($\alpha \ll 1/a$) we simply have

$$Q_{abs} = n^2\alpha a, \tag{147}$$

or in the case of a sparse ensemble

$$C_{abs} = n^2\alpha\langle V\rangle, \tag{148}$$

that is, the absorption is proportional the particle volume. For strong absorption, $F(i\alpha) \to 0$ and

$$Q_{abs} = T_{out}, \tag{149}$$

which means that any ray that entered the particle is absorbed, and the absorption is proportional to the particle cross-section area:

$$C_{abs} = T_{out}\langle S_{\perp}\rangle. \tag{150}$$

For the ideally random mixture with Markov's statistics (the exponential CLD), Eq. (146) becomes

$$Q_{abs} = T_{out}\frac{\alpha a}{\alpha a + T_{in}} = \frac{n^2\alpha a T_{out}}{n^2\alpha a + T_{out}}. \tag{151}$$

The single scattering albedo ω_0 (photon survival probability) is

$$\omega_0 = \frac{Q_{sca}}{Q_{ext}} = 1 - Q_{abs}, \tag{152}$$

and can be derived from Eq. (146). We will get, of course, the same result if we sum the energy of rays that go out from a particle after one external and a number of internal reflections.

5.2 Scattering Phase Function

We consider the facets as independent scatterers, every facet being oriented isotropically. Let the orientation of a facet be (θ_i, φ_i), polar and azimuth angle between the normal to the facet and the direction of the incident ray. The reflected ray has the direction (θ, φ_i), azimuth φ_i remaining the same, θ being the scattering angle

$$\theta = \pi - 2\theta_i. \tag{153}$$

The fraction of light flux, coming to the facets with orientation (θ_i, φ_i), is

$$\frac{1}{\pi}\cos\theta_i \sin\theta_i d\theta_i d\varphi_i. \tag{154}$$

So, the fraction of incident energy W_r that is reflected in direction (θ, φ_i) into solid angle $\sin\theta\, d\theta\, d\varphi_i$ is equal to the product of the Fresnel reflection coefficient by the Jacobian of the transformation:

$$W_r(\theta) = R_{out}(\theta_i)\left|\frac{\cos\theta_i \sin\theta_i d\theta_i d\varphi_i}{\pi \sin\theta\, d\theta\, d\varphi_i}\right| = \frac{R_{out}(\theta_i)}{4\pi}. \tag{155}$$

Zero and the first moments of this function can be written analytically:

$$r_0 = 2\pi \int_0^{\pi} W_r(\theta)\sin\theta\, d\theta = 2\int_0^{\pi/2} R_{out}(\theta_i)\cos\theta_i \sin\theta_i d\theta_i = R_{out} = 1 - T_{out},$$

$$r_1 = 2\pi \int_0^{\pi} W_r(\theta)\cos\theta\sin\theta\, d\theta$$

$$= \frac{n(3n^{11} + 3n^{10} + 25n^9 + 25n^8 + 22n^7 - 282n^6 + 138n^5 + 186n^4 + 151n^3 - 89n^2 + 13n - 3)}{24(n+1)(n^4-1)(n^2+1)^2}$$

$$+ \frac{8n^4(n^6 - 3n^4 + n^2 - 1)}{(n^4-1)^2(n^2+1)^2}\ln n - \frac{(n^8 + 12n^6 + 54n^4 - 4n^2 + 1)(n^2-1)^2}{16(n^2+1)^4}\ln\frac{n+1}{n-1}. \tag{156}$$

As expected, the reflection by the randomly oriented facets is identical to that by a sphere with the same refractive index. Equation (156), to the best of our knowledge, was first obtained by Barun and Gavrilovich (1987) when considering scattering in coarse aerosols consisting of absorbing spherical particles. (Their expression for r_1 differs from ours in a factor of 4, though.)

The transmission through the irregular grain is somewhat more complex.

The part of energy W_t transmitted through the same facet in direction (θ, φ_i) inside the grain is

$$W_t(\theta) = T_{out}(\theta_i)\left|\frac{\cos\theta_i \sin\theta_i d\theta_i d\varphi_i}{\pi \sin\theta\, d\theta\, d\varphi_i}\right|, \tag{157}$$

where the scattering angle θ, i.e., the angle the ray deviates because of refraction, is

$$\theta = \theta_i - \theta_t = \theta_i - \arcsin\frac{\sin\theta_i}{n}, \tag{158}$$

where θ_i and θ_t are the angles of incidence and refraction, respectively. The Jacobian in this case is

$$J(\theta) = \left|\frac{\cos\theta_i \sin\theta_i d\theta_i d\varphi_i}{\pi \sin\theta\, d\theta\ d\varphi_i}\right| = \frac{n^2(n\mu - 1)(n - \mu)}{\pi(n^2 - 2n\mu + 1)^2}, \tag{159}$$

where $\mu = \cos\theta$ is the cosine of the scattering angle. Both values, $T_{out}(\theta_i)$ and $J(\theta)$, are equal to zero for $\mu < 1/n$.

Function $W_t(\theta)$ represents the angular distribution of light for rays that are refracted once by the boundary. For a ray that goes out from the grain because of refraction after the internal incidence (the transmitted rays in Fig. 8), it is convenient to interchange the notation for angles of incidence and refraction: this will allow us to use the theorem of reciprocity and will not change relationship (158). So, let the incident angle be θ_t and the refractive angle be

$$\theta_i = \arcsin(n\sin\theta_t). \tag{160}$$

The part of energy, propagating in direction (θ, φ) after the ray goes out from the grain, is:

$$T_{in}(\theta_t)\left|\frac{\cos\theta_t \sin\theta_t d\theta_t d\varphi}{\pi \sin\theta\, d\theta\ d\varphi}\right|, \tag{161}$$

where $T_{in}(\theta_t)$ is the transmittance of the boundary for the internal incidence at angle θ_t According to the reciprocity theorem

$$T_{in}(\theta_t) = T_{out}(\theta_i), \tag{162}$$

for angles of incidence related with Eq. (160). Moreover, it follows from relationship (160) that

$$\cos\theta_t \sin\theta_t d\theta_t = \frac{1}{n^2}\cos\theta_i \sin\theta_i d\theta_i. \tag{163}$$

So, the part of energy given by Eq. (161) can be written as

$$T_{out}(\theta_i)\left|\frac{\cos\theta_i \sin\theta_i d\theta_i d\varphi}{\pi \sin\theta\, d\theta\ d\varphi}\right|\frac{1}{n^2} = \frac{W_t(\theta)}{n^2}. \tag{164}$$

Hence, the part of energy scattered into solid angle $\sin\theta d\theta d\varphi$ after two refractions is the integral over all possible angles of internal incidence

$$\int W_t(\Delta_0)\frac{W_t(\Delta_1)}{n^2}\, e^{-\alpha\xi_1} \sin\Delta_0 d\Delta_0 d\varphi_0, \tag{165}$$

where

$$\Delta_1 = \arccos(\cos\Delta_0 \cos\theta + \sin\Delta_0 \sin\theta \cos(\varphi - \varphi_0)). \tag{166}$$

Integral (165) can be written using the Legendre polynomial expansion. Let

$$W_t(\theta) = \sum_l \frac{2l+1}{4\pi} t_l P_l(\mu). \tag{167}$$

First two coefficients of the expansion have the analytical expressions:

$$\begin{aligned} t_0 &= T_{out}, \\ t_1 &= \frac{3n^8 + 3n^7 - 17n^6 + 55n^5 - 39n^4 - 7n^3 - 27n^2 - 11n - 8}{24(n+1)(n^4-1)n} \\ &\quad - \frac{(n^2-1)^4}{16(n^2+1)^2 n}\ln\frac{n+1}{n-1} + \frac{4n^5}{(n^4-1)^2}\ln n. \end{aligned} \tag{168}$$

Putting expansion (167) into integral (165), we get

$$\frac{1}{n^2}\sum\frac{2l+1}{4\pi}t_l^2 e^{-\alpha\xi_1}P_l(\mu). \tag{169}$$

After averaging over ξ_1:

$$\frac{1}{n^2}\sum\frac{2l+1}{4\pi}t_l^2 F(i\alpha)P_l(\mu). \tag{170}$$

Expression (170) gives the intensity of the ray, refracted by a grain without internal reflections, after averaging over the irregular grain shape and size.

For the process of internal reflection, we can write analogously:

$$W_{in}(\theta) = R_{in}(\theta_t)\left|\frac{\cos\theta_t\sin\theta_t d\theta_t d\varphi}{\pi\sin\theta\, d\theta\ d\varphi}\right| = \frac{R_{in}(\theta_t)}{4\pi}, \tag{171}$$

where θ_t is the angle of internal incidence

$$\theta_t = \frac{\pi-\theta}{2}, \tag{172}$$

and

$$R_{in}(\theta) = 1, \tag{173}$$

at $\mu \geq 2\big/n^2 - 1$, (total internal reflection).

Function $W_{in}(\theta)$ has the analogous expansion

$$W_{in}(\theta) == \sum\frac{2l+1}{4\pi}r_l^{in}P_l(\mu). \tag{174}$$

First two coefficients are related to the coefficients of external reflection (156):

$$\begin{aligned} r_0^{in} &= 1 - \frac{1-r_0}{n^2} = R_{in}, \\ r_1^{in} &= \frac{r_1}{n^4} + (1-r_0)\frac{n^2-1}{n^4}. \end{aligned} \tag{175}$$

For the ray subjected to one internal reflection and two refractions, the fraction of energy scattered into solid angle $\sin\theta d\theta d\varphi$ is

$$\int W_t(\Delta_0)e^{-\alpha\xi_1}W_{in}(\Delta_1)e^{-\alpha\xi_2}\frac{W_t(\Delta_2)}{n^2}\sin\Delta_0 d\Delta_0 d\varphi_0 \sin\Delta_1 d\Delta_1 d\varphi_1, \tag{176}$$

where

$$\Delta_1 = \arccos(\cos\Delta_0 \cos\Delta_1 + \sin\Delta_0 \sin\Delta_1 \cos(\varphi_1 - \varphi_0)) \tag{177}$$

$$\Delta_2 = \arccos(\cos\theta \cos\Delta_1 + \sin\theta \sin\Delta_1 \cos(\varphi - \varphi_1)). \tag{178}$$

Convolution (176) equals

$$\frac{1}{n^2}\sum \frac{2l+1}{4\pi} t_l^2 r_l^{in} e^{-\alpha\xi_1} e^{-\alpha\xi_2} P_l(\mu). \tag{179}$$

After averaging over ξ_1 and ξ_2:

$$\frac{1}{n^2}\sum \frac{2l+1}{4\pi} t_l^2 r_l F^2(i\alpha) P_l(\mu). \tag{180}$$

Having summed all the internal reflections, we have

$$\frac{1}{n^2}\sum \frac{2l+1}{4\pi} \frac{t_l^2 F(i\alpha)}{1 - r_l^{in} F(i\alpha)} P_l(\mu). \tag{181}$$

Adding the external reflection part (155) to (181), we get the single scattering albedo

$$\begin{aligned}\omega_0 &= \int_0^\pi \left(W_r(\theta) + \frac{1}{n^2}\sum \frac{2l+1}{4\pi} \frac{t_l^2 F(i\alpha)}{1 - r_l^{in} F(i\alpha)} P_l(\mu) \right) 2\pi \sin\theta \, d\theta \\ &= r_0 + \frac{1}{n^2} \frac{t_0^2 F(i\alpha)}{1 - r_0^{in} F(i\alpha)} = 1 - \frac{t_0(1 - F(i\alpha))}{1 - r_0^{in} F(i\alpha)},\end{aligned} \tag{182}$$

which matches Eq. (146).

Scattering phase function $p(\theta)$ is normalized to be equal to unit for the isotropic scattering, so

$$\begin{aligned}p(\theta) &= \frac{4\pi}{\omega_0}\left[W_r(\theta) + \frac{1}{n^2}\sum \frac{2l+1}{4\pi} \frac{t_l^2 F(i\alpha)}{1 - r_l^{in} F(i\alpha)} P_l(\mu) \right] \\ &= \frac{1}{\omega_0}\left[R_{out}(\theta_i) + \frac{1}{n^2}\sum (2l+1) \frac{t_l^2 F(i\alpha)}{1 - r_l^{in} F(i\alpha)} P_l(\mu) \right].\end{aligned} \tag{183}$$

The average cosine g of the scattering angle is

$$g = \frac{1}{2}\int_0^\pi p(\theta) \cos\theta \sin\theta d\theta = \frac{1}{\omega_0}\left(r_1 + \frac{1}{n^2} \frac{t_1^2 F(i\alpha)}{1 - r_1^{in} F(i\alpha)} \right), \tag{184}$$

where r_1, t_1, and r_1^{in} are given in an analytic way by Eqs. (156), (168), and (175).

For weak absorption ($\alpha a \ll 1$), the terms of the first and greater orders of αa can be neglected, and the scattering pattern is independent of the microstructure and completely determined by the real part of the refractive index:

$$p(\theta) = R_{out}(\theta_i) + \frac{1}{n^2} \sum (2l+1) \frac{t_l^2}{1 - r_l^{in}} P_l(\mu). \tag{185}$$

For the random mixture with the exponential CLD

$$p(\theta) = \frac{1}{\omega_0} \left[R_{out}(\theta_i) + \frac{1}{n^2} \sum (2l+1) \frac{t_l^2}{1 + \alpha a - r_l^{in}} P_l(\mu) \right]. \tag{186}$$

5.3 Polarization

Scattering of polarized light is described with a scattering matrix (Mueller matrix), instead of a scattering phase function, which for isotropic media without an optical activity has the form (see, e.g., Bohren and Huffman 1983 for details)

$$\mathbf{F}(\theta) = \begin{pmatrix} a_1(\theta) & b_1(\theta) & 0 & 0 \\ b_1(\theta) & a_2(\theta) & 0 & 0 \\ 0 & 0 & a_3(\theta) & b_2(\theta) \\ 0 & 0 & -b_2(\theta) & a_4(\theta) \end{pmatrix}, \tag{187}$$

where element a_1 is the phase function $p(\theta)$ and the other elements describe the polarization state of the beam. All the findings made in the previous section can be generalized to the polarization case.

The most natural technique to consider the polarization is the use of the generalized spherical functions $P_{nm}^l(\mu)$. These functions are orthogonal on the sphere and satisfy the addition theorem. The detailed description of the generalized spherical functions is given by Gelfand et al. (1963), and their applications to scattering of polarized light can be found in the basic work of Hovenier and Mee (1983).

With this technique, the elements of the scattering matrix (Eq. (187)) has the expansion in the generalized spherical functions:

$$\begin{aligned} a_1(\theta) &= \sum (2l+1) a_1^l P_{00}^l(\mu), \\ a_2(\theta) &= \sum (2l+1) \left[a_+^l P_{22}^l(\mu) + a_-^l P_{2,-2}^l(\mu) \right], \\ a_3(\theta) &= \sum (2l+1) \left[a_+^l P_{22}^l(\mu) - a_-^l P_{2,-2}^l(\mu) \right] \\ a_4(\theta) &= \sum (2l+1) a_4^l P_{00}^l(\mu), \end{aligned}$$

$$b_1(\theta) = \sum (2l+1) b_1^l P_{02}^l(\mu),$$
$$b_2(\theta) = \sum (2l+1) b_2^l P_{02}^l(\mu), \tag{188}$$

with the expansion coefficients equal to

$$a_1^l = \frac{1}{2}\int_0^\pi a_1(\theta) P_{00}^l(\mu) \sin\theta d\theta,$$
$$a_+^l = \frac{1}{2}\int_0^\pi \frac{a_2(\theta)+a_3(\theta)}{2} P_{22}^l(\mu) \sin\theta d\theta,$$
$$a_-^l = \frac{1}{2}\int_0^\pi \frac{a_2(\theta)-a_3(\theta)}{2} P_{2,-2}^l(\mu) \sin\theta d\theta,$$
$$a_4^l = \frac{1}{2}\int_0^\pi a_4(\theta) P_{00}^l(\mu) \sin\theta d\theta,$$
$$b_1^l = \frac{1}{2}\int_0^\pi b_1(\theta) P_{02}^l(\mu) \sin\theta d\theta,$$
$$b_2^l = \frac{1}{2}\int_0^\pi b_2(\theta) P_{02}^l(\cos\theta) \sin\theta d\theta. \tag{189}$$

The coefficients (189) form the expansion matrix

$$\mathbf{F}_l = \begin{pmatrix} a_1^l & b_1^l & 0 & 0 \\ b_1^l & a_+^l + a_-^l & 0 & 0 \\ 0 & 0 & a_+^l - a_-^l & b_2^l \\ 0 & 0 & -b_2^l & a_4^l \end{pmatrix}. \tag{190}$$

The key point of this expansion is that if we have two successive events of scattering with matrices $\mathbf{F}^1(\theta)$ and $\mathbf{F}^2(\theta)$, which have the expansion coefficients matrices $\mathbf{F}_l^1$ and $\mathbf{F}_l^2$, respectively, then the resulting scattering matrix has the expansion equal to matrix product $\mathbf{F}_l^2\mathbf{F}_l^1$. In view of that, Eq. (181) can be easily written in the matrix form: the expansion $\mathbf{G}_l$ of the Mueller matrix for the ray that was multiply reflected inside the grain and went out is

$$\mathbf{G}_l = \frac{F(i\alpha)}{n^2}\mathbf{T}_l\left[1 - \mathbf{R}_l^{in} F(i\alpha)\right]^{-1}\mathbf{T}_l, \tag{191}$$

where $\mathbf{T}_l$ and $\mathbf{R}_l^{in}$ are expansions (189) for the matrices of transmission through the boundary $\mathbf{T}(\theta)$ and internal reflection $\mathbf{R}^{in}(\theta)$, respectively.

The Mueller matrix for the Fresnel transmission through the boundary is:

$$\mathbf{T}(\theta) = 4\pi J(\theta)\frac{n\mu_t}{\mu_i}\begin{pmatrix} \frac{t_\parallel^2+t_\perp^2}{2} & \frac{t_\parallel^2-t_\perp^2}{2} & 0 & 0 \\ \frac{t_\parallel^2-t_\perp^2}{2} & \frac{t_\parallel^2+t_\perp^2}{2} & 0 & 0 \\ 0 & 0 & t_\perp t_\parallel & 0 \\ 0 & 0 & 0 & t_\perp t_\parallel \end{pmatrix} = \frac{16n^3}{(n^2-1)^2}\frac{\mu_i^2\mu_t^2}{\mu^2}\begin{pmatrix} \frac{1+\mu^2}{2} & \frac{1-\mu^2}{2} & 0 & 0 \\ \frac{1-\mu^2}{2} & \frac{1+\mu^2}{2} & 0 & 0 \\ 0 & 0 & \mu & 0 \\ 0 & 0 & 0 & \mu \end{pmatrix}, \tag{192}$$

where $J(\theta)$ is the Jacobian (159), μ_i and μ_t are the cosines of the incidence and refraction angles:

$$\mu_i = \frac{n\mu - 1}{\sqrt{n^2 - 2\mu n + 1}}, \quad \mu_t = \frac{n - \mu}{\sqrt{n^2 - 2\mu n + 1}}; \tag{193}$$

$t_\parallel$ and $t_\perp$ are the Fresnel transmission coefficients

$$t_\perp = \frac{2\mu_i}{\mu_i + n\mu_t}, \quad t_\parallel = \frac{2\mu_i}{n\mu_i + \mu_t}. \tag{194}$$

For $\mu < 1/n$, the transmission coefficients and all the elements of $\mathbf{T}(\theta)$ are equal to zero.

The matrix of the internal reflection is

$$\mathbf{R}^{in}(\theta) = \begin{pmatrix} \frac{|r_\parallel^{in}|^2+|r_\perp^{in}|^2}{2} & \frac{|r_\parallel^{in}|^2-|r_\perp^{in}|^2}{2} & 0 & 0 \\ \frac{|r_\parallel^{in}|^2-|r_\perp^{in}|^2}{2} & \frac{|r_\parallel^{in}|^2+|r_\perp^{in}|^2}{2} & 0 & 0 \\ 0 & 0 & \mathrm{Re}\left(r_\perp^{in*}r_\parallel^{in}\right) & \mathrm{Im}\left(r_{\perp in*}r_\parallel^{in}\right) \\ 0 & 0 & -\mathrm{Im}\left(r_\perp^{in*}r_\parallel^{in}\right) & \mathrm{Re}\left(r_\perp^{in*}r_\parallel^{in}\right) \end{pmatrix}, \tag{195}$$

where $r_\perp^{in}$ and $r_\parallel^{in}$ are the internal reflection coefficients

$$r_\perp^{in} = \frac{\sin(\theta_i - \theta_t)}{\sin(\theta_i + \theta_t)}, \quad r_\parallel^{in} = -\frac{\tan(\theta_i - \theta_t)}{\tan(\theta_i + \theta_t)}. \tag{196}$$

Angles θ_i and θ_t relate to θ as

$$\theta_t = \frac{\pi - \theta}{2}, \quad \theta_i = \arcsin(n \sin\theta_t). \tag{197}$$

The external reflection matrix is

$$\mathbf{R}(\theta) = \begin{pmatrix} \frac{|r_\parallel|^2+|r_\perp|^2}{2} & \frac{|r_\parallel|^2-|r_\perp|^2}{2} & 0 & 0 \\ \frac{|r_\parallel|^2-|r_\perp|^2}{2} & \frac{|r_\parallel|^2+|r_\perp|^2}{2} & 0 & 0 \\ 0 & 0 & \mathrm{Re}\left(r_\perp^* r_\parallel\right) & \mathrm{Im}\left(r_\perp^* r_\parallel\right) \\ 0 & 0 & -\mathrm{Im}\left(r_\perp^* r_\parallel\right) & \mathrm{Re}\left(r_\perp^* r_\parallel\right) \end{pmatrix}, \tag{198}$$

where $r_\perp$ and $r_\parallel$ are the reflection coefficients

$$r_\perp = \frac{\sin(\theta_i - \theta_t)}{\sin(\theta_i + \theta_t)}, \quad r_\parallel = -\frac{\tan(\theta_i - \theta_t)}{\tan(\theta_i + \theta_t)}. \tag{199}$$

Angles θ_i and θ_t relate to θ as

$$\theta_i = \frac{\pi - \theta}{2}, \quad \theta_t = \arcsin\left(\frac{\sin\theta_i}{m}\right). \tag{200}$$

Finally, the scattering matrix $\mathbf{F}(\theta)$ is the normalized sum of the external reflection (198) and matrix $\mathbf{G}(\theta)$, which is the result of transformation (188) of matrix $\mathbf{G}_l$ given by Eq. (191):

$$\mathbf{F}(\theta) = \frac{1}{\omega_0}(\mathbf{R}(\theta) + \mathbf{G}(\theta)). \tag{201}$$

We kept the complex refractive index m in Eqs. (198)–(200) in order to include particles, whose refractive index has significant imaginary part, e.g., metal ones. In this case, any ray transmitted by a boundary into a particle is absorbed, and scattering is completely described by the external reflection. However, when the imaginary part is neither significant nor negligible, the same thing cannot be done. In this case, the imaginary part should be accounted for not only in the external reflection but also in the internal reflection and refraction. But if the refraction index is complex, then the wave inside a particle has a complex wavevector and, as a result, the complex angle of incidence onto the inner side of the boundary. However, the imaginary part of this complex incident angle is unknown, because it is not linked generally with the real part and depends on the orientation of the boundary where the wave was refracted when entering the particle. Therefore, we prefer to assume that the refractive index is real when considering refraction and internal reflection.

5.4 Numerical Comparison with Some Models

5.4.1 Spheroids

Here we compare the stochastic model that uses the laws of geometrical optics with the DDA calculations from Sec. 4.2 (the ensembles of prolate and oblate spheroids with the dimensionless sizes $25 \times 25 \times 100$ and $100 \times 100 \times 25$, respectively).

Table 1 Absorption efficiencies of the prolate and oblate spheroids calculated in the DDA and in the stochastic model that uses the CLD and geometrical optics (GO)

m	1.001		1.01		1.05		1.1		1.2	
	$10^{-3}i$	$10^{-2}i$	$10^{-3}i$	$10^{-2}i$	$10^{-3}i$	$10^{-2}i$	$10^{-3}i$	$10^{-2}i$	$10^{-3}i$	$10^{-2}i$
DDA prolate	0.0404	0.328	0.0411	0.333	0.0442	0.355	0.0481	0.380	0.0562	0.426
GO prolate	0.0404	0.327	0.0411	0.331	0.0443	0.347	0.0483	0.366	0.0569	0.403
DDA oblate	0.0567	0.416	0.0576	0.422	0.0619	0.445	0.0672	0.468	0.0780	0.507
GO oblate	0.0566	0.414	0.0575	0.418	0.0619	0.435	0.0674	0.455	0.0791	0.492

The stochastic model calculations imply the random particle shape with the same CLD as that of the spheroids. The extinction efficiency in geometrical optics is equal to 1 (or to 2 if we add diffraction); its values calculated in the DDA are shown in Sec. 4.2. Table 1 shows the absorption efficiencies.

It is a surprise that the stochastic model that uses the laws of geometrical optics gives the values of absorption that are so close to those calculated with the DDA code, although the refractive index does not differ strongly from unit and the particles are not so large (the mean chords are 20.7 and 29.4 for prolate and oblate spheroids, respectively). The refractive index in the range 1.1–1.2 is too high for the WKB and the more so for the RG approximations to be applicable, but at the same time it is not high enough for geometric optics. Nevertheless, we can consider the particles with the refractive index 1.1 and 1.2 as an intermediate case between optically soft and hard particles where both the WKB and geometrical optics approximations give reasonable results. Geometrical optics is slightly more accurate in this case.

Figure 9 shows the angular pattern of the Mueller matrix elements for the spheroids with the refractive index of 1.1. The differential scattering efficiency $Q_{sca}a_1(\theta)$ is plotted instead of the phase function $a_1(\theta)$ itself in order to remove the effect of normalization, which violates the match of the phase functions' values outside the forward scattering peak.

Spheroids are undoubtedly particles of a regular shape; nevertheless, the model of randomly shaped particles works quit well. This means that even a slight deviation from the ideal sphere is enough to assume that the ray length inside a particle is weakly correlated with the refractive angle. As a result, the CLD is more important for the scattering properties than the particle shape itself.

5.4.2 Spheres and Hexagonal Prisms

Now we consider two more shapes: hexagonal prisms with a rough surface (Gaussian tilt distribution with $\sigma = 1$) and polydispersed spheres with the gamma size distribution

$$\frac{dp}{dR} = \frac{R^m \exp\left(-R/R_0\right)}{R_0^{m+1}\Gamma(m+1)}, \tag{202}$$

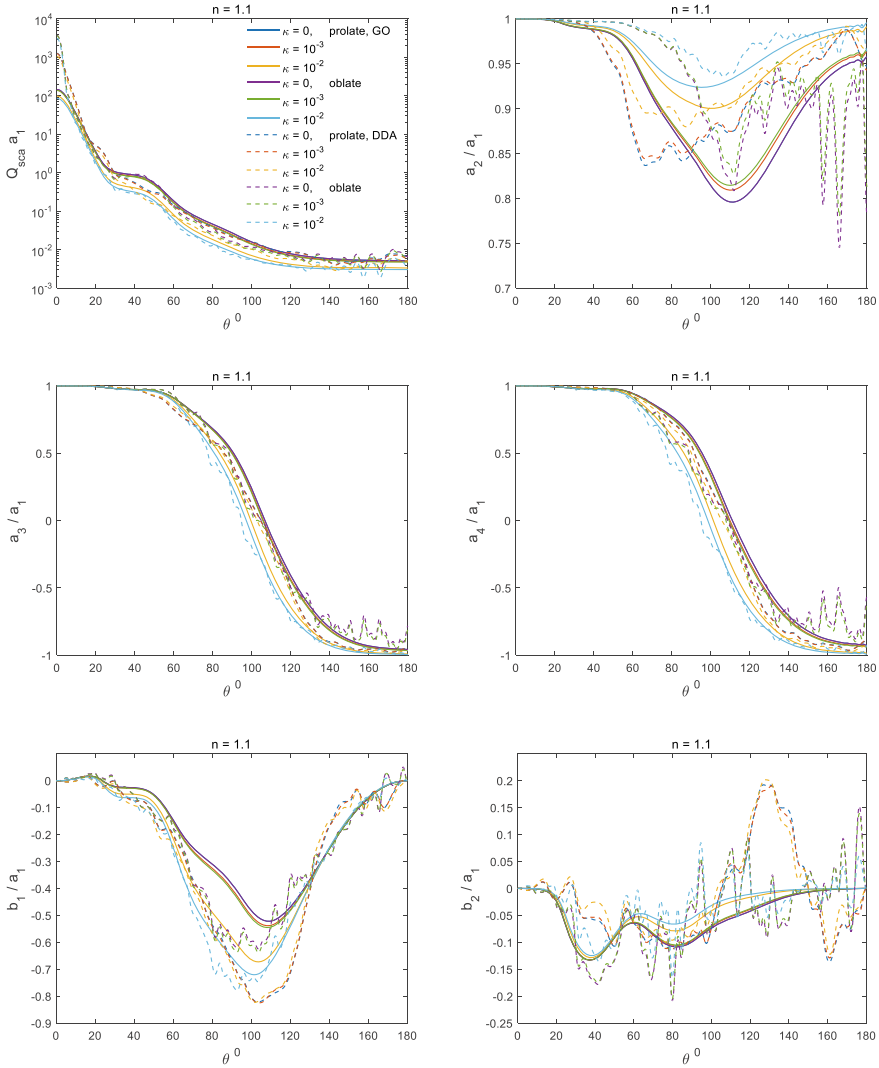

Fig. 9 Mueller matrix elements of the prolate and oblate spheroids with $n = 1.1$ and different absorption, calculated in the DDA and geometrical optics

where $p(R)$ is the probability that the particle radius is less than R.

The CLD of a polydispersion is the area-weighted average of the CLD of a single particle $f_p(\xi)$:

$$f(\xi) = \frac{1}{\langle R^2 \rangle} \int_0^\infty f_p(\xi) R^2 \frac{dp}{dR} dR. \tag{203}$$

Table 2 Absorption efficiency of ice grains at 1.24 μm, depending on the mean chord length, in different approaches

Mean chord length	40 μm	133 μm	400 μm	1333 μm
Spheres (Mie)	6.86×10^{-3}	2.12×10^{-2}	6.11×10^{-2}	1.87×10^{-1}
Hexagonal plates (H:D = 1:4)	7.72×10^{-3}	2.54×10^{-2}	7.31×10^{-2}	2.14×10^{-1}
Hexagonal columns (H:D = 4:1)	7.95×10^{-3}	2.61×10^{-2}	7.47×10^{-2}	2.15×10^{-1}
Random mixture	8.25×10^{-3}	2.69×10^{-2}	7.65×10^{-2}	2.14×10^{-1}
Rough spheres	8.27×10^{-3}	2.71×10^{-2}	7.78×10^{-2}	2.25×10^{-1}

For a single sphere, $f_p(\xi)$ is given by Eq. (98), so the CLD of a spherical polydispersion equals

$$f(\xi) = \frac{1}{\langle R^2 \rangle} \int_{\xi/2}^{\infty} \frac{\xi}{2R^2} R^2 \frac{dp}{dR} dR = \xi \frac{1 - p(\xi/2)}{2\langle R^2 \rangle}. \tag{204}$$

For the gamma distribution (202), it becomes

$$f(\xi) = \frac{\xi}{2R_0^2 \Gamma(m+3)} \Gamma\left(m+1, \frac{\xi}{2R_0}\right), \tag{205}$$

where $\Gamma(m, x)$ is the incomplete gamma function. The Fourier transform of Eq. (205) is

$$F(i\alpha) = \frac{1}{2\alpha^2 R_0^2 (m+1)(m+2)} \left(1 - \frac{1 + 2(m+2)\alpha R_0}{(1 + 2\alpha R_0)^{m+2}}\right). \tag{206}$$

For this comparison, we used the quite wide distribution ($m = 7$) to avoid the Mie resonances. R_0 was chosen to provide the same mean chord as that of the prims:

$$\langle \xi \rangle = \frac{4}{3} R_0 (m+3) = \frac{4V_{\text{prism}}}{S_{\text{prism}}}. \tag{207}$$

The scattering and absorption properties of the prisms (plates and columns with the aspect ratio 1:4 and 4:1) were calculated with the code of Yang and Liou (1996) (see also the monograph Liou and Yang 2016). The optical properties of the spheres were calculated with the Mie code and with the stochastic model with the same, 'spherical,' CLD (Eqs. (205) and (206)). We will refer to the latter as spheres with a rough surface.

As an example of solid material, we considered ice with the complex refractive index taken from (Warren and Brandt 2008): $1.2973 + 1.22 \times 10^{-5} i$ at wavelength 1.24 μm.

Table 2 presents the absorption efficiencies of the particles described above and of the random mixture with the exponential CLD. It is seen that the random mixture, as well as the rough spheres, gives the slightly higher absorption efficiencies than Yang and Liou' calculations; however, these values are much closer to each other than to those of the Mie solution. Apparently, both the prisms and rough spheres are much closer to the random mixture than to the ideal spheres, because of their rough surface, which introduces the element of stochasticity. The random tilt of a surface element makes a ray deviate to the random angle, and the path length inside is no more related to the initial angle of incidence. Thus, the surface roughness is the main factor that brings the ensemble of regular particles closer to the random mixture, for which the path length and the angle of incidence are completely independent.

Figure 10 present the Mueller matrix elements of these particles and the random mixture with the mean chord length of 40 μm. It is seen that the scattering properties of the hexagonal plates and columns with a rough surface are very close to each other and quite close to that of the random mixture, especially in the forward hemisphere (except for the diffraction peak, which is not considered in geometrical optics). In particular, they do not demonstrate halos as ideal hexagonal prisms with a flat surface do. The scattering properties of the ideal spheres predictably differ from any kind of particles with a rough surface. At the same time, the scattering pattern of the rough spheres, including polarization, coincide with that of the random mixture. This is because the rough surface deviate a ray by a random angle making a ray path within the particle independent of the incident angle. In addition, the angular pattern of scattering by the random mixture with weak absorption depends on the refractive index only (see Eq. (185)) and the CLD does not matter.

6 Application to Optics of Snow and White Ice

6.1 Theory

Snow and ice covers are important factors governing the Earth radiative budget (see, e.g., Curry et al. 1995; Køltzow 2007; Pirazzini 2008; Shindell and Faluvegi 2009). There is a great variety of ice types (Bogorodskii 1970; Byshuev et al. 1974; Untersteiner 1990; Perovich et al. 2009; Nicolaus et al. 2010; WMO 2014). "White ice" is not a strict term from the nomenclature; rather it puts together the various types of ice with high albedo and got its name because of its white appearance, produced by a highly scattering top layer (Grenfell and Maykut 1977; Perovich 1996). This layer is formed after meltwater has drained off from the surface elevations into the depressions. It consists of ice grains of the order of millimeters in size and, thus, can be described within the same approach as snow, but with larger grains. Also known as the surface scattering layer, it provides stable high reflectance and, in fact, determines the reflective properties of white ice (Perovich et al. 2002; Herzfeld et al. 2006). White ice and snow are one of the brightest objects on the Earth's surface and

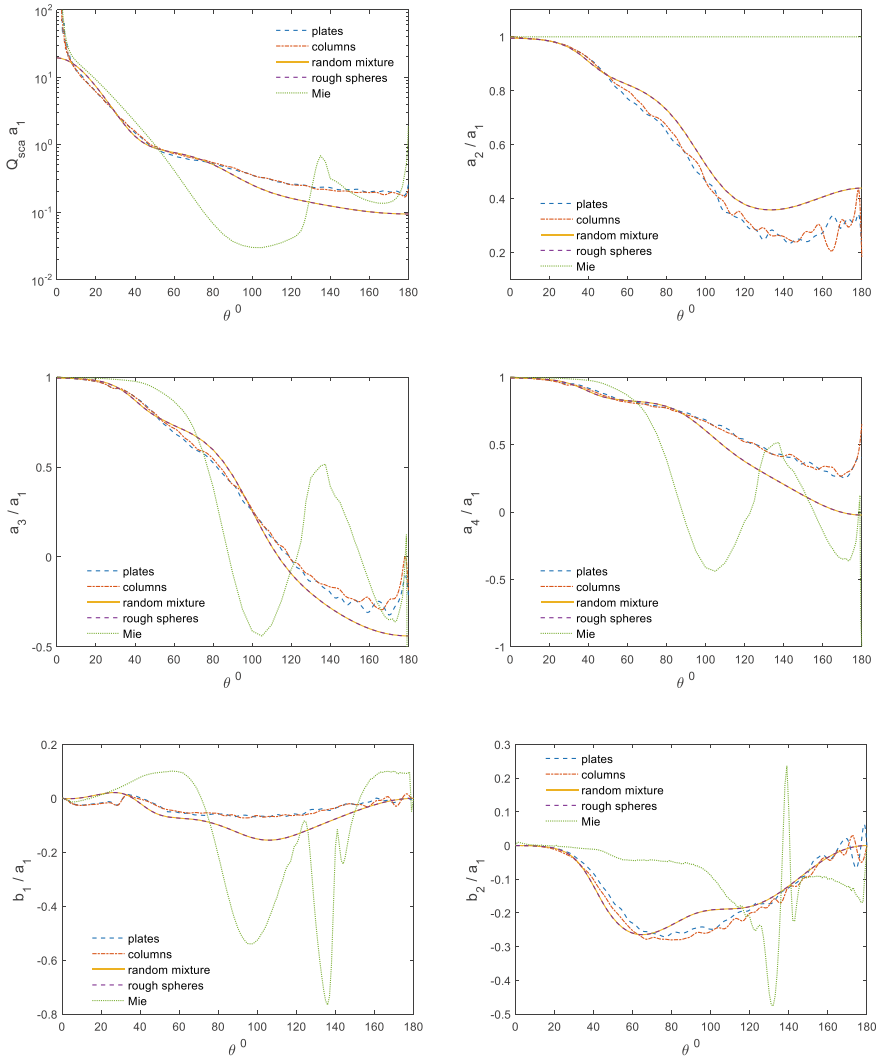

Fig. 10 Mueller matrix elements of the hexagonal plates and columns, random mixture, rough and ideal (Mie) spheres. The mean chord is 40 μm, the wavelength is 1.24 μm, the refractive index is $1.2973 + 1.22 \times 10^{-5} i$

occupy a large part of its area. The common way to model the reflection of white ice and snow is to interpret them as consisting of independent spherical scatterers and to use the Mie solution (e.g., Bohren and Barkstrom 1974; Choudhury and Chang 1979; Wiscombe and Warren 1980; Warren 1982; Grenfell et al. 1994). However, a set of spherical scatterers, even polydispersed, has a number of typical scattering features, such as a minimum at the scattering angle of about 100°, a rainbow, or a glory (see Fig. 10). Neither white ice nor snow demonstrate these scattering features,

so the Henyey-Greenstein scattering function is often used instead of the Mie one in the radiative transfer simulations (e.g., Light et al. 1998; Grenfell and Warren 1999; Aoki et al. 2000; Hamre et al. 2004; Light 2010). At the same time, both optical and microphysical measurements show that the ice grains in snow and in the granular layer of white ice are really far from spheres and, in fact, irregularly shaped (e.g., Massom et al. 2001; Kokhanovsky et al. 2005; Matzl and Schneebeli 2006; Kerbrat et al. 2008; Domine et al. 2008; Picard et al. 2009). So the model of the random mixture described in the previous Section seems to be a more consistent way to describe snow and white ice.

The examples of the spectral dependence of the photon survival probability ω_0 and the average cosine g for the random ice–air mixtures with $a = 30\,\mu m$ (fresh fine snow grains) $a = 3$ mm (aged white ice) are shown in Fig. 11.

It is seen that these media are practically nonabsorbing in the visible and near IR range. Even for the aged white ice $\omega_0 > 0.85$ in the interval 0.3–1.1 μm and $\omega_0 > 0.997$ in the visible range, which justifies the name of "white ice." The average cosine g takes the values from 0.63 at 0.3 μm to 0.69 at 1.1 μm with a mean value of about 0.67. Note that this value refers to the geometrical optics being applied to the random mixture. When considering a separate particle, the total average cosine (geometrical optics + diffraction) will approximately be $(1 + g)/2 \approx 0.84$.

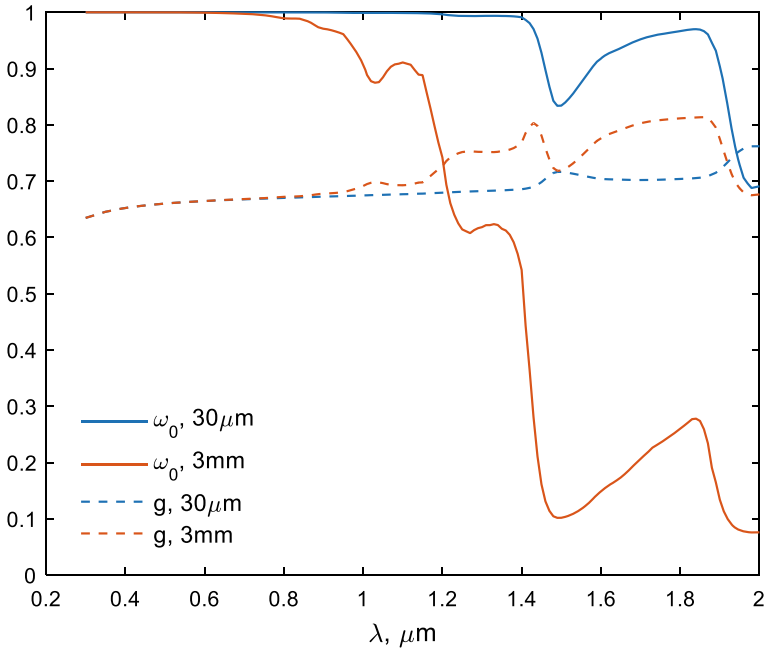

Fig. 11 Spectral dependence of the photon survival probability ω_0 and the average cosine g for the random ice–air mixture with mean chords of 30 μm and 3 mm

The spectral absorption of the random mixture is mainly determined by the imaginary part of the refractive index. In the case of ice, it has a pronounced minimum at about 0.3–0.4 μm. However, the spectral behavior of white ice reflectance measured in situ shows the decrease in the blue range in many cases (see Figures below). This effect could be explained by the measurement geometry, when light from the sky and direct sunlight are added in different proportions at different wavelengths. However, careful analysis of the albedo field measurements, as well as the satellite data, shows that this effect is not sufficient to explain the spectral behavior. This means that some absorbing contaminant is present.

There can be different contaminants in ice and snow. The particles of sediments from the atmosphere, which could be both long-distance-transferred (as Saharan dust) or local (pollution from industrial centers), can affect the sea ice albedo (e.g., Light et al. 1998; Dombrovsky and Kokhanovsky 2019). For example, clay, slit, and sand particles are found in the ice situated far from a coastline in the Beaufort Sea (Reimnitz et al. 1993) and in the Central Arctic (Nürnberg et al. 1994). However, from our perspective, the yellow substance—dissolved organic matter (DOM) from seawater—is ideally suited to the role of a contaminant in ice. The presence of the yellow substance in both Arctic and Antarctic ice was reported by many authors (e.g., Thomas et al. 1995, 2001; Norman et al. 2011; Beine et al. 2012; Grannas et al. 2014; Hansell and Carlson 2014) and was sufficient to represent the shape of most of the white ice reflection spectra we have analyzed. Its spectral absorption given by Jerlov (1968) is:

$$\alpha_y(\lambda) = \alpha_y(390)\exp[-0.015\,(\lambda - 390)], \tag{208}$$

where λ is the wavelength in nanometers and $\alpha_y(390)$ is the free parameter that determines the spectrum.

The main contaminant of snow affecting its albedo is soot, which primary consists of black carbon (e.g., Tollefson 2009). The absorption coefficient of snow polluted by soot particles is

$$\alpha = Q_{abs}^{sn}\frac{\beta_{sn}}{a} + Q_{abs}^{st}\frac{3\beta_{st}}{4r_{32}}, \tag{209}$$

where Q_{abs}^{sn} and Q_{abs}^{st} are the pure snow and soot absorption efficiencies, respectively; β_{sn} and β_{st} are their volumetric concentrations, a is the snow mean chord and r_{32} is the effective radius of soot particles. As the absorption coefficient of ice is significant in the IR, soot affects the snow albedo only in the visible range, where ice absorption is weak. Thus, we can use Eq. (148) for weak ice absorption and modify Eq. (209) as follows:

$$\alpha = 2n_{ice}^2 k\beta_{sn}\left(\kappa_{ice} + \frac{3Q_{abs}^{st}}{8n_{ice}^2 k r_{32}}C_{st}\right), \tag{210}$$

where $C_{st} = \beta_{st}/\beta_{sn}$ is the relative soot concentration. According to the standard soot model (WMO 1986), the soot particles are distributed log-normally with the median radius of 11.8 nm and the standard deviation equal to ln 2.0; the refractive index in the visible range is $1.75 + 0.44i$. The effective radius r_{32} for this distribution is 39 nm, and the absorption efficiency Q_{abs}^{st} calculated with a Mie code at the wavelength 550 nm is 0.38. With these values, the coefficient followed by C_{st} in Eq. (210) is approximately equal to 0.2.

The concentration of DOM in Eq. (208) does not have the explicit value and is represented implicitly through its absorption coefficient $\alpha_y(\lambda)$ at $\lambda = 390$nm. This is a conventional way to describe the DOM absorption used in the ocean optics.

Finally, we use the refractive index with the imaginary part equal to

$$\kappa = \kappa_{ice} + \frac{\lambda}{4\pi}\alpha_y, \tag{211}$$

in order to take the absorption by the yellow substance into account and

$$\kappa = \kappa_{ice} + 0.2C_{st}, \tag{212}$$

for the absorption by soot. If the specific spectral features of other contaminants appear, their absorption spectra can be easily added to the right-hand part of Eqs. (211) or (212).

From the point of view of apparent optical properties, a layer of snow or white ice is fully characterized by three values: its optical thickness τ, the mean chord of the ice phase a, and the absorption of a contaminant given by $\alpha_y(390)$ in white ice or by C_{st} in snow.

6.2 In Situ Measurements

One of the first experiments on the in situ measurements of the sea ice reflectance, as for our knowledge, was performed by Perovich (1994). The albedo and bidirectional reflectance factor (BRF) of various types of ice were measured in the interval from 400 to 1000 nm. We processed a case of snow-covered ice. First, we found the optical thickness τ and grain size a from the albedo values (we assumed here that there was no contaminant). Then, we calculated the BRF of a layer of the random ice-air mixture with these characteristics. The results are presented in Fig. 12. As seen from the Figure, all the experimental points fit the theoretical curve, except for the point $\theta = 60°$, $\phi = 0°$. A pronounced peak in reflectance was observed in the direction of specular reflection of the direct solar beam, which had a zenith angle of 56°. In Fig. 12, we showed a sun glint produced by the partially oriented ice facets with the standard deviation of 0.7° from the vertical direction.

The spectral albedo of various types of sea ice was systematically measured in situ in the Arctic during the R/V *Polarstern* cruise from August till October

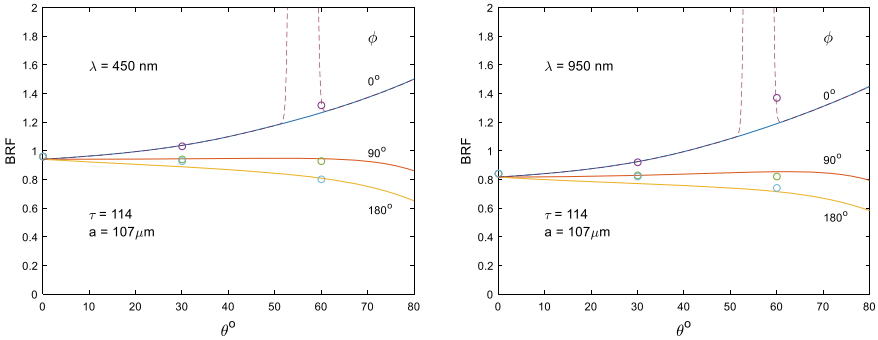

Fig. 12 Bidirectional reflectance factor of snow-covered ice measured in situ (o) and simulated with the model of the random ice-air mixture (–). The glint is shown with dashes

2012 (Istomina et al. 2016). The sea ice surface featured a variety of crystal sizes, from very fine fresh fallen snow to ice granules of about 2–3 mm. The ASD FieldSpec Pro III spectroradiometer was used for these measurements. Every spectrum consisted of 1000 points of the measured values from 0.35 μm to 1.35 μm. These points were approximated with a curve of the spectral albedo calculated with the method of spherical harmonics (Lenoble 1985), by fitting the three parameters: τ, a, and $\alpha_y(390)$. The best fit was understood in the least squares sense. During the cruise, a variety of field conditions were observed, including clear and cloudy skies of various cloud coverage. Illumination conditions were taken into account, when processing the measurement data, in the manner described by Malinka et al. (2016).

Figure 13 presents the comparison of the measured and retrieved albedo spectra for some typical cases. The left upper plot represents the bright surface with a typical grain size of about 500 μm. This is an intermediate case between the typical snow and the typical white ice. The surface could be treated as aged snow when snow grains become larger. This case clearly demonstrates that there is no strict separation between snow and white ice. Also the spectrum is affected by the yellow substance (decrease in the blue range). The right upper plot shows the case of typical white ice with the grain size of almost 3 mm and without visible pollution. The left lower plot represents the melt ice. The surface is dark and water-saturated. The layer is characterized by low optical thickness (about 5) and large ice grains (almost 5 mm). This case is important because it does not belong to the initial scope of the developed model, which is not presumed to describe wet snow or ice. A snow-covered surface is presented in the right lower plot. The optical thickness is high (greater than 30), and the grain size is about 200 μm, which is typical for fresh snow.

In general, the analysis of the experimental data shows that the model of the ice–air random mixture describes the reflective properties of typical white ice and snow excellently. A more extensive analysis has shown that the cases that are beyond the initial framework of the model, such as wet ice/snow, crusted snow, frozen cracks, and snow-covered ponds, can also be described by this model quite satisfactorily.

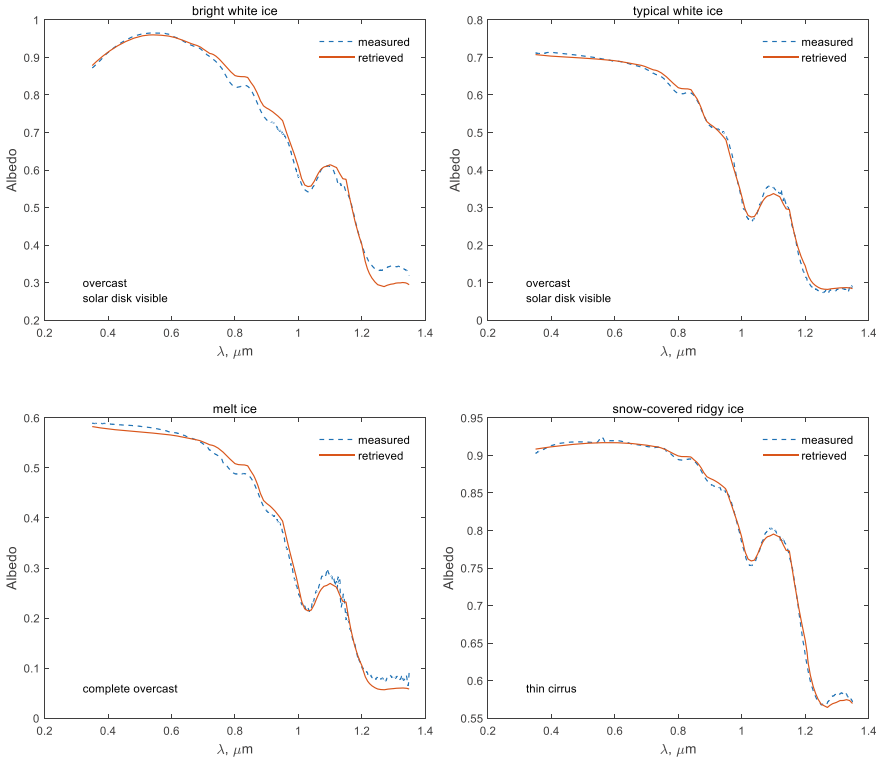

Fig. 13 Measured (--) and retrieved (–) spectral albedo of sea ice of various types at various illumination conditions

6.3 Laboratory Measurements

Two experiments on the snow reflective properties were taken in the Laboratory of Glaciology in Grenoble. The first one (Dumont et al. 2010) provided the high-accuracy measurements of the snow BRF together with the snow density and specific surface area (SSA) for some samples. In the second experiment (Dumont et al. TBP), in addition to the reflectance, the snow microstructure was investigated with the X-ray computed tomography. In both experiments, the snow albedo was calculated via the BRF values by means of the interpolation.

Figure 14 shows the spectral albedo of a sample from (Dumont et al. 2010) that was taken at Argentière (Mont Blanc, French Alps) at an altitude of 1250 m. Clustered, melt–freeze, rounded grains were observed at the surface, while deeper layers consisted of mixed forms, rounded and faceted. As the sample density ρ and thickness z were known (310 kg/m^3 and 12 cm, respectively), we retrieved all the three values—τ, a, and C_{st}— given the relationship

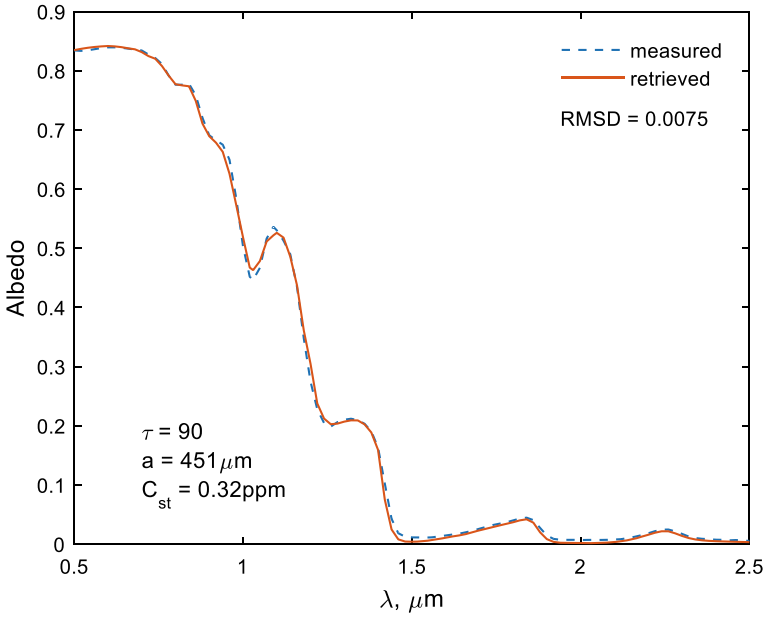

Fig. 14 Measured (--) and retrieved (–) spectral albedo of the snow sample at nadir incidence

$$\tau = \frac{\rho z}{\rho_{ice} a}, \tag{213}$$

which follows from Eq. (2), Eq. (137), and the definition of optical thickness $\tau = \varepsilon z$.

The retrieved values are also shown in Fig. 14. Although lots of impurities in the sample were reported by Dumont et al. (2010), the soot concentration turned out to be not so high (0.32 ppm). The SSA value retrieved with Eq. (12) is 9.7 versus 12.6 m^2/kg measured. The discrepancy is likely explained by the sample heterogeneity because the reflectance is mainly determined by the top layer, while the SSA was measured using methane absorption (Legagneux et al., 2002) in the deeper layers.

Figure 15 shows the BRF measured at the wavelengths of 0.5, 0.9, and 1.24 μm and simulated with the retrieved parameters.

In the second experiment (Dumont et al. TBP), the X-ray tomography images were performed for the snow samples at a resolution of 5 to 10 μm. The BRF measurements were carried out using the same set-up as in the previous experiment. We consider here two samples. The first one was the natural snow sampled in Grenoble directly after a snowfall. The second one was the natural snow taken at Chamrousse (the Belledonne mountain range, about 1700 m). It was then sieved in the laboratory and placed in the temperature gradient box, where it was stored for 16 days before the measurements. Figure 16 presents the measured and retrieved spectral albedo of the two samples at 30° incidence.

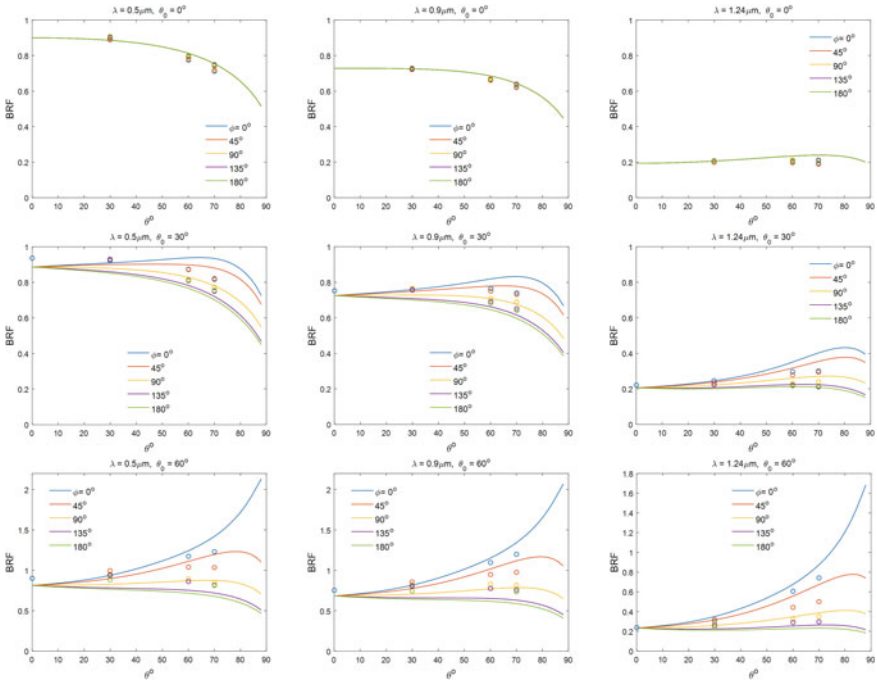

Fig. 15 Measured (o) and simulated (–) BRF of the snow sample at wavelengths of 0.5, 0.9, and 1.24 μm and incidence of 0°, 30°, and 60°

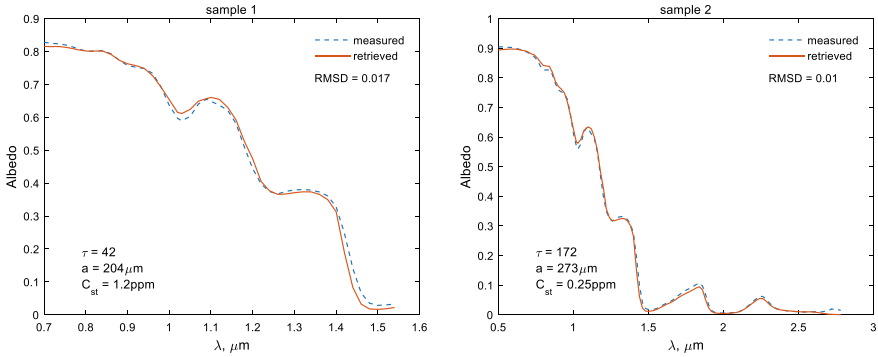

Fig. 16 Measured (--) and retrieved (–) albedo spectra of two samples at 30° incidence

The first sample was significantly thinner than the second one (6.5 and 16.5 cm, respectively), so the retrieved optical thicknesses are predictably different (42 vs. 172). As a consequence, the difference in the albedo values in the visible part of the spectrum is also apparent (about 0.8 for the first sample vs. 0.9 for the second one). The mean chord lengths of the ice phase calculated from the X-ray images taken

at different points of the samples were 205.5 ± 5.5 μm and 260. ± 23. μm for the first and second sample, respectively. Grains in the first sample were smaller because the snow there was fresh, taken immediately after a snowfall, while the snow in the second sample was older. The retrieved mean chords of 204 and 273 μm fit these values perfectly. Also, the retrieval shows that the snow taken in the mountains was much more pure: the soot concentration in it was 5 times less than that in the snow taken in the urban area.

Figures 17 and 18 show the BRF of these two sample at wavelengths of 0.8 and 1.3 μm. The BRF was measured at 0°, 30°, and 60° zenith incidence. The measurements were taken at three detector azimuths for the vertical incidence, seven azimuths for 30° incidence, and only one azimuth (forward scattering in the principal plane) for 60° incidence.

Figures 17–18 demonstrate slight underestimation of the measured BRF in the directions close to vertical, especially for the sample with the lower optical thickness. As well, anisotropy of the simulated BRF is stronger than that of the measured one, which means that the reflectance is overestimated in the forward direction and underestimated in the backward one, especially for oblique viewing and incidence. However, in general, the simulated and measured data agree very well.

7 Conclusion

The above investigation shows how useful the stochastic approach to the problems of light scattering could be. It gives analytical solutions in terms of the chord length distribution to the problems of scattering by irregularly shaped particles in the Fraunhofer diffraction, Rayleigh–Gans, Wentzel–Kramers–Brillouin, and geometrical optics approximations. Calculation of the characteristic function of a given particle shape is much more time-consuming than numeric simulations with more strict methods, such as DDA or Monte-Carlo. Moreover, the stereological approach describes in a natural way not only a single particle but also to a densely packed ensemble represented by a mosaic or a mixture, thus allowing us to define an elementary volume of a porous material and determine its optical characteristics, which can further be used in the radiative transfer theory. On the other hand, the stereological approach does not require that the particle shape is strictly random; it may be applied to chaotically oriented particles of a regular nonspherical shape, as well.

The assumption that snow and white ice are the random mixtures of air and ice gives an elegant and quite simple way to calculate their optical properties, including the spectral albedo and bidirectional reflectance. The verification with field data has shown that this model is sufficiently reliable: most of the measured spectra are retrieved with a high degree of accuracy by fitting only few parameters.

As a whole, the stereological approach can be useful both for direct and inverse problems of light scattering. It can help in studying the radiance distribution in composite materials and densely packed geophysical media, as well as in developing various retrieval techniques.

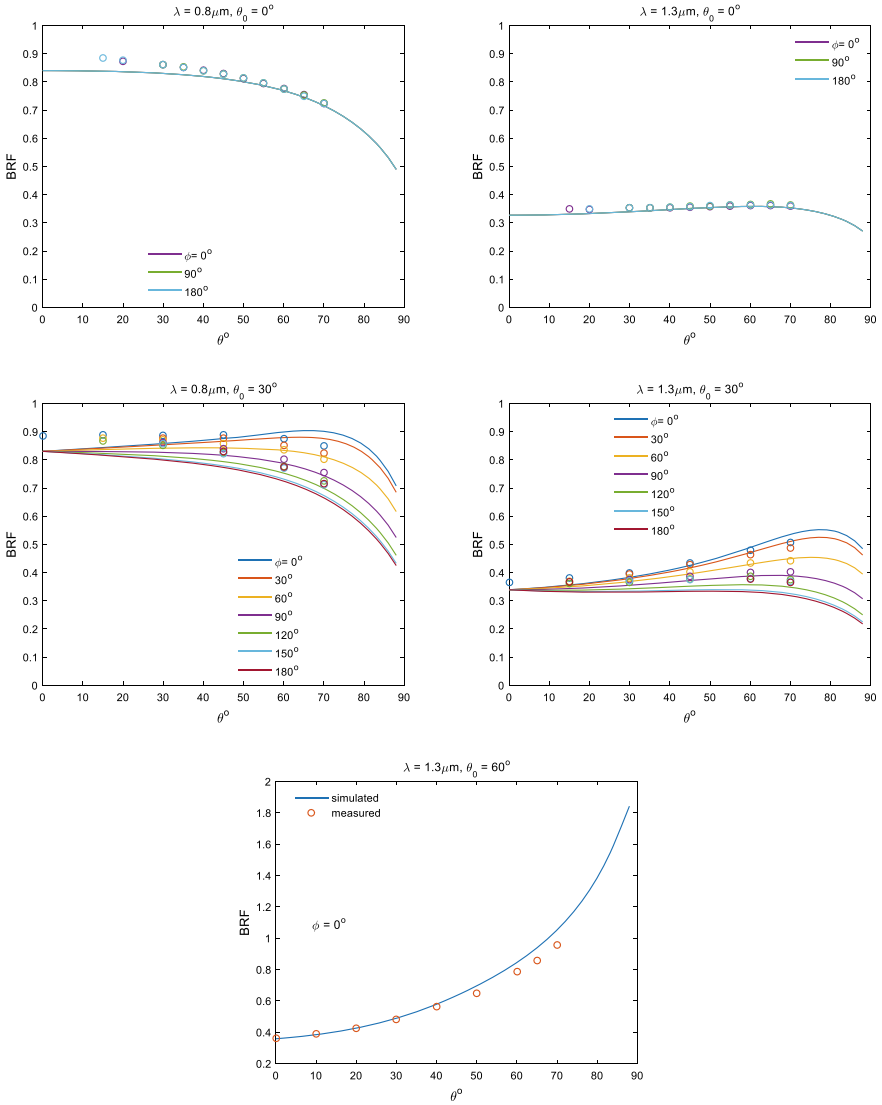

Fig. 17 Measured (o) and simulated (–) BRF of sample 1 at wavelengths of 0.8 and 1.3 μm and incidence of 0°, 30°, and 60°

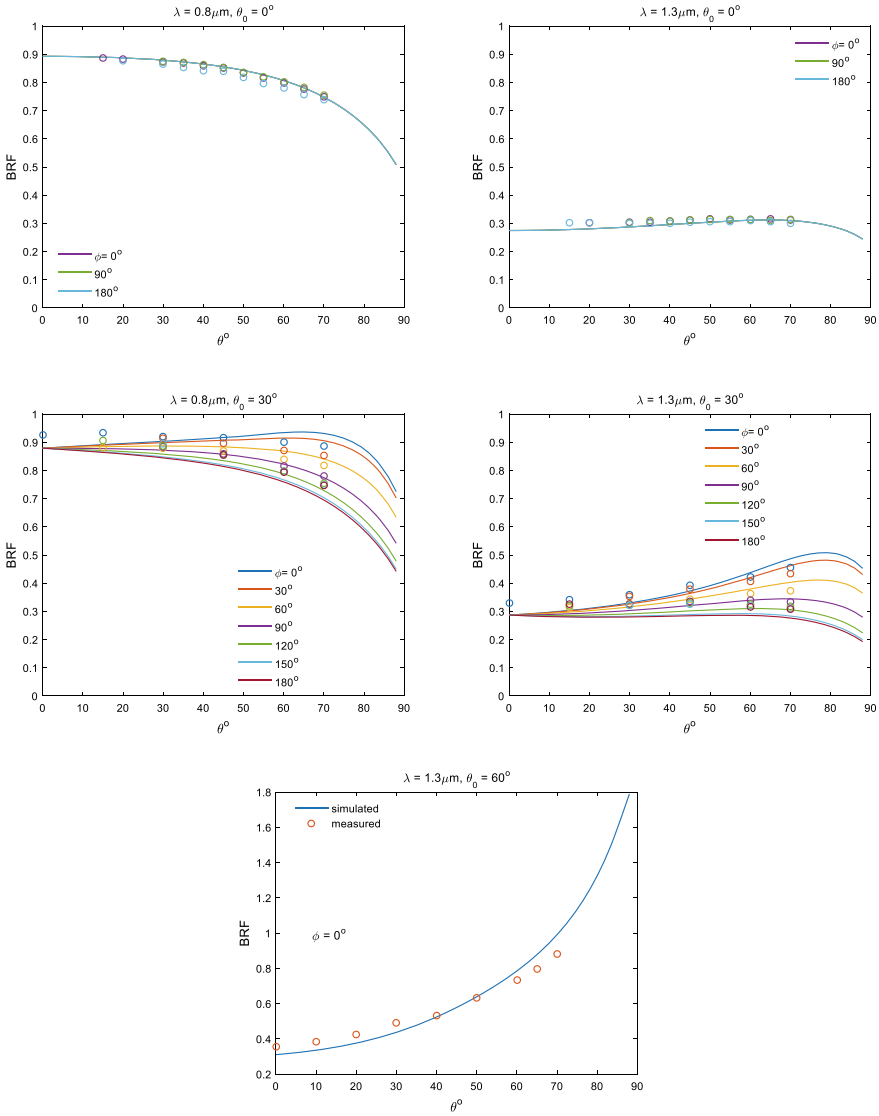

Fig. 18 Measured (o) and simulated (–) BRF of sample 2 at wavelengths of 0.8 and 1.3 μm and incidence of 0°, 30°, and 60°

Acknowledgements The author is grateful to Larisa Istomina and Marie Dumont, who performed the high-accuracy and reliable—and sometimes very difficult—measurements of ice and snow reflectance.

References

Aoki T, Fukabori M, Hachikubo A, Tachibana Y, Nishio F (2000) Effects of snow physical parameters on spectral albedo and bi-directional reflectance of snow surface. J Geophys Res 105(D8):10219–10236

Barun VV, Gavrilovich AB (1987) Spectral characteristics of the light scattering of ground aerosols. J Appl Spectrosc 47:932–938. https://doi.org/10.1007/BF00659439

Beine H, Anastasio FC, Domine F, Douglas T, Barret M, France J, King M, Hall S, Ullmann K (2012) Soluble chromophores in marine snow, seawater, sea ice and frost flowers near Barrow, Alaska. J Geophys Res 117:D00R15. doi:https://doi.org/10.1029/2011JD016650

Bogorodskii VV (ed) (1970) The Physics of Ice. Translated from Russian, Isr Program for Sci Transl, Jerusalem

Bohren CF, Barkstrom BR (1974) Theory of the optical properties of snow. J Geophys Res 79:4527–4535

Bohren CF, Huffman DR (1983) Absorption and scattering of light by small particles. John Wiley & Sons, New York

Boors BN, Burns RK (1984) Analyzing the spatial distribution of drumlins: a two-phase mosaic approach. J Glaciol 30:302–307

Born M, Wolf E (1968) Principles of optics. Pergamon Press, Oxford

Borovoi AG (2006) Multiple scattering of short waves by uncorrelated and correlated scatterers. In: Kokhanovsky AA (eds) Light Scattering reviews. springer praxis books. Springer, Berlin, Heidelberg

Brillouin L (1926) La mécanique ondulatoire de Schrödinger: une méthode générale de resolution par approximations successives. Comptes Rendus De l'Academie Des Sciences 183:24–26

Byshuev A, Volkov N, Loschilov V (1974) Atlas of the Ice formations. Hydrometeoizdat, Leningrad (in Russian)

Choudhury BJ, Chang ATC (1979) The solar reflectance of a snow field. Cold Reg Sci Technol 1:121–128

Coleman R (1981) Intercept lengths of random probes through boxes. J Appl Prob 18:276–282

Curry JA, Schramm JL, Ebert EE (1995) Sea-ice albedo climate feedback mechanism. J Climate 8:240–247

Debye P, Anderson HR Jr, Brumberger H (1957) Scattering by an Inhomogeneous Solid. II. The Correlation Function and Its Application. J Appl Phys 28:679–683

Dirac PAM (1943) Approximate Rate of Neutron Multiplication for a Solid of Arbitrary Shape and Uniform Density. Declassified British Report MS-D-5, part I. Second World War Atomic Energy Research in Britain

Dobbins RA, Jizmagian GS (1966) Optical Scattering Cross Sections for Polydispersions of Dielectric Spheres. J Opt Soc Am 56:1345–1349

Dombrovsky LA, Kokhanovsky AA (2019) The influence of pollution on solar heating and melting of a snowpack. J Quant Spectrosc Ra 233:42–51

Domine F, Albert M, Huthwelker T, Jacobi H-W, Kokhanovsky AA, Lehning M, Picard G, Simpson WR (2008) Snow physics as relevant to snow photochemistry. Atmos Chem Phys 8:171–208

Duck FA (1990) Physical properties of tissue: a comprehensive reference book. Academic Press, London

Dumont M, Brissaud O, Picard G, Schmitt B, Gallet J-C, Arnaud Y (2010) High-accuracy measurements of snow Bidirectional Reflectance Distribution Function at visible and NIR wavelengths – comparison with modelling results. Atmos Chem Phys 10:2507–2520. https://doi.org/10.5194/acp-10-2507-2010

Dumont M, Flin F, Malinka A, Brissaud O, Hagenmuller P, Lapalus Ph, Lesaffre B, Dufour A, Calonne N, Roscoat SR du, Ando E (to be published) Experimental and model based investigation of the links between snow bidirectional reflectance and snow microstructure

Feigin LA, Svergun DI (1987) Structure analysis by small angle X-ray and neutron scattering. Plenum Press, New York

Gelfand IM, Minlos RA, Shapiro ZYa, (1963) Representations of the rotation and Lorentz groups and their applications. Pergamon Press, Oxford
Gershun AA (1937) On the problem of diffuse light transmission. Proc GOI 4:12–40 (in Russian)
Gilbert EN (1962) Random subdivisions of space into crystals. Ann Math Stat 33:958–972
Gille W (2000) Chord length distributions and small-angle scattering. Eur Phys J B 17:371–383
Gille W, Kabisch O, Reichl S, Enke D, Fürst D, Janowski F (2002) Characterization of porous glasses via small-angle scattering and other methods. Micropor Mesopor Mat 54:145–153
Gommes CJ, Jiao Y, Roberts AP, Jeulind D (2020) Chord-length distributions cannot generally be obtained from small-angle scattering. Appl Cryst 53:127–132. https://doi.org/10.1107/S1600576719016133
Grannas A, Pagano L, Pierce B, Bobby R, Fede AS (2014) Role of dissolved organic matter in ice photochemistry. Environ Sci Technol 48:10725–10733. https://doi.org/10.1021/es5023834
Grenfell TC, Maykut GA (1977) The optical properties of ice and snow in the Arctic basin. J Glaciol 18:445–463
Grenfell TC, Warren SG (1999) Representation of a nonspherical ice particle by a collection of independent spheres for scattering and absorption of radiation. J Geophys Res 104(D24):31697–31709
Grenfell TC, Warren SG, Mullen PC (1994) Reflection of solar radiation by the Antarctic snow surface at ultraviolet, visible, and near-infrared wavelengths. J Geophys Res 99(D9):18669–18684
Guinier A, Fournet G (1955) Small Angle Scattering of X-rays. John Wiley & Sons, New York
Hamre B, Winther J-G, Gerland S, Stamnes J, Stamnes K (2004) Modeled and measured optical transmittance of snow-covered first-year sea ice in Kongsfjorden. Svalbard. J Geophys Res 109:C10006. https://doi.org/10.1029/2003jc001926
Hansell DA, Carlson CA (2014) Biogeochemistry of marine dissolved organic matter. Academic Press, Amsterdam
Hansen JE, Travis LD (1974) Light scattering in planetary atmospheres. Space Sci Rev 16:527–610
Henyey LC, Greenstein JL (1941) Diffuse radiation in the galaxy. Astrophys J 93:70–83
Herzfeld UC, Maslanik JA, Sturm M (2006) Geostatistical Characterization of Snow-Depth Structures on Sea Ice Near Point Barrow, Alaska—A Contribution to the AMSR-Ice03 Field Validation Campaign. IEEE T Geosci Remote 44:3038–3056
Heygster G, Alexandrov V, Dybkjær G, von Hoyningen-Huene W, Girard-Ardhuin F, Katsev I, Kokhanovsky A, Lavergne T, Malinka A, Melsheimer C, Toudal Pedersen L, Prikhach A, Saldo R, Tonboe R, Wiebe H, Zege E (2012) Remote sensing of sea ice: advances during the DAMOCLES project. Cryosphere 6:1411–1434. https://doi.org/10.5194/tc-6-1411-2012
Hovenier JW, van der Mee CVM (1983) Fundamental relationships relevant to the transfer of polarized light in a scattering atmosphere. Astron Astrophys 128:1–16
van de Hulst HC (1957) Light scattering by small particles. John Wiley & Sons, New York
Ishimaru A (1978) Wave propagation and scattering in random media. Academic Press, New York
Ishimoto H, Zaizen Y, Uchiyama A, Masuda K, Mano Y (2010) Shape modeling of mineral dust particles for light-scattering calculations using the spatial Poisson-Voronoi tessellation. J Quant Spectrosc Ra 111:2434–2443
Istomina L, Heygster G, Huntemann M, Schwarz P, Birnbaum G, Scharien R, Polashenski C, Perovich D, Zege E, Malinka A, Prikhach A, Katsev I (2015) Melt pond fraction and spectral sea ice albedo retrieval from MERIS data – Part 1: Validation against in situ, aerial, and ship cruise data. Cryosphere 9:1551–1566. https://doi.org/10.5194/tc-9-1551-2015
Istomina L, Heygster G, Huntemann M, Marks H, Melsheimer C, Zege E, Malinka A, Prikhach A, Katsev I (2015) Melt pond fraction and spectral sea ice albedo retrieval from MERIS data – Part 2: Case studies and trends of sea ice albedo and melt ponds in the Arctic for years 2002–2011. Cryosphere 9:1567–1578. https://doi.org/10.5194/tc-9-1567-2015
Istomina L, Nicolaus M, Perovich DK (2016) Surface spectral albedo complementary to ROV transmittance measurements at 6 ice stations during POLARSTERN cruise ARK XXVII/3 (IceArc) in, (2012) Institut für Umweltphysik. Universität Bremen, Bremen. https://doi.org/10.1594/PANGAEA.867292

Jacquier S, Gruy F (2008) Anomalous diffraction approximation for light scattering cross section: case of ordered clusters of non-absorbent spheres. J Quant Spectrosc Ra 109:789–810
Jerlov NG (1968) Optical oceanography. Elsevier, Amsterdam
Jeulin D (2000) Random texture models for material structures. Stat Comput 10:121–132
Kellerer AM (1971) Considerations on the random traversal of convex bodies and solutions for general cylinders. Radiat Res 47:359–376
Kellerer AM (1984) Chord-Length Distributions and Related Quantities for Spheroids. Radiat Res 98:425–437
Kendall MG, Moran PAP (1963) Geometrical probabilities. Griffins statistical monographs and courses, No. 5, London, C. Griffin
Kerbrat M, Pinzer B, Huthwelker T, Gäggeler HW, Ammann M, Schneebeli M (2008) Measuring the specific surface area of snow with X-ray tomography and gas adsorption: comparison and implications for surface smoothness. Atmos Chem Phys 8:1261–1275
Klett JD, Sutherland RA (1992) Approximate methods for modeling the scattering properties of nonspherical particles: evaluation of the Wentzel–Kramers–Brillouin method. Appl Opt 31:373–386
Kokhanovsky AA, Zege EP (2004) Scattering optics of snow. Appl Opt 43:1589–1602
Kokhanovsky AA, Aoki T, Hachikubo A, Hori M, Zege EP (2005) Reflective properties of natural snow: approximate asymptotic theory versus in situ measurements. IEEE T Geosci Remote 43:1529–1535
Køltzow M (2007) The effect of a new snow and sea ice albedo scheme on regional climate model simulations. J Geophys Res 112:D07110. https://doi.org/10.1029/2006JD007693
Kopelevich OV (1983) Low-parametric model of seawater optical properties. In: Monin AS (ed) Ocean optics i: physical ocean optics. Nauka, Moscow, pp 208–234 (in Russian)
Kramers HA (1926) Wellenmechanik Und Halbzählige Quantisierung. Z Phys 39:828–840. https://doi.org/10.1007/BF01451751
Lane DE, Kristen G, Somerville RCJ (2002) Radiative transfer through broken clouds: observations and model validation. J Climate 15:2921–2933
Legagneux L, Cabanes A, Domine F (2002) Measurement of the specific surface area of 176 snow samples using methane adsorption at 77 K. J Geophys Res 107:D174335. https://doi.org/10.1029/2001JD001016
Lenoble J (ed) (1985) Radiative transfer in scattering and absorbing atmospheres: standard computational procedures. Deepak, Hampton
Light B (2010) Theoretical and observational techniques for estimating light scattering in first-year Arctic sea ice. In: Kokhanovsky A (ed) Light scattering reviews 5: single light scattering and radiative transfer. Springer, Berlin, pp 331–391
Light B, Eicken H, Maykut GA, Grenfell TC (1998) The effect of included particulates on the spectral albedo of sea ice. J Geophys Res 103(C12):27739–27752
Liou KN, Yang P (2016) Light scattering by ice crystals: fundamentals and applications. Cambridge University Press, Cambridge. https://doi.org/10.1017/CBO9781139030052
Loiko VA, Konkolovich AV, Miskevich AA (2016) Light Scattering by a Nematic liquid crystal droplet: Wentzel–Kramers–Brillouin approximation. J Exp Theor Phys+ 122:176–192
Lopatin VN, Shepelevich NV (1996) Consequences of the Integral wave equation in the Wentzel–Kramers–Brillouin approximation. Opt Spectrosc+ 81:103–106
Mäder U (1980) Chord length distributions for circular cylinders. Radiat Res 82:454–466
Malinka A (2010) Approximation of the Fraunhofer diffraction peak, produced by particles of arbitrary shape. Opt Lett 35:3411–3413
Malinka A (2011) Fraunhofer diffraction by a random screen. J Opt Soc Am a 28:1656–1661
Malinka A (2011) Light scattering by optically soft large particles of arbitrary shape. J Opt Soc Am a 28:2086–2090
Malinka A (2014) Light scattering in porous materials: Geometrical optics and stereological approach. J Quant Spectrosc Ra 141:14–23

Malinka A (2014) Comment to the paper "Light scattering in porous materials: Geometrical optics and stereological approach"—Phase shift between the parallel and perpendicular components in total internal reflection. J Quant Spectrosc Ra 147:60–62. https://doi.org/10.1016/j.jqsrt.2014.05.018

Malinka A (2015) Analytical expressions for characteristics of light scattering by arbitrarily shaped particles in the WKB approximation. J Opt Soc Am a 32:1344–1351. https://doi.org/10.1364/JOSAA.32.001344

Malinka A (2015b) Analytical description of light scattering by phytoplankton particles in the WKB approximation. In: Proceedings of VIII International Conference "Current Problems in Optics of Natural Waters" (ONW-2015), 8–12 September 2015, St.-Petersburg, Russia. Nauka, St.-Petersburg, pp 113–118

Malinka A (2020) Asymptotic methods in the theory of light scattering by nonspherical particles. Springer Series in Light Scattering, Kokhanovsky A (ed), Springer, Cham, 5:193–234.https://doi.org/10.1007/978-3-030-38696-2_5

Malinka A, Zege E, Heygster G, Istomina L (2016) Reflective properties of white sea ice and snow. Cryosphere 10:2541–2557. https://doi.org/10.5194/tc-10-2541-2016

Malinka AV, Zege EP, Katsev IL, Prikhach AS, Istomina L (2016) Accounting for Atmospheric Effects in the Interpretation of Satellite and Ground-Based Optical Measurements. J Appl Spectrosc 83:741–749. https://doi.org/10.1007/s10812-016-0357-3

Malinka A, Zege E, Istomina L, Heygster G, Spreen G, Perovich D, Polashenski C (2018) Reflective properties of melt ponds on sea ice. Cryosphere 12:1921–1937. https://doi.org/10.5194/tc-12-1921-2018

Massom RA, Eicken H, Haas C, Jeffries MO, Drinkwater MR, Sturm M, Worby AP, Wu X, Lytle VI, Ushio S, Morris K, Reid PA, Warren S, Allison I (2001) Snow on Antarctic ice. Rev Geophys 39:413–445

Matzl M, Schneebeli M (2006) Measuring specific surface area of snow by near-infrared photography. J Glaciol 52:558–564

McLean JW, Voss KJ (1991) Point spread function in ocean water: comparison between theory and experiment. Appl Opt 30:2027–2030

Meijering JL (1953) Interface area, edge length, and number of vertices in crystal aggregates with random nucleation. Philips Res Rep 8:270–290

Miller M (1969) Bounds for the effective electrical, thermal and magnetic properties of heterogeneous materials. J Math Phys 10:1988–2004

Naumenko YeK (1971) The feasibility of obtaining data on the microstructure of an atmospheric aerosol by laser probing. Izv Atmos Ocean Phy+ 7:605–608 [MGA 23.6–4081]

Nicolaus M, Gerland S, Hudson SR, Hanson S, Haapala J, Perovich DK (2010) Seasonality of spectral albedo and transmittance as observed in the Arctic Transpolar Drift in 2007. J Geophys Res 115:C11011. https://doi.org/10.1029/2009JC006074

Norman L, Thomas DN, Stedmon CA, Granskog MA, Papadimitriou S, Krapp RH, Meiners KM, Lannuzel D, van der Merwe P, Dieckmann GS (2011) The characteristics of dissolved organic matter (DOM) and chromophoric dissolved organic matter (CDOM) in Antarctic sea ice. Deep Sea Res Part II 58:1075–1091. https://doi.org/10.1016/j.dsr2.2010.10.030

Norrisa JG, Wyllie-Echeverria S, Mumford T, Bailey A, Turner T (1997) Estimating basal area coverage of subtidal seagrass beds using underwater videography. Aquat Bot 58:269–287

Nürnberg D, Wollenburg I, Dethleff D, Eicken H, Kassens H, Letzig T, Reimnitz E, Thiede J (1994) Sediments in Arctic sea ice – Implications for entrainment, transport and release. Mar Geol 119:185–214

Perovich DK (1994) Light reflection from sea ice during the onset of melt. J Geophys Res 99(C2):3351–3359

Perovich DK (1996) The optical properties of sea ice. US Army Cold Regions Research and Engineering Laboratory (CRREL) Report 96–1, Hanover, NH, USA. www.dtic.mil/cgi-bin/GetTRDoc?AD=ADA310586 (access: 01/05/2020)

Perovich DK, Grenfell TC, Light B, Hobbs PV (2002) Seasonal evolution of the albedo of multiyear Arctic sea ice. J Geophys Res 107:C108044

Perovich DK, Grenfell TC, Light B, Elder BC, Harbeck J, Polashenski C, Tucker III WB, Stelmach C (2009) Transpolar observations of the morphological properties of Arctic sea ice. J Geophys Res 114:C00A04. doi:https://doi.org/10.1029/2008JC004892

Picard G, Arnaud L, Domine F, Fily M (2009) Determining snow specific surface area from near-infrared reflectance measurements: Numerical study of the influence of grain shape. Cold Reg Sci Technol 56:10–17

Pielou EC (1964) The spatial pattern of two-phase patchworks of vegetation. Biometrics 20:156–167

Pirazzini R (2008) Factors controlling the surface energy budget over snow and ice. Academic dissertation in meteorology, Finnish Meteorological Institute, Helsinki

Pomraning GC (1988) Radiative transfer in random media with scattering. J Quant Spectrosc Ra 17:595–613

Pomraning GC (1991) Linear Kinetic Theory and Particle Transport in Stochastic Mixtures. World Scientific Publishing, Singapore

Porod G (1982) General theory. In: Glatter O, Kratky O (eds) Small Angle X-ray Scattering. Academic Press, New York, pp 17–51

Reimnitz E, McCormick M, McDougall K, Brouwers E (1993) Sediment export by ice rafting from a coastal polynya, Arctic Alaska, U.S.A. Arctic Alpine Res 25:83–98

Roberts AP, Torquato S (1999) Chord-distribution functions of three-dimensional random media: Approximate first-passage times of Gaussian processes. Phys Rev E 59:4953–4963

Sahni DC (1989) An application of reactor noise techniques to neutron transport problems in a random medium. Ann Nucl Energy 16:397–408

Schmidt J, Wandinger U, Malinka A (2013) Dual-field-of-view Raman lidar measurements for the retrieval of cloud microphysical properties. Appl Opt 52:2235–2247

Shindell D, Faluvegi G (2009) Climate response to regional radiative forcing during the twentieth century. Nat Geosci 2:294–300. https://doi.org/10.1038/ngeo473

Switzer P (1965) A random set process in the plane with a Markovian property. Ann Math Statist 36:1859–1863

Tollefson J (2009) Atmospheric science: climate's smoky spectre. Nature 460:29–32. https://doi.org/10.1038/460029a

Thomas DN, Lara RJ, Eicken H, Kattner G, Skoog A (1995) Dissolved organic matter in Arctic multi-year sea ice during winter: major components and relationship to ice characteristics. Polar Biol 15:477–483

Thomas DN, Kattner G, Engbrodt R, Gianelli V, Kennedy H, Haas C, Dieckmann G (2001) Dissolved organic matter in Antarctic sea ice. Ann Glaciol 33:297–303

Untersteiner N (1990) Structure and dynamics of the Arctic Ocean ice cover. In: Grantz A, Johnson L, Sweeney JF (eds) The Arctic Ocean Region. Geol Soc of Am, Boulder, Colorado, pp 37–51

Warren SG (1982) Optical properties of snow. Rev Geophys Space Phys 20:67–89

Warren SG, Brandt RE (2008) Optical constants of ice from the ultraviolet to the microwave: A revised compilation. J Geophys Res 113:D14220. https://doi.org/10.1029/2007JD009744

Wells WH (1973) Theory of small angle scattering. AGARD Lect Ser, No 61 (NATO)

Wentzel G (1926) Eine Verallgemeinerung der Quantenbedingungen für die Zwecke der Wellenmechanik. Z Phys 38:518–529. https://doi.org/10.1007/BF01397171

Wiscombe WJ, Warren SG (1980) A model for the spectral albedo of snow. I. Pure Snow, J Atmos Sci 37:2712–2733

WMO (1986) A preliminary cloudless standard atmosphere for radiation computation. WCP 112, WMO/TD 24. https://library.wmo.int/index.php?lvl=notice_display&id=11668. Accessed 01 June 2020

WMO (2014) Sea ice nomenclature. WMO 259, Suppl 5. https://www.ioc-unesco.org/index.php?option=com_oe&task=viewDocumentRecord&docID=4438. accessed 01 June 2020

Yang P, Liou KN (1996) Geometric-optics–integral-equation method for light scattering by nonspherical ice crystals. Appl Opt 35:6568–6584

Yurkin MA, Hoekstra AG (2011) The discrete-dipole-approximation code ADDA: capabilities and known limitations. J Quant Spectrosc Ra 112:2234–2247

Zege EP, Katsev IL, Prikhach AS, Gilbert G, Witherspoon N (2006) Simple model of the optical characteristics of bubbles and sediments in seawater of the surf zone. Appl Opt 45:6577–6585

Zege E, Katsev I, Malinka A, Prikhach A, Polonsky I (2008) New algorithm to retrieve the effective snow grain size and pollution amount from satellite data. Ann Glaciol 49:139–144

Zege EP, Katsev IL, Malinka AV, Prikhach AS, Heygster G, Wiebe H (2011) Algorithm for retrieval of the effective snow grain size and pollution amount from satellite measurements. Remote Sens Environ 115:2674–2685

Zege EP, Malinka AV, Katsev IL, Prikhach AS, Heygster G, Istomina L (2013) Optical methods and algorithms for satellite remote sensing of sea ice in arctic region. In: Proceedings of VII International Conference "Current Problems in Optics of Natural Waters" (ONW-2013), 10–14 September 2013, St.-Petersburg, Russia. Nauka, St.-Petersburg, pp 36–40

Zege EP, Malinka AV, Katsev IL, Prikhach AS (2015a) Sea ice optics. In: Proceedings of VIII International Conference "Current Problems in Optics of Natural Waters" (ONW-2015), 8–12 September 2015, St.-Petersburg, Russia. Nauka, St.-Petersburg, pp 26–31

Zege EP, Malinka AV, Katsev IL, Prikhach AS, Heygster G, Istomina L (2015) Algorithm to retrieve the melt pond fraction and the spectral albedo of Arctic summer ice from satellite optical data. Remote Sens Environ 163:153–164. https://doi.org/10.1016/j.rse.2015.03.012

Zege E, Malinka A, Katsev I, Prikhach A, Istomina L, Heygster G, Spreen G (2018) Reflective properties of summer Arctic sea ice in visible and near infrared. Fundamentalnaya I Prikladnaya Gidrofizika 11:17–25. https://doi.org/10.7868/S2073667318030024

Zege E, Malinka A, Katsev I, Prikhach A, Heygster G, Spreen G. (2019) Retrieval of the structure of pixels of the Arctic Ocean ice cover and characteristics of its components from satellite data. In: Proceedings of XX All-Russian conference with international participation "Current Problems in Optics of Natural Waters" (ONW-2019), 9–11 October 2019, St.-Petersburg, Russia. Himizdat Publishing, St.-Petersburg, pp 37–41

Inverse Methods in Studies of Terrestrial Atmosphere

Michael Yu. Kataev

1 Introduction

The cloudless terrestrial atmosphere is composed of various gases and atmospheric aerosols. The load of atmospheric species varies with height having harmful effects on people, animals and plants in case the concentration of some gases and atmospheric particulate matter (e.g., NO_2, O_3, dust and soot aerosols) exceeds certain levels. Therefore, corresponding parameters are measured on the ground by various state environmental organizations. Recently the regular survey of air quality using satellite instrumentation has been started. The results are reported on TV together with weather broadcasts (https://climate.copernicus.eu/euronews-and-copernicus-provide-exclusive-daily-24-hour-air-quality-forecast-and-monthly-climate). The superiority of satellite observations as compared to ground stations is due to the global nature of satellite observations. The results can be derived at any point—even in such remote areas, which have not been visited by humans (say, in Antarctica, where often ozone hole is detected).

Satellite observations are performed using passive and active remote systems, which often operate in the optical range electromagnetic spectrum (e.g., lidars, spectrometers, radiometers, and polarimeters). An important point is to understand the mathematical relationships between the measured and transmitted to the ground stations optical signals and concentration of various atmospheric species and also their horizontal and vertical distributions (e.g., smoke, volcanic and dust plumes, tropospheric ozone and nitrous oxide spatial distributions). This includes the formulation of direct problem, which relates concentration of species with (for passive systems) spectral top-of-atmosphere solar light reflectance. In some cases

M. Yu. Kataev (✉)
Department Control Systems, Tomsk State University of Control Systems and Radioelectronics, Tomsk, Russia
e-mail: kataev89@gmail.com

© The Author(s), under exclusive license to Springer Nature Switzerland AG 2021

A. Kokhanovsky (ed.), *Springer Series in Light Scattering*, Springer Series in Light Scattering, https://doi.org/10.1007/978-3-030-71254-9_4

the Stokes vector of the reflected solar light is measured. The measurements are performed at discrete wavelengths and observation directions. On the second stage one needs to solve the inverse problem and derive necessary parameters from indirect optical measurements. Although the direct problem always has a solution, the inverse problem in some cases can not be solved (for example, due to measurements performed in a such spectral range, where a given atmospheric parameter has almost influence on the optical signal). Also inverse problems are often ill–posed. It means that even small errors in the experimental data lead to large errors in the retrieved atmospheric parameters.

The information obtained through processing of satellite data is necessary for the development of computer models of various classes that reflect the behavior of various components of the atmosphere in time and space. The information databases compiled during measurements and modeling make it possible to solve numerous scientific and practical problems including air quality monitoring, chemical weather and climate change (https://climate.copernicus.eu/euronews-and-copernicus-provide-exclusive-daily-24-hour-air-quality-forecast-and-monthly-climate).

Satellite remote sensing is a technology used for obtaining information about an object of research through analysis of radiance reaching the satellite device. Solution of scientific and practical problems relies on information on different types of atmosphere and land objects, their distribution, and transformation in space and time. In the atmosphere and on land, a satellite device registers radiance absorbed, reflected, transmitted or emitted by the objects (for example, by gases or aerosol). Remote sensing data is very important for a wide range of applications: atmosphere physics, environmental, climate change, weather forecast, etc. Today, there are hundreds of satellites of all types in space, including those used for remote sensing.

The focus of this paper is on providing a description of techniques for retrieval of data on trace gases and aerosols from satellite remote sensing data. Some of the retrieving techniques are well known (for example, optimal estimation method, nonlinear regression, regularization), while others (neural network, random forest, support vector machine) have not yet been extensively used and discussed in publications on atmospheric remote sensing yet.

2 Remote Sensing Instrumentation

Remote sensing devices (instruments or sensors) record the radiance in different spectral regions and provide information about the Earth surface and atmosphere. Some of the spectral regions to obtain information on parameters of precipitation, vegetation, soil, dust, land surface temperature, and other parameters associated with trace gases or atmospheric aerosol are used.

Satellite remote devices measure the radiance that interacts with the Earth's surface and atmosphere. In processes of such interactions, radiance changes its direction, intensity, and polarization. The value of these changes depends on chemical and physical processes, spatial structure, illumination, and many other parameters. The technical feature of the device associated with spectral and precision characteristics is of great importance. In itself, the result of measuring radiation by a satellite device is an important and complex task, but the relevance of the measurement depends on the methods of information extraction and analysis.

The radiation measured by a satellite device depends on many factors associated with its passage through the atmosphere and reflection from the Earth's surface. Remote-sensing satellite devices are divided into types based on measurement schemes (nadir, limb, occultation or another), on the type of spectral device (spectrometer, radiometer, polarimeter, Fourier spectrometer or others). The main source of information on the concentration of gas components in the atmosphere and aerosol load is the ultraviolet, visible and near IR spectral range (0.3–3.0 μm). The main absorption bands of many gas components are within this spectral range (see Fig. 1), as are transparency windows in which the properties of aerosol are determined (Lenoble 1985; Rozanov et al. 2001, 2005; Thomas and Stamnes 1999; Timofeev and Vasilyev 2003; Hansen 1971; Hansen and Travis 1974; Mitsel et al. 1995; Schott 1999; Sobolev 1956).

When addressing the problem of extracting useful information from radiation measured on the board of the satellite, it is necessary to consider the entire measurement process. The main elements of the satellite measurement process shown in Fig. 2.

An important step in the development of remote sensing technologies is the launch of hyperspectral devices into space. The abundance of spectral information is a positive factor as it makes it possible to improve retrieval, as well as a challenge, as it requires a massive amount of measurements and development of special methods of processing, storage, and analysis (big data technology). Table 1 shows characteristics of selected hyperspectral devices.

Satellite measurements are performed using devices with certain characteristics, some of which are shown in Fig. 3. Depending on the measurement scheme, all these parameters are central and determine the processing techniques.

There are four main geometric measurement schemes (see Fig. 4): (a) nadir; (b) occultation; (c) limb and (d) emission. For each scheme, the altitude range, spatial resolution, spectral range, spectral resolution, field of view can vary substantially. As a result, each measurement scheme is associated with its own measurement model.

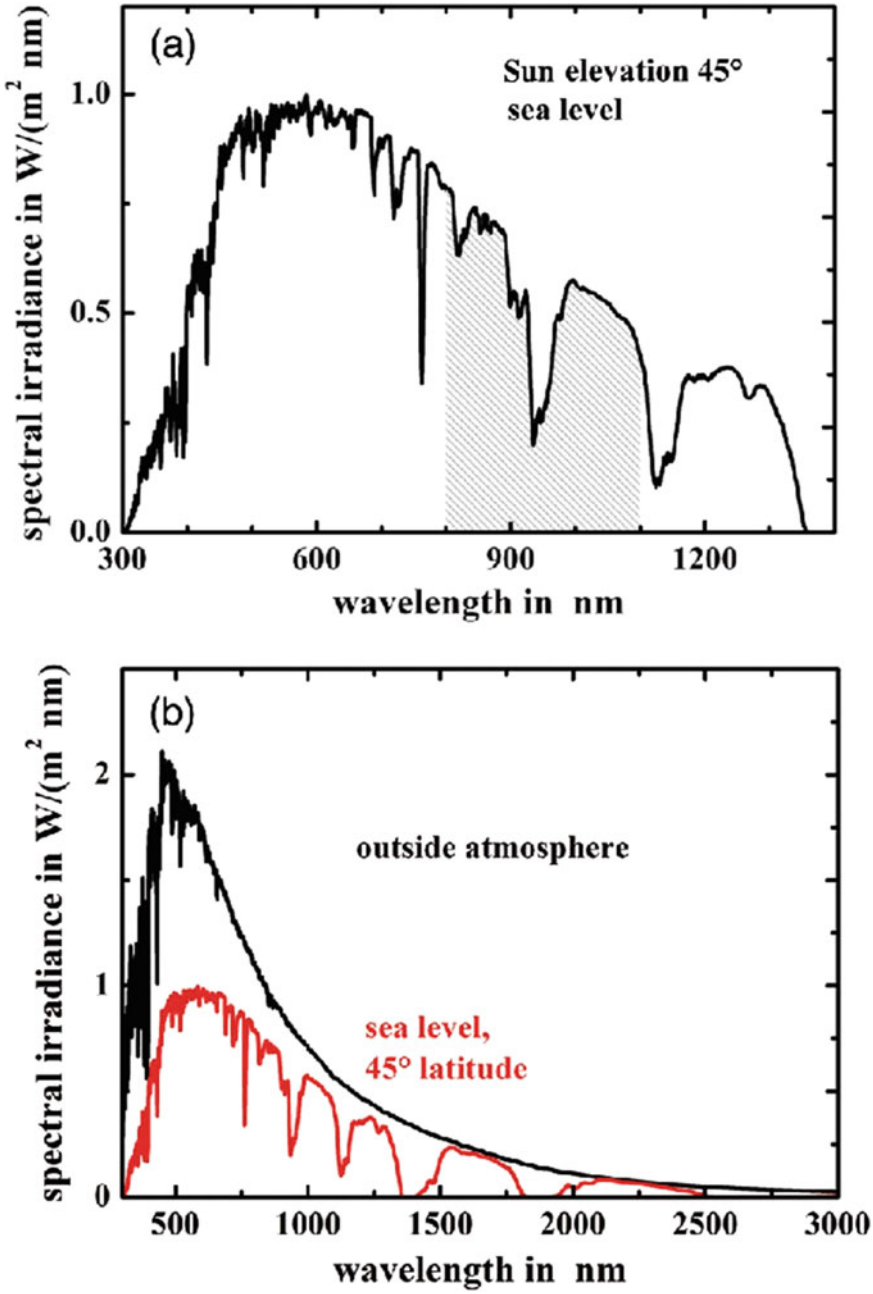

Fig. 1 Theoretical MODTRAN (MODTRAN.spectral.com) downwelling spectral irradiance (Vollmer and Shaw 2017) at sea (**a**) and top-of-atmosphere (**b**) levels for 45 degrees solar zenith angle and the 1976 U.S. Standard Atmosphere (no aerosols). The integral of the entire curve of solar irradiance at the mean Earth—Sun distance (outside the Earth's atmosphere) yields approximately 1370 W/m^2

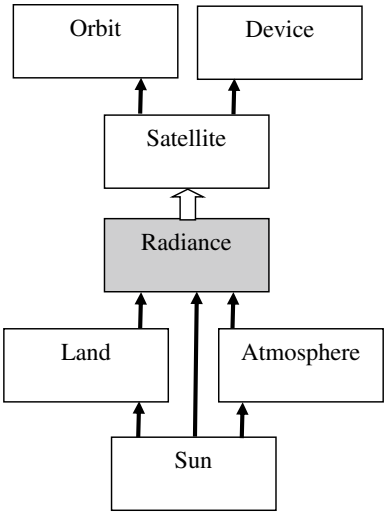

Fig. 2 Main elements of satellite measurement

Table 1 Parameters of space borne hyperspectral devices (https://oco.jpl.nasa.gov, https://iasi.cnes.fr/, https://airs.jpl.nasa.gov/, https://www.iup.uni-bremen.de/sciamachy/, https://www.gosat.nies.go.jp/en/)

Parameter	GOSAT	OCO	SCIAMACHY	IASI	AIRS
Launch date	2009	2014	2002	2006	2002
Altitude, km	666	705	790	820	705
Viewing modes	Nadir, glint, target	Nadir, glint, target	Nadir, limb	Nadir	Nadir
Type of instrument	Fourier transform spectrometer	Grating spectrometer	Grating spectrometer	Fourier transform spectrometer	Grating spectrometer
Spatial resolution, km	10	1.3 × 2.3	30 × 60	15	12
Temporal revisit, days	3	16	35	16	72
Spectral bandpass, microns	0.758–0.775 1.56–1.72 1.92–2.08	0.757–0.772 1.59–1.62 2.04–2.08	0.24–0.44 0.4–1.0 1.0–1.70 1.94–2.04 2.265–2.380	3.740–4.610 6.20–8.220 8.80–15.40	3.620–5.0 5.0–8.260 8.260–15.50
Gases	CO_2, CH_4, O_2, O_3, H_2O	CO_2, O_2	CO_2, CH_4, O_4, O_3, H_2O, CO, NO_2, N_2O, SO_2	CO_2, CH_4, O3, H_2O, CO, SO_2, N_2O	CO_2, CH_4, O_3, CO, H_2O, SO_2
aerosol	Yes	Yes	Yes	Yes	Yes

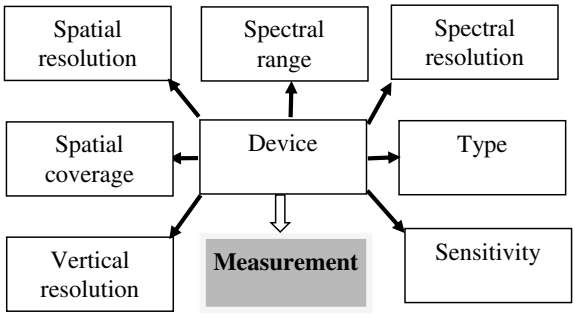

Fig. 3 Basic parameters of satellite instruments and measurement modes

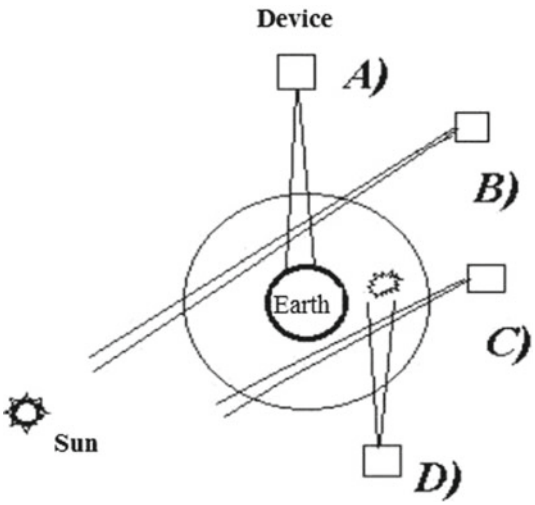

Fig. 4 Various schemes for remote sensing of the atmosphere: **a** nadir; **b** occultation; **c** limb and **d** emission

3 The Coupled Atmosphere—Surface Properties and Satellite Processing Chains

When studying the processes taking place in the atmosphere, it is necessary to know what constituents are present in it and how they interact with each other under various spatial—temporal scales. Figure 5 shows the main components of the atmosphere, which determine the state of the atmosphere. The state of the atmosphere is determined by many parameters, such as: pressure and temperature; field of the wind velocity; concentration of gases; water phase; size distribution and optical parameters of aerosol and cloud particles; reflection and emission surface properties; temperature; geometric structure of clouds; etc.

An important characteristic of the atmosphere is its structure (troposphere, stratosphere, etc.). Therefore, one needs to retrieve vertical profiles of various atmospheric constitutes. For example, the main bulk of the atmospheric gases and atmospheric

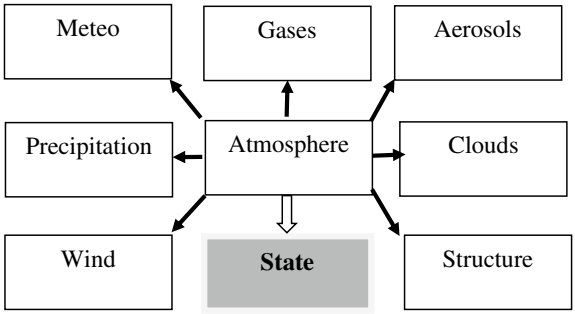

Fig. 5 Main components of the Earth's atmosphere

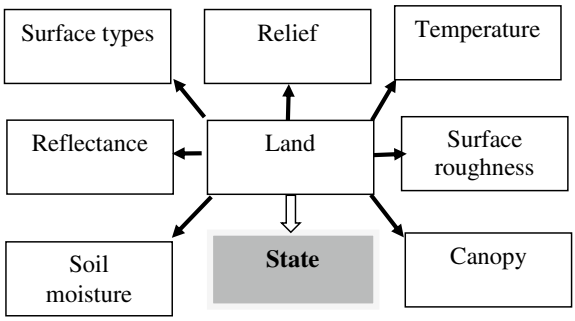

Fig. 6 Main elements of the Earth's surface that define its state

aerosol is located in the troposphere, which makes it necessary to develop not only the appropriate instruments, but processing techniques as well.

In order to use satellite data to determine one of the parameters of the state of the atmosphere, many other parameters need to be known. For individual measurement schemes, it is necessary to take into account the effects (reflection and relief) characteristic for the surface of the Earth. All effects, depending on the season (snow, soil moisture, temperature, etc.) determine the state of the Earth's surface. Figure 6 shows the main elements of the Earth's surface that define its state.

Processing of the remote sensing measurements is a complicated process, as it requires numerous manipulations to be performed with data in order to obtain a result of a desired quality. The accuracy of the result with respect to the object of the study, its reproducibility, and its comparability with other results depends on the sequence of these manipulations with the measurement data. Figure 7 shows the main elements of the sequence of manipulations over the measurement data. The first block is the preprocessing block where the data is converted from the internal recording format onboard the satellite to the physical radiation values. The second block of transformations is associated with the selection of the accounting sun-satellite geometry, selection of the spatial region, selection of the wavelengths range associated with the object of study, search for the optimal wavelengths, etc.

The processing block is important as it relies on a priori information and a numerical model of inversion to obtain the result or information associated with the object

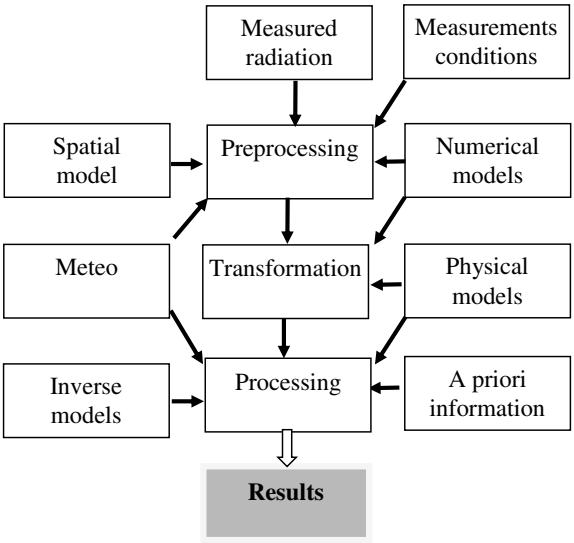

Fig. 7 Main elements of the sequence of manipulations over remote sensing measurement data

of study. For example, if the object to study is the atmospheric gaseous composition, this may be the gas total column (content), extinction profile, mixing ratios profile. For aerosol, the parameters of interest are the aerosol optical thickness, single scattering albedo, aerosol layer height and position in atmosphere, chemical composition of aerosol, aerosol load, and particle size distribution.

4 Inverse Problems

4.1 Classification of Inverse Problems

Radiation entering the satellite device at a set of wavelengths goes through stages of preprocessing, after which it must be processed using various methods for the solution of the inverse problem of atmospheric optics. The goal of solving the inverse problem is to search for parameters in such a way that would reduce differences between measurements and modelled radiance or Stokes vector of reflected light observed at a number of spectral channels, observation directions (viewing zenith angle and azimuth), and polarization state.

This is a challenging problem, which requires understanding how radiation propagates from the Sun through the atmosphere—underlying surface system to the downward looking optical instrument orbiting the planet. The theory of radiative transfer offers robust approaches to simulate the radiance or Stokes vector of radiation passing

through the atmosphere to the surface of the planet and back to the spaceborne optical instrument.

Taking into account a priori knowledge with respect to the optical instrument characteristics, atmosphere and land states, it is possible to obtain accurate information about the parameters of the atmosphere and the Earth's surface. It is of importance to develop instrumentation, which is capable to provide information on all main characteristics of atmosphere-underlying surface system as a result of the inverse radiative transfer problem solution. Therefore, the number of a priori assumptions is reduced.

The inverse problem associated with satellite observations of the radiance/Stokes vector (for various schemes of measurements: spectral, angular, polarimetric or combined) is to obtain the parameters of the atmosphere. The set of measurement schemes, instrument types, measurement conditions and information that is taken into account during processing determines a sufficiently wide range of options for the solution of the inverse problem.

Methods for the solution of the inverse problem can be grouped into two types: parametric and nonparametric. In parametric methods, solution of the inverse problem is based on the equation for the calculation of radiation transfer in the atmosphere, the parameters of which are related to characteristics of the object of study. The nonparametric methods rely on the statistical interrelation of measurements and the desired characteristics of the object of study. Figure 8 shows the generalized parametric and nonparametric variants of the inverse problem.

In the case of parametric techniques, the inversion of physically based models (radiative transfer) is a complicated task (associated with sensitivity to measurement errors, a large number of search parameters, complex mathematical formulations, etc.) that demands specific computer resources necessary to solve many problems that are ill-posed. Parametric methods for solution of the inverse problem rely on the radiation transfer equation, which is solved in an explicit or a transformed form, which makes it possible to find a linear or nonlinear dependence of the measurement signal on the parameters that characterize the object of study (in our case, properties of trace gases or atmospheric aerosol).

In this paper, we will focus on the solution of the inverse problem for the case, when the results of the measurements and parameters to be retrieved are connected by statistical dependences.

We must note that the determination of atmospheric and surface parameters from the measured radiation can be written in the language of integral equations or continuous functions (taking into account the continuous altitude dependences of atmospheric parameters and spectral dependences of atmospheric transmittance) and in the language of discrete finite-dimensional functions in Euclidean space (taking into account the tabular representation of atmospheric parameters on a given grid of heights (pressures) and a set of spectral channels). Since the goal of the paper is not to provide a strict sequential presentation of the mathematical theory for the solution of inverse problems, but to offer a brief review of the currently known techniques (methods) for solution of inverse problems in the context of remote sensing of the atmosphere, we will focus on the discrete point of view as the most convenient approach to the numerical implementation of any inverse problem method.

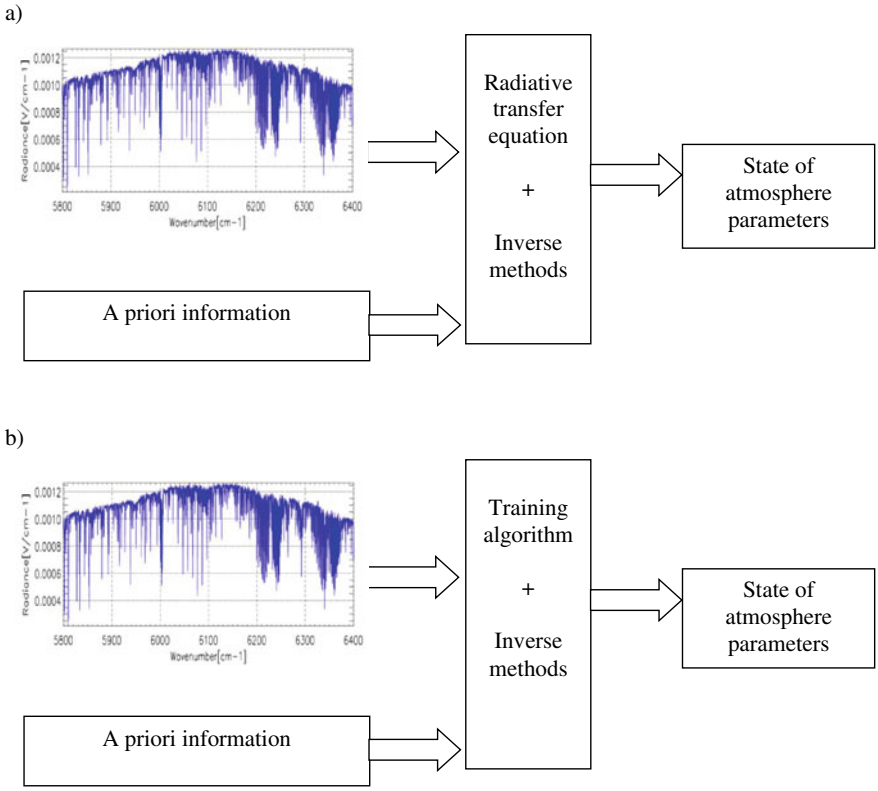

Fig. 8 Differences of the inverse problem approaches: **a** Parametric, **b** Nonparametric

4.2 The Inversion Theory

The inverse problem can be formulated mathematically as a transformation of an observation vector (say, spectral and angular variation of the Stokes vector of reflected solar light) into a vector, which represents the unknown atmospheric state (e.g., concentrations of atmospheric trace gases and aerosol particles, their vertical distributions, etc.).

The spaces of solutions and measurements are interrelated. For each solution, it is possible to construct a model measurement that will be the basis for the solution of the inverse problem. However, in reality, each measurement has errors that make the interrelation of these two spaces ambiguous. In this case, parametric approaches to solve an inverse problem are based on various advanced mathematical techniques (e.g., regularization, optimal estimation).

Radiative transfer is associated with the process of radiative exchange between the atmosphere and the surface accounting for the structure of the atmosphere and the

Earth's surface. These processes essentially depend on the spectral range. The interaction of solar radiation with the cloudless atmosphere—underlying surface system results in scattering and absorption processes that are quantitatively determined by the underlying surface properties (vegetation, bare snow, ice, snow, etc.) and also by load and vertical distribution of atmospheric gases and aerosol particles(dust, soot, water soluble aerosols).

Remote sensing devices measure the radiance or the Stokes vector of the reflected light that is a function of wavelength and spectral resolution, time of exposure, device optics field-of-view, angles of observation and illumination by the Sun, and sensitivity of the detector.

The solution of the inverse problem by means of the parametric method has been discussed many times (Tikhonov and Arsenin 1986; Engl et al. 1996; Chevallier and Mahfouf 2001; Spurr 2002; Eyre 2002; Doicu et al. 2010; Twomey 1977; Rodgers 1976, 2000; Gabriel et al. 2006; Spurr et al. 2001; Bates and Watts 1988; Kataev et al. 1996; Katae and Mitsel 1998; Bösch et al. 2006; Christi and Stephens 2004; Engelbrecht 2007). The measurement vector Y is connected to the unknown vector of atmospheric state P by the forward model F:

$$Y = F(P, B) + E \tag{1}$$

where the vector E represents the noise of measurements and the error of the forward model and the vector B is the vector of a priori parameters. It is natural to expect that the initial state of the atmosphere, at the time of measurement, will to some extent differ from the state that can be obtained from the previously accumulated data represented by the vector B. This leads to a systematic error in the solution of the inverse problem.

In general, the forward model F (based on the radiative transfer equation with respective boundary conditions) is a nonlinear function of P. Linearized Eq. (1) with respect to the assumed state P_0 can be represented in the following form:

$$Y = Yo + K \cdot (P - Po) + E, \tag{2}$$

where Yo = F(Po) is the vector computed using the forward model F with the assumed state vector Po (a priori knowledge of P), P is the vector of true state (unknown), E is the vector containing the errors, and K is the Jacobian (K = dF(P)/dP) or weighting function that has peaks distributed in height, which allows one to obtain information on the height distribution of the desired component.

Let us assume at first that the errors E can be neglected. Than in case of the quadratic matrix K, one derives:

$$P = Po + K^{-1}Y - Yo \tag{3}$$

Usually the matrix K is not quadratic. However, the matrix K^TK is always quadratic. Therefore, we can derive from Eq. (2) at E = 0:

$$K^T(Y - Yo) = K^TK(P - Po) \tag{4}$$

and

$$P = Po + (K^TK)^{-1}K^T(Y - Yo) \tag{5}$$

Equation (5) can be presented in another, iteration form:

$$P_n = P_{n-1} + (K_{n-1}^T K_{n-1})^{-1}(Y - F(P_{n-1})), \tag{6}$$

where P_n is the solution after the n-th iteration and $[K^T{}_{n\text{-}1}K_{n\text{-}1}]^{-1}$ is the inverse matrix with weighting functions $K_n = dF(P_n)/dP_n$. The kernel calculation for the first iteration step begins with a known a priori value of Po, the kernel K is recalculated at each iteration stage.

Let us account for the vector of errors E. Then it follows instead of Eq. (5) (Kostsov 2015):

$$P = Po + (K^TS^{-1}K + G)^{-1}K^TS^{-1}(Y - Yo \tag{7}$$

Here S is the covariance matrix of measurement errors. We also have introduced the regularization matrix G. Eq. (7) transforms to Eq. (5) at S = I (no errors of measurements) and G = 0 (no regularization procedure). Here I is the identity matrix.

A constrained matrix retrieval (Twomey) can be implemented to increase the kernel matrix stability (and thus decrease error amplification) under inversion. The solution can be written as:

$$P_n = (K_{n-1}^T K_{n-1} + G)^{-1}K_{n-1}(Y - F(P_{n-1}) + K_{n-1}^T P_{n-1}),\ G = \gamma I, \tag{8}$$

where I is the identity matrix and γ is a vector of Lagrangian multipliers. This equation can also written to make use of a priori state P_o, as an additional constraint:

$$P_n = Po + (K_{n-1}^T K_{n-1} + G)^{-1}K_{n-1}^T(Y - F(P_{n-1}) + K_{n-1}^T(Po - P_{n-1})) \tag{9}$$

The optimal estimation solution of the inverse problem (known as a Rodgers technique) can be presented in the following form:

$$P_n = P_{n-1} + S_x K_{n-1}^T (K_{n-1} S_x K_{n-1}^T + S_y)^{-1} (Y - K_{n-1} P_{n-1}), \quad (10)$$

where S_x is the covariance matrix of a priori data and S_y is the covariance matrix of the measurement errors. In case when $S_y = \varepsilon^2 I$ (diagonal matrix), and $S_x = \mu^2 I$, Eq. (10) can be rewritten in a form:

$$P_n = P_{n-1} + K_{n-1}^T (K_{n-1} S_x K_{n-1}^T + c)^{-1} (Y - K_{n-1} P_{n-1}), \quad (11)$$

where $c = (\mu/\varepsilon)^2$ is the adjustable parameter.

4.3 Machine Learning Methodologies

Modern development of technology makes it possible to develop spectral devices with wide possibilities for implementation of complex scientific experiments. Such devices have a variety of spectral channels with high spectral and spatial resolution and a high signal-to-noise ratio. The developed technologies for processing and accumulating measurement data make it possible to carry out experiments with a group of satellites, with many viewing angles. This is the case for the optical instruments on geostationary satellites as well. As a result, satellite observations produce a large number of remote sensing data.

For conventional, parametric approaches, the numerical implementation of approaches for modern hyperspectral devices becomes challenging when the number of wavelengths exceeding 10^3. In this case, the matrix to be inverted becomes large and it is necessary to apply advanced approaches to the solution of a system of linear algebraic equations. As a rule, the choice of the regularization parameter leads to the use of iteration techniques, which also requires additional time and effort in order to obtain a stable solution. Despite these and other features, the methods considered are effective in solving inverse problems of atmospheric optics when restoring atmospheric parameters.

One aspect of conventional methods is the need to make use of a large volume of a priori information to obtain effective and accurate solutions. Therefore, such techniques are difficult to adapt to new conditions, new devices, and other changes. With the use of a priori information, it is necessary to introduce some assumptions about the desired parameters, which, on the one hand, simplify the solution, and on the other hand, restrict it. In parallel with the conventional approaches to solving the inverse problem, for quite a long time, advanced inversion methods gradually developed based on the use of statistical information. These approaches have their own peculiarities of development, practical application and accuracy, and they are not inferior to the conventional ones and actually surpass them in terms of stability of solutions and the speed of the process.

Conventional approaches (more based on regression methods) rely on physical models of radiative transfer with the high complexity and non-linearity. This significantly complicates the solution of inverse problems and the practical application of these approaches.

A new class of non-parametric approaches to the solution of the inverse problem is based on statistical methods and consists of two stages: training and processing. In addition, due to advanced approaches to learning, nonparametric methods can assimilate a variety of a priori data more easily than is possible in traditional approaches. Among all methods of solving the inverse problem of atmospheric optics, several are the most popular, one of them being the method of artificial neural networks (ANN). Support vector regression (SVR) has also become quite popular in the last few years.

The block diagram of training (stage 1) and processing (stage 2) using nonparametric approaches is shown in Fig. 9. At the first stage, all information about the spatiotemporal behavior of the target parameter of the atmosphere and all the a priori data accompanying these changes are collected. The sample is divided into the following parts: training, testing, and validation sampling. Each change in parameters (state of the atmosphere) is compared to a measurement in some learning algorithm. The learning process is used to determine the coefficients that are the basis of the processing algorithm. After training, the second stage is to determine the accuracy characteristics of the coefficients found on the test sample of the data. If the learning and testing process was successful, the coefficients found can be used in practice, otherwise the learning process is repeated with various other combinations of the pair (measurement-data).

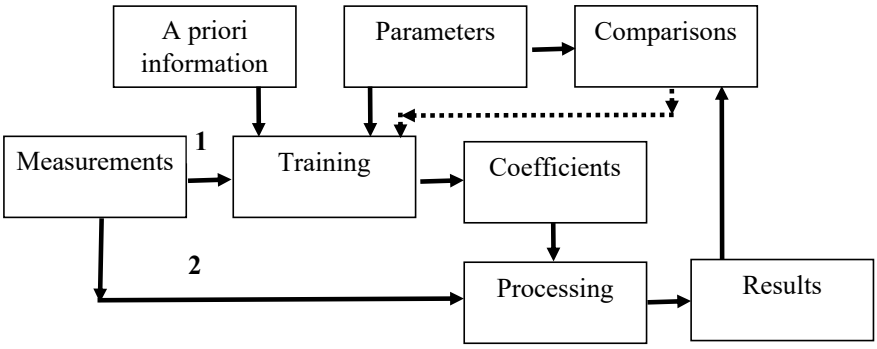

Fig. 9 Block diagram of the main elements for remote sensing data processing with the help of nonparametric methods

4.4 Artificial Neural Networks (ANN)

The technology of neural network structures is one of the fastest developing technologies that offers a number of important advantages, such as speed, learning ability, good approximation properties, etc. The potential ability of artificial neural networks (ANN) (McCulloch and Pitts 1943; Hebb 1949; Rosenblatt 1958; Minsky and Papert 1969; Rumelhart et al. 1986a,1986b; Haykin 1994; Hornik et al. 1989; Park and Sandberg 1991; Sellitto et al. 2011; Butler et al. 1996; Frate et al. 2001; Escobar-Munoz et al. 1993; Hadji-Lazaro and C., and Thiria S, 1999; Jimenez and Eriksson 2001; Motteler et al. 1995; Kataev and Sukhanov 2004; Kataev and Sykhanov 2006; Kamgar- and Gualteri 1990) to generalize the representation of any class of functions, as well as a number of properties mentioned above, leads to the fact that they find a number of applications in the field of atmospheric remote sensing. Integrated with all levels of intelligent control, this approach makes it possible to construct various research models and algorithms with a high degree of reliability. The high speed of ANN functioning makes it possible to use them as an independent link, occupying both an independent position, integrated into the general cycle of calculations, and implementing specific control laws. An important advantage of the ANN is the possibility of self-learning, which eliminates the need for a sophisticated mathematical device that would be conventionally used in to solve inverse problems. Advantages of the ANN include:

- An ability to learn how to perform tasks based on the data given for training or initial experience.
- An ANN can create its own organization or representation of the information it receives during learning.
- ANN computations can be performed simultaneously, and special hardware devices are being designed and manufactured that take advantage of this capability.
- Partial destruction of a network leads to the corresponding degradation of performance. However, some network capabilities may be retained even with major network damage.
- A neural network can perform tasks that a linear program cannot.
- When an element of the neural network fails, it can continue without any problem due to their parallel nature.
- A neural network learns and does not need to be reprogrammed.
- It can be implemented in any application.
- It can be implemented without any problem.

The disadvantages are:

- The neural network needs training to operate.
- The architecture of a neural network is different from the architecture of microprocessors, therefore, needs to be emulated.
- Large neural networks require high processing time.

4.5 Random Forests

The concept of a random forest (RF) was introduced into scientific practice by the works of L. Breiman. The method is based on constructing a large number (ensembles) of decision trees (this number is a parameter of the method), each constructed from a sample obtained from the specially prepared a priori training sample using a bootstrap algorithm (that is, a training sample with a return) (Brence and Brown 2004; Friedman et al. 2001; Smola and Scholkopf 2004; Pal 2005; Breiman 2001). In order to construct decision trees in the random forest method, only a fixed number of randomly selected traits of the training sample (the second parameter of the method) is used in constructing each tree at the stages of vertex splitting, and a complete tree is constructed (without truncation). Each tree sheet contains observations of only one class. The random forest method quickly finds popularity among various fields of remote sensing. The accuracy (the probability of correct classification of all samples on individual parts) depends on the set of classifiers that make up the ensemble.

Random forest regression is a non-parametric regression technique. For a training data set $T = \{(Y_i,P_i), i = 1,2,\ldots,M\}$, the algorithm generates a forest of L trees, $T = \{T_1, T_2,\ldots, T_L\}$ using M dimension vectors $P = \{P1,P2,\ldots,PM\}$ and $Y = \{Y1,Y2,\ldots,YM\}$. For each tree $T_i(P)$, the formed N outputs are represented as: $S = \{S1 = T_1(Y,P), S2 = T_2(Y,P),\ldots, SL = T_L(Y,P)\}$,where S_l, $l = 1,L$ is the output of L-th tree. The average of all individual regression tree outputs as the response from the random forest is considered. The random forest algorithm can be explained as the following procedure:

- Select random samples from a given training dataset.
- For a given training data select random samples of the L trees with replacement.
- Construct a decision tree for each sample and get a prediction result from each decision tree.
- Perform a vote for each predicted result.
- Repeat the second step until a satisfied number of trees generated.
- Select the prediction result with the most votes as the final prediction.

Each tree is constructed using the following algorithms:

- Let the number of training cases be N, and the number of variables in the classifier be M.
- We are given the number m of input variables to be used to determine the decision at a node of the tree; m should be much less than M.
- Choose a training set for this tree by choosing n times with replacement from all N available training cases (i.e. take a bootstrap sample). Use the rest of the cases to estimate the error of the tree by predicting their classes.
- For each node of the tree, randomly choose m variables on which to base the decision at that node. Calculate the best split based on these m variables in the training set.
- Each tree is fully grown and not pruned (as may be done in constructing a normal tree classifier).

For prediction, a new sample is pushed down from the tree. It is assigned the label of the training sample in the terminal node it ends up in. This procedure is iterated over all trees in the ensemble, and the average vote of all trees is reported as random forest prediction.

5 Conclusions

The inverse problem solution algorithms can be conditionally divided into two groups: parametric and nonparametric. The parametric approach is based on the inverse radiative transfer theory. The nonparametric approach is understood as a situation, where the desired parameter is not directly related to the measurements but is determined from learning based on a set of known pairs of situations (*measurement, required parameter*). In this paper we have made a survey of both parametric and nonparamertric inverse problem solution algorithms. An information on additional algorithms such as support vector mashines, orthogonal functions, etc. can be found in (Brence and Brown 2004, 2002; Friedman et al. 2001; Smola and Scholkopf 2004; Pal 2005; Breiman 2001; Vapnik 1998; Chang and Lin 2011; Burges 1998; Kataev et al. 2011a, 2011b,2018; Frate and Schiavon 1998, 1999; Bril et al. 2017; Smith et al. 2012).

References

Bates DM, Watts DG (1988) Nonlinear regression analysis and its applications. Wiley, New York

Bösch H, Toon GC, Sen B, Washenfelder RA, Wennberg PO, de Beek R et al (2006) Space-based near-infrared CO2 measurements: testing the orbiting carbon observatory retrieval algorithm and validation concept using SCIAMACHY observations over Park Falls, Wisconsin. J Geophys Res 111:D23302. https://doi.org/10.1029/2006JD007080

Breiman L (2001) Random forests. Mach Learn 45:5–32

Brence JR, Brown DE (2002) Data mining corrosion from Eddy current non-destructive tests, computers and industrial engineering: data mining and knowledge discovery in industrial. Engineering 43:821–840

Brence JR, Brown DE (2004) Analysis of robust measures in random forest regression, submitted to data mining and knowledge discovery, Kluwer Academic Publishers

Bril A, Maksyutov S, Belikov D, Oshchepkov S, Yoshida Y, Deutscher NM, Griffith D, Hase F, Kivi R, Morino I, Velazco V et al (2017) EOF-based regression algorithm for the fast retrieval of atmospheric CO2 total column amount from the GOSAT observations. J Quant Spectrosc Radiat Transfer 189:258–266

Burges CJC (1998) A tutorial on support vector machines for pattern recognition, Data Min Knowl Disc 2:121–167

Butler CT, Meredith RZ, Stogryn AP (1996) Retrieving atmospheric temperature parameters from DMSP SSM/T-1 data with a neural network. J Geophys Res 101:7075–7083

Chang C-C, Lin C-J (2011) LIBSVM: a library for support vector machines. ACM Trans Intell Syst Technol 27(2):1–27

Chevallier F, Mahfouf JF (2001) Evaluation of Jacobians of infrared models for variational assimilation applications. J Appl Meteor 40:1445

Christi MJ, Stephens GL (2004) Retrieving profiles of atmospheric CO2 in clear sky and in the presence of thin cloud using spectroscopy from the near and thermal infrared: a preliminary case study. J Geophys Res 109:D04316. https://doi.org/10.1029/2003JD004058

Del Frate F, Ortenzi A, Casadio S, Zehner C (2001) Application of neural algorithms for a real time estimation of ozone profiles from GOME measurements. IEEE Trans Geosci Remote Sens 40:2263–2270

Doicu A, Trautmann T, Schreier F (2010) Numerical regularization for atmospheric inverse problems Springer–praxis books in environmental sciences

Engelbrecht AP (2007) Computational intelligence: an introduction. John Wiley & Sons Ltd

Engl HW, Hanke M, Neubauer A (1996) Regularization of inverse problems. Kluwer Academic Publisher, Dordrecht, NL

Escobar-Munoz J, Chedin A, Cheury F, Scott N (1993) Multi-layer neural networks for the retrieval of atmospheric variables from satellite-borne vertical sounding. Atmos Phys Numer Anal 317:911–918

Eyre JR (2002) Inversion methods for satellite sounding data Meteorological Training Course Lecture Series ECMWF

Frate FD, Schiavon G (1998) A combined natural orthogonal functions/neural network technique for radiometric estimations of atmospheric profiles. Radio Science 33:405–410

Frate FD, Schiavon G (1999) Nonlinear principal component analysis for the radiometric inversion of atmospheric profiles by using neural networks. IEEE Trans Geosci Remote Sensing 37:2335–2342

Friedman J, Hastie T, Tibshirani R (2001) The elements of statistical learning. Springer Science & Business Media, Berlin, Germany

Gabriel P, Christi M, Stephens GL (2006) Calculation of Jacobians for inverse radiative transfer: an efficient hybrid method. J Quant Spectrosc Radiat Transfer 97(2):209–227

Hadji-Lazaro CJ, Thiria S (1999) An inversion algorithm using neural networks to retrieve atmospheric CO total columns from highresolution nadir radiances. J Geophys Res 104:23841–23854

Hansen JE (1971) Multiple scattering of polarized light in planetary atmospheres. Part II. Sunlight reflected by terrestrial water clouds, J Atm Sci 28(8):1400–1426

Hansen JE, Travis LD (1974) Light scattering in planetary atmospheres. Space Sci Rev 16(4):527–610

Haykin S (1994) Neural network. New York, Macmillan College Publishing Company, A Comprehensive Foundation

Hebb DO (1949) The organization of behavior: a neuropsychological theory. NewYork: Wiley

Hornik K, Stinchcomb M, White H (1989) Multilayer feedforward networks are universal approximators. Neural Netw 2:359–366

Jimenez C, Eriksson P (2001) A neural network technique for inversion of atmospheric observations from microwave limb sounders. Radio Sci 36:941–953

Kamgar-Parsi B, Gualteri J (1990) Solving inversion problems with neural networks. In: Proceedings of International Joint Conference on neural networks, 955–960

Kataev MY, Mitsel AA (1998) New approach to solution of the inverse problem of thermal sounding of the atmosphere from satellites Atmospheric and oceanic optics, (in Russian) 11(12):1123–1128

Kataev MYu, Sukhanov AY (2004) Application of neural networks for retrieving atmospheric gases concentration profile for lidar sounding data. Proc SPIE 397:161–168

Kataev MYu, Sykhanov AY (2006) Application of the neural network approach for retrieving of gas concentration from CO2 laser data. Proc SPIE 6160:75–79

Kataev MY, Mitsel AA, Ptashnik IV, Firsov KM (1996) Software package for modeling and processing of the data on remote sensing of the atmospheric gas composition by spectrophotometric methods Atmospheric and oceanic optics, (in Russian) 9(10):898–901

Kataev MY, Kataev SG, Andreev AG, Bazelyuk SA (2011) Comparison of the nonparametric approaches to retrieving of CO2 total content from satellites measurements. In: International

Conference computational information technologies for environmental sciences (CITES-2011), Tomsk, Russia

Kataev MYu, Kataev SG, Andreev AG, Bazeluyuk SV, Lukyanov AK (2011) Nonparametric approaches retrieving of the CO2 total content from data of satellite monitoring. TUSUR Reports (in Russian) 2(24):181–186

Kataev MY, Lukyanov AK, Bekerov AA (2018) Modification of the empirical orthogonal functions method for solving the inverse task of retrieving of the CO2 total content from satellite data. J Sib Fed Univ Eng Technol 11(1):77–85

Klaus M, Shaw AM, Vollmer V (2013) The physics of near-infrared photography. Eur J Phys 34(6):S51–S71

Kostsov VS (2015) General approach to the formulation and solution of the multi-parameter inverse problems of atmospheric remote sensing with measurements and constraints of different types. Int J Remote Sen 36:2973–3004

Lenoble J (1985) Radiative Transfer in Scattering and Absorbing Atmospheres. Deepak Publishing, Hampton, VA, USA, Standard Computational Procedures. A

McCulloch WS, Pitts W (1943) A logical calculus of ideas imminent in nervous activity. Bulletin Mathematical Biophysics 5(4):115–133

Minsky ML, Papert SA (1969) Perceptrons. MIT Press, Cambridge, MA

Mitsel AA, Ponomarev YN, Firsov KM, Ptashnic IV, Kataev MYu (1995) The computer codes LARA and AIRA for simulating the atmospheric transmittance and radiance: current status. J Quant Spectrosc Radiat Transfer 54(3):559–572

Motteler HE, Strow LL, McMillin L, Gualtery JA (1995) Comparison of neural network and regression-based method for temperature retrievals. Appl Opt 34:5390–5397

Pal M (2005) Random forest classifier for remote sensing classification. Int J Remote Sens 26:217–222

Park J, Sandberg IW (1991) Universal approximation using radial basis function networks. Neural Comput 3(246):257

Rodgers CD (1976) Retrieval of atmospheric temperature and composition from remote measurements of thermal radiation. Rev Geophys 14:609–624

Rodgers CD (2000) Inverse methods for atmospheric sounding: theory and practice. Series on atmospheric, oceanic and planetary physics, vol 2, World Scientific

Rosenblatt F (1958) The perceptron: a probabilistic model for information storage and organization in the brain. Psychol Rev 65:386–407

Rozanov A, Rozanov V, Burrows JP (2001) A numerical radiative transfer model for a spherical planetary atmosphere: combined differential-integral approach involving the Picard iterative approximation. J Quant Spectr Rad Transfer 69:491–512

Rozanov A, Rozanov V, Buchwitz M, Kokhanovsky A, Burrows JP (2005) SCIATRAN 2.0—A new radiative transfer model for geophysical applications in the 175–2400 nm spectral region. Adv Space Res 36:1015–1019

Rumelhart DE, Hinton GE, Williams RJ (1986) Learning internal representation by error propagation. Parallel distributed processing, I Foundations. Cambridge, MA: MIT Press, 318–362

Rumelhart DE, Hinton GE, Williams RJ (1986) Learning representation by back—propagating errors. Nature 323:533–536

Schott JR (1999) Fundamentals of Polarimetric Remote Sensing. SPIE Tutorial Text TT81, SPIE Press, Bellingham

Sellitto P, Bojkov BR, Liu X, Chance K, Del Frate F (2011) Tropospheric ozone column retrieval at northern mid-latitudes from the Ozone Monitoring Instrument by means of a neural network algorithm. Atmos Meas Tech 4:2375–2388

Smith Sr WL, Weisz E, Kireev SV, Zhou DK, Li Z, Borbas EE (2012) Dual-regression retrieval algorithm for real-time processing of satellite ultraspectral radiances. J Appl Meteorol Climatol 51(8):1455–1476

Smola AJ, Scholkopf B (2004) A tutorial on support vector regression. Stat Comput 14:199–222

Sobolev VV (1956) The transmission of radiation through an inhomogeneous medium. Dokl Akad Nauk SSSR (in Russian) 111:1000–1003

Spurr RJD (2002) Simultaneous derivation of intensities and weighting functions in a general pseudo-spherical discrete ordinate radiative transfer treatment. JQSRT 75(2):129–175

Spurr RJD, Kurosu TP, Chance KV (2001) A linearized discrete ordinate radiative transfer model for atmospheric remote-sensing retrieval. J Quant Spectrosc Radiat Transfer 68(6):689–735

Thomas GE, Stamnes K (1999) Radiative transfer in the atmosphere and ocean. Cambridge University Press, Cambridge

Tikhonov AN, Arsenin VY (1986) Methods for solution of incorrect problems. Nauka, Moscow

Timofeev YuM, Vasilyev AV (2003) Theoretical principles of the atmospheric optics. Nauka, St Petersburg

Twomey S (1977) Introduction to the Mathematics of Inversion in Remote Sensing and Indirect Measurements. Dover Publications Inc

Vapnik V (1998) Statistical Learning Theory. Wiley, New York

Vollmer V, Shaw JA (2017) Atmospheric optics in the near infrared. Applied Optics 56(19):G145–G155

Index

A
Absorption, 55, 65, 68–71, 79–86, 88–96, 98, 99, 137–142, 144, 145, 150, 154–157, 160, 161, 164, 177, 185
Albedo, 53, 60, 69–71, 79, 80, 89, 92, 96
Analysis, 54, 59, 77, 83, 84, 90–95, 97, 99
Analytical, 54, 61, 63, 65, 70, 72, 74, 79, 83, 86, 87, 90, 93, 99
Anomalous diffraction, 115, 135, 136, 138, 139
Approximate, 53, 65, 93, 95, 99
Atmosphere state, 180, 181, 183, 185, 188

B
Biberman–Holstein equation, 12, 13
Big-data, 177
Boundary layer, 1, 3, 18, 19, 26–28, 32, 33, 37
Bubbles, 53, 54, 89–94, 96–99

C
Calculation, 57, 66, 68, 70, 71, 73, 74, 77, 78, 81–84, 86, 88, 90–95, 97, 99
Chord length distribution, 111–114, 119–121, 127, 128, 132–134, 138–141, 145, 150, 154–157, 166
Conduction, 66, 68, 76, 77, 97, 99
Continuum absorption, 3, 24–26
Convection, 65, 74, 77, 85, 86, 90, 97
Cooling, 53, 66, 74, 76–78, 83, 85, 86, 88, 97–99

E
Emergent radiation, 21, 31
Extinction, 137–142, 154

F
Forward, 185
Fraunhofer diffraction, 115, 116, 119, 120, 129, 135, 137, 166

G
Geometrical optics, 115, 141, 142, 144, 153–155, 157, 159, 166
Grains, 69–74, 78–85, 89, 99

H
Hanle effect, 39, 40, 45, 48
Heating, 53, 54, 65, 68–73, 76–79, 83, 85, 86, 88–91, 97–99
H–function, 8, 9, 12, 21, 24, 34, 46
Hopf–Bronstein relation, 11, 12, 18, 37, 39
Hyperspectral, 177, 179, 187

I
Ice, 53–55, 59, 62, 65, 66, 68–74, 78–86, 88–99
Ill-posed, 183
Infrared, 53, 55, 66, 68, 69, 72, 73, 77, 79, 84, 86, 90, 95, 97–99
Interior solution, 31

© The Editor(s) (if applicable) and The Author(s), under exclusive license to Springer Nature Switzerland AG 2021

A. Kokhanovsky (ed.), *Springer Series in Light Scattering*, Springer Series in Light Scattering, https://doi.org/10.1007/978-3-030-71254-9

L
Lévy flights, 1, 4, 12, 15–18, 20, 21, 24, 29, 30, 33, 39, 41–44, 46
Linear equation, 185, 187

M
Melting, 66, 68, 76–78, 85, 86, 88, 90, 97, 99
Milne–Eddington model, 9, 10, 26
Milne equation, 10–12
Modeling, 53, 55, 69, 79, 93, 99
Multiple scattering, 3, 12, 24, 25, 30, 37

N
Neural network, 176, 188, 189
Nonspherical particles, 166
Numerical, 57, 63, 64, 66, 68, 71, 72, 77, 86, 90, 97, 99

O
Optics, 69, 78, 79, 83, 91, 92

P
Particles, 63, 69, 70, 72, 78–84, 88, 92, 94, 98, 99
Polar, 53, 54, 86, 91, 99
Pollution, 78–81, 85, 89, 99
Porous materials, 114, 133, 166

R
Radiation, 53–55, 57–64, 66, 68, 69, 71–75, 77, 80, 81, 83–86, 88–98
Random forests, 176, 190, 191
Random mixture, 112, 115, 145, 150, 156–160, 162, 166
Random shape, 116
Random walks, 1, 4, 6, 15–17, 33, 34, 44
Rayleigh–Gans approximation, 129, 133, 135, 136, 138, 139, 154
Reflection, 62, 63, 71, 72, 79, 91
Refraction, 62, 64, 68, 69, 81, 82, 92, 93
Regularization, 176, 184, 186, 187
Resonance lines, 1, 3, 12–14, 18, 27, 41
Resonance scattering, 3, 34, 35, 37, 38, 45, 48
Retrieval, 176, 177, 186

S
Satellite observations, 175, 183, 187
Scattering, 54–60, 62, 64, 65, 70–72, 80–84, 89–99, 111, 112, 115, 116, 121, 125, 128–130, 132–134, 136, 139–141, 145, 146, 149–151, 153, 154, 156–159, 166, 182, 185
Scattering atmosphere, 2, 3, 7, 27, 38
Second solar spectrum, 34
Snow, 53–55, 59, 61, 62, 64–66, 68–74, 76–80, 82–89, 91, 96, 97, 99, 111, 114, 115, 141, 157–166, 168
Solar, 53, 54, 59–62, 64, 66, 68, 69, 71–75, 77, 78, 84–86, 88–91, 94–99
Soot, 78–86, 88, 89, 99
Source function, 6, 13, 19, 21, 23–26, 28, 31, 35–40, 46
Stereology, 111, 114
Support vector machine, 176

T
Thermalization length, 19, 26, 33

V
Visible, 55, 68, 69, 71–74, 77, 79, 81, 82, 84, 89, 92–96, 98, 99

W
Wentzel–Kramers–Brillouin approximation, 115, 135
Wiener–Hopf equation, 3, 4, 7, 8, 12, 13, 17, 23, 28, 29, 34, 35, 38, 41, 43–45